COLLECTED PAPERS on Nanophotonics

Vol. 25

August 2009 – July 2010

Prof. Motoichi OHTSU

MEMBERS

(From April 1, 2010)

*[I] THE UNIVERSITY OF TOKYO**

Professor

Motoichi OHTSU[(a-d)] (Dr. Eng.)

Associate Professor

Takashi YATSUI (Dr. Eng.)

Graduate Student (Doctor Candidate)

Takumi YAMAMOTO
Yang LIU

Graduate Students (Master Course)

Tetsu MORISHIMA
Ryoma OYAMA
Hiroaki TAKAGI
Masahiro TUJI
Kazunori IIJIMA
Fumihiro MORIGAKI
Kousuke NAKANISHI
Hironao TANOUCHI

Undergraduate Students

Takuro HAYASHI
Park SANG HOON
Mueed M A
Takahiro MOCHIZUKI

Secretaries

Sachiyo KOJIMA
Toshiko TERADA

a) Also a director “Nanophotonics Research Center, The Institute of Engineering

Innovation, School of Engineering The University of Tokyo”

b) Also a director, “NEDO Special Courses: A comprehensive activity for personnel training and industry-academia collaboration based on NEDO projects”, METI (Ministry of Economy, Trade and Industry) and NEDO (New Energy and Industrial Technology Development Organization)
c) Also a director, “Innovative Nanophotonics Components Development” project, METI (Ministry of Economy, Trade and Industry) and NEDO (New Energy and Industrial Technology Development Organization)
d) Also a director, NPO-Research Institute of Nanophotonics

(*)
Department of Electronics Engineering and Information Systems,
Graduate School of Engineering,
The University of Tokyo
(Room 215, Bldg. Eng. 9)
2-11-16 Yayoi, Bunkyo-ku, Tokyo 113-8656, Japan
Phone: +81-3-5841-1189
FAX: +81-3-5841-1140
E-mail: ohtsu@ee.t.u-tokyo.ac.jp
URL(1):http://uuu.t.u-tokyo.ac.jp/
URL(2):http://www.nanophotonics.info/

東京大学大学院 工学系研究科 電気系工学専攻
〒113-8656 東京都文京区弥生 2-11-16 工学部 9 号館 215 号室
電話: 03-5841-1189, ファックス: 03-5841-1140
E-mail: ohtsu@ee.t.u-tokyo.ac.jp
URL(1): http://uuu.t.u-tokyo.ac.jp/
URL(2):http://www.nanophotonics.info/

[II] NEDO Special Courses
A comprehensive activity for personnel training and industry-academia collaboration based on NEDO projects†

Visiting Project Associate Professor

Makoto NARUSE[(e)] (Dr. Eng.)

Project Research Associate

Kokoro KITAMURA (Dr. Eng.)
Wataru NOMURA (Dr. Eng.)
Naoya TATE (Dr. Eng.)

Manager

Kazuhiko TAMAKI

Secretaries

Kumiko NOZAWA
Kayoko SUZUKI

Visiting Scientists

Hiroyasu FUJIWARA[(f)]
Kazuya HIRATA[(g)]
Takashi MORIMOTO[(g)]
Tsutomu INOUE[(h)]
Syohei KURODA [(i)]

(e) Permanent affiliation: National Institute of Information and Communications Technology
(f) Permanent affiliation: Hamamatsu Photonics. K.K.
(g) Permanent affiliation: Sigma Koki Co., Ltd.
(h) Permanent affiliation: JASCO Corporation
(i) Permanent affiliation: POLA CHEMICAL INDUSTRIES, INC.

(†)
Department of Electronics Engineering and Information Systems,
Graduate School of Engineering,
The University of Tokyo
(Room 219, Bldg. Eng.-9)
2-11-16 Yayoi, Bunkyo-ku, Tokyo 113-8656, Japan
Phone: +81-3-5841-1670
FAX: +81-3-5841-1140
E-mail: info@ nanophotonics.t.u-tokyo.ac.jp
URL: http://uuu.t.u-tokyo.ac.jp/

東京大学大学院 工学系研究科 電気系工学専攻
〒113-8656 東京都文京区弥生 2-11-16 工学部 9 号館 219 号室
電話：+81-3-5841-1670, ファックス: +81-3-5841-1140
E-mail: info@ nanophotonics.t.u-tokyo.ac.jp
URL: http://uuu.t.u-tokyo.ac.jp/

[III] Innovative Nanophotonics Components Development Project (NEDO)[*]

Project Associate Professor

Tadashi KAWAZOE (Dr. Sci.)

Research Assistants

Susumu KAWADA
Etsuko OHTA
Katsuhito TAKAHASHI

(*)
Department of Electronics Engineering and Information Systems,
Graduate School of Engineering,
The University of Tokyo
(Room 408, Bldg. Eng.-9)
2-11-16 Yayoi, Bunkyo-ku, Tokyo 113-8656, Japan
Phone: +81-3-5841-1670
FAX: +81-3-5841-1140
URL: http://uuu.t.u-tokyo.ac.jp/

東京大学大学院 工学系研究科 電気系工学専攻
〒113-8656 東京都文京区弥生 2-11-16 工学部 9 号館 408 号室
電話: 03-5841-1670, ファックス: 03-5841-1140
URL: http://uuu.t.u-tokyo.ac.jp/

[IV] Strategic Development on Rationalization Technology using Energy (NEDO)‡

Research Assistants

Ayako MIZUSHIMA

(‡)

Department of Electronics Engineering and Information Systems,
Graduate School of Engineering,
The University of Tokyo
(Room 213, Bldg. Eng.-9)
2-11-16 Yayoi, Bunkyo-ku, Tokyo 113-8656, Japan
Phone: +81-3-5841-0416
FAX: +81-3-5841-0406
URL: http://uuu.t.u-tokyo.ac.jp

東京大学大学院 工学系研究科 電気系工学専攻
〒113-8656 東京都文京区弥生 2-11-16 工学部 9 号館 213 号室
電話: 03-5841-0416, ファックス: 03-5841-0406
URL: http://uuu.t.u-tokyo.ac.jp/
http://www.lux.t.u-tokyo.ac.jp/

[V] RESEARCH INSTITUTE OF NANOPHOTONICS†

Director

Motoichi OHTSU

(†)

Research Institute of Nanophotonics,
Nonprofit Organization
1-20-10 Sekiguchi, Bunkyo-ku, Tokyo 112-0014, Japan
Phone: +81-3-5225-6432. Fax: +81-3-5225-6435
E-mail: ohtsu-rinps@nanophotonics.t.u-tokyo.ac.jp
URL: http://www.nanophotonics.info/

特定非営利法人 ナノフォトニクス工学推進機構
〒112-0014 東京都文京区関口 1-20-10
電話: 03-5225-6432, ファックス: 03-5225-6435
E-mail: ohtsu-rinps@nanophotonics.t.u-tokyo.ac.jp
URL: http://www.nanophotonics.info/

LIST OF PAPERS

[(pp. XX-XX); pages in this issue of the COLLECTED PAPERS**]**

[I] ORIGINAL PAPERS

[1] H. Fujiwara, T. Kawazoe, and M. Ohtsu, "Nonadiabatic nondegenerate excitation by optical near-field and its application to optical pulse-shape measurement, " Appl. Phys. B- Lasers and Optics, Vol. 100, No. 1, July 2010, pp. 85-91

(pp. 1-7)

[2] W. Nomura, T. Yatsui, T. Kawazoe, M. Naruse, and M. Ohtsu, "Structural dependency of optical excitation transfer via optical near-field interactions between semiconductor quantum dots," Appl. Phys. B- Lasers and Optics, Vol. 100, No. 1, July 2010, pp. 181-187

(pp. 9-15)

[3] K. Kitamura, T. Yatsui, T. Kawazoe, M. Sugiyama, and M. Ohtsu, "Site-selective deposition of gold nanoparticles using non-adiabatic reaction induced by optical near-fields," Nanotechnology, Vol. 21, No. 28, July 2010, pp. 285302 1-4

(pp. 17-20)

[4] S. Yukutake, T. Kawazoe, T. Yatsui, W. Nomura, K. Kitamura, and M. Ohtsu, "Selective photocurrent generation in the transparent wavelength range of a semiconductor photovoltaic device using a phonon-assisted optical near-field process," Appl. Phys. B- Lasers and Optics, Vol. 99, No. 3, May 2010, pp. 415-422

(pp. 21-28)

[5] N. Tate, M. Naruse, T. Yatsui, T. Kawazoe, M. Hoga, Y. Ohyagi, T. Fukuyama, M. Kitamura, and M. Ohtsu, "Nanophotonic code embedded in embossed hologram for hierarchical information retrieval," Opt. Exp., Vol. 18, No. 7, March 2010, pp. 7497-7505

(pp. 29-37)

[6] T. Yatsui, Y. Ryu, T. Morishima, W. Nomura, T. Kawazoe, T. Yonezawa, M. Washizu, H. Fujita, and M. Ohtsu, "Self-assembly method of linearly aligning ZnO quantum dots for a nanophotonic signal transmission device," Appl. Phys. Lett., Vol. 96, No.13, March 2010, pp. 133106 1-3

(pp. 39-41)

[7] W. Nomura, T. Yatsui, Y. Yanase, K. Suzuki, M. Fujita, A. Kamata, M. Naruse, and M. Ohtsu, "Repairing nanoscale scratched grooves on polycrystalline ceramics using optical near-field assisted sputtering," Appl. Phys. B- Lasers and Optics, Vol. 99, No. 1-2, April 2010, pp. 75-78

(pp. 43-46)

[8] N. Tate, H. Tokoro, K. Takeda, W. Nomura, T. Yatsui, T. Kawazoe, M. Naruse, S-i, Ohkoshi, and M. Ohtsu, "Transcription of optical near-fields by photoinduced structural change in single crystal metal complexes for parallel nanophotonic processing," Appl. Phys. B- Lasers and Optics, Vol. 98, No. 4, March 2010, (pp. 685-689)

(pp. 47-51)

[9] H. Fujiwara, T. Kawazoe, and M. Ohtsu, "Nonadiabatic multi-step excitation for the blue–green light emission from dye grains induced by the near-infrared optical near-field," Appl. Phys. B- Lasers and Optics, Vol. 98, No. 2-3, February 2010, pp. 283-289

(pp. 53-59)

[10] T. Kawazoe, T. Takahashi, and M. Ohtsu, "Evaluation of the dynamic range and spatial resolution of nonadiabatic optical near-field lithography through fabrication of Fresnel zone plates," Appl. Phys. B- Lasers and Optics, Vol. 98, No. 1, January 2010, pp. 5-11

(pp. 61-67)

[11] K. Kitamura, T. Yatsui, and M. Ohtsu, "Observation of quantum confinement in ZnO nanorods fabricated using a two-temperature growth method," Appl. Phys. B-Lasers and Optics, Vol. 97, No. 4, December 2009, pp. 825-828

(pp. 69-72)

[12] T. Yatsui, S. Yamazaki, K. Ito, H. Kawamura, M. Mizumura, T. Kawazoe, and M. Ohtsu, "Increased spatial homogeneity in a light-emitting InGaN thin film using optical near-field desorption," Appl. Phys. B- Lasers and Optics, Vol. 97, No. 2, October 2009, pp. 375-378

(pp. 73-76)

[13] K. Nishibayashi, T. Kawazoe, M. Ohtsu, K. Akahane, and N. Yamamoto, "Observation of energy transfer between InAs quantum dots by pump-and-probe micro-photoluminescence measurement," J. of Luminescence, Vol. 129, Issue 12, December 2009, pp. 1912-1915

(pp. 77-80)

[14] T. Kawazoe, H. Fujiwara, K. Kobayashi, and M. Ohtsu, "Visible light emission from dye molecular grains via infrared excitation based on the nonadiabatic transition induced by the optical near field," J. of Selected Topics in Quantum Electronics, Vol. 15, Issue 5, September-October 2009, pp. 1380-1386

(pp. 81-87)

[15] M. Naruse, T. Kawazoe, R. Ohta, W. Nomura, and M. Ohtsu, "Optimal mixture of randomly dispersed quantum dots for optical excitation transfer via optical near-field interactions," Physical Review B, Vol. 80, No. 12, September 2009, pp. 125325 1-7
(selected for Virtual Journal of Nanoscale Science & Technology-- September 5,

2009, Vol. 20, Issue 14)

(pp. 89-95)

[16] M. Naruse, H. Hori, K. Kobayashi, M. Ishikawa, K. Leibnitz, M. Murata, N. Tate, and M. Ohtsu, "Information theoretical analysis of hierarchical nano-optical systems in the subwavelength regime," J. of the Opt. Soc. of Am. B, Vol. 26, No. 9, September. 2009, pp. 1772-1779

(pp. 97-104)

[II] PRESENTATIONS IN INTERNATIONAL CONFERENCES

[1] M. Mascheck, S. Schmidt, M. Silies, P. Vasa, D. Leipold, E. Runge, K. Kitamura, T. Yatsui, M. Ohtsu, and C. Lienau, "Localizing Few-Cycle Light Pulses in Space and Time in Random Dielectric Media," 17th International Conference on Ultrafast Phenomena, July 18-23, San Francisco, CA, USA (TuB6)

(pp. 105-106)

[2] M. Ohtsu, "Dressed photon technology for innovative optical devices, fabrications, and systems," Abstract Booklet of the 2010 International Symposium on Organic and Inorganic Electronic Materials and Related Nanotechnologies, The Japan Society of Applied Physics, June 22-25, Toyama, Japan, p. 26 (B-1)
[Invited presentation]

(p. 107)

[3] M. Ohtsu, "Nanophotonics: Dressed Photon Technology for innovative devices, fabrications, and systems," Proceedings of The International Conference of Nanophotonics 2010, May 30-June 3, 2010, Ibaragi, Japan, p. 1
[Keynote Lecture]

(p. 109)

[4] M. Naruse, T. Kawazoe, and M. Ohtsu, "Efficient and Robust Energy Transfer Network in Quantum Dot Mixtures via Optical Near-Fields Interactions," Technical Digest, CLEO/QELS 2010, May 16-21, 2010, San Jose, CA, USA (JThE18)

(pp. 111-112)

[5] W. Nomura, T. Yatsui, Y. Yanase, K. Suzuki, M. Fujita, A. Kamata, M. Naruse, and M. Ohtsu, "Self-organized Nonadiabatic Optical Near-field Assisted Sputtering for Repairing Surface Scratches on Al_2O_3 Ceramic Substrate," Technical Digest, CLEO/QELS 2010, May 16-21, 2010, San Jose, CA, USA (JTuC4)

(pp. 113-114)

[6] T. Yatsui, Y. Ryu, T. Morishima, W. Nomura, T. Yonezawa, M. Washizu, H. Fujita, and M. Ohtsu, "Self-organized nanophotonic signal transmission device," Technical Digest, CLEO/QELS 2010, May 16-21, 2010, San Jose, CA, USA (QFC6)

(pp. 115-116)

[7] M. Ohtsu, "Nanophotonic Devices by Dressed Photon Exchange," Technical Digest, Optical Fiber Communication Conference 2010, March 21-25, 2010, San Diego, CA , USA, p.54 (OMH2)

[Invited presentation]

(pp. 117-119)

[8] K. Kitamura, T. Yatsui, H. Yasuda, T. Kawazoe, and M. Ohtsu, "Phonon-assisted visible light photocatalyst using ZnO nanorods," International Symposium on Nano-Micro Multi-Functional Devices, March 18-19, 2010, Kawasaki, Japan, p. 48

(p. 121)

[9] T. Yatsui, and M. Ohtsu, "Progress in developing nano-scale photonic devices driven by an optical near-field," Frontier Photonics and Electronics, Proceedings of the Joint Workshop on Frontier Photonics and Electronics, March 4-5, 2010, Sydney, Australia, pp. 23-26
[Invited presentation]

(pp. 123-126)

[10] T. Yatsui, and M. Ohtsu, "Nanophotonic fabrication in sub-nm scale, " Photonic West 2010, Proceedings of SPIE Vol. 7586, Jan. 23-28, 2010, San Francisco, CA, USA, pp.75860D 1-8
[Invited Paper]

(pp. 127-134)

[11] M. Ohtsu, "Nanophotonics: Application to nonadiabatic fabrication," Technical Digest, The 7th Asia-Pacific Conference on Near-Field Optics, November 25-27, 2009, Jeju, Korea, p. 5
[Plenary presentation]

(p. 135)

[12] M. Naruse, H. Hori, K. Kobayashi, N. Tate, and M. Ohtsu**,** "Information Theoretic Analysis of Hierarchical Nano-Optical Systems," Technical Digest, The 7th Asia-Pacific Conference on Near-Field Optics, November 25-27, 2009, Jeju, Korea, p. 18 (I(2)-AW4)

(p. 137)

[13] S. Yukutake, T. Kawazoe, T. Yatsui, and M. Ohtsu, "Nonadiabatic wavelength-selective sensitization of the P3HT/ZnO photodetector using optical near field.," Technical Digest, The 7th Asia-Pacific Conference on Near-Field Optics, November 25-27, 2009, Jeju, Korea, I(2)-AW4, (p. 105)

(p. 139)

[14] Y. Fujiyoshi, M. Haraguchi, M. Fukui, T. Okamoto, T. Yatsui, and M. Ohtsu, "Numerical simulation for nonadiabatic optical near-field etching," Technical Digest, The 7th Asia-Pacific Conference on Near-Field Optics, November 25-27,

2009, Jeju, Korea, p. 182 (VI-PT-2)

(pp.141)

[15] T. Kawazoe, H. Fujiwara, and M. Ohtsu, "Visible light emission from DCM dye grains via infrared excitation due to the nonadiabatic transition induced by the optical near field," Technical Digest, The 7th Asia-Pacific Conference on Near-Field Optics, November 25-27, 2009, Jeju, Korea, p. 131 (I-PT-5)

(p. 143)

[16] T. Yatsui, Y. Ryu, T. Morishima, W. Nomura, T. Yonezawa, M. Washizu, H. Fujita, and M. Ohtsu, "Self-organized nanophotonic signal transmission device," Final program and Abstract, ISQNN 2009, November 18-20, 2009, Tokyo, Japan, p. 12

(pp. 145)

[17] M. Ohtsu, "Nanophotonics: Dressed photon science and technology," Abstracts of Final Program μTAS 2009 The 13th International Conference on Miniaturized Systems for Chemistry and Life Sciences, November 1-5, 2009, Jeju, Korea, pp. 39-40
[Plenary presentation]

(pp. 147-148)

[18] T. Yatsui and M. Ohtsu, "Progress in developing nanophotonic fabrication," 2009 IEEE LEOS Annual Meeting Conference Proceedings Pre-Proceedings, The 22nd Annual Meeting of the IEEE Photonics Society, October 4-8, 2009, Antalya, Turkey, pp. 22-23 (MC1)
[Invited presentation]

(pp. 149-150)

[19] N. Tate, W. Nomura, T. Yatsui, T. Kawazoe, M. Naruse, and M. Ohtsu, "Parallel retrieval of nanometer-scale light-matter interactions for nanophotonic systems," Pre-Proceedings, 4th International Workshop on Natural Computing, September 23-25, 2009, Hyogo, Japan, pp. 262-271

(pp. 151-160)

[20] M. Ohtsu, "Tutorial: Nanophotonics: Dressed Photon Technology for Innovative Optical Devices, Fabrications and Systems," Proceedings of the 35th European Conference on Optical Communication, September 20-24, 2009, Vienna, Austria, (3.6.1)
[Tutorial presentation]

(p. 161)

[21] M. Naruse, N. Tate, and M. Ohtsu, "System Architectures for

Nanophotonics for Information and Communications Applications," Proceedings of The 8th Pacific Rim Conference on Lasers and Electro-Optics (CLEO Pacific Rim 2009), August 31-September 3, 2009, Shanghai, China (WJ2-2)
[Invited presentation]

(pp. 163-164)

[III] REVIEW PAPERS

[1] M. Ohtsu, “NEDO Special Course: On-the-Research-Training of Engineers and Scientists for Promoting Advanced Optical Technology,” Kogaku Japanese Journal of Optics, Vol. 39, No.6, June, 2010, p.277(19)-281(23)
【大津元一、「NEDO 特別講座　－光技術の最先端分野を推進する技術者・研究者育成－」、～光学分野における人材育成～、『光学』、第 39 巻、第 6 号、2010 年 6 月、(pp. 277(19)-281(23))】

(pp. 165-169)

[2] T. Yatsui, and M. Ohtsu, “Nanophotonic devices,” O plus E, Vol. 32, No.2, February, 2010, pp. 136-139
【八井崇、大津元一、「ナノフォトニックデバイス」、～特集：ナノフォトニクス～、『O plus E』、第 32 巻、第 2 号、通巻 363 号、2010 年 2 月、pp. 136-139】

(pp. 171-174)

[3] T. Yatsui, and M. Ohtsu, “Progress in nanophotonic fabrication,” Optical and Electro-Optical Engineering Contact, Vol. 47, No.11, November, 2009, pp. 563-569 (pp. 3-9)
【八井崇、大津元一、「最近のナノフォトニック加工技術」、～特集：最近のナノフォトニクス（2）～、『光技術コンタクト』、第 47 巻、第 11 号、通巻 552 号、2009 年 11 月号、pp. 563-569 (pp. 3-9)】

(pp. 175-180)

[4] M. Ohtsu, “Progress in Light-matter Fusion Science and Technology,” Preface, Journal of The Surface Science Society of Japan HYOMEN KAGAKU, Vol. 30, No.11, November, 2009, p.599
【大津元一、「光・物質融合科学技術が進む」、 巻頭言、 ～特集：近接場光を用いた光工学技術の革新的発展～、『表面科学』、第 30 巻、第 11 号、2009 年 11 月、p. 599】

(p. 181)

[5] M. Ohtsu, “Qualitative Innovation of Optical Technology by Optical Near Fields,” Journal of The Surface Science Society of Japan HYOMEN KAGAKU, Vol. 30, No.11, November, 2009, pp. 600-606
【大津元一、「近接場光による光技術の質的変革」、 ～特集：近接場光を用いた光工学技術の革新的発展～、『表面科学』、第 30 巻、第 11 号、2009 年 11 月、pp. 600-606】

(pp. 183-189)

[6] M. Ohtsu, “Ohtsu-Yatsui Laboratory, Graduate School of Engineering The University of Tokyo,” Vol. 20, No.11, September, 2009, p. 60-61
【大津元一、「東京大学大学院工学系研究科大津・八井研究室　＝ドレスト光子の科学とナノフォトニクス技術の開拓＝」、研究室紹介、『光アライアンス』、第 20 巻、第 11 号、2009 年 11 月、pp. 60-61】

(pp. 191-192)

[7] M. Ohtsu, “NEDO Special Course: On-the-Research-Training of Engineers and Scientists for Promoting Advanced Optical Technology,” Vol. 20, No.9, September, 2009, p. 19-23
【大津元一、「NEDO 特別講座「ナノフォトニクスの総合的展開」、『特集：光科学の研究拠点へ ～創出ラッシュ～、『光アライアンス』、第 20 巻、第 9 号、2009 年 9 月、pp. 19-23】

(pp. 193-197)

[Ⅳ] AWARDS

[1] M. Ohtsu, *Julius Springer Prize 2009*, Springer, September 22, 2009
【大津元一、「*Julius Springer Prize 2009*」シュプリンガー、2009 年 9 月 22 日】

[I] ORIGINAL PAPERS

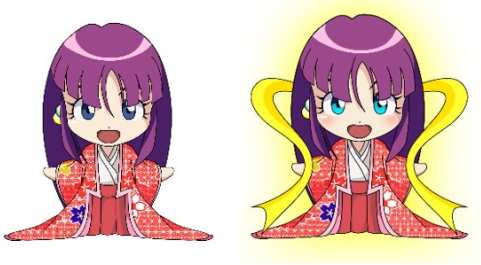

Appl Phys B (2010) 100: 85–91
DOI 10.1007/s00340-010-3976-z

Applied Physics B
Lasers and Optics

Nonadiabatic nondegenerate excitation by optical near-field and its application to optical pulse-shape measurement

H. Fujiwara · T. Kawazoe · M. Ohtsu

Received: 12 February 2010 / Published online: 16 March 2010

Abstract Using DCM dye grains and light of different wavelengths generated by two CW laser diodes that oscillate in the near-infrared wavelength region, visible light emission from dye grains due to near-infrared excitation based on a nonadiabatic, nondegenerate excitation process was observed for the first time. Unlike sum-frequency generation with nonlinear polarization, the difference in polarization angles of the two beams did not affect the emitted light intensity. Optical sampling based on this nonadiabatic, nondegenerate excitation principle was demonstrated for the first time. The optical pulse shape in the wavelength band of $\lambda = 1250$–1350 nm, which is close to the wavelength range used for optical fiber communications, was measured with a temporal resolution of 0.8–1.1 ps.

1 Introduction

There is much demand for optical pulse measurement in the near infrared region at wavelengths of about 1–1.5 μm, which includes optical pulses used in optical fiber communication and pulses from fiber lasers that oscillate in the near infrared region [1–3]. However, the measurement is not easy because there is no photodetector with a high enough sensitivity and a high temporal resolution for this wavelength region. In order to measure optical pulse shapes in the picosecond/femotosecond regime in this wavelength band, sum-frequency generation (SFG) with nonlinear crystals can be used to convert light of a certain wavelength to a shorter wavelength, whose intensity can then be measured with a photodetector that is sensitive to visible light [4–7]. Because the temporal resolution is determined by the width of the sampling pulse, a high temporal resolution can be obtained by using a short laser pulse. With this method, however, the signal beam (beam to be measured), the sampling beam, and the converted beam (to a short wavelength) must satisfy phase matching conditions [8–11]. As a result, depending on the wavelength of the beam to be measured, it is necessary to provide an optical element for polarization control, such as a wavelength plate, to adjust the incident angle to nonlinear crystals; therefore, this method may not be suitable for measuring beams with a wide wavelength band or exhibiting polarization dependence.

In our past research, we have succeeded in generating visible light through nonadiabatic excitation of dye grains using near-infrared light [12, 13]. These dyes are transparent to near-infrared light; however, individual protrusions on the dye grains serve as sources of optical near-fields. The energy of these optical near-fields is transferred to dye grains in the vicinity, and their dye molecules are nonadiabatically excited to a vibrational state of higher energy with the aid of the phonon energy in the grains (Fig. 1). Because this intermediate excited state ($|E_g; \mathrm{el}\rangle \bigotimes |E_a; \mathrm{vib}\rangle$) is a real energy state, excitation to an even higher energy state ($|E_{\mathrm{ex}}; \mathrm{el}\rangle \bigotimes |E_b; \mathrm{vib}\rangle$ or $|E_g; \mathrm{el}\rangle \bigotimes |E_c; \mathrm{vib}\rangle$) is pos-

H. Fujiwara (✉)
Central Research Laboratories, Hamamatsu Photonics K.K., Hirakuchi 5000, Hamakita-ku, Hamamatsu 434-8601, Japan
e-mail: fujiwara@crl.hpk.co.jp
Fax: +81-53-585-0673

T. Kawazoe · M. Ohtsu
Department of Electrical Engineering and Information Systems, Graduate School of Engineering, The University of Tokyo, 2-11-16 Yayoi, Bunkyo-ku, Tokyo 113-8656, Japan

T. Kawazoe · M. Ohtsu
Nanophotonics Research Center, Graduate School of Engineering, The University of Tokyo, 2-11-16 Yayoi, Bunkyo-ku, Tokyo 113-8656, Japan

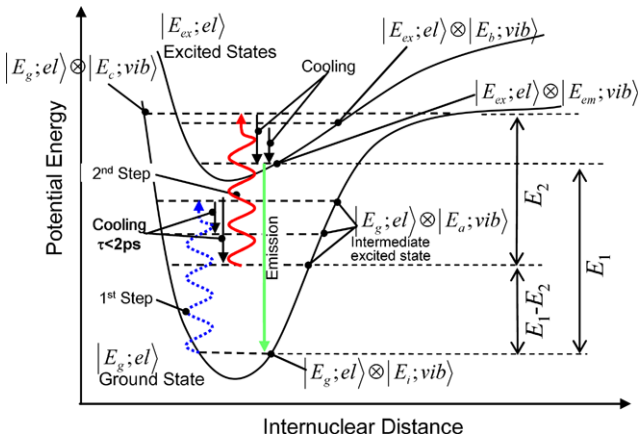

Fig. 1 Illustration explaining the origin of the visible light emission by a two-step process based on the nonadiabatic excitation induced by an optical near-field

sible with the subsequent transfer of the optical near-field energy. Eventually, the dye molecules are excited to an electronic excited state ($|E_{ex}; el\rangle \bigotimes |E_{em}; vib\rangle$), generating visible light.

It has been speculated that nonadiabatic excitation is possible even if the excitation beam used to cause excitation to this intermediate excited state (indicated as 1st step in Fig. 1) and the second excitation beam (2nd step) differ from each other in terms of wavelength, etc. (i.e., mutually nondegenerate). Also, because the energy of the intermediate excited state is greater than the thermal energy, which is determined by the sample temperature, it cools to a lower energy state; however, in the case of dye grains, the amount of time that the dye molecules maintain the energy difference E1–E2 (defined as the lifetime of the intermediate excited state, τ), where E1 is the energy needed for excitation to the electronic excited state (i.e., the origin of light emission) and E2 is the light energy needed for the second excitation from the intermediate excited state, has been experimentally shown to be extremely rapid, at about 2 ps or less [13].

By exploiting this phenomenon, assuming the signal beam to be the beam for the first excitation, the sampling beam to be the beam for the second excitation, and visible light emission of the dye to be the resultant sampling signal, optical measurement with a temporal resolution of 2 ps should be possible. This optical measurement method does not use nonlinear polarization with polarization dependence but makes use of the vibrational level of molecules with a continuous energy distribution as an intermediate excited state. Therefore, an optical measurement device with a simple optical system, free of polarization dependence, and with a wide measurable wavelength band should be possible. In this paper, we reveal the existence of a nonadiabatic excitation process induced by mutually nondegenerate beams, and we discuss the potential application of this excitation process to optical pulse-shape measurement.

2 Nonadiabatic excitation and light emission with two nondegenerate beams

Using the dye 4-dicyanomethylene-2-methyl-6-p-dimethylaminostyryl-4H-pyran (DCM), dye grains were obtained by dispersing DCM powder in ethanol solution, placing the solution in quartz cells, and evaporating the solution. The size of dye grains is distributed between 10 nm and several microns. The resulting thickness of dye grains in the quartz cells was 1 mm. DCM has an absorption edge wavelength of about 560 nm and does not absorb near-infrared light in the wavelength range of about 750–1350 nm [14]. However, our previous research has shown that, by irradiating the dye with near-infrared light at wavelengths of about 750–808 nm, the dye molecules are nonadiabatically excited, generating visible light at wavelengths of about 650–700 nm [12].

Using two laser diodes that generated two beams of differing wavelengths as excitation light sources, the emitted light intensities obtained by irradiating the dye grains with the generated CW beams simultaneously or separately were measured and compared. The properties of the first beam (referred to as "signal beam" hereafter) were: wavelength $\lambda_1 = 1150$ nm; intensity $I_{ex(1150)} = 0.55$–2.28 W/cm^2; and linear polarization. The properties of the second beam (referred to as "sampling beam" hereafter) were: wavelength $\lambda_2 = 808$ nm; intensity $I_{ex(808)} = 2.0$–19.9 W/cm^2; and elliptical polarization. Emission spectra of the dye grains were measured using a CCD linear image sensor with a spectrometer (C10027-02 Hamamatsu Photonics KK).

The emission spectra are shown in Fig. 2a. The broken-line curve indicates the emitted light intensity, $I_{1150}(\lambda)$, obtained when the signal beam alone was radiated. The dotted-line curve indicates the emitted light intensity, $I_{808}(\lambda)$, obtained when the sampling beam alone was radiated. The solid curve indicates the emitted light intensity, $I_{1150+808}(\lambda)$, obtained when the two beams were radiated simultaneously. The value of $I_{1150}(\lambda)$ was small, approximately equivalent to the noise level of the detector; nonetheless. The value of $I_{1150+808}(\lambda)$ was larger than the sum of the emitted light intensities obtained by separately radiating the signal beam or the sampling beam, i.e. $I_{1150}(\lambda) + I_{808}(\lambda)$. This result suggests that there is an excitation process induced by the simultaneous radiation of the signal beam and the sampling beam. The triangles in Fig. 2b show the relationship between the emitted light intensity $I_{1150}(\lambda)$ at $\lambda = 680$ nm (i.e., $I_{1150}(680)$) and the excitation light intensity $I_{ex(1150)}$ (signal beam intensity). Similarly, squares show the relationship between the emitted light intensity $I_{808}(\lambda)$ at $\lambda = 680$ nm (i.e., $I_{808}(680)$) and the excitation light intensity $I_{ex(808)}$ (sampling beam intensity). Because the values of $I_{1150}(680)$ were small, being approximately equivalent to the noise level of the detector, the relationship between $I_{1150}(680)$ and $I_{ex(1150)}$ is not clear. On the other hand, $I_{808}(680)$ was proportional to $I_{ex(808)}$ under weak excitation and proportional

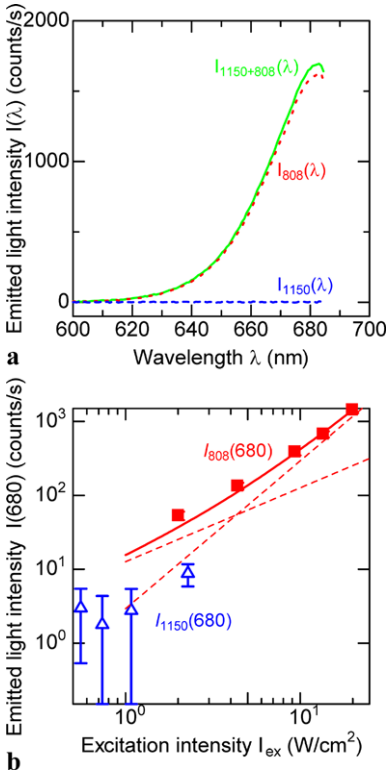

Fig. 2 **a** Emitted light spectra of visible light emission from the DCM dye grains due to near-infrared excitation. Wavelength region greater than $\lambda = 685$ nm is not shown due to optical attenuation by a short-pass filter used for eliminating stray light. The *broken-line curve* is the result for irradiation with the signal beam only (signal beam intensity $I_{\mathrm{ex}(1150)} = 0.55$ W/cm^2). The *dotted-line curve* is the result for irradiation with the sampling beam only (excitation beam intensity $I_{\mathrm{ex}(808)} = 19.9$ W/cm^2). The *solid-line curve* is the result for simultaneous irradiation with the signal beam and the sampling beam. **b** The excitation intensity dependence of the emitted light intensity. *Triangles* indicate the excitation intensity $I_{\mathrm{ex}(1150)}$ dependence of the emitted light intensity $I_{1150}(680)$. *Squares* indicate the excitation intensity $I_{\mathrm{ex}(808)}$ dependence of the emitted light intensity $I_{808}(680)$. The *solid-line curve* is the result of curve fitting for $I_{808}(680)$ with a quadratic function

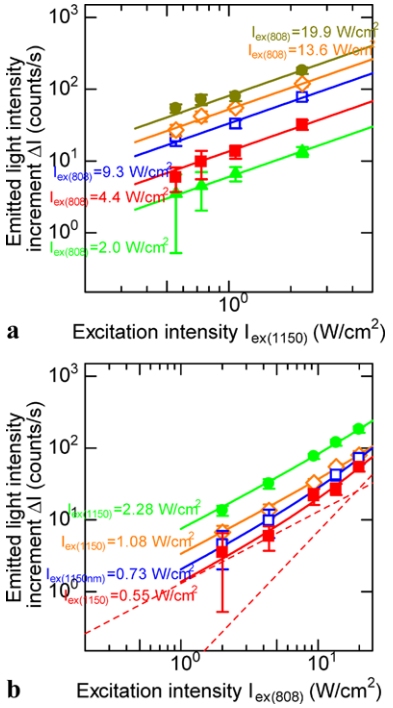

Fig. 3 **a** The signal beam intensity $I_{\mathrm{ex}(1150)}$ dependence of the emitted light intensity increment ΔI. The *solid straight lines* are the results of curve fitting for ΔI with linear functions. **b** The sampling beam intensity $I_{\mathrm{ex}(808)}$ dependence of the emitted light intensity increment ΔI. The *solid-line curves* are the results of curve fitting ΔI with quadratic functions

to $I^2_{\mathrm{ex}(808)}$ under strong excitation. The solid-line curve in the figure was obtained by least squares fitting of a quadratic function, and the broken-line curves show components proportional to $I_{\mathrm{ex}(808)}$ and $I^2_{\mathrm{ex}(808)}$. These components correspond to the one step and the two steps of the nonadiabatic excitation process, respectively [12, 13].

The excitation process responsible for ΔI will now be discussed, where ΔI is the emitted light intensity increment caused by the simultaneous radiation of the signal beam and the sampling beam, defined as $\Delta I = I_{1150+808}(680) - \{I_{1150}(680) + I_{808}(680)\}$. Figure 3a shows the relationship between ΔI and the intensity of the signal beam used for excitation, $I_{\mathrm{ex}(1150)}$, with the intensity of the sampling beam, $I_{\mathrm{ex}(808)}$, as a parameter. The solid straight lines in the figure were obtained by least squares fitting of linear functions, and their agreement with the experimental values indicates that one photon of the signal beam contributes to the excitation process. On the other hand, Fig. 3b shows the relationship between ΔI and the intensity of the sampling beam used for excitation, $I_{\mathrm{ex}(808)}$, with the intensity of the signal beam $I_{\mathrm{ex}(1150)}$ as a parameter. The solid-line curves in the figure were obtained by least squares fitting of quadratic functions, and the straight lines shown in broken lines represent values proportional to $I_{\mathrm{ex}(808)}$ and $I^2_{\mathrm{ex}(808)}$ when $I_{\mathrm{ex}(1150)} = 0.55$ W/cm^2. These results show that ΔI was proportional to $I_{\mathrm{ex}(808)}$ under weak excitation and proportional to $I^2_{\mathrm{ex}(808)}$ under strong excitation. The components that are proportional to $I_{\mathrm{ex}(808)}$ and $I^2_{\mathrm{ex}(808)}$ correspond to the one step and the two steps of the nonadiabatic excitation process, respectively.

The signal beam and the sampling beam were mutually nondegenerate, having no correlation in their phases, and they were also low intensity CW beams. Therefore, the excitation process due to the simultaneous radiation of the signal beam and the sampling beam is likely not a multi-photon excitation process via a virtual energy state, but a nonadiabatic multi-step excitation process brought about by the two mutually nondegenerate beams.

Considering the dependence of ΔI on the excitation intensities (i.e., $I_{\mathrm{ex}(1150)}$ and $I_{\mathrm{ex}(808)}$), seven potential excitation processes (Processes 1–7) were identified, as shown

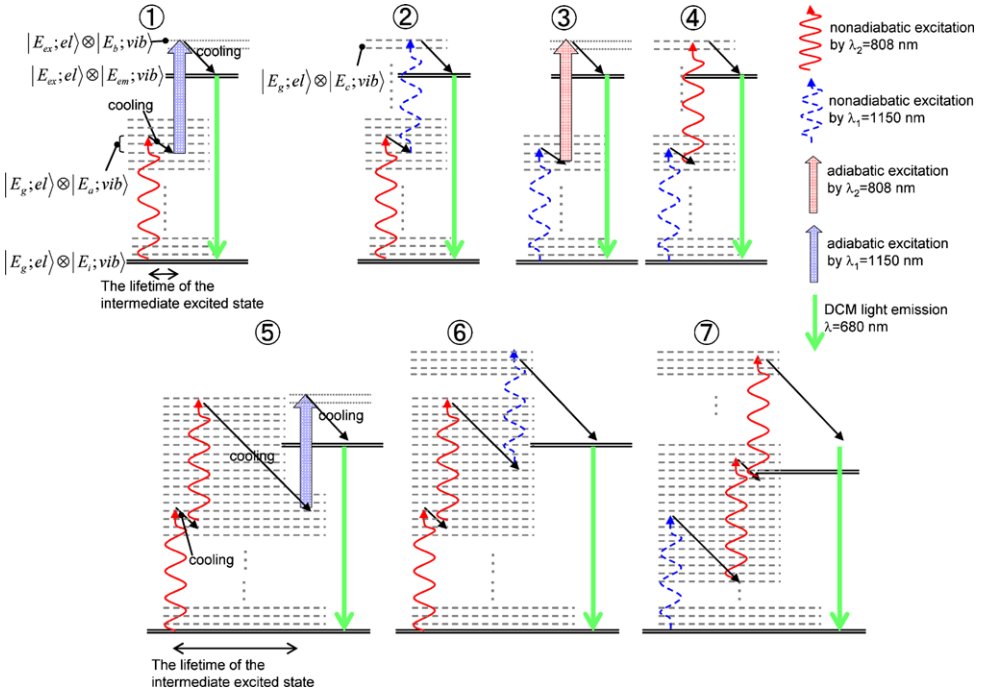

Fig. 4 Energy diagrams of nonadiabatic excitation process of the DCM dye grains by the sampling beam and the signal beam. The *broken lines* represent vibrational states of dye molecules at electronic ground states, the *dotted lines* represent the vibrational states of dye molecules at electronic excited states. The *elapsed time* from the initial excitation of dye molecules at the ground state $|E_g; \mathrm{el}\rangle \bigotimes |E_i; \mathrm{vib}\rangle$ is shown on the *horizontal axes*

in Fig. 4. For all seven cases, the elapsed time after excitation of dye molecules from the ground state, i.e., $|E_g; \mathrm{el}\rangle \bigotimes |E_i; \mathrm{vib}\rangle$, is shown on the horizontal axes.

Process 1 Dye molecules are excited to an intermediate excited state, $|E_g; \mathrm{el}\rangle \bigotimes |E_a; \mathrm{vib}\rangle$, by nonadiabatic excitation by the sampling beam, after which, they cool to a lower energy state, approaching thermal equilibrium, $|E_g; \mathrm{el}\rangle \bigotimes |E_i; \mathrm{vib}\rangle$. In this process, however, the molecules are adiabatically excited to an excited state, $|E_{\mathrm{ex}}; \mathrm{el}\rangle \bigotimes |E_b; \mathrm{vib}\rangle$, by the signal beam, eventually transiting to an electronic excited state, $|E_{\mathrm{ex}}; \mathrm{el}\rangle \bigotimes |E_{\mathrm{em}}; \mathrm{vib}\rangle$, which is the origin of light emission.

Process 2 This process is similar to Process 1 described above, but the excitation by the signal beam is nonadiabatic. In this case, the dye molecules are excited by the signal beam from the intermediate excited state, $|E_g; \mathrm{el}\rangle \bigotimes |E_a; \mathrm{vib}\rangle$, to an even higher vibrational state, $|E_g; \mathrm{el}\rangle \bigotimes |E_c; \mathrm{vib}\rangle$. Eventually, transition to $|E_{\mathrm{ex}}; \mathrm{el}\rangle \bigotimes |E_{\mathrm{em}}; \mathrm{vib}\rangle$ occurs by coupling of a higher vibrational state with an electronic excited state.

Process 3 Molecules are excited to an intermediate excited state by the nonadiabatic excitation by the signal beam, after which, they cool to a lower energy state; however, in this process, they are adiabatically excited by the sampling beam to $|E_{\mathrm{ex}}; \mathrm{el}\rangle \bigotimes |E_{\mathrm{em}}; \mathrm{vib}\rangle$.

Process 4 This process is similar to Process 3 described above, but the excitation by the sampling beam is nonadiabatic, causing an excitation to $|E_{\mathrm{ex}}; \mathrm{el}\rangle \bigotimes |E_{\mathrm{em}}; \mathrm{vib}\rangle$.

Process 5 Nonadiabatic excitation by the sampling beam is repeated twice in exciting the molecules to the intermediate excited state, after which, they cool to a lower energy state; however, in this process, they are adiabatically excited by the signal beam to $|E_{\mathrm{ex}}; \mathrm{el}\rangle \bigotimes |E_{\mathrm{em}}; \mathrm{vib}\rangle$.

Process 6 This process is similar to Process 5 described above, but the excitation by the signal beam is nonadiabatic, causing an excitation to $|E_{\mathrm{ex}}; \mathrm{el}\rangle \bigotimes |E_{\mathrm{em}}; \mathrm{vib}\rangle$.

Process 7 The molecules are nonadiabatically excited to the intermediate excited state by the signal beam, after which, they cool to a lower energy state, then they are nonadiabatically excited by the sampling beam, twice in succession, to $|E_{\mathrm{ex}}; \mathrm{el}\rangle \bigotimes |E_{\mathrm{em}}; \mathrm{vib}\rangle$.

In Fig. 3b, because ΔI has a primary dependency of the sampling beam intensity $I_{\mathrm{ex}(808)}$ under weak excitation, two-photon energy associated with Processes 1–4 is sufficient as the excitation energy required for light emission from the dyes. Nevertheless, Processes 5–7, involving three photons, appeared because there are dye molecules having low coupling efficiency between the electronic excited state and the molecular higher vibrational state of the ground state, and, in Processes 2 and 4, they do not relax to the electronic excited state $|E_{\mathrm{ex}}; \mathrm{el}\rangle \bigotimes |E_{\mathrm{em}}; \mathrm{vib}\rangle$ but approach thermal equilibrium by cooling. In these Processes 5–7, the time required

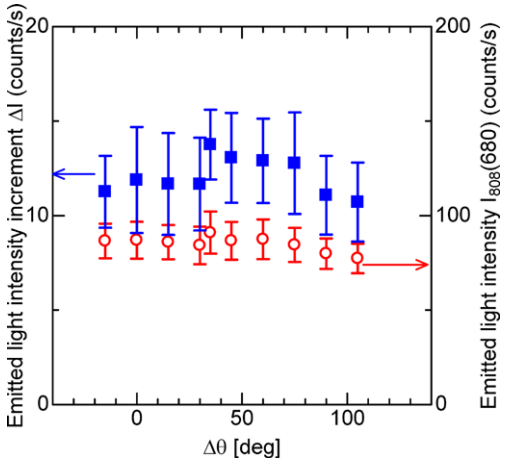

Fig. 5 The relationship between the emitted light intensity increment ΔI and the polarization angle difference $\Delta\theta$ between the signal beam and the sampling beam

to reach the electronic excited state $|E_{ex}; \mathrm{el}\rangle \bigotimes |E_{em}; \mathrm{vib}\rangle$, which is the origin of the dye light emission, after the dye molecules in the ground state are excited (i.e., the lifetime of the intermediate excited state) is longer than it is in Processes 1–4.

Next, in order to investigate the dependence of the difference in polarization angle between the sampling beam and the signal beam, $\Delta\theta$, on ΔI, the following experiment was conducted. A polarizer and a neutral density (ND) filter were placed in the optical path of the sampling beam, and the polarization direction of the linearly polarized sampling beam was controlled while keeping the intensity of a sampling beam incident on the sample constant, i.e., $I_{ex(808)} = 2.2\ \mathrm{W/cm^2}$. The relationship between ΔI and $\Delta\theta$ is shown in Fig. 5. The values of ΔI showed nearly no change with respect to $\Delta\theta$. Fluctuations in the values are likely due to the precision in adjusting the sampling beam intensity $I_{ex(808)}$ with the ND filter. In support of this, when dye grains are singly irradiated with a sampling beam whose polarization direction is tilted from that of the signal beam by $\Delta\theta$, the resulting emitted light intensity $I_{808}(680)$ actually shows a fluctuation similar to ΔI. Therefore, ΔI is independent of the difference in polarization angle between the sampling beam and the signal beam. Possible reasons for this lack of dependence are that the orientation of the dye grains is random, and that the intermediate excited state is a real energy state and information about the polarization direction of the beam that excites the dye molecules to the intermediate excited state is lost. This non-dependence of the emitted light intensity on the difference in polarization angle between the two beams is a considerably different property from sum-frequency generation with nonlinear polarization, in which there is a dependence on the polarization angles of the sampling beam and the signal beam [15].

The above experimental results showed, for the first time, the existence of a nonadiabatic excitation process by two mutually nondegenerate beams. In addition, unlike sum-frequency generation with nonlinear polarization, with this excitation process, the emitted light intensity did not change with respect to the difference in polarization angle between the two beams.

3 Application to optical pulse-shape measurement

Turning now to a practical application of the nonadiabatic excitation process by two mutually nondegenerate beams discussed in the previous section, if the sampling beam and light emission from the dye grains were considered as an optical pulse and a result of sampling, respectively, application to optical sampling for measuring the pulse shape of a signal beam is possible. Pulse-shape measurement using such a method was attempted for the first time with the measuring device illustrated in Fig. 6a. The signal pulse (center wavelength $\lambda_1 = 1250$–1350 nm; mean intensity $I_1 = 1.3\ \mathrm{W/cm^2}$; repetition frequency = 80 MHz) to be measured was generated with a Ti:sapphire laser and an optical parametric oscillator (OPO). Light at this wavelength can also be used for optical fiber communication. Also, the pump beam of the OPO was used as the sampling pulse (center wavelength $\lambda_2 = 750$–775 nm; intensity $I_2 = 3.2$–$5.1\ \mathrm{W/cm^2}$; repetition frequency = 80 MHz). After passing through separate optical paths, the two pulses were directed to the same optical path using half mirrors and were made incident on DCM dye grains at an identical position. Note that the polarization directions of the signal beam and the sampling beams were perpendicular to each other. The length of the optical path for the optical pulse to be measured was made variable to control the difference in time at which the two optical pulses were incident on the dye grains (i.e., delay time), Δt. Components of the emitted light intensity $I(\lambda, \Delta t)$ at the wavelength $\lambda = 680$ nm (i.e., $I(680, \Delta t)$) were extracted with a spectrometer; and the measurement was made using a photomultiplier tube (H7421-40, Hamamatsu Photonics K. K.). When $\Delta t < 0$, the sampling beam reaches the dye grain before the signal beam does, making it possible to observe light emission by Processes 1, 2, 5, and 6 in Fig. 4. On the other hand, when $\Delta t > 0$, the sampling beam reaches the dye grains after the signal beam, making it possible to observe light emission by Processes 3, 4, and 7.

Figure 6b shows the results of pulse-shape measurement for the signal beam (wavelength $\lambda_1 = 1250$ nm, intensity $I_1 = 1.3\ \mathrm{W/cm^2}$), where the sampling beam had a wavelength $\lambda_2 = 750$ nm and intensity $I_2 = 3.2\ \mathrm{W/cm^2}$. The vertical axis in the figure shows the increment in emitted light intensity, $\Delta I(680, \Delta t)$, defined as: $\Delta I(680, \Delta t) = (I(680, \Delta t) - I(680, -\infty))$. In the vicinity of $\Delta t = 0$, values of $\Delta I(680, \Delta t)$ can be clearly observed because of the

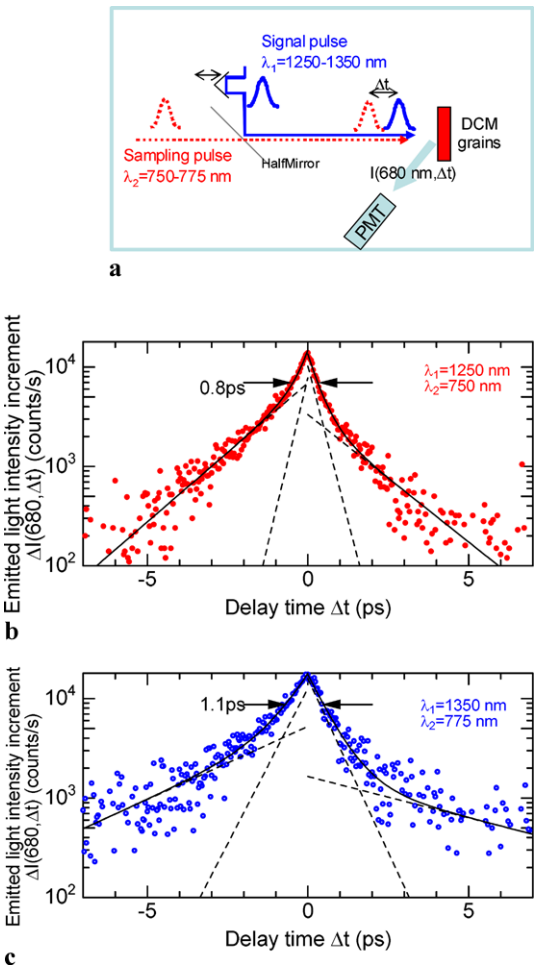

Fig. 6 **a** Schematic representation of the optical pulse measurement system using the nonadiabatic excitation light emission induced by nondegenerate beams. **b** Signal wave profiles with $\lambda_1 = 1250$ nm and intensity $I_1 = 1.3$ W/cm^2, and with $\lambda_2 = 750$ nm and $I_2 = 3.2$ W/cm^2. **c** Signal wave profiles with $\lambda_1 = 1350$ nm and intensity $I_1 = 1.3$ W/cm^2, and with $\lambda_2 = 775$ nm and intensity $I_2 = 5.1$ W/cm^2. The *solid-line curves* in **b** and **c** are the results of curve fitting ΔI with the sum of two exponential functions. The *broken lines* indicate the respective exponential functions: $A\exp(-\Delta t/\tau_{\text{fast}}) + B\exp(-\Delta t/\tau_{\text{slow}})$ for $\Delta t > 0$, and $C\exp(\Delta t/\tau_{\text{fast}}) + D\exp(\Delta t/\tau_{\text{slow}})$ for $\Delta t < 0$

light emission based on the nonadiabatic excitation process induced by the nondegenerate beams (i.e., the signal beam and the sampling beam). The signal to noise ratio (S/N) of this signal wave profile was 34, and its full width at half maximum was about 0.8 ps. The actual time interval of an incident optical pulse can be estimated from its spectral width, and the pulse widths for the signal beam and the sampling beam were estimated to be about 0.2 ps and 0.1 ps, respectively. These estimated widths are smaller than those determined by the measurements in this study. The reasons for this inconsistency were considered. Curve fitting for $\Delta I(680, \Delta t)$ was possible with use of the sum of two exponential functions for the time regions $\Delta t < 0$ and $\Delta t > 0$, respectively (i.e., $A\exp(-\Delta t/\tau_{\text{fast}}) + B\exp(-\Delta t/\tau_{\text{slow}})$ for $\Delta t > 0$ and $C\exp(\Delta t/\tau_{\text{fast}}) + D\exp(\Delta t/\tau_{\text{slow}})$ for $\Delta t < 0$). Solid-line curves in Fig. 6b are the results of least squares fitting. For the region $\Delta t > 0$, decay time constants τ_{fast} and τ_{slow} were 0.35 ps and 1.7 ps, respectively. The coefficient B of the decay component with the decay time constant τ_{slow} is about 1/4 of the coefficient A of the decay component with the decay time constant τ_{fast}. On the other hand, for the region $\Delta t < 0$, the decay time constants τ_{fast} and τ_{slow} were 0.3 ps and 1.6 ps. There is no substantial difference between the coefficient D of the decay component with the decay time constant τ_{slow} and the coefficient C of the decay component with the decay time constant τ_{fast}. Also, as compared with the region $\Delta t > 0$, the decay component with τ_{slow} has a greater proportion with respect to $\Delta I(680, \Delta t)$. Consequently, the signal waveform profile shown in Fig. 6b is not symmetrical around $\Delta t = 0$, and compared with the region $\Delta t < 0$, the curve shows a steeper slope in the region $\Delta t > 0$. The decay time constants τ_{fast} and τ_{slow} can be considered as the lifetime of the intermediate excited state, because the values of τ_{fast} and τ_{slow} (i.e., 0.3–1.7 ps) were approximately equivalent to the lifetime of the intermediate excited states obtained for Coumarin 480 and Coumarin 540A dye grains (i.e., 1.1–1.9 ps) in an experiment on nonadiabatic excitation light emission induced by degenerate beams [13]. Therefore, the temporal resolution of this measurement method (i.e., full width at half maximum of 0.8 ps) is likely determined by the lifetime of the intermediate excited state. Although further investigation is needed to provide a detailed explanation, the presence of the two decay time constants, τ_{fast} and τ_{slow} may be explained by the sampling beam contributing to $\Delta I(680, \Delta t)$ through both the two-step (Processes 1, 2 ($\Delta t < 0$), 3, and 4 ($\Delta t > 0$)) and the three-step (Processes 5, 6 ($\Delta t < 0$), and 7 ($\Delta t > 0$)) of the nonadiabatic nondegenerate excitation process.

The signal waveform profile shown in Fig. 6b is not symmetrical around $\Delta t = 0$ because the dye grains receive different levels of excitation energy from the beam that reaches them first, depending on the excitation routes (Processes 1, 2, 5, and 6 vs. Processes 3, 4, and 7), and because the lifetime of the intermediate excited states differ accordingly. When $\Delta t > 0$, a signal beam with a long wavelength reaches the dye grains first to excite them to the intermediate excited state, but the photon energy of this excited state is lower than that of the sampling beam with a short wavelength. Therefore, because the lifetime of the intermediate excited state is short, the waveform profile in the $\Delta t > 0$ region is steeply sloping downward.

Figure 6c shows the results of pulse-shape measurement for the signal beam (wavelength $\lambda_1 = 1350$ nm, intensity $I_1 = 1.3$ W/cm^2) where the sampling beam had a wavelength $\lambda_2 = 775$ nm and intensity $I_2 = 5.1$ W/cm^2. Keeping the incident angle to the sample identical to the case

shown in Fig. 6b, a signal waveform with an S/N of 19 and a full width at half maximum of about 1.1 ps was measured. As with Fig. 6b, curve fitting for the signal waveform $\Delta I(680, \Delta t)$ is possible with use of the sum of two exponential functions for the time regions $\Delta t < 0$ and $\Delta t > 0$, respectively. For the region $\Delta t > 0$, decay time constants τ_{fast} and τ_{slow} were 0.62 ps and 5.2 ps, respectively, and, for the region $\Delta t < 0$, decay time constants τ_{fast} and τ_{slow} were 0.69 ps and 3.0 ps, respectively. Similarly to Fig. 6b, the signal waveform profile is not symmetrical around $\Delta t = 0$, and, compared with the region $\Delta t < 0$, the curve is steeply sloping downward in the region $\Delta t > 0$.

As shown by the above experimental results, the signal waveform obtained by the optical pulse-shape measurement using nonadiabatic excitation light emission from the DCM dye grains induced by nondegenerate beams had an S/N of about 19–34 and a measurement wavelength range of 1250–1350 nm. The full width at half maximum was about 0.8–1.1 ps, which is likely constrained by the lifetime of intermediate excited state. The signal waveform was skewed around $\Delta t = 0$ because the levels of the excitation energy imparted to the dye molecules by the beam reaching them first were different between the regions before and after $\Delta t = 0$. With this measurement method, there is no restriction on angular correlation between the polarization directions of the signal beam and the sampling beam, nor is there any need for a device for controlling the polarization direction before the beam reaches the dye grains, such as a wavelength plate. In addition, a wide wavelength region can be measured with this method because the incident angle to the dye grains can be fixed independent of the wavelength of the signal beam.

4 Conclusions

Using DCM dye grains and mutually nondegenerate beams generated by two CW laser diodes, visible light emission from the dyes by near-infrared excitation based on a nonadiabatic, nondegenerate excitation process was observed for the first time. In addition, this excitation principle was applied, for the first time, to optical sampling as a measurement method. As a result, the optical pulse shape in the wavelength band of $\lambda = 1250$–1350 nm, which is close to the wavelength range used for optical fiber communications, was measured with a temporal resolution of 0.8–1.1 ps.

Acknowledgements This work was partially supported by a New Energy and Industrial Technology Development Organization (NEDO) project on a comprehensive activity for personal training and industry–academia collaboration.

References

1. A. Takada, M. Saruwatari, Electron. Lett. **24**, 1406 (1988)
2. H. Lobentanzer, H.-J. Polland, W.W. Rühle, W. Stolz, K. Ploog, Appl. Phys. Lett. **51**, 673 (1987)
3. M.E. Fermann, A. Galvanauskas, M.L. Stock, K.K. Wong, D. Harter, L. Goldberg, Opt. Lett. **24**, 1428 (1999)
4. C. Dorrer, IEEE J. Sel. Top. Quantum Electron. **12**, 843 (2006)
5. H. Ohta, S. Nogiwa, Y. Kawaguchi, Y. Endo, Electron. Lett. **36**, 737 (2000)
6. H. Ohta, N. Banjo, N. Yamada, S. Nogiwa, Y. Yanagisawa, Electron. Lett. **37**, 1541 (2001)
7. H. Takara, S. Kawanishi, A. Yokoo, S. Tomaru, T. Kitoh, M. Saruwatari, Electron. Lett. **32**, 2256 (1996)
8. A. Yariv, W.H. Louisell, IEEE J. Quantum Electron. **QE-2**, 418 (1966)
9. S. Umegaki, S. Yabumoto, S. Tanaka, Appl. Phys. Lett. **21**, 400 (1972)
10. S. Umegaki, S. Tanaka, Jpn. J. Appl. Phys. **16**, 775 (1977)
11. G.C. Bhar, U. Chatterjee, Jpn. J. Appl. Phys. **29**, 1103 (1990)
12. T. Kawazoe, H. Fujiwara, K. Kobayashi, M. Ohtsu, IEEE J. Sel. Top. Quantum Electron. **15**, 1380 (2009)
13. H. Fujiwara, T. Kawazoe, M. Ohtsu, Appl. Phys. B **98**, 283 (2010)
14. U. Brackmann, "Lambdachrome Laser Dyes" LAMBDA PHYSIK
15. K. Kato, IEEE J. Quantum Electron. **QE-22**, 1013 (1986)

Appl Phys B (2010) 100: 181–187
DOI 10.1007/s00340-010-3977-y

Applied Physics B
Lasers and Optics

Structural dependency of optical excitation transfer via optical near-field interactions between semiconductor quantum dots

W. Nomura · T. Yatsui · T. Kawazoe · M. Naruse · M. Ohtsu

Received: 23 February 2010 / Published online: 17 March 2010

Abstract The distribution dependency of quantum dots was theoretically and experimentally investigated with respect to the basic properties optical excitation transfer via optical near-field interactions between quantum dots. The effects of three-dimensional structure and arraying precision of quantum dots on the signal transfer performance were analyzed. In addition, the quantum dot distribution dependency of the signal transfer performance was experimentally evaluated by using stacked CdSe quantum dots and an optical near-field fiber probe tip laminated with quantum dots serving as an output terminal, showing good agreement with theory. These results demonstrate the basic properties of signal transfer via optical near-field interactions and serve as guidelines for a nanostructure design optimized to attain the desired signal transfer performances.

1 Introduction

Optical near-field interactions, occurring locally in the nanometer scale by photons dressed by material excitations, have unique properties that cannot be found in propagating light, and they have allowed realization of not only integration below the diffraction limit, but also various new functions [1]. In particular, optical excitation transfer between nanoscale matter, such as quantum dots, quantum wells, etc., via optical near-field interactions is one of the most unique features of nanophotonics [2, 3], and allows transitions to energy levels that are electric-dipole forbidden with conventional propagating light. On the basis of this property, a diverse range of practical applications has been developed, for example, logic devices such as AND gate [4, 5], nanofabrication [6–8], information and communication systems [9, 10], and so on. Theoretically, a dressed photon model has been formulated in which light–matter interactions on the nanometric scale are considered as photons dressed by material excitation [1]. As will be introduced in Sect. 3 of this paper, insights gained from the model include that optical near-field interactions between nanoscale matter are described by Yukawa potential functions and theories of optical excitation transfer even to conventionally electric-dipole forbidden energy levels.

However, in order to utilize optical excitation transfer via optical near-field interactions in devices and systems, an understanding of the signal transfer between functional elements is essential. Furthermore, this signal transfer needs to be capable of, not to mention extremely short-distance signal transfer such as that between a small number of pieces of adjacent nanoscale matter, but also long-distance signal transfer, in some cases, beyond the wavelength dimension, in order to connect a macroscale external system with nanoscale devices.

Regarding such signal transfer using optical near-field interactions, we have already achieved, for example, concentration of optical excitations from smaller quantum dots to larger ones using the optical-nanofountain, having a structure in which the larger quantum dots are surrounded by the

W. Nomura (✉) · T. Yatsui · T. Kawazoe · M. Naruse · M. Ohtsu
School of Engineering, The University of Tokyo, 2-11-16, Yayoi, Bunkyo-ku, Tokyo 113-8656, Japan
e-mail: nomura@nanophotonics.t.u-tokyo.ac.jp

W. Nomura · T. Yatsui · T. Kawazoe · M. Naruse · M. Ohtsu
The Nanophotonics Research Center, The University of Tokyo, 2-11-16, Yayoi, Bunkyo-ku, Tokyo 113-8656, Japan

M. Naruse
National Institute of Information and Communications Technology, 4-2-1 Nukui-kita, Koganei, Tokyo 184-8795, Japan

smaller ones [11]. In addition, we have demonstrated a system that realizes simultaneous distribution (broadcasting) of signals to multiple quantum dots by controlling the dot size and selecting the frequency of propagating light [12].

Although signal transfer using optical near-field interactions has been partially realized with these methods, many basic and important issues remain to be resolved. For example, distance dependency of signal transfer via optical near-field interactions has not been elucidated. In addition, as was begun in a previous study [13], error-resistance (robustness) of the optical near-field interactions between quantum dots is being addressed. However, despite its extreme importance for implementation of nanophotonics, the capacity for controlling quantum dot position has not been subjected to a systematic evaluation from the standpoint of signal transfer; and thus, it remains as a priority task. Furthermore, there are other critical issues, including an ideal nanostructure design for realizing desired signal transfer performance.

Therefore, in this paper, array dependency of quantum dots was theoretically and experimentally analyzed with respect to the basic properties of signal transfer using optical near-field interactions. More specifically, for signal transfer between quantum dots serving as signal input and output, the three-dimensional structure of the dot-array between the two ends was varied, and the resulting variation in the signal transfer performance was evaluated. The effects of dot-array control precision on the signal transfer performance were also evaluated by giving a certain randomness to the dot-array. In addition, signal transfer via stacked CdSe quantum dots was evaluated using a near-field optical probe that had a relatively large quantum dot, to which optical excitation was transported, provided at its tip. Here, the dot-array dependency of the signal transfer was experimentally evaluated by controlling the array structure of the quantum dots that acted as a transfer medium for signal. With these examinations, structural dependency of the signal transfer via optical near-field interactions was demonstrated, and basic insights were gained for achieving a nanostructure optimized for signal transfer.

The paper is organized as follows. The basic elements of optical excitation transfer via optical near-field interactions will be reviewed and an overview of the signal transfer system will be given in Sect. 2. In Sect. 3, a theoretical model for evaluating the structural dependency will be introduced and evaluated by simulation. The experiment will be discussed in Sect. 4, and Sect. 5 concludes the paper.

2 Basic elements of optical excitation transfer via optical near-field interactions

Figure 1(a) shows a schematic representation of the optical excitation transfer via optical near-field interactions, showing an optical excitation in QD_S, in a state in which small

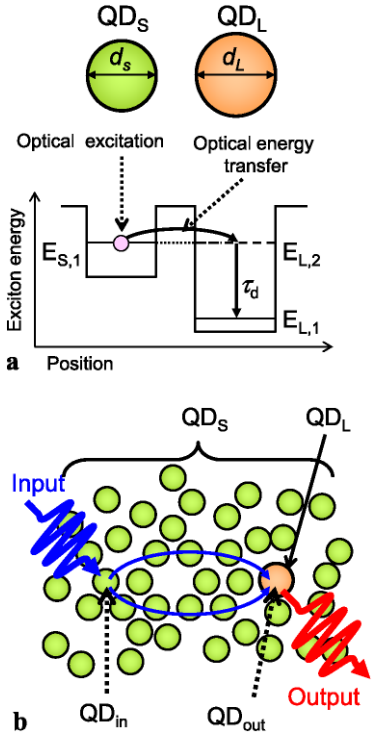

Fig. 1 (**a**) Schematic representation of optical excitation transfer via optical near-field interactions. (**b**) Schematic representation of signal transfer system via optical near-field interactions

spherical quantum dots QD_S with diameter d_S are adjacent to spherical quantum dots QD_L with diameter d_L, which is comparatively larger than d_S. When the diameter of QD_L is given by $d_L = 1.43 \times d_S$, the ground level $E_{S,1}$ of an exciton of QD_S and the excited level $E_{L,2}$ of QD_L resonate [14]. In this case, please note that $E_{L,2}$ is a dipole-forbidden energy level, which is not populated by propagating light. However, when QD_S and QD_L are closely arranged, transition from $E_{S,1}$ to $E_{L,2}$ is permissible by optical near-field interactions that occur between the two [1]. Because there is ground level $E_{L,1}$ for QD_L, which is more stable than $E_{L,2}$, the optical excitation immediately relaxes to $E_{L,1}$. Due to this dissipation, the energy of the optical excitation is in a nonresonant state with QD_S (because $E_{S,1} = E_{L,2} > E_{L,1}$), and thus, the transferred optical excitation cannot revert back to QD_S. In other words, the energy dissipation that occurs in QD_L ensures unidirectional optical excitation transfer from QD_S to QD_L.

If QD_{in} (QD_S at the signal input) and QD_{out} (QD_L at the signal output) are spatially arranged at a distance so that there is no optical near-field interaction between them, naturally, optical excitation transfer from QD_{in} to QD_{out} does not occur. However, by filling the space between QD_{in} and QD_{out} with the same-sized QD_S's as QD_{in}, optical near-field interactions can occur between adjacent quantum dots, and an optical excitation occurring in QD_{in} can be consecutively transferred from one quantum dot to the next. As described

above, unidirectional optical excitation transfer occurs at the output quantum dot, QD_{out}, due to the energy dissipation that occurs at QD_{out}. As a result, optical excitation transfers from QD_{in} to QD_{out}.

Therefore, even when QD_{in} and QD_{out} are arranged with a spatial separation, by appropriately arranging QD_S's between the two, long-distance signal transfer becomes possible. In addition, the optical near-field interactions that are basis of the optical excitation transfer between quantum dots depends on the interdot distance; however, as shown in Fig. 1(b), as long as the interdot distance is maintained within a range allowing the optical near-field interactions to occur, the quantum dots need not be in an orderly array. Therefore, the proposed optical signal transfer system is expected to be highly resistant to positional displacement of the quantum dots. This characteristic will be described in more detail in the following section.

3 Theoretical analyses

A three-dimensional distribution model of quantum dots, as shown in Fig. 1(b), was formulated in order to evaluate the structural dependency of the optical excitation transfer in the system formed of QD_S and QD_L described in the previous section. Here, the performance of the signal transfer between QD_{in} and QD_{out} was analyzed with respect to the effects of the distance between the input quantum dot QD_{in} and the output quantum dot QD_{out}, and the structure of the internal dot distribution.

The formulated model is based on a system composed of $(N-1)$ smaller quantum dots QD_S and one larger quantum dot QD_L. Here, it is assumed that QD_S and QD_L have a size ratio as described in the previous section, and optical excitation transfer via optical near-field interactions can occur. QD_S's are denoted as $QD_1, \ldots, QD_{N-1}$, and QD_L is denoted as QD_N, distinguishing individual quantum dots with subscripts 1 through N. The following rate equation is introduced, assuming optical near-field interactions between two arbitrary quantum dots QD_i and QD_j:

$$\frac{dn_i}{dt} = \sum_{j=1}^{N}\left(\frac{n_j}{\tau_{ji}}\right) - \sum_{i=1}^{N}\left(\frac{n_i}{\tau_{ij}}\right) - \frac{n_i}{\tau_i}. \tag{1}$$

Here n_i is the probability of optical excitation occurring at the ith quantum dot; τ_{ij} is the interaction time of the optical near-field interaction between QD_i and QD_j, satisfying the relation $\tau_{ij} = \tau_{ji}$; and τ_i is, for $i = 1$ to $N-1$, the optical excitation relaxation lifetime of QD_S and, for $i = N$, the sublevel relaxation time from excitation level $E_{L,2}$ of QD_L to the ground level $E_{L,1}$. Here, the interdot interaction time is defined the reciprocal of the optical near-field interaction, and is described by the following Yukawa function [1]:

$$\hbar U_{ij} = \frac{1}{\tau_{ij}} = A_{ij}\frac{\exp(-\mu r_{ij})}{r_{ij}}. \tag{2}$$

Here $\hbar$ is Planck's constant divided by 2π. U_{ij} is the optical near-field coupling strength between QD_i and QD_j; r_{ij} is the center-to-center distance between QD_i and QD_j; A_{ij} is a constant; and μ is the effective mass of the Yukawa function, which is given by

$$\mu = \frac{\sqrt{2E_p(E_m + E_p)}}{\hbar c} \tag{3}$$

where E_p and E_m, when applying them to the experimental conditions described in Sect. 4, indicate the exciton energies of the CdSe quantum dots and the ZnS shell layer, respectively; and c is speed of light. Here, the output signal from the output quantum dot, I_{out}, can be defined by

$$\frac{dI_{\text{out}}}{dt} = \frac{n_N}{\tau_N} \tag{4}$$

assuming that QD_N is the output quantum dot QD_{out}, and that the time integral of the optical excitation probability for QD_N at the ground state is I_{out}.

Parameters of the above theoretical model were set based on preliminary experimental results of CdSe/ZnS core-shell quantum dots used in the experiment described later. First, in a previous study [15], by evaluating time-resolved spectral properties of fluorescence lifetime from a mixed system with CdSe/ZnS core-shell quantum dots of 2.8 and 4.1 nm diameters, optical excitation transfer due to optical near-field interactions was indirectly confirmed in this system. Based on this insight, the optical excitation transfer time between QD_S and QD_L via optical near-field interactions at a center-to-center distance of 7.3 nm was set at 135 ps. In the CdSe/ZnS core-shell quantum dots of 2.8 nm diameter, E_p and E_m are 2.25 eV and 2.54 eV, respectively. Based on these, the coefficient $A_{iN}(= A_{Ni})$ in (3) was determined to be 65.3 s^{-1}. In addition, A_{ij}, which is a constant that defines the optical excitation transfer time between QD_S's via optical near-field interactions, was defined as $A_{ij} = A_{ji} = 3 \times A_{iN}$ $(i, j \neq N)$, based on the density of states ratio of excitons, estimated from the absorption coefficient of energy levels $E_{L,2}$ and $E_{L,1}$. Also, the optical excitation lifetime of QD_S was experimentally determined as $\tau_i = 2.2$ ns $(i, j \neq N)$, and the sublevel relaxation time τ_N for QD_L was set at 1 ps based on a previous study [16].

Furthermore, to evaluate the spatial array structure dependency of quantum dots between QD_{in} and QD_{out}, the three-dimensional structure shown in Fig. 2(a) was used.

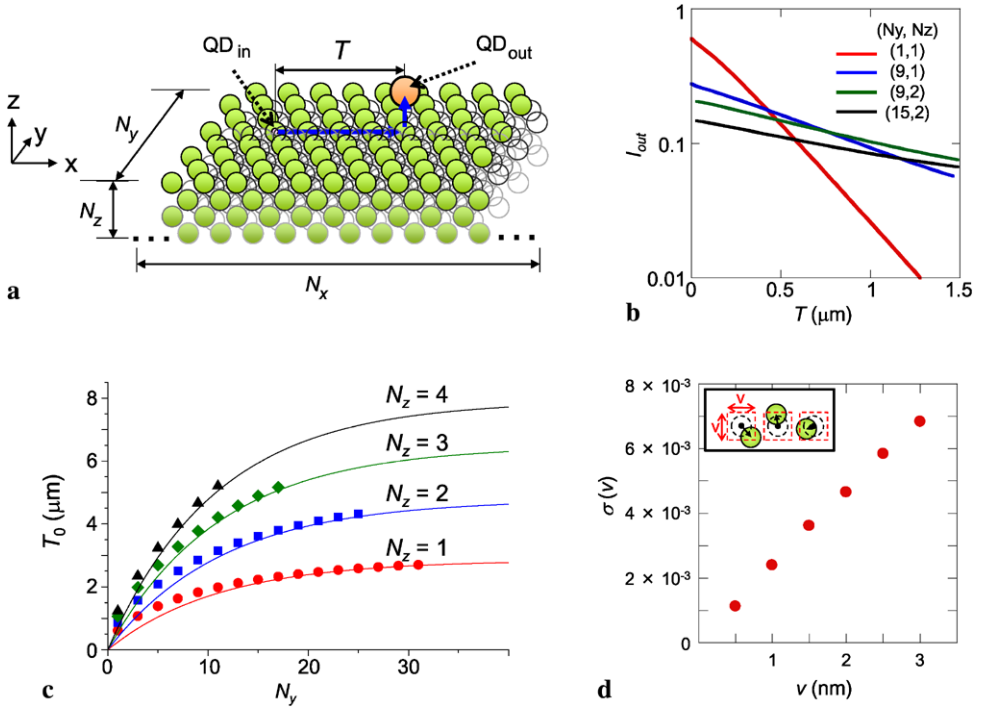

Fig. 2 (**a**) Schematic representation of the calculation model. (**b**) Calculation results of $I_{\text{out}}(N_y, N_z)$ for $(N_y, N_z) = (1, 1), (9, 1), (9, 2)$, and $(15, 2)$. *Red curve* $= I_{\text{out}}(1, 1)$, *blue curve* $= I_{\text{out}}(9, 1)$, *green curve* $= I_{\text{out}}(9, 2)$, *black curve* $= I_{\text{out}}(15, 2)$. (**c**) Calculation results of $T_0(N_y, N_z)$. *Red circles* $= T_0(N_y, 1)$, *blue squares* $= T_0(N_y, 2)$, *green diamonds* $= T_0(N_y, 3)$, *black triangles* $= T_0(N_y, 4)$, and *solid lines* of corresponding colors are approximation curves, where $T_0(N_y, 1) = 2.85 - 2.85\exp(-N_y/11.0)$, $T_0(N_y, 2) = 4.77 - 4.77\exp(-N_y/11.5)$, $T_0(N_y, 3) = 6.48 - 6.48\exp(-N_y/11.2)$, $T_0(N_y, 4) = 7.91 - 7.91\exp(-N_y/10.8)$. (**d**) Standard deviation $\sigma(v)$ of $I^v_{\text{out}}/I^0_{\text{out}}$ (change in output signal with respect to v, the displacement of QD_S). *Inset*: schematic representation of QD_S position displacement model. *Black dashed circles* indicate positions of QD_S's without displacement; *black arrows* indicate destinations of centers of QD_S's. *Side length of squares* shown in *red dashed lines* is v, and the tips of *the black arrows* always fall within these *squares*

More specifically, QD_S's N_x, N_y, and N_z were arrayed in the x, y, and z directions, respectively, and QD_{out} was placed adjacent to a QD_S that a distance T away from QD_{in} in the x direction. Distance dependency of the signal transfer was evaluated based on output signals from the output quantum dot at varying positions. The effects of arrangement of the nanostructure composed of QD_S's on the distance dependency were also evaluated.

Further details of the model are as follows: the center position of the input quantum dot QD_{in} is set at the origin $(0, 0, 0)$. QD_S's are arrayed, 10 in $-x$ direction and 306 in $+x$ direction (i.e., $N_x = 317$). The center-to-center distance between adjacent dots is 7.3 nm. The number of quantum dots in the y and z directions are given by N_y and N_z; however, because they are arrayed in the most densely filled structure, quantum dots in adjacent rows are staggered by half of the interdot distance, as shown in Fig. 2(a). Assuming the initial values at $t = 0$ for the probability of optical excitation for QD_{in} and output signal intensity to be $n_1 = 1$ and $I_{\text{out}} = 0$, respectively, the evolution of the optical excitation of individual quantum dots over time was numerically solved using (1) to (4). The output signal of (4) was evaluated at $t = 12$ ns, which is over 5 times the relaxation lifetime of optical excitation from QD_S, namely, 2.2 ns.

Figure 2(b) shows the distance dependency of the output signal when the dot-array structures were $(N_y, N_z) = (1, 1), (9, 1), (9, 2)$, and $(15, 2)$. With respect to the varying x positions T of QD_L, the output signals showed nearly linear decays on a log scale, indicating that the output signals have decaying properties of a monoexponential function with respect to the transfer distance. However, it is noteworthy that the decay trend greatly differs depending on the dot-array structures. That is, within a range of small transfer distance T, I_{out} is larger when the overall scale of the dot-array is smaller (i.e., when N_y and N_z are smaller); however, when the transfer distance T increases, the decay is moderate with larger N_y and N_z. Therefore, these results suggest that, strategically, it is better to keep the number of quantum dots small for a short-distance signal transfer and to increase it for a long-distance signal transfer.

Table 1

N_z	B (μm)	C
1	2.85	11.0
2	4.77	11.5
3	6.48	11.2
4	7.91	10.8

Because I_{out} tends to show a decay described by a mono-exponential function with respect to the transfer distance T, it has properties defined by

$$\frac{dI_{\text{out}}}{dT} = \exp\left(\frac{-2T}{T_0}\right) \tag{5}$$

Therefore, T_0 in (5) can be considered as the signal transfer distance, which is an index characterizing the signal transfer. Assuming this, how T_0 changes with respect to the dot-array dimensions N_y and N_z was analyzed. Figure 2(c) shows the N_y dependency of T_0 for $N_z = 1$, 2, 3, and 4, indicating monotonic increases of T_0 with increasing N_y and N_z, respectively. Furthermore, because T_0 shows a saturating trend with respect to N_y, the dependency of $T_0(N_y, N_z)$ on N_y is evaluated by

$$T_0(N_y, N_z) = B - B\exp(-N_y/C) \tag{6}$$

where the constant B is an index providing the maximum distance of the optical excitation transfer, and the constant C is an index characterizing the saturation of the maximum distance. As a result, the constants B and C can be obtained, as shown in Table 1, for $N_z = 1$, 2, 3, and 4, respectively. Corresponding curves are shown in Fig. 2(c). For example, when $N_z = 1$, the maximum transfer distance is 2.85 μm, whereas when $N_z = 4$, it is 7.92 μm, indicating also that a long-distance transfer is possible by increasing the number of QD_S's involved in the transfer.

In the above analyses, it is assumed that the dot-array is orderly with equal intervals, as in Fig. 2(a). In reality, however, it is likely that the quantum dots are variously positioned, and therefore, it is important to evaluate the effects of position variability on the signal transfer performance. The evaluation was conducted as follows. A system of $(N_y, N_z) = (5, 1)$ was analyzed. The x- and y-coordinates of center positions of all QD_S's except QD_{in} were randomly shifted by uniform random numbers between $-v/2$ and $+v/2$, as illustrated in the inset in Fig. 2(d). Given this, QD_{out} is set at a point 1000 nm away from QD_{in} in $+x$ direction to evaluate the output signal I^v_{out}. The rates of change, $I^v_{\text{out}}/I^0_{\text{out}}$, from the output signal with no displacement, I^0_{out}, was examined with 500 iterations of position shifts by random numbers, the results of which were used to calculate the standard deviation $\sigma(v)$. Corresponding to the increase in the maximum value of position displacement $|v|$, $\sigma(v)$ increased nearly linearly; however, even when $|v| = 3$ nm, $\sigma(3)$ was merely 6.8×10^{-3}. As indicated by the Yukawa function of (2), the interdot interaction time between nearest neighbors is short with the optical excitation transfer via optical near-infrared interactions, and it is likely that the optical excitation transfer is occurring preferentially. Therefore, even when the overall distribution is random, the signal at QD_{in} is transferred to QD_{out} as long as there is a highly efficient transfer route in the system, which is likely reflected in the robustness of the signal transfer against positional displacements shown above.

4 Experiment

An experimental test of the above-described signal transfer performance was conducted as follows. CdSe/ZnS core-shell quantum dots (Evidot by Evident Technologies) of 2.8 nm and 4.1 nm diameters were used for the smaller quantum dots QD_S's and the larger quantum dot QD_L, respectively. Figure 3(a) shows a transmission electron microscope image of QD_S's distributed in a single layer, which was prepared by dropping QD_S's dispersed in 1-phenyloctane at a concentration of 1 mg/mL onto a mica substrate. A certain distance was maintained between quantum dots due to modified groups on the surface of the quantum dots, and the mean center-to-center distance between adjacent quantum dots was estimated to be 7.3 nm.

The sample was prepared following the procedure below.

1. Al light shielding film was applied to a SiO_2 substrate at 50 nm thickness by sputtering.
2. An aperture of 500 nm diameter was made in the Al light shielding film using EB lithography and ICP.
3. An SiO_2 film was formed on the Al light shielding film at 20 nm thickness by sputtering.
4. QD_S solution in 1-phenyloctane was dropped on the substrate treated as above, and excess solution was blown off after leaving it for 10 min.

The SiO_2 film sputtered in Step 3 was formed for the purpose of preventing excitation energy loss due to optical near-field interactions between QD_S and the Al light shielding film. In Step 4, the concentration of the solution was varied at 0.5, 1.0, and 3.0 mg/mL to prepare samples A, B, and C, in which the heights of distributed QD_S's were determined by atomic force microcopy to be $H = 10$, 20, and 50 nm, respectively.

The following fiber probe was prepared for the measurement of the above samples. First, a fiber probe with nanometric protrusion [17], in which a sharpened core protrudes from an Au light shielding film of a 800 nm thickness, was

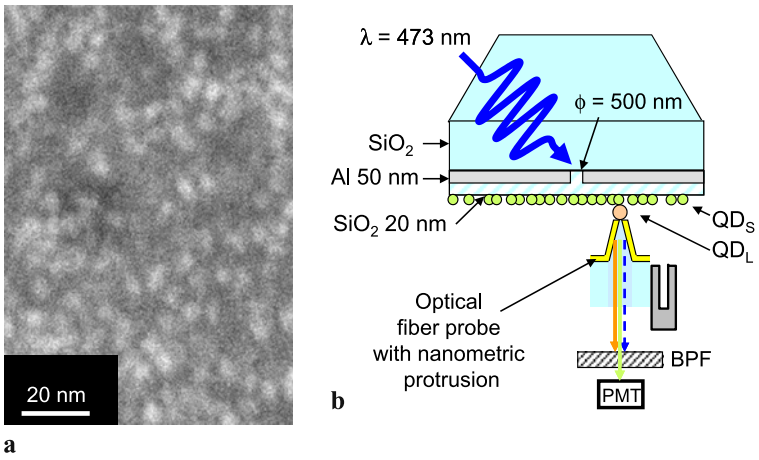

Fig. 3 (**a**) Transmission electron microscope image of a single-layer CdSe/ZnS core-shell quantum dot. (**b**) Schematic representation of experimental system for near-field optical microscope measurements

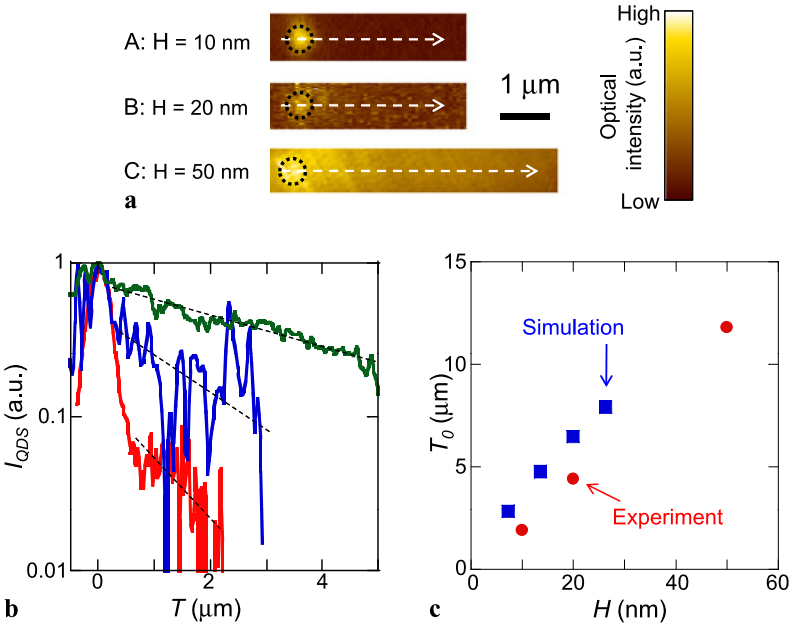

Fig. 4 (**a**) Distribution of I_{QDS} of samples A, B, and C obtained with the near-field optical microscope. (**b**) Profiles along *white dashed arrows* in (**a**). *Red* = sample A, *blue* = sample B, *green* = sample C. *Black dashed lines* indicate monoexponential approximation curves for the range $T > 500$ nm. (**c**) Dependency of transfer distance T_0 on height H of distributed QD_S's. *Red circles* = experimental result, *blue squares* = theoretical results

prepared, and then QD_L's were attached to the tip of the probe by immersing the probe for 10 min in a QD_L solution (1-phenyloctane solution at 1 mg/mL).

By using this fiber probe, the fluorescence distribution was measured with the measuring system shown in Fig. 3(b). CW laser light ($\lambda = 473$ nm) was radiated from the back of the substrate at a power density of 1.27 W/cm^2, thus exciting only QD_S's at the aperture. At this time, by scanning near the aperture with the fiber probe at a controlled distance of 10 nm or less to the sample, QD_L's adhered to the tip of the probe served as the output quantum dot, and the excitation energy unidirectionally flowed toward the probe. The beam collected by the probe was passed through a bandpass filter with a center wavelength of $\lambda = 540$ nm and was detected by a photomultiplier tube, giving the measured value of emission intensity I_{QDS} of QD_S. Because the output signal I_{out} at QD_L is proportional to the total level of the optical excitation of QD_S's in the vicinity, it is possible to estimate the decay of I_{out} from the point of excitation beam introduction to the distance T, by measuring I_{QDS} under the CW excitation.

Measurement results for samples A, B, and C are shown in Fig. 4(a). Because the excitation intensity at the aperture on the substrates (dashed circles in the figure) was high enough for the signal to pass through the filter, the signal intensity at that point was high for all samples. Then, the signal intensity declined as the distance from the aperture increased. Setting $T = 0$ at the position with the maximum light intensity at the aperture, this maximum value was used to obtain normalized light intensity values I_{QDS} along the white dashed arrows in Fig. 4(a), the profiles of which are shown in Fig. 4(b). Profiles for samples A, B, and C are shown by red, blue, and green lines, respectively. In the region where $T \leq 500$ nm, it is assumed that the results re-

flect the distribution of the excitation intensity at the aperture, and, for the range $T > 500$ nm, approximation with a monoexponential function was performed for each profile. Based on each approximation, a transfer distance T_0, which is defined by $\frac{dI_{\text{out}}}{dT} = \exp(\frac{-2T}{T_0})$, was calculated. As a result, approximated curves, shown as black dashed lines in Fig. 4(b), were obtained, and T_0 values were calculated to be 1.92 µm, 4.40 µm, and 11.8 µm for samples A, B, and C, respectively. As described above, I_{out} is proportional to I_{QDS}, and therefore, the calculated T_0 corresponds to the maximum transfer distance evaluated as the constant B in (6) in the previous section. The experimentally determined transfer distance and decay distance obtained from B in Table 1 are indicated in Fig. 4(c) with circles and squares, respectively. The increasing trend in the transfer distance with an increase in the height of the distributed QD_S's, H, observed in the theoretical and experimental results show good agreement with each other. It is speculated that the experimentally obtained transfer distance is generally low because the relaxation time of optical excitation of QD_S's is reduced by optical near-field interactions with metal, such as the Al light shielding film on the substrate, the Au light shielding film of the probe, etc. [18]. These results demonstrated the signal transfer performance between quantum dots via optical near-field interactions.

5 Conclusions

The array dependency of quantum dots was theoretically and experimentally analyzed with respect to the basic properties of transfer via optical near-field interactions. Effects of the array structure of the quantum dots, which act as a medium, on the signal transfer performance were analyzed with a theoretical model using a rate equation. Increasing the number of quantum dots in the dot-array is detrimental to short-distance signal transfer (signal intensity decreases); however, it allows for long-distance transfer because decaying of the signal with respect to the transfer distance is alleviated. In addition, a high resistance against positional variations of quantum dots was shown. Using different-height, stacked CdSe quantum dots and a near-field optical probe whose tip had CdSe quantum dots that serves as an output end, the dependency of signal transfer performance on the structure of distributed quantum dots was experimentally evaluated, and the obtained results were consistent with the theoretical calculations. These results demonstrate the basic properties of signal transfer in nanophotonics, which will serve as design guidelines for realizing an optimal nanostructure that gives desired signal transfer performance.

Acknowledgements The authors would like to thank Prof. Christoph Lienau of Oldenburg University for helpful discussions on optical excitation transfer. This work is partially supported by the Japan Science and Technology Agency (JST) and the German Research Foundation (DFG) under the Strategic International Cooperative Program, by the New Energy and Industrial Technology Development Organization (NEDO) under a program for Comprehensive Activity for Personnel training and Industry-Academia Collaboration based on NEDO projects, and by The University of Tokyo Global COE Program "Secure-Life Electronics".

References

1. M. Ohtsu, K. Kobayashi, T. Kawazoe, T. Yatsui, M. Naruse, *Principles of Nanophotonics* (Taylor and Francis, Boca Raton, 2008)
2. M. Ohtsu, K. Kobayashi, T. Kawazoe, S. Sangu, T. Yatsui, IEEE J. Sel. Top. Quantum Electron. **8**, 839 (2002)
3. T. Unold, K. Mueller, C. Lienau, T. Elsaesser, A.D. Wieck, Phys. Rev. Lett. **94**, 137404 (2005)
4. T. Kawazoe, K. Kobayashi, M. Ohtsu, Appl. Phys. Lett. **86**, 103102 (2005)
5. T. Yatsui, S. Sangu, T. Kawazoe, M. Ohtsu, S.J. An, J. Yoo, G.-C. Yi, Appl. Phys. Lett. **90**, 223110 (2007)
6. T. Kawazoe, K. Kobayashi, M. Ohtsu, Appl. Phys. B **84**, 247 (2006)
7. H. Yonemitsu, T. Kawazoe, K. Kobayashi, M. Ohtsu, J. Lumines **122–123**, 230 (2007)
8. T. Yatsui, K. Hirata, W. Nomura, Y. Tabata, M. Ohtsu, Appl. Phys. B **93**, 55 (2008)
9. M. Naruse, T. Miyazaki, F. Kubota, T. Kawazoe, K. Kobayashi, S. Sangu, M. Ohtsu, Opt. Lett. **30**, 201 (2005)
10. M. Naruse, H. Hori, K. Kobayashi, M. Ohtsu, Opt. Lett. **32**, 1761 (2007)
11. T. Kawazoe, K. Kobayashi, M. Ohtsu, Appl. Phys. Lett. **86**, 103102 1-3 (2005)
12. M. Naruse, T. Kawazoe, S. Sangu, K. Kobayashi, M. Ohtsu, Opt. Express **14**, 306 (2006)
13. M. Naruse, T. Kawazoe, R. Ohta, W. Nomura, M. Ohtsu, Phys. Rev. B **80**, 125325 (2009)
14. N. Sakakura, Y. Masumoto, Phys. Rev. B **56**, 4051 (1997)
15. W. Nomura, T. Yatsui, T. Kawazoe, M. Ohtsu, J. Nanophot. **1**, 011591 (2007)
16. P. Guyot-Sionnest, M. Shim, C. Matranga, M. Hines, Phys. Rev. B **60**, R2181 (1999)
17. S. Mononobe, M. Naya, T. Saiki, M. Ohtsu, Appl. Optics **36**, 1496 (1997)
18. N. Hosaka, T. Saiki, J. Microscopy **202**, 362 (2001)

Nanotechnology **21** (2010) 285302 (4pp) doi:10.1088/0957-4484/21/28/285302

Site-selective deposition of gold nanoparticles using non-adiabatic reaction induced by optical near-fields

Kokoro Kitamura, Takashi Yatsui, Tadashi Kawazoe, Masakazu Sugiyama and Motoichi Ohtsu

Department of Electrical Engineering and Information Systems, School of Engineering, The University of Tokyo, Tokyo 113-8656, Japan
and
Nanophotonics Research Center, The University of Tokyo, Tokyo 113-8656, Japan

E-mail: kitamura@nanophotonics.t.u-tokyo.ac.jp

Received 26 February 2010, in final form 26 April 2010
Published 18 June 2010
Online at stacks.iop.org/Nano/21/285302

Abstract

In this paper, we report on site-selective deposition of metal nanoparticles using a non-adiabatic photochemical reaction. Photoreduction of gold was performed in a silica gel membrane containing tetrachloroaurate ($AuCl_4^-$) ions, using ZnO nanorods as the sources of optical near-field light, resulting in deposition of gold nanoparticles with an average diameter of 17.7 nm. The distribution of distances between the gold nanoparticles and nanorod traces revealed that the gold nanoparticles were deposited adjacent to the ZnO nanorods, reflecting the attenuation of the optical near-fields in the vicinity of the ZnO nanorods. We found that the emission wavelength from the ZnO nanorods was longer than the absorption edge wavelength of the tetrachloroaurate. Additionally, from the intensity distribution obtained by a finite-difference time-domain method, the gold deposited around the ZnO nanorods was found to be due to a non-adiabatic photochemical reaction.

(Some figures in this article are in colour only in the electronic version)

1. Introduction

Metal nanoparticles have been attracting attention as materials for nanoscale photonic and electronic devices [1–4]. Gold nanoparticles in particular have been studied extensively because of their chemical stability [5]. There are several methods of producing gold nanoparticles, such as sputtering [6] and photochemical synthesis [7]. Among these methods, photochemical fabrication using $AuCl_4^-$ ions has the advantage of deposition-site selectivity by selecting the light irradiation area. However, although positional control of gold nanoparticles using interference of laser light has been reported [8], positional control on the nanometric scale has been difficult because of the diffraction limit of light. In this study, we succeeded in selectively depositing gold only in an area below the optical diffraction limit by using a non-adiabatic reaction induced by optical near-fields as the photochemical reaction.

Recently, methods involving the use of optical near-fields have been considered for positional control on the nanometric scale using light [9]. In addition, with a non-adiabatic process mediated by coherent phonons induced close to the surface of a nanomaterial by optical near-fields, it is possible to induce novel reactions that are impossible with conventional approaches involving propagating light [10]. Typical features of this method are:

(1) Because the reaction is mediated by coherent phonons, it is possible to induce a photochemical reaction in the material even when using light having a photon energy lower than the absorption edge of the material. As a result, a short wavelength light source is not required.
(2) It is possible to process a nanostructure on the material surface to function as a nanometric light source simply by using propagating light, eliminating the need for a probe and mask [11, 12]. As a result, processing of large surface areas is possible.

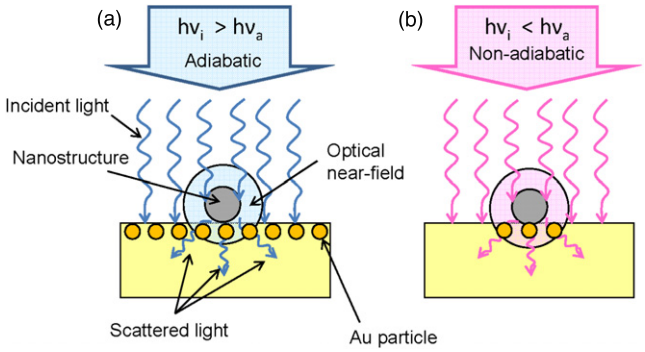

Figure 1. Schematic diagram of photodeposition of gold nanoparticles using optical near-fields: (a) adiabatic process, (b) non-adiabatic process.

Here we explain deposition of gold particles by a non-adiabatic process, which is the principle of the present study. For comparison, we also explain an adiabatic process that has often been used conventionally. We consider a case where a nanostructure is placed in contact on top of a film containing $AuCl_4^-$ serving as a source of gold particles. When this nanostructure is irradiated with light, optical near-fields are generated around the nanostructure. If the photon energy of the irradiated light ($h\nu_i$) is greater than the photoreduction energy of the $AuCl_4^-$ ions ($h\nu_a$), gold nanoparticles are deposited via a normal photochemical reaction in the entire irradiated region by the incident light and scattered light (figure 1(a)). This reaction process is called an adiabatic process. In contrast, if $h\nu_i < h\nu_a$, it is normally not possible to bring about a photoreaction, and thus no gold particles are deposited in the area irradiated with incident light and scattered light. However, optical near-fields are generated close to the surface of the nanostructure, and gold nanoparticles are deposited by these optical near-fields even if $h\nu_i < h\nu_a$ (figure 1(b)). This is because the optical near-fields can induce a reaction with the $AuCl_4^-$ ions by binding with coherent phonons. Phonon level can be excited with optical near-field. The energy required to excite the phonon level is lower than the electronic excited level, therefore reduction of the $AuCl_4^-$ ions can be realized with lower photon energy than the absorption bandgap energy. This reaction process is called a non-adiabatic process and occurs only around the nanostructures which generate the optical near-fields. The detail of non-adiabatic process has been reported in [10, 13]. By using the non-adiabatic process, it is possible to eliminate the influence of propagating light, that is, incident light and scattered light, allowing only the optical near-field effect to be utilized [11–14]. In this paper, we report on the formation of gold nanoparticles using optical near-fields, which enables positional control on the nanometric scale.

2. Experimental technique

In order to achieve deposition of gold nanoparticles, we used a silica gel film containing $AuCl_4^-$ ions as the gold source. First, we fabricated silica sol. The silica sol was fabricated by combining $HAuCl_4$ ethanol solution (0.5 g cm^{-3}), spin-on glass (SOG) material (Tokyo Ohka Kogyo Co., Ltd, Tokyo, Japan; OCD15000-T), and dimethylformamide at a ratio of 1:2:1 by volume. The dimethylformamide was used to prevent cracks when drying the film. A film of the silica sol was coated on a silicon substrate with a spin coater. To prevent progression of the reduction reaction of the $AuCl_4^-$ ions due to heat, the film was vacuum dried at room temperature. During this drying process, the silica sol film was transformed to a silica gel film. The fabricated gel film was about 200 nm thick and contained $AuCl_4^-$ at a concentration of 6.0 mg cm^{-3}.

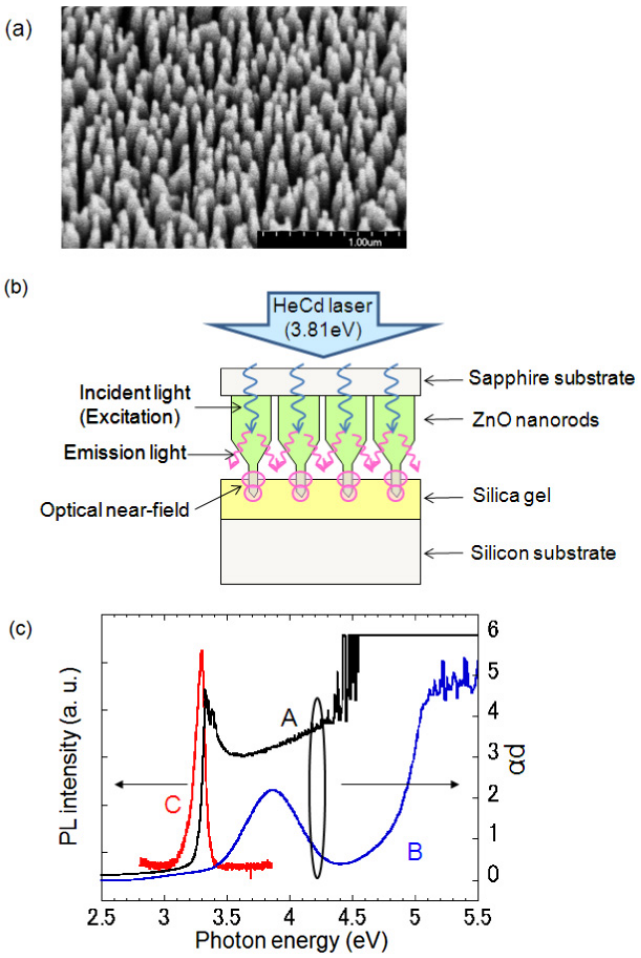

Figure 2. (a) SEM image of ZnO nanorods used as sources of optical near-field light; (b) experimental setup; (c) absorption spectra of ZnO nanorods (curve A) and $HAuCl_4$ solution (curve B), and photoluminescence (PL) spectrum of ZnO nanorods (curve C).

To control the gold deposition position, we used ZnO nanorods as the nanostructures for generating the optical near-fields. The ZnO nanorods were grown on a sapphire substrate by metal organic chemical vapour deposition (MOCVD) using a two-temperature growth technique (figure 2(a)) [15]. This growth technique involved growth in two stages: a first stage in which thick ZnO nanorods were grown at low temperature and a second stage in which thin ZnO nanorods were grown at high temperature. The thin ZnO nanorods in the second stage were grown from the tips of the thick ZnO nanorods in the first stage. The diameters of the nanorods in the second stage, measured from SEM images, were 52 ± 6 nm. Figure 2(b)

shows the experimental setup. The substrate on which the ZnO nanorods were grown was pressed into the silica gel film containing the $AuCl_4^-$ and was irradiated with HeCd laser light (3.81 eV, 15 mW, 1 mm irradiation spot diameter) from the ZnO nanorod side for 1 min.

3. Result and discussion

Figure 2(c) shows the absorption spectra of the ZnO nanorods (curve A) and the $HAuCl_4$ solution (curve B). From these results, we found that the absorption edge energy of the $AuCl_4^-$ ions in the solution was 3.44 eV. Curve C in figure 2(c) is the ZnO nanorod photoluminescence (PL) spectrum due to excitation with the HeCd laser. The peak wavelength of the PL spectrum was at 3.30 eV. The approximate length, diameter, and density of first-stage ZnO nanorods were 1 μm, 70 nm, and 160 μm^{-2}, respectively. The reported absorption coefficient of ZnO thin film was 1–2 $\times$ 10^5 μm^{-1} [16, 17]. These findings show that the excitation light was absorbed by the first-stage ZnO nanorods and did not reach the silica sol film. In addition, the photon energy of light emitted from the ZnO nanorods was smaller than the absorption energy of the $AuCl_4^-$ ions, making it impossible to achieve gold deposition via the adiabatic process. Therefore, in this experiment, the gold deposition occurred only via the non-adiabatic process by light emission from the ZnO nanorods.

Figures 3(a) and (b) are top-view and perspective-view SEM images of the surface of the silica gel film after the ZnO nanorods were pressed into it and irradiated with light. The white points indicated by the solid-line arrows show the deposited gold nanoparticles, and the dark points, indicated by the broken-line arrows, show indentations of traces left by pressing the ZnO nanorods. The surface density of the ZnO nanorod traces was smaller than the surface density of the ZnO nanorods themselves. This is because of some variation in the lengths of the ZnO nanorods employed, meaning that only ZnO nanorods with a large height were pressed into the silica gel. Also, the sites where deposited gold particles were produced were sparse despite the fact that the spot irradiated by the HeCd laser light was 1 mm in diameter. We evaluated the gaps between the gold nanoparticles and the nanorod traces. The shapes of the gold nanoparticles and the ZnO nanorods were approximated by circles of equal area. Figure 3(c) shows the distribution of distances between the centers of gravity of the gold nanoparticles and the nearest ZnO nanorod traces, normalized by the radii of the ZnO nanorod traces. This distribution was calculated using figure 3(a). We consider this distribution to be enough to evaluate the effect of the non-adiabatic process. Regarding the distances between the centers of gravity, 36% of the total were 2–3 times greater than the radii of the nanorod traces, and 30% were 3–4 times greater; thus, considering that the actual shape is non-circular, it means that the gold nanoparticles were deposited adjacent to the nanorod traces. The average diameter of the gold nanoparticles obtained from SEM measurements was 17.7 $\pm$ 6.1 nm.

We performed numerical calculations to show that the deposition of gold only in the vicinity of the nanorods was due to the non-adiabatic process. A non-adiabatic reaction

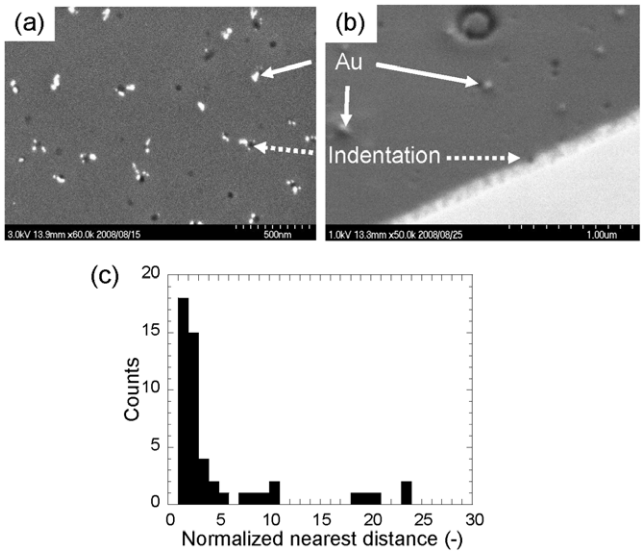

Figure 3. (a) Top-view SEM image of the silica gel surface after laser irradiation; (b) perspective-view SEM image of the cleaved substrate; (c) distribution of distances between gold nanoparticles and nearest nanorod traces, normalized to the radius of the nanorod trace.

involving excitation of coherent phonons is described by the virtual exciton–phonon–polariton (EPP) model; however, in finite-difference time-domain (FDTD) numerical analysis, the spatial distribution of virtual EPPs, that is to say, the rate of the photochemical reaction, is represented by $I(r)\,\mathrm{d}I(r)/\mathrm{d}r$. Here, $I(r)$ is the photon intensity and $\mathrm{d}I(r)/\mathrm{d}r$ is the photon intensity gradient [10].

The model used in the FDTD simulation is shown in figure 4(a). The first-stage nanorod is rectangular with a side of 100 nm, and the second-stage nanorod is a hexagonal rod with a side of 10 nm. The tip of each rod-like structure is pyramidal. A 100 nm portion at the tip of the second-stage nanorod is surrounded by SiO_2, corresponding to the silica gel film. These nanorods are periodically arrayed at a pitch of 20 nm. The light source was plane wave propagating to the $-z$ direction and had a wavelength of 325 nm. As optical constants, we assumed $n = 2.0$ and $k = 0.35$ for ZnO [18], and $n = 1.5$ and $k = 0$ for SiO_2 [19]. The calculated intensity distributions, $I(r)$, in the YZ plane ($x = 0$) and the XY plane ($z = 0$) are shown in figures 4(b) and (c).

Curve A in figure 4(d) shows the spatial distribution of $I(r)$ at the SiO_2 surface as a function of the distance, d, from the ZnO nanorod surface. Here the intensity was normalized to the value at $d = 0$ nm. The intensity was 0.45 at $d = 40$ nm and did not greatly decrease with increasing d. Therefore, when deposition of gold nanoparticles proceeds via the adiabatic process, gold nanoparticles should be deposited in the entire irradiated area, not just in the vicinity of the ZnO nanorods. In contrast, curve B in figure 4(d) shows the distribution of $I(r)\,\mathrm{d}I(r)/\mathrm{d}r$, thus showing the distribution of virtual EPPs. The intensity gradient $\mathrm{d}I(r)/\mathrm{d}r$ is given by

$$\mathrm{d}I(r)/\mathrm{d}r = \sqrt{\{\partial I(x,y,z)/\partial x\}^2 + \{\partial I(x,y,z)/\partial y\}^2 + \{\partial I(x,y,z)/\partial z\}^2}.$$

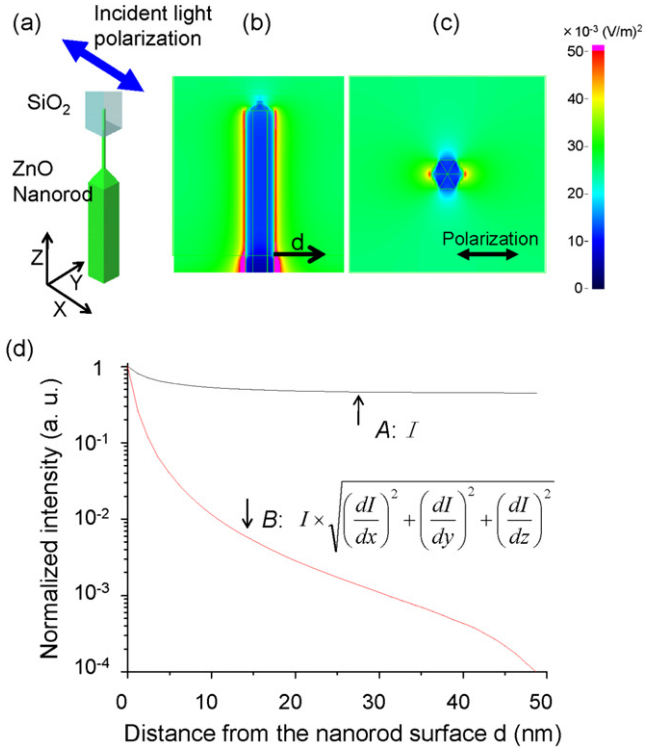

Figure 4. (a) Configuration of the model used in the FDTD simulation. Calculated electric field intensity distributions in (b) YZ plane (axis center) and (c) XY plane (SiO_2 surface). (d) Intensity distributions versus distance from nanorod surface for I (curve A) and $I \times \mathrm{d}I/\mathrm{d}r$ (curve B).

The values of $I(r)\,\mathrm{d}I(r)/\mathrm{d}r$ were also normalized to the value at $d = 0$ nm. Compared with $I(r)$, $I(r)\,\mathrm{d}I(r)/\mathrm{d}r$ showed a sharp decrease with increasing d. In the curves of $I(r)$ and $I(r)\,\mathrm{d}I(r)/\mathrm{d}r$, we compare the distances at which the intensity falls to $1/e$, as the attenuation length. $I(r)$ does not fall to $1/e$ at I (50 nm), whereas the attenuation length for $I(r)\,\mathrm{d}I(r)/\mathrm{d}r$ is 0.9 nm. These results show that the effect of the non-adiabatic process is localized close to the nanorods. These simulation results show good agreement with the experimental result that the gold particles are in contact with the nanorod traces, indicating that the deposition reaction of gold nanoparticles deposited close to the ZnO nanorods in the experiment was due to the non-adiabatic process.

In addition, as shown in figure 4(c), the intensity distribution obtained from the FDTD calculation shows a strong polarization dependence. In the experiment, however, the gold nanoparticles were deposited in random directions relative to the nanorod traces. This difference arises because the deposition reaction of the gold particles is not an adiabatic reaction due to the excitation light but is a non-adiabatic reaction due to light emission from the ZnO nanorods. Because the exciton emission shows no polarization dependence, the non-adiabatic photoreaction which induces this exciton emission as a light source also shows no polarization dependence. Therefore, the directions of gold particle deposition are random.

4. Conclusion

In this paper we have reported on the deposition of gold nanoparticles using the non-adiabatic reaction. Gold nanoparticles were deposited adjacent to ZnO nanorods, reflecting the attenuation of the optical near-fields in the vicinity of the ZnO nanorods, which acted as sources of optical near-field light. The average diameter of the gold nanoparticles obtained from SEM images was 17.7 ± 6.1 nm. The emission wavelength from the ZnO nanorods was found to be longer than the absorption edge wavelength of the tetrachloroaurate ($AuCl_4^-$). Also, from the intensity distribution obtained by FDTD calculations, the gold deposited around the ZnO nanorods was found to be due to a non-adiabatic photochemical reaction. By using a non-adiabatic reaction induced by optical near-fields in photodeposition, we successfully realized selective deposition of gold nanoparticles only at sites adjacent to the sources of optical near-field light.

Acknowledgments

This work was supported in part by a comprehensive program for personnel training and industry–academia collaboration based on projects funded by the New Energy and Industrial Technology Organization (NEDO), Japan, the Global Center of Excellence (G-COE) 'Secure-Life Electronics' project, and Special Coordination Funds for Promoting Science and Technology sponsored by the Ministry of Education, Culture, Sports, Science and Technology (MEXT), Japan.

References

[1] Hutter E and Fendler J H 2004 *Adv. Mater.* **16** 1685
[2] Nomura W, Yatsui T and Ohtsu M 2006 *Appl. Phys.* B **84** 257
[3] Bolotin K I, Kuemmeth F, Pasupathy A N and Ralph D C 2004 *Appl. Phys. Lett.* **84** 3154
[4] Nomura W, Ohtsu M and Yatsui T 2005 *Appl. Phys. Lett.* **86** 181108
[5] Daniel M-C and Astruc D 2004 *Chem. Rev.* **104** 293
[6] Tanahashi I, Manabe Y, Tohda T, Sasaki S and Nakamura A 1996 *J. Appl. Phys.* **79** 1244
[7] Tanahashi I and Tohda T 1996 *J. Am. Ceram. Soc.* **79** 796
[8] Sugiyama M, Inasawa S, Koda S, Hirose T, Yonekawa T, Omatsu T and Takami A 2001 *Appl. Phys. Lett.* **79** 1528
[9] Ohtsu M, Kawazoe T, Yatsui T and Naruse M 2008 *IEEE J. Sel. Top. Quantum Electron.* **14** 1404
[10] Kawazoe T, Kobayashi K, Takubo S and Ohtsu M 2004 *J. Chem. Phys.* **122** 024715
[11] Yatsui T, Hirata K, Nomura W, Ohtsu M and Tabata Y 2008 *Appl. Phys.* B **93** 55
[12] Yatsui T and Ohtsu M 2009 *Appl. Phys. Lett.* **95** 043104
[13] Yonemitsu H, Kawazoe T, Kobayashi K and Ohtsu M 2007 *J. Lumin.* **122/123** 230
[14] Kawazoe T, Ohtsu M, Inao Y and Kuroda R 2007 *J. Nanophoton.* **1** 011595
[15] Kitamura K, Yatsui T, Ohtsu M and Yi G-C 2008 *Nanotechnology* **19** 175305
[16] Muth J F, Kolbas R M, Sharma A K, Oktyabrsky S and Narayan J 1999 *J. Appl. Phys.* **85** 7884
[17] Liang W Y and Yoffe A D 1968 *Phys. Rev. Lett.* **20** 59
[18] Kim T W, Kwack K D, Kim H-K, Yoon Y S, Bahang J H and Park H L 2003 *Solid State Commun.* **127** 635
[19] Thielsch R, Gatto A, Heber J and Kaiser N 2002 *Thin Solid Films* **410** 86

Appl Phys B (2010) 99: 415–422
DOI 10.1007/s00340-010-3999-5

Applied Physics B
Lasers and Optics

Selective photocurrent generation in the transparent wavelength range of a semiconductor photovoltaic device using a phonon-assisted optical near-field process

S. Yukutake · T. Kawazoe · T. Yatsui · W. Nomura · K. Kitamura · M. Ohtsu

Received: 9 March 2010 / Published online: 30 March 2010

Abstract In this paper, we propose a novel photovoltaic device using P3HT and ZnO as test materials for the p-type and n-type semiconductors, respectively. To fabricate an electrode of this device, Ag was deposited on a P3HT film by RF-sputtering under light illumination (wavelength $\lambda_0 = 660$ nm) while reversely biasing the P3HT/ZnO pn-junction. As a result, a unique granular Ag film was formed, which originated from a phonon-assisted process induced by an optical near-field in a self-organized manner. The fabricated device generated a photocurrent even though the incident light wavelength was as long as 670 nm, which is longer than the long-wavelength cutoff λ_c (= 570 nm) of the P3HT. The photocurrent was generated in a wavelength-selective manner, showing a maximum at the incident light wavelength of 620 nm, which was shorter than λ_0 because of the Stark effect brought about by the reverse bias DC electric field applied during the Ag deposition.

1 Introduction

A key issue in the progress of optical technologies is to improve the performance of semiconductor photovoltaic devices, for example, increasing their conversion efficiency. Although it is also essential to expand their working wavelength ranges, the long-wavelength cutoff λ_c is governed by the bandgap energy E_g of the semiconductor material to be used as the active medium for these devices; for example, the long-wavelength cutoffs are 390 nm, 1100 nm, and 3000 nm for GaN, Si, and InGaAs, respectively. To expand the wavelength range, higher E_g is required, which can be met by exploring novel materials or structures of semiconductors.

This paper proposes a novel method of expanding the working wavelength range of a photovoltaic device beyond the one limited by E_g, even though the semiconductor materials remain untreated. It utilizes a phonon-assisted process (also called a nonadiabatic process [1]) induced by an optical near-field. Furthermore, a wavelength-selective feature of photocurrent generation is realized by controlling the morphology of a metallic electrode surface by utilizing this phonon-assisted process.

It has been found that optical near-fields can excite coherent phonons on the surface of a nanometric particle, and that, together with the optical near-fields, these excited coherent phonons form a coupled state which is called a virtual exciton-phonon-polariton [1]. This coupled state is used in the phonon-assisted process, by which electron-hole pairs can be created in the semiconductor even though the incident photon energy is lower than E_g. This is because the energies of both the optical near-field and the induced phonon contribute to this photocurrent generation via an electric dipole-forbidden transition. Previous theoretical studies support the possibility of exciting electrons by a two-step phonon-assisted process for creating electron-hole pairs (Fig. 1) [2, 3].

(1) The first step is the transition from the initial state in the valence band ($|E_g; el\rangle \otimes |E_{\mathrm{ex,thermal}}; phonon\rangle$) to the intermediate state ($|E_g; el\rangle \otimes |E_{\mathrm{ex}}; phonon\rangle$) by the optical near-field. Here, $|E_g; el\rangle$ represents the ground state

S. Yukutake · T. Kawazoe (✉) · T. Yatsui · W. Nomura · K. Kitamura · M. Ohtsu
Department of Electrical Engineering and Information Systems, Graduate School of Engineering, The University of Tokyo, 2-11-16 Yayoi, Bunkyo-ku, Tokyo 113-8656, Japan
e-mail: kawazoe@ee.t.u-tokyo.ac.jp
Fax: +81-3-58411140

T. Kawazoe · T. Yatsui · W. Nomura · K. Kitamura · M. Ohtsu
Nanophotonic Research Center, Graduate School of Engineering, The University of Tokyo, 2-11-16 Yayoi, Bunkyo-ku, Tokyo 113-8656, Japan

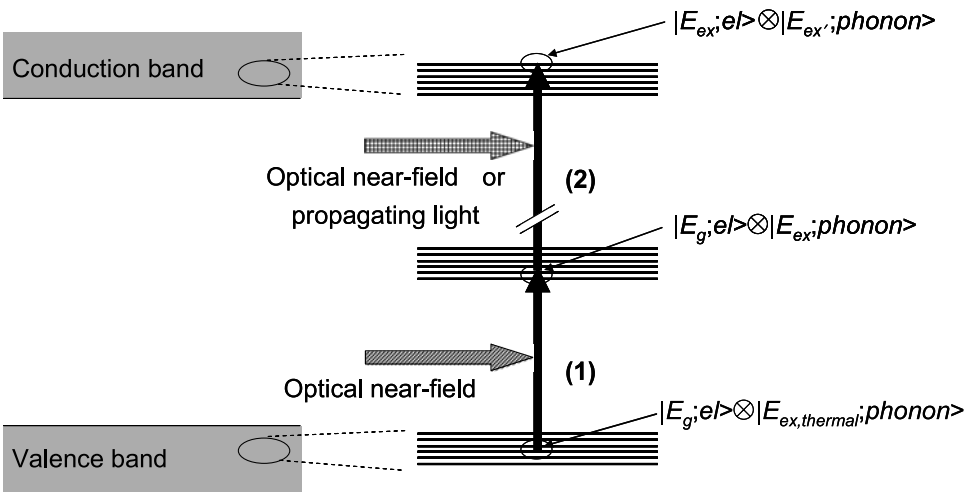

Fig. 1 Exciting an electron by the two-step phonon-assisted process. (1) and (2) represent the first and second steps of the excitation, respectively

of the electron, $|E_{\mathrm{ex,thermal}}; phonon\rangle$ represents the excited state of a phonon whose energy is determined by the lattice temperature, and $|E_{\mathrm{ex}}; phonon\rangle$ represents the excited state of a phonon whose energy depends on the energy of the optical near-field. The optical near-field is indispensable for this transition because it is electric dipole-forbidden.

(2) The second step is the transition from the intermediate state to the final excited state in the conduction band ($|E_{\mathrm{ex}}; el\rangle \otimes |E_{\mathrm{ex}'}; phonon\rangle$) by the optical near-field or conventional propagating light. Here, $|E_{\mathrm{ex}}; el\rangle$ represents the excited state of the electron, and $|E_{\mathrm{ex}'}; phonon\rangle$ represents the excited state of a phonon whose energy depends on the photon energy used for transition. Since this transition is electric dipole-allowed, it can be brought about not only by the optical near-fields but also by the conventional propagating light. After this transition, the excited phonon relaxes to the thermal equilibrium state $|E_{\mathrm{ex}',\mathrm{thermal}}; phonon\rangle$.

This phonon-assisted process has already been applied in the development of novel photochemical vapor deposition [3], photolithography [4], self-organized photochemical etching [5], and optical frequency up-conversion [6].

2 Control of the morphology of a metallic electrode surface by a phonon-assisted process

In the present study we utilized the phonon-assisted process twice: once for efficient photocurrent generation in the wavelength range beyond the one limited by E_g, as was described in Sect. 1, and once for fabricating a metallic electrode of the photovoltaic device, in which the morphology of the electrode surface can be controlled in a self-organized manner so that the phonon-assisted process is efficiently induced for photocurrent generation.

Poly(3-hexylthiophene) (P3HT) was used as a test material of a p-type semiconductor material for the photovoltaic device because it was straightforward to fabricate in a thin film without using any specialized equipment. It has been popularly used as a hole-conduction component [7]. Preliminary experiments confirmed that (1) the P3HT used showed maximum photo-absorption at the wavelength $\lambda_p = 430$ nm, (2) its long-wavelength cutoff λ_c was 570 nm, and (3) the magnitude of the photo-absorption at λ_c was less than $1/100$ times that at λ_p, which was negligibly low for the present study, and thus, the P3HT was transparent in the wavelength range longer than λ_c. A ZnO thin film was used as an n-type semiconductor material because it is transparent in the wavelength range longer than 400 nm, and also because the energies of its valence and conduction bands allow efficient photocurrent generation [8]. The ITO and Ag films were used as the two electrodes. The P3HT played the main role in determining the device operation because the depletion layer of the pn-junction was formed in the P3HT.

Thin films of these materials were deposited on a sapphire substrate by a series of processes: (1) After successive ultrasonic cleaning steps of the sapphire substrate using acetone, methanol, and pure water, respectively, an ITO film of 200 nm thickness was deposited on the sapphire substrate by sputtering. (2) A ZnO film of 100 nm thickness was deposited on the ITO film by sputtering. (3) A 10 mg/ml chloroform solution of P3HT was spin-coated on the ZnO film, followed by baking at 120°C for 6 hours in vacuum in order to remove impurities, such as the residual chloroform. As a result, a P3HT film of 50 nm thickness was formed. (4) An Ag thin film with a thickness of a few nanometers was deposited on the P3HT film. As a result, a multilayered film covering an area of 30 mm^2 was obtained on the sapphire substrate (Fig. 2(a)).

At the last stage of the fabrication process, Ag was further deposited on the Ag thin film made in step (4) in order to efficiently bring about the phonon-induced process

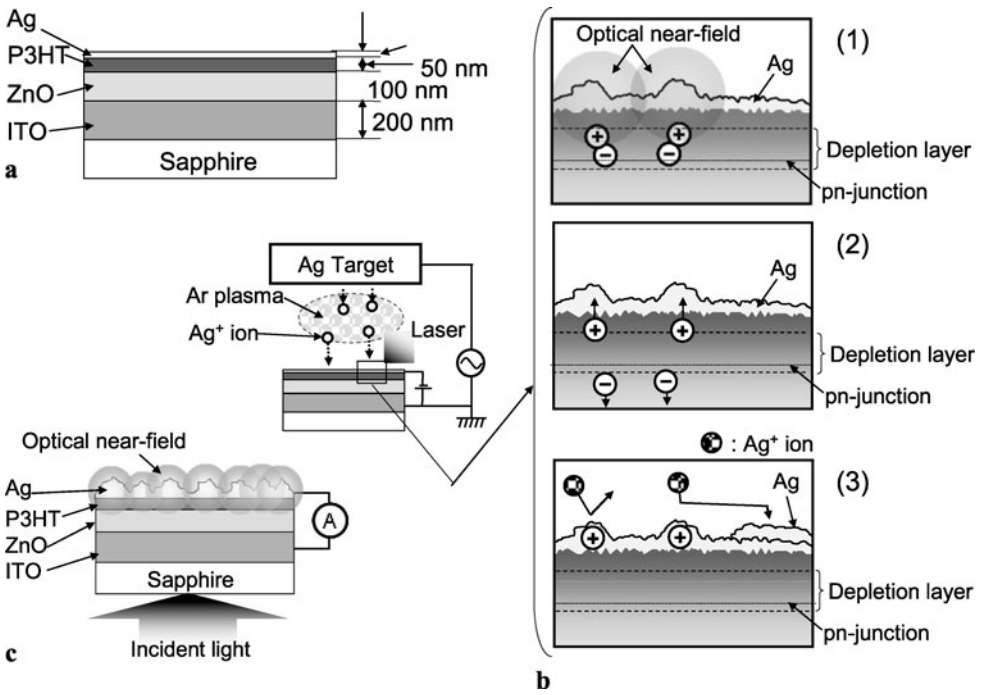

Fig. 2 Schematic diagram illustrating fabrication of a photovoltaic device. (**a**) Cross-sectional structure of the films stacked on a sapphire substrate. (**b**) Ag deposition. The encircled + and − symbols in (1)–(3) represent holes and electrons, respectively. (**c**) Application of the incident light from the rear surface of the sapphire substrate for photocurrent generation

for photocurrent generation. Figure 2(b) schematically explains this deposition, which was proposed by referring to the authors' previous work on size- and position-controlled self-assembling optical near-field deposition of nanometric metallic particles [9]. Briefly, the Ag was deposited by RF-sputtering under light illumination on the previously deposited Ag thin film of step (4) while the P3HT/ZnO pn-junction was reversely biased with a DC voltage V_b. Here, V_b was fixed to -1.5 V, and the wavelength λ_0 of the incident light was 660 nm, which is longer than λ_c of the P3HT. The diameter of the light beam used to illuminate the central part of the Ag film surface of Fig. 2(a) was 3 mm. It is expected that this deposition with light illumination controls the morphology of the Ag film as a result of the phonon-assisted process induced by the optical near-field. When the Ag film with this controlled morphology is used as an electrode of the device, it is also expected that a conspicuous phonon-assisted process will be induced for photocurrent generation.

The mechanism of controlling the morphology is:

(1) [Step (1) in Fig. 2(b)] Under light illumination, an optical near-field is generated on the Ag surface. This optical near-field excites a coherent phonon at the pn-junction, resulting in generation of a virtual exciton-phonon-polariton [1, 2]. By the two-step phonon-assisted process described in Sect. 1, electrons can be excited to create the electron-hole pair at the pn-junction even though the photon energy of the incident light is lower than E_g.

(2) [Step (2) in Fig. 2(b)] The created electron-hole pairs disappear because the electrons and positive holes are separated from each other due to the electric field of the reversely biased voltage. As a result, the positive holes are injected into the deposited Ag.

(3) [Step (3) in Fig. 2(b)] Since the sputtered Ag is positively ionized due to the transmission of the Ag through the argon plasma (argon gas pressure: 0.6 Pa) or due to the collision of the argon plasma with the Ag-target used for RF-sputtering [10], these positively ionized Ag particles are repulsed from the area of the positively charged Ag film in which the positive holes have been injected in the manner described in (2). This means that subsequent deposition of Ag is suppressed in the area in which the optical near-fields are generated efficiently. As a result, a unique granular Ag film is formed, which depends on the spatial distribution of the optical near-field energy. This granular Ag film grows in a self-assembled manner with increasing RF-sputtering time, resulting in the formation of a unique morphology.

By using this morphology-controlled Ag film as an electrode of the photovoltaic device and by applying the incident light from the rear surface of the sapphire substrate (Fig. 2(c)), it is expected that the optical near-field can be efficiently generated on the electrode. Thus, electron-hole pairs can be created efficiently by the phonon-assisted process if the photovoltaic device is illuminated by light with the same wavelength λ_0 as the one used for controlling the morphology of the Ag film. On the other hand, if it is illuminated by light of a different wavelength λ_1, the efficiency of the electron-hole pair creation should be

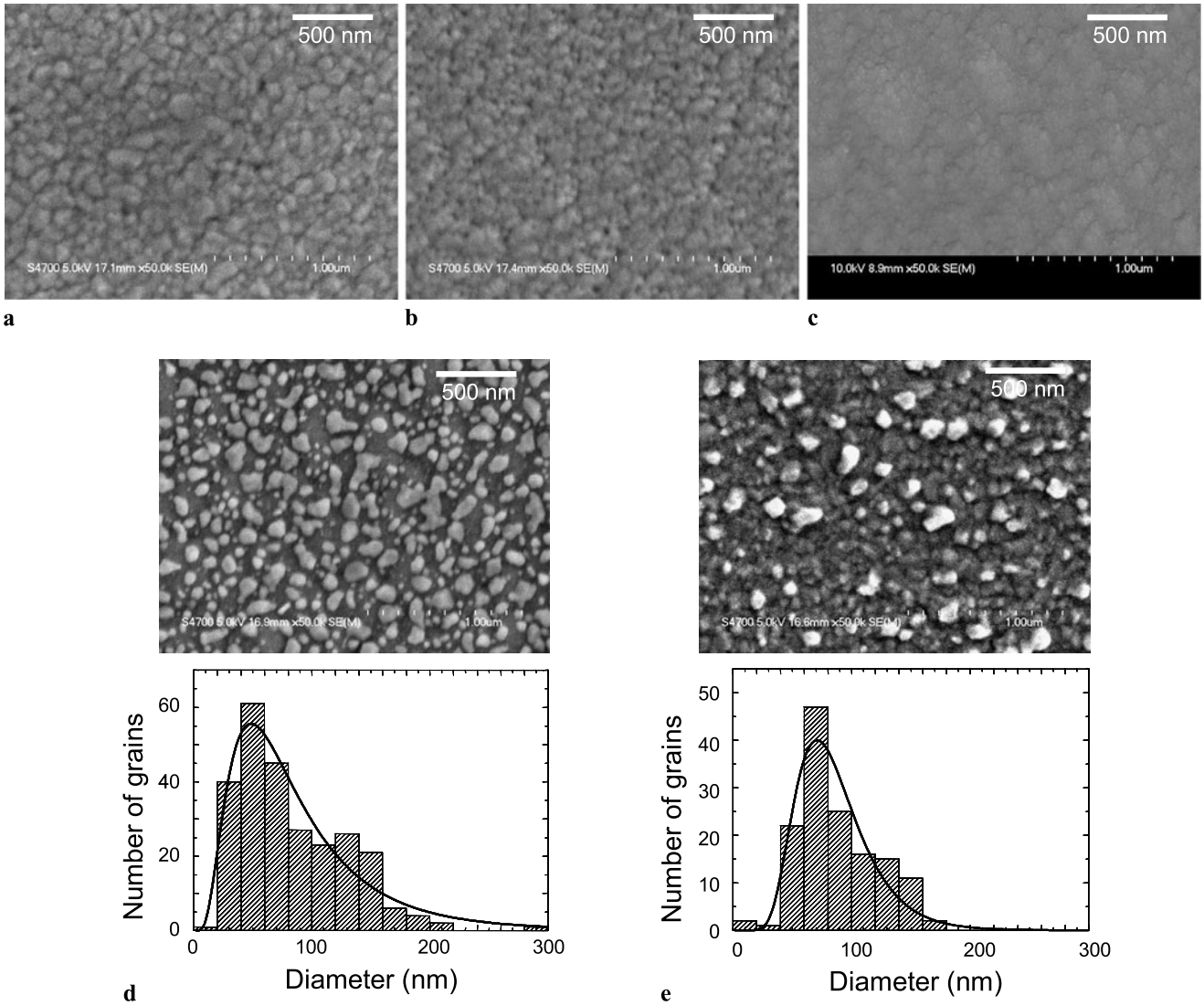

Fig. 3 SEM images of the Ag film surfaces. (**a**)–(**e**) are for Devices 1–5, respectively. Histograms in (**d**) and (**e**) represent the distributions of the grain diameters in the SEM images. The *solid curves* in these figures are the lognormal size distributions fitted to the histograms

lower because the spatial profile and the photon energy of the generated optical near-field are different from those in the case of using λ_0 for controlling the morphology. Thus, this device should exhibit wavelength-selectivity in the photocurrent generation, which should take a maximum at the wavelength λ_0. Furthermore, since this wavelength is longer than λ_c, the working wavelength becomes longer than the one limited by E_g.

By employing several values of V_b and the incident light power P, Ag was deposited on the previously fabricated Ag film of step (4) by 30 minutes of RF-sputtering. Finally, five devices were fabricated; the values of V_b and P were $V_b = 0$ and $P = 0$ (Device 1), $V_b = 0$ and $P = 30$ mW (Device 2), $V_b = 0$ and $P = 80$ mW (Device 3), $V_b = -1.5$ V and $P = 50$ mW (Device 4), and $V_b = -1.5$ V and $P = 70$ mW (Device 5). Device 1, fabricated without applying V_b and P, was used as a reference to evaluate the performance of the other devices.

Figures 3(a)–(e) show SEM images of the Ag-film surfaces of Devices 1–5. By comparing them, it is clear that the Ag surfaces of Devices 4 and 5 (Figs. 3(d) and (e)) were very rough, with larger grains than those of Devices 1–3 (Figs. 3(a)–(c)). Furthermore, since the grain sizes in Figs. 3(d) and (e) were different from each other, these figures were analyzed to evaluate the size distribution of the grains. The figures were digitized, and the shapes of the grains were approximated by circles of equal area. After this approximation, the distribution of the diameters was fitted by a lognormal size-distribution function, which has been popularly used for representing the size distribution in particle growth processes [11, (1)]. The results are shown in Figs. 3(d) and (e). From the lognormal size-distribution

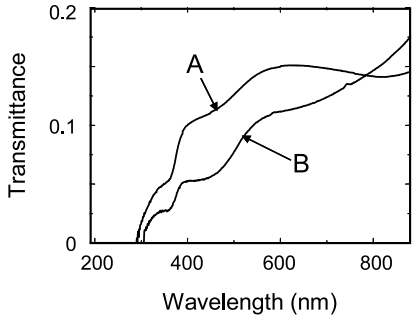

Fig. 4 Optical transmittance of the device measured by applying the incident light from the rear surface of the sapphire substrate. Curves A and B are for Devices 5 and 4, respectively

curves fitted to the histograms, the average and standard deviation of the diameters of Fig. 3(d) were found to be 90 nm and 64 nm, respectively. Those of Fig. 3(e) were 86 nm and 32 nm, respectively. These results show a decrease of the standard deviation with increasing incident light power for controlling the morphology, indicating that these granular surfaces were formed in a self-organized manner.

It should be possible for the optical near-field on the Ag grains of Figs. 3(d) and (e) to extend to the pn-junction because the decay length of the optical near-field on a nanometric particle is equivalent to the particle size. This possibility was confirmed by evaluating the optical transmittance of the devices by applying the incident light (light beam diameter: 2 mm) from the rear surface of the sapphire substrate. As shown by curve A in Fig. 4, the optical transmittance of Device 5 was higher than 0.1 in the wavelength range 400–880 nm. Curve B also shows a high optical transmittance for Device 4. From these curves, it was confirmed that the thicknesses of the Ag film in Figs. 3(d) and (e), averaged over the illuminated area, were less than 20 nm. Thus, the sum of the thicknesses of the Ag and P3HT was estimated to be less than 70 nm. Therefore, it is expected that the optical near-field generated on the Ag grains of Figs. 3(d) and (e) can extend to the pn-junction because the average diameters of these grains were 90 nm and 86 nm, respectively. As a result, it is expected that this optical near-field efficiently creates electron-hole pairs at the pn-junction by the phonon-assisted process. On the other hand, the optical transmittances of Devices 1–3 were as low as 1×10^{-5} in the whole wavelength range of Fig. 4, indicating the high reflection and absorption by the Ag films. This is because these Ag films were as thick as 800 nm, which was measured directly by using a surface profiler.

3 Evaluation of the wavelength dependence of the generated photocurrent

In order to evaluate the dependence of the generated photocurrent on the incident light wavelength λ_i, in the first measurement we employed a halogen lamp as a light source, whose emission wavelength range was 350–1500 nm and whose light beam diameter was 1 mm. The light was incident on the device through the sapphire substrate (Fig. 2(c)). The first row of Table 1 represents the measured values of the photocurrent $i_{\mathrm{p,whole},j}$ ($j = 1$–5 for Devices 1–5) generated by the incident light in the wavelength range 350 nm $\leq \lambda_i \leq$ 1500 nm. The incident light power P_{whole} integrated over this wavelength range was 5.5 mW. The second row is the photocurrent $i_{\mathrm{p,long},j}$ for the wavelength range 600 nm $\leq \lambda_i \leq$ 1500 nm, which is longer than λ_c of P3HT. This long-wavelength light component was extracted from the light source by using a long-pass optical filter. The incident light power P_{long} was calibrated to 5.0 mW by taking the optical transmittance ($= 0.96$) of the long-pass optical filter into account. The third row represents the photocurrent $i_{\mathrm{p,short},j}$ for the wavelength range 350 nm $\leq \lambda_i \leq$ 600 nm, which was obtained by simply taking the difference between the measured values of $i_{\mathrm{p,whole},j}$ and $i_{\mathrm{p,long},j}$.

This table clearly shows that Devices 4 and 5 generated the photocurrents $i_{\mathrm{p,long},4}$ and $i_{\mathrm{p,long},5}$ even in the longer wavelength range beyond E_g of the P3HT, whereas Devices 1–3 generated the photocurrents $i_{\mathrm{p,short},j}$ ($j = 1$–3) only in the shorter wavelength range limited by E_g. It also shows that the photocurrent $i_{\mathrm{p,long},5}$ was much higher than $i_{\mathrm{p,long},4}$. This is attributed to the fact that the phonon-assisted process was induced more strongly in Device 5 for generating photocurrent from Device 5 because the Ag film had a more effective morphology due to the higher optical power illumination in the RF-sputtering process.

Table 1 also shows that the photocurrent $i_{\mathrm{p,short},5}$ from Device 5 in the short wavelength range $\lambda_i \leq 600$ nm (2.07 eV photon energy) was much lower than $i_{\mathrm{p,short},1}$ of Device 1. The photocurrent $i_{\mathrm{p,short},4}$ of Device 4 was also lower than $i_{\mathrm{p,short},1}$. These lower photocurrents are attributed to de-excitation of electrons by another two-step phonon-assisted process, which is opposite to that illustrated in Fig. 1. Because the incident light wavelength for generating $i_{\mathrm{p,short},j}$ is shorter than the one limited by E_g of P3HT, the electrons in Device 1 can be directly excited by a conventional electric dipole-allowed transition from HOMO to LUMO (from the valence to the conduction band in the case of Fig. 1: $|E_g; el\rangle \otimes |E_{\mathrm{ex,thermal}}; phonon\rangle \rightarrow |E_{\mathrm{ex}}; el\rangle \otimes |E_{\mathrm{ex}'}; phonon\rangle$) to create the electron-hole pairs. The phonons subsequently relax to the thermal equilibrium phonon state $|E_{\mathrm{ex,thermal}}; phonon\rangle$). Afterwards, the created electron-hole pairs are spent to generate the photocurrent. Simultaneously, however, electron-hole recombination is also possible, resulting in conventional propagating light emission via the electric dipole-allowed transition ($|E_{\mathrm{ex}}; el\rangle \otimes |E_{\mathrm{ex,thermal}}; phonon\rangle \rightarrow |E_g; el\rangle \otimes |E_{\mathrm{ex}'}; phonon\rangle$) (Fig. 5(a)). As a result, the higher the magnitude of this recombination, the lower the generated photocurrent.

Table 1 Photocurrent generated by a halogen lamp (in units of nA)

	Device 1	Device 2	Device 3	Device 4	Device 5
$i_{\mathrm{p,whole},j}$ (350 nm $\leq \lambda_i \leq$ 1500 nm) ($P_{\mathrm{whole},j} = 5.5$ mW)	2.18	3.01	2.32	1.65	5.17
$i_{\mathrm{p,long},j}$ (600 nm $\leq \lambda_i \leq$ 1500 nm) ($P_{\mathrm{long},j} = 5.0$ mW)	0.02	0.02	0.04	0.34	5.10
$i_{\mathrm{p,short},j}$ (350 nm $\leq \lambda_i \leq$ 600 nm) ($= i_{\mathrm{p,whole},j} - i_{\mathrm{p,long},j}$)	2.16	2.99	2.28	1.31	0.07

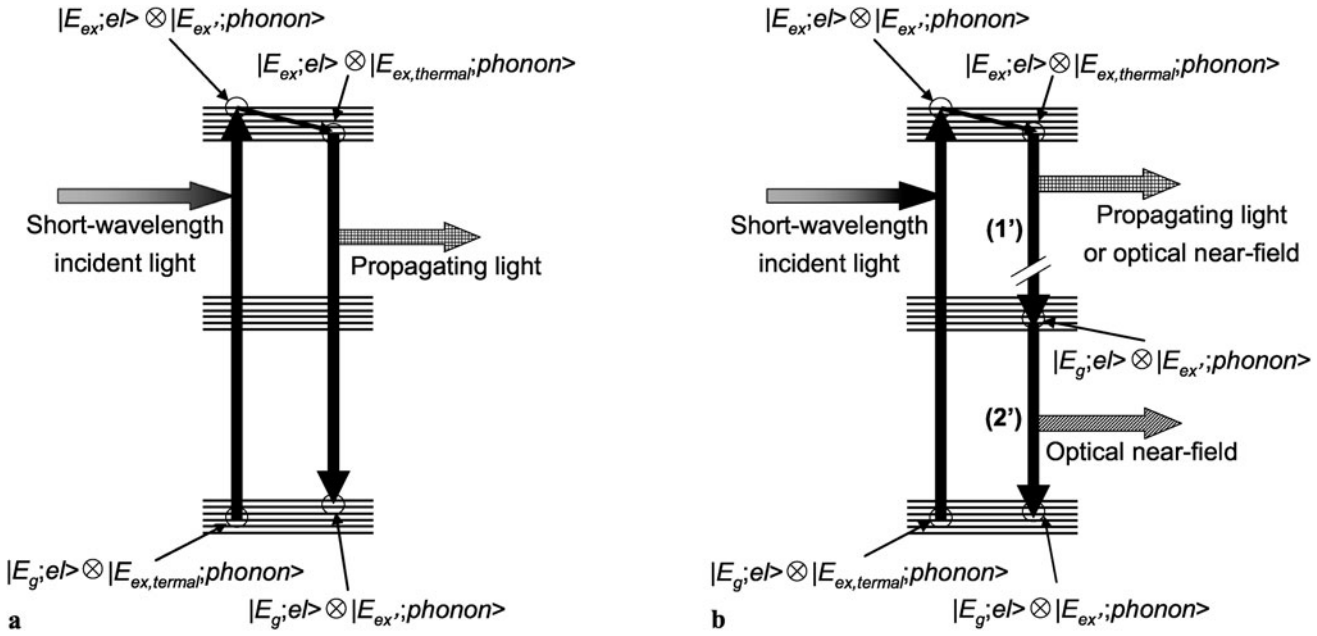

Fig. 5 Schematic explanation of exciting an electron with incident light whose wavelength is shorter than the one limited by E_g of P3HT. Subsequent de-excitation is also illustrated. (**a**) is applied to all Devices 1–5. (**b**) is also applied to Devices 4 and 5. (1) and (2) in (**b**) represent the first and second steps of the de-excitation, respectively

In the case of Devices 4 and 5, on the other hand, a further decrease of the photocurrent is expected by de-excitation of electrons through the two-step phonon-assisted process ((1′) and (2′) in Fig. 5(b)):

(1′) The first-step de-excitation is through the transition from the initial state in LUMO ($|E_{\mathrm{ex}}; el\rangle \otimes |E_{\mathrm{ex,thermal}}; phonon\rangle$) to the intermediate state ($|E_g; el\rangle \otimes |E_{\mathrm{ex}'}; phonon\rangle$. Since this transition is electric dipole-allowed, it can emit conventional propagating light, as well as generating the optical near-field.

(2′) The second-step de-excitation is through the transition from the intermediate state to the ground state in HOMO ($|E_g; el\rangle \otimes |E_{\mathrm{ex}',\mathrm{thermal}}; phonon\rangle$). Since this transition is electric dipole-forbidden, only the optical near-field is generated.

De-excitation through the two-step phonon-assisted process in Device 5 was confirmed by measuring the photoluminescence (PL), i.e., the propagating light emitted as a result of the first-step de-excitation (1′), using the second harmonic of a Ti:Al_2O_3 laser as a light source (wavelength: 430 nm). It should be pointed out that pump-probe spectroscopy has previously enabled measuring the lifetimes of the intermediate state $|E_g; el\rangle \otimes |E_{\mathrm{ex}'}; phonon\rangle$ in Coumarin 480 and 540A dye grains [12]. The results of the present measurements are shown in Fig. 6. As a reference, the curve of Fig. 6(a) represents the PL spectrum emitted from Device 1. Its peak wavelength was 585 nm, which was 15 nm longer than λ_c of P3HT due to the conventional Stokes-shift of P3HT [13]. The full-width at half-maximum (FWHM) of this spectral curve was 90 nm. This spectrum is attributed to the conventional propagating light emission of Fig. 5(a).

On the other hand, curve A of Fig. 6(b) is the PL spectrum from Device 5. Its peak wavelength was 620 nm, i.e., the red-shift from λ_c was as large as 50 nm. This red-shifted PL was attributed to the propagating light emission due to

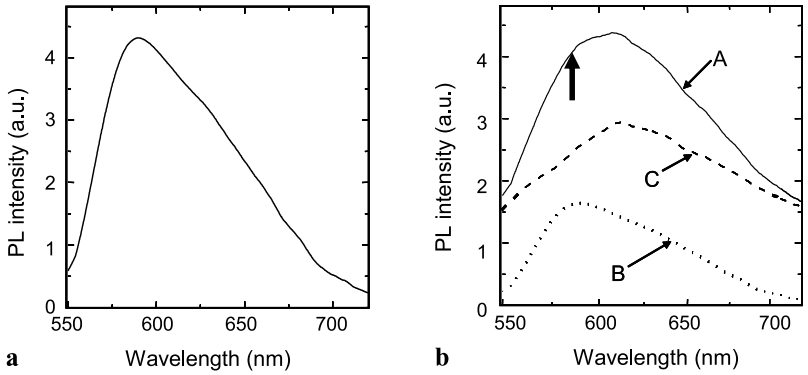

Fig. 6 Photoluminescence (PL) spectra of the devices. (**a**) The PL spectrum of Device 1. (**b**) Curve A represents the PL spectrum of Device 5. The upward-pointing *black arrow* indicates a kink in this curve. Curve B represents the PL spectral component due to the conventional propagating light emission, as in the case of (**a**). Curve C represents the remaining component

the first-step de-excitation of Fig. 5(b). The FWHM of this spectral profile was as wide as 150 nm, which was attributed to the several PL spectral components which overlap each other due to the multiple closely spaced phonon energy levels. Furthermore, curve A has a kink at 585 nm, as is indicated by the upward-pointing arrow. This is because curve A also contains the PL spectral component due to the conventional propagating light emission, as was the case of Device 1. By referring to the spectral profile of Fig. 6(a), the spectral component at the kink was extracted from curve A, and the result is represented by curve B. The remaining component is represented by curve C. By this extraction, the magnitudes of the contributions of the conventional de-excitation (Fig. 5(a)) and the first-step phonon-assisted process ((1′) of Fig. 5(b)) to curve A were evaluated by comparing the areas bounded by curves B and C and the horizontal axis. As a result, the ratio of the calculated areas was 1:4, from which it was found that the PL and the de-excitation of Device 5 was dominated by the phonon-assisted process of Fig. 5(b).

The second measurements evaluated the detailed wavelength dependences of the photocurrent generation in the longer wavelength range beyond E_g of P3HT, using a Ti:Al_2O_3 laser-pumped wavelength-tunable optical parametric oscillator as a light source. Experimental results for the wavelength range 580 nm $\leq \lambda_i \leq$ 670 nm are shown in Fig. 7. Since a limited area of the device surface was illuminated by a 1 mm-diameter incident light beam, the generated photocurrent density was employed to draw this figure, as has been popularly employed in previous work [7]. A linear relation between the incident light power and the generated photocurrent density was confirmed by preliminary experiments by applying low-power incident light (0.02–2 mW, corresponding to 2.5 mW/cm^2–250 mW/cm^2 density). This linear relation was attributed to the fact that the rate of creating electron-hole pairs was governed only by the electric dipole-forbidden transition of the first-step excitation of Fig. 1 under low light power-density excitation. The creation rate by the second-step excitation of Fig. 1 was sufficiently high because of the electric dipole-allowed transition. Based on this linear relation, the incident light power

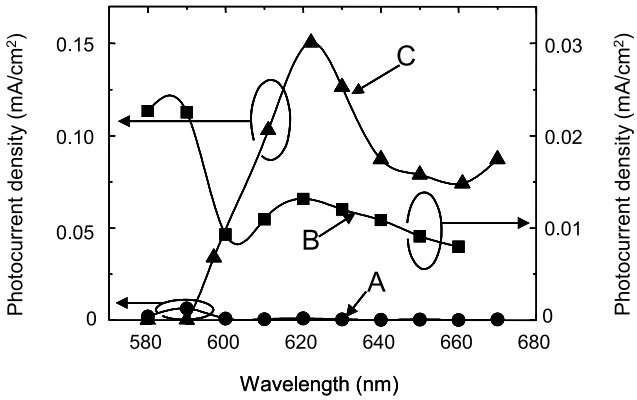

Fig. 7 Dependences of the generated photocurrent densities on the wavelength of the incident light. Curves A, B, and C are for Devices 1, 4, and 5, respectively

density was fixed to 125 mW/cm^2 (1 mW optical power) for photocurrent density measurements. The photocurrent densities from Devices 2 and 3 are not shown in this figure because they were negligibly low. That from Device 1 was also very low, but it is shown by curve A as a reference.

Curves B and C represent the measured photocurrent densities from Devices 4 and 5, respectively, generated by incident light with wavelengths up to $\lambda_i = 670$ nm, which clearly demonstrates the expansion of the working wavelength range beyond that limited by E_g of P3HT. These curves also indicate the possibility of photocurrent generation even in the wavelength range longer than 670 nm. The photocurrent of curve C was the highest at $\lambda_{i_p} = 620$ nm, whereas it was very low in the range $\lambda_i \leq 600$ nm, due to the strong phonon-assisted process, as was shown in Table 1. Thus, Device 5 is effectively a wavelength-selective photovoltaic device for incident light with a wavelength beyond that limited by E_g, which was the aim of this study. The photocurrent density was 0.15 mW/cm^2 at the peak of curve C ($\lambda_{i_p} = 620$ nm), which corresponds to a quantum efficiency of 0.24% because the incident light power density was 125 mW/cm^2. This efficiency is as high as that of a conventional hetero-junction photovoltaic device using P3HT [14]. However, it should be pointed out that De-

vice 5 realized such a high quantum efficiency even for wavelengths longer than the one limited by E_g of P3HT.

The wavelength λ_{i_p} ($= 620$ nm) at the peak of curve C was 40 nm shorter than λ_0 ($= 660$ nm) used for controlling the morphology of the Ag film. This difference was attributed to the DC Stark effect induced by the reverse bias voltage V_b ($= -1.5$ V) applied in the process of controlling the morphology of the Ag film: It is known that the width of the depletion layer of a pn-junction is about 10 nm for general organic semiconductors [15]. Also, the relative dielectric constant of P3HT is 3.0 [16]. By using these values, it is estimated that a DC electric field of 1×10^6 V/m was applied to the depletion layer of the P3HT/ZnO due to V_b. Furthermore, by approximating the reduced mass of the electron–hole pair in the pn-junction as the mass of an electron in vacuum, the shift of the long-wavelength cutoff λ_c induced by the applied DC electric field was estimated by using a formula for the photo-absorption coefficient [17, (23)]. As a result, the estimated value was 40 nm, which agrees with the measured wavelength difference given above.

4 Summary

P3HT and ZnO were used as test materials for the p-type and n-type semiconductors, respectively. In order to fabricate an electrode, Ag was deposited on the P3HT film by RF-sputtering under light illumination (wavelength $\lambda_0 =$ 660 nm) while the P3HT/ZnO pn-junction was reversely biased. As a result, a unique morphology was formed on the Ag film, which originated from the phonon-assisted process brought about by the optical near-field in a self-organized manner. The fabricated devices generated photocurrent by the phonon-assisted process brought about by the optical near-fields even with incident light of 670 nm wavelength, which was longer than the long-wavelength cutoff λ_c ($= 570$ nm) limited by the bandgap energy E_g of P3HT. On the other hand, the photocurrent was extremely low for incident light wavelengths shorter than λ_c, which was attributed to de-excitation by the phonon-assisted process. Thus, it was concluded that the photocurrent was generated in a wavelength-selective manner, exhibiting a maximum at the incident light wavelength of 620 nm, which was attributed to the Stark effect due to the reversely biased DC electric field applied in the Ag deposition process.

It is expected that the present method can be applied not only to P3HT but also to other organic and inorganic semiconductors because the phonon-assisted process was induced merely by controlling the morphology of the electrode, while the semiconductor materials remained untreated. Higher efficiency can be expected by fine adjustment of the reverse bias voltage, light power, and wavelength used for controlling the morphology.

References

1. K. Kobayashi, S. Sangu, H. Ito, M. Ohtsu, Phys. Rev. A **63**, 013806 (2001)
2. Y. Tanaka, K. Kobayashi, Physica E **40**, 297 (2007)
3. T. Kawazoe, K. Kobayashi, S. Takubo, M. Ohtsu, J. Chem. Phys. **122**, 024715 (2005)
4. T. Kawazoe, M. Ohtsu, Y. Inao, R. Kuroda, J. Nanophoton **1**, 011595 (2007)
5. T. Yatsui, K. Hirata, W. Nomura, Y. Tabata, M. Ohtsu, Appl. Phys. B **93**, 55 (2008)
6. T. Kawazoe, H. Fujiwara, K. Kobayashi, M. Ohtsu, J. Sel. Top. Quantum Electron. **15**, 1380 (2009)
7. M. Bredol, K. Matras, A. Szatkowski, J. Sanetra, A. Prodi-Schwab, Sol. Energy Mater. Sol. Cells **93**, 662 (2009)
8. X. Ju, F. Wei, K. Varutt, T. Hori, A. Fujii, M. Ozaki, Nanotechnology **19**, 435706 (2008)
9. T. Yatsui, W. Nomura, M. Ohtsu, Nano Lett. **5**, 2548 (2005)
10. J. Joo, J. Vac. Sci. Technol. A **18**, 23 (2000)
11. J. Soederlund, L.B. Kiss, G.A. Niklasson, C.G. Granqvist, Phys. Rev. Lett. **80**, 2386 (1998)
12. H. Fujiwara, T. Kawazoe, M. Ohtsu, Appl. Phys. B **98**, 283 (2010)
13. M. Wang, X. Wang, Sol. Energy Mater. Sol. Cells **91**, 1782 (2007)
14. S. Guenes, H. Neugebauer, S. Sariciftci, Chem. Rev. **107**, 1324 (2007)
15. M. Onoda, K. Tada, H. Nakayama, J. Appl. Phys. **86**, 2110 (1999)
16. A. Khaliq, F. Xue, K. Varahramyan, Microelectron. Eng. **86**, 2312 (2009)
17. J. Callaway, Phys. Rev. **130**, 549 (1963)

Nanophotonic code embedded in embossed hologram for hierarchical information retrieval

Naoya Tate[1,2*], Makoto Naruse[1,2,3], Takashi Yatsui[1,2], Tadashi Kawazoe[1,2], Morihisa Hoga[4], Yasuyuki Ohyagi[4], Tokuhiro Fukuyama[5], Mitsuru Kitamura[4], and Motoichi Ohtsu[1,2]

[1]*Department of Electrical Engineering and Information Systems, School of Engineering, The University of Tokyo, 2-11-16 Yayoi, Bunkyo-ku, Tokyo, 113-8656, Japan*

[2]*Nanophotonics Research Center, School of Engineering, The University of Tokyo, 2-11-16 Yayoi, Bunkyo-ku, Tokyo, 113-8656, Japan*

[3]*National Institute of Information and Communications Technology, 4-2-1 Nukuikita, Koganei, Tokyo, 184-8795 Japan*

[4]*Dai Nippon Printing Co. Ltd., Research and Development Center, 250-1 Wakashiba, Kashiwa, Chiba, 277-0871 Japan*

[5]*Dai Nippon Printing Co. Ltd., Corporate R&D Division, 1-1 Ichigaya-kagacho, Shinjuku-ku, Tokyo, 162-8001 Japan*

tate@nanophotonics.t.u-tokyo.ac.jp

Abstract: A *hierarchical hologram* works in both optical far-fields and near-fields, the former being associated with conventional holographic images, and the latter being associated with the optical intensity distribution based on a nanometric structure that is accessible only via optical near-fields. We propose embedding a *nanophotonic code*, which is retrievable via optical near-field interactions involving nanometric structures, *within* an embossed hologram. Due to the one-dimensional grid structure of the hologram, evident polarization dependence appears in retrieving the code. Here we describe the basic concepts, numerical simulations, and experimental results in fabrication of a prototype hierarchical hologram and describe its optical characterization.

OCIS codes: (090.0090) Holography; (200.4560) Optical data processing; (220.4241) Nanostructure fabrication; (230.0230) Optical devices; (350.4238) Nanophotonics and photonic crystals.

References and links

1. R. L. Van Renesse (ed), *Optical document scanning*, (Altech House Optoelectronics Library, 1998).
2. S. P. McGrew, "Hologram counterfeiting: problems and solutions," Proc. SPIE, Optical Security and Anticounterfeiting Systems, **1210**, 66-76 (1990).
3. N. Tate, W. Nomura, T. Yatsui, M. Naruse, and M. Ohtsu, "Hierarchical Hologram based on Optical Near- and Far-Field Responses," Opt. Express **16,** 607-612 (2008).
4. M. Ohtsu, K. Kobayashi, T. Kawazoe, T. Yatsui, and M. Naruse (ed), *Principles of Nanophotonics*, (Taylor and Francis, Boca Raton, 2008).
5. M. Ohtsu, T. Kawazoe, T. Yatsui, and M. Naruse, "Single-photon emitter using excitation energy transfer between quantum dots," IEEE J. Sel. Top. Quantum Electron. **14**, 1404-1417 (2008).

#121248 - $15.00 USD Received 9 Dec 2009; revised 18 Feb 2010; accepted 25 Mar 2010; published 26 Mar 2010

6. M. Naruse, T. Yatsui, W. Nomura, N. Hirose, and M. Ohtsu, "Hierarchy in optical near-fields and its application to memory retrieval," Opt. Express **13,** 9265-9271 (2005).
7. M. Naruse, H. Hori, K. Kobayashi, M. Ishikawa, K. Leibnitz, M. Murata, N. Tate, and M. Ohtsu, "Information theoretical analysis of hierarchical nano-optical systems in the subwavelength regime," J. Opt. Soc. Am. B **26,** 1772–1779 (2009).
8. N. Tate, H. Tokoro, K. Takeda, W. Nomura, T. Yatsui, T. Kawazoe, M. Naruse, S.-i. Ohkoshi and M. Ohtsu, "Transcription of optical near-fields by photoinduced structural change in single crystal metal complexes for parallel nanophotonic processing," Appl. Phys. B, in print (2009).

1. Introduction

Holography, which generates natural three-dimensional images, is one of the most common anti-counterfeiting techniques [1]. In the case of a volume hologram, the surface is ingeniously formed into microscopic periodic structures which diffract incident light in specific directions. A number of diffracted light beams can form an arbitrary three-dimensional image. Generally, these microscopic structures are recognized as being difficult to duplicate, and therefore, holograms have been widely used in the anti-counterfeiting of bank notes, credit cards, etc. However, conventional anti-counterfeiting methods based on the physical appearance of holograms are less than 100% secure [2]. Although they provide ease of authentication, adding other security functions without degrading the appearance is quite difficult.

Previously, we have proposed a *hierarchical hologram*, which is created by applying nanometric structural changes to the surface structure of a conventional hologram [3]. The physical scales of the nanometric structural changes and the elemental structures of the hologram are less than 100 nm and larger than 100 nm, respectively. In principle, a structural change occurring at the subwavelength scale does not affect the optical response functions, which are dominated by propagating light. Therefore, the visual aspect of the hologram is not affected by such a small structural change on the surface. Additional data can thus be written by engineering structural changes in the subwavelength regime so that they are only accessible via optical near-field interactions (we call such information retrieval *near-mode* retrieval) without having any influence on the optical responses obtained via the conventional far-field light (what we call *far-mode* retrieval). By applying this hierarchy, new functions can be added to conventional holograms.

In this paper, we propose embedding a *nanophotonic code*, which is physically a subwavelength-scale shape-engineered metal nanostructure, in a hierarchical hologram to implement a near-mode function. The basic concept of the nanophotonic code and fabrication of a sample device are described. In particular, since our proposed approach is to embed a nanophotonic code *within* the patterns of the hologram, which is basically composed of one-dimensional grating structures, it yields clear polarization dependence compared with the case where it is not embedded within the hologram or arrayed structures. There are also other benefits with the proposed approach; a major benefit is that we can fully utilize the existing industrial facilities and fabrication technologies that have been developed so far for conventional holograms, yet adding novel new functionalities to the hologram.

Here we numerically and experimentally demonstrate those features of embedding a nanophotonic code in an embossed hologram for hierarchical information retrieval. Section 2 describes the design and fabrication of the prototype device. Section 3 shows numerical characterizations, and Section 4 gives experimental results. Section 5 concludes the paper.

2. Design and fabrication of the hierarchical hologram: A nanophotonic code embedded in an embossed hologram

Our nanophotonic code is defined by induced optical near-fields, which are generated by irradiating a nanometric structure with light. An optical near-field is a non-propagating light field generated in a space extremely close to the surface of a nanometric structure [4]. Because the

#121248 - $15.00 USD Received 9 Dec 2009; revised 18 Feb 2010; accepted 25 Mar 2010; published 26 Mar 2010

light distribution depends on several parameters of the structure and the retrieving setup, various types of coding can be considered. Moreover, several novel features of nanophotonics, such as energy transfer [5] and hierarchy [6], may be exploited.

As shown in Fig. 1, we created a sample device to experimentally demonstrate the retrieval of a nanophotonic code within an embossed hologram. The entire device structure, whose size was 15 mm $\times$ 20 mm, was fabricated by electron-beam lithography on a Si substrate, followed by sputtering a 50-nm-thick Au layer, as schematically shown in the cross-sectional profile in Fig. 1(b).

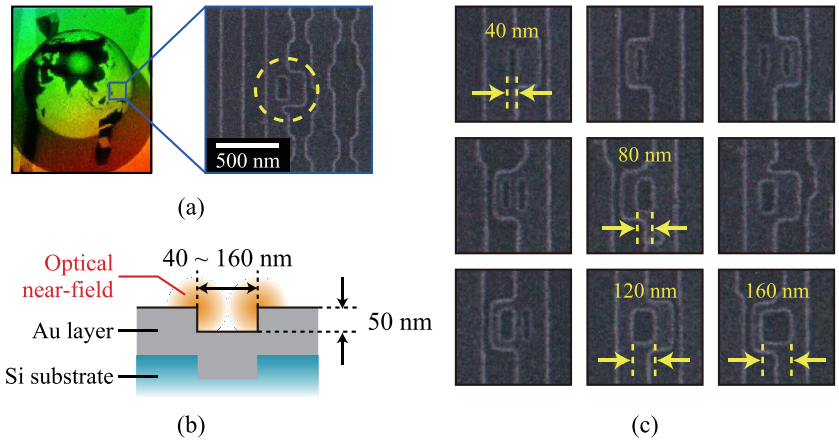

Fig. 1. (a) Fabrication of a nanometric structure as a nanophotonic code within the embossed structure of Virtuagram®. (b) Schematic diagram of fabricated sample device, and (c) SEM images of various designed patterns serving as nanophotonic codes.

As indicated in the left-hand side of Fig. 1(a), we can observe a three-dimensional image of the earth from the device. More specifically, our prototype device was essentially based on the design of *Virtuagram*®, developed by Dai Nippon Printing Co., Ltd., Japan, which is a high-definition computer-generated hologram composed of binary-level one-dimensional modulated gratings, as shown in Fig. 1(a). Within the device, we slightly modified the shape of the structure so that near-mode information is accessible only via optical near-field interactions. As shown in Figs. 1(a) and (c), square- or rectangle-shaped structures, whose associated optical near-fields correspond to the near-mode information, were embedded in the original hologram structures. We call such embedded nanostructures *nanophotonic codes*. The unit size of the nanophotonic codes ranged from 40 nm to 160 nm.

Note that the original hologram was composed of arrays of one-dimensional grid structures, spanning along the vertical direction in Fig. 1(c). To embed the nanophotonic codes, the grid structures were partially modified in order to implement the nanophotonic codes. Nevertheless, the grid structures remained topologically continuously connected along the vertical direction. On the other hand, the nanophotonic codes were always isolated from the original grid structures. Those geometrical characteristics provide interesting polarization dependence, which is discussed in detail in Sec. 3.

3. Numerical evaluations

First, electric fields at the surface of nanometric structures were numerically calculated by a finite-difference time-domain (FDTD) method based on electromagnetic simulation with *Poynting for Optics*, a product of Fujitsu, Japan.

#121248 - $15.00 USD Received 9 Dec 2009; revised 18 Feb 2010; accepted 25 Mar 2010; published 26 Mar 2010

As shown in Figs. 2 and 3, two types of calculation models were created in order to examine polarization dependencies due to the existence of environmental structures in retrieving the nanophotonic code. The calculated layer is set 10 nm above the surface of structures. The nanophotonic code was represented by a square-shaped Au structure whose side length was 150 nm and whose depth was 100 nm, which is shown near the center in Figs. 2(a) and 3(a).

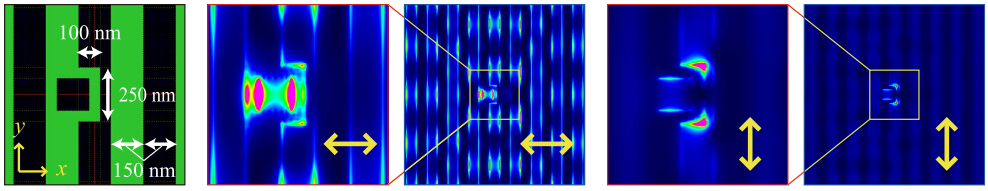

(a) (b) (c)

Fig. 2. (a) Calculation model of embedded nanophotonic code with environmental structures and calculated intensity distribution of electric field produced by (b) *x*-polarized input light and (c) *y*-polarized input light.

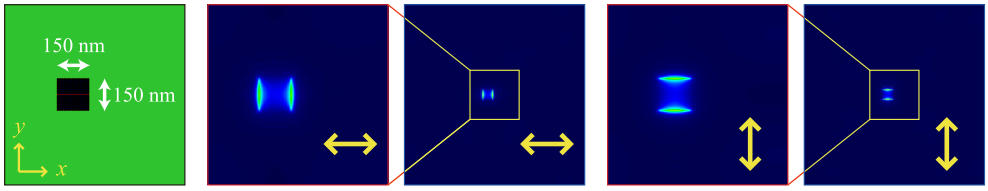

(a) (b) (c)

Fig. 3. (a) Calculation model of isolated nanophotonic code and calculated intensity distribution of electric field produced by (b) *x*-polarized input light and (c) *y*-polarized input light.

As shown in Fig. 2, the square-shaped structure was embedded in a periodic one-dimensional wire-grid structure, whose pitch was 150 nm, which models the typical structure of an embossed hologram. As shown in Fig. 3, on the other hand, the square-shaped structure, whose size was the same as that in Fig. 2(a), was not provided with any grid structure. By comparing those two cases, we can evaluate the effect of the environmental structures around the nanophotonic code. Also, we chose the square-shaped structure that is isotropic in both the *x* and *y* directions in order to clearly evaluate the effects of environmental structures and ignore the polarization dependency originating in the structure of the nanophotonic code itself. Periodic-conditioned computational boundaries were located 1.5 μm away from the center of the square-shaped structure. The wavelength was set to 785 nm.

Figures 2(b), 3(b) and 2(c), 3(c) show the electric field intensity distribution on the surface of the structure assuming *x*-polarized and *y*-polarized input light irradiation, respectively. We then investigated how the environmental structures affected the electric fields in the vicinity of the nanophotonic code and the influence of input light polarization. For such purposes, we first evaluated the average electric field intensity in the area of the nanophotonic code, denoted by $\langle I \rangle_{\mathrm{signal}}$, and that in the area including the surrounding areas, denoted by $\langle I \rangle_{\mathrm{env}}$. More specifically, $\langle I \rangle_{\mathrm{signal}}$ represents the average electric field intensity in the 0.6 μm 0.6 μm area covering the nanophotonic code, as shown by the dotted square in Fig. 4(a), whereas $\langle I \rangle_{\mathrm{env}}$ indicates that in the 2.5 μm $\times$ 2.5 μm area marked by the dashed square in Fig. 4(a). Figure 4(b) summarizes the calculated $\langle I \rangle_{\mathrm{signal}}$ and $\langle I \rangle_{\mathrm{env}}$, respectively shown by the red and blue bars.

#121248 - $15.00 USD Received 9 Dec 2009; revised 18 Feb 2010; accepted 25 Mar 2010; published 26 Mar 2010

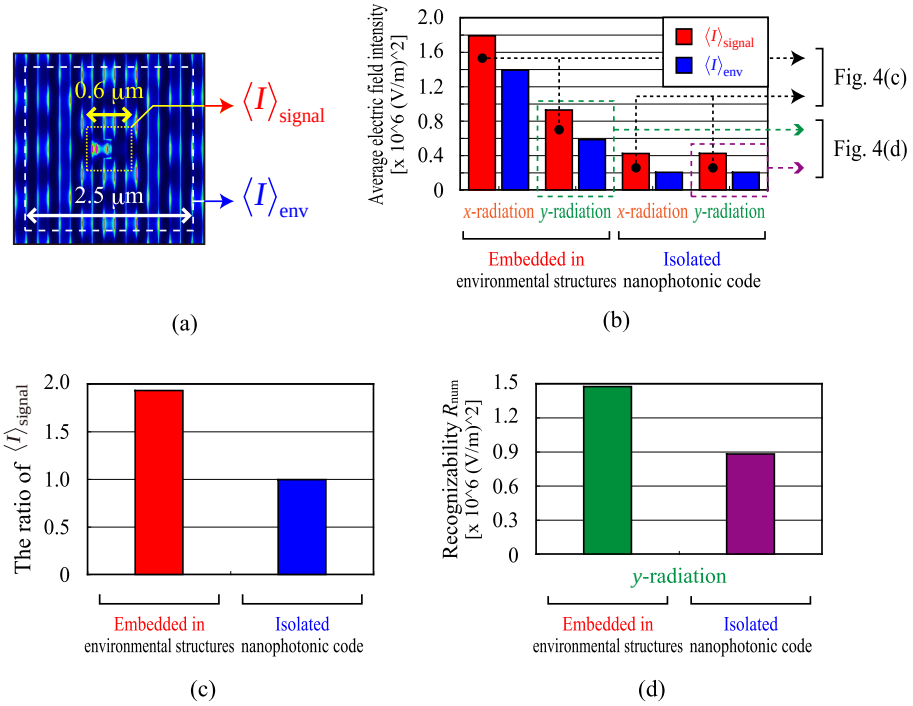

Fig. 4. (a) Schematic diagram explaining definition of average electric field intensity $\langle I\rangle_{\text{signal}}$ and $\langle I\rangle_{\text{env}}$, and (b) their graphical representations in each calculation model. Evident polarization dependency was exhibited in the case of nanometric code embedded in environmental structures. (c) The ratio of $\langle I\rangle_{\text{signal}}$ with *x*-polarized input to that with *y*-polarized input light for the embedded and isolated structures. (d) Numerical recognizability R_{num} in two types of models with *y*-polarized input light. The result indicates that the recognizability of the nanophotonic code was greatly enhanced by embedding it in the environmental structure.

We first investigated the polarization dependencies. In the case of the nanophotonic code embedded in environmental periodic structures, evident polarization dependency was observed for both $\langle I\rangle_{\text{signal}}$ and $\langle I\rangle_{\text{env}}$. For example, $\langle I\rangle_{\text{signal}}$ with *x*-polarized input was about two times larger than $\langle I\rangle_{\text{signal}}$ with *y*-polarized input light. On the other hand, the isolated nanophotonic code did not show any polarization dependency. Figure 4(c) compares the ratio of $\langle I\rangle_{\text{signal}}$ with *x*-polarized input light to that with *y*-polarized input light for the embedded and isolated structures.

Second, from the viewpoint of facilitating recognition of the nanophotonic code embedded in the hologram, it would be important to obtain a kind of higher *recognizability* for the signals associated with the nanophotonic codes. In order to evaluate such recognizability, here we define a figure-of-merit R_{num} as

$$R_{\text{num}} = \frac{\langle I\rangle_{\text{signal}}}{\langle I\rangle_{\text{env}}} \times \langle I\rangle_{\text{signal}} \tag{1}$$

which yields a higher value with higher contrast with respect to $\langle I\rangle_{\text{signal}}$ and $\langle I\rangle_{\text{env}}$ (indicated by the term $\langle I\rangle_{\text{signal}}/\langle I\rangle_{\text{env}}$) and with higher signal intensity (indicated by $\langle I\rangle_{\text{signal}}$). Figure 4(d) shows the calculated R_{num} in the case of *y*-polarized light input to the two types of models. The result indicates that the nanophotonic code embedded in environmental structure is superior to

#121248 - $15.00 USD Received 9 Dec 2009; revised 18 Feb 2010; accepted 25 Mar 2010; published 26 Mar 2010

that of the isolated code in terms of the recognizability defined by eq. (1).

We consider that such a polarization dependency and the recognizability of nanophotonic codes are based on the environmental grid structures that span along the vertical direction. The input light induces oscillating surface charge distributions due to the coupling between the light and electrons in the metal. In the present case, the *y*-polarized input light induces surface charges along the vertical grids; since the grid structure continuously exists along the *y*-direction, there is no chance for the charges to be concentrated. However, in the area of the embedded nanophotonic code, we can find structural discontinuity in the grid; this results in higher charge concentrations at the edges of the embedded nanophotonic code.

On the other hand, the *x*-polarized input light sees structural discontinuity along the horizontal direction due to the vertical grid structures, as well as in the areas of the nanophotonic codes. It turns out that charge concentrations occur not only in the edges of the nanophotonic codes but also at other horizontal edges of the environmental grid structures. In contrast to these nanophotonic codes embedded in holograms, for the isolated square-shaped nanophotonic codes, both *x*- and *y*-polarized input light have equal effects on the nanostructures.

These mechanisms indicate that such nanophotonic codes embedded in holograms could also exploit these polarization and structural dependences, not only retrieving near-mode information via optical near-field interactions. For instance, we could facilitate near-mode information retrieval using suitable input light polarization and environmental structures.

4. Experiment

In the experimental demonstration, optical responses during near-mode observation were detected using a near-field optical microscope (NOM). A schematic diagram of the detecting setup is shown in Fig. 5(a), in which the NOM was operated in an illumination-collection mode with a near-field probe having a tip with a radius of curvature of 5 nm. The fiber probe was connected to a tuning fork. Its position was finely regulated by sensing a shear force with the tuning fork, which was fed back to a piezoelectric actuator. The observation distance between the tip of the probe and the sample device was set at less than 50 nm. The light source used was a laser diode (LD) with an operating wavelength of 785 nm, and scattered light was detected by a photomultiplier tube (PMT). A Glan-Thomson polarizer (extinction ratio 10^{-6}) selected only linearly polarized light as the radiation source, and a half-wave plate (HWP) rotated the polarization.

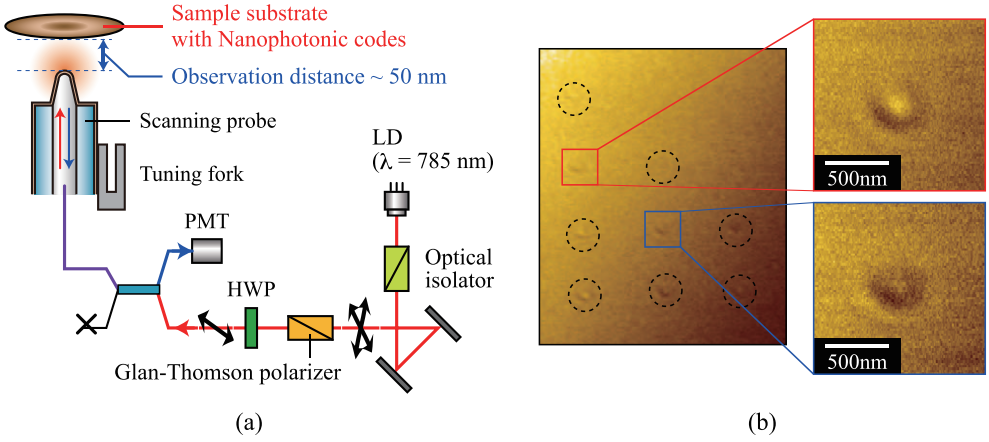

Fig. 5. (a) Schematic diagram of the experimental setup for retrieving a nanophotonic code, and (b) observed optical image as basic retrieval results.

#121248 - $15.00 USD Received 9 Dec 2009; revised 18 Feb 2010; accepted 25 Mar 2010; published 26 Mar 2010

Figure 5(b) summarizes the experimental results obtained in retrieving nanophotonic codes which were *not* embedded in the hologram. In this demonstration, different shapes of nanophotonic codes were formed in the positions marked by the dashed circles in Fig. 5(b). For the first step of our demonstration, the device was irradiated with randomly polarized light by removing the polarizer from the experimental setup. Clear near-field optical distributions that depended on the structures of the nanophotonic codes were obtained.

Figures 6 and 7 show other retrieved results of nanophotonic codes that were embedded in the hologram and *not* embedded in the hologram, respectively, using a linearly polarized radiation source. Figures 6(a) and 6(b) respectively show observed NOM images of the nanophotonic code embedded in the hologram with a standard polarization (defined as 100-degree polarization) and 60-degree-rotated polarization. Figure 6(c) summarizes the NOM images obtained with input polarizations from 0-degree to 180-degree rotated polarizations at 20-degree intervals. Also, Figs. 7(a), 7(b), and 7(c) represent the NOM images of the nanophotonic code which was not embedded in the hologram. As is evident, in the case of the nanophotonic code embedded in the hologram, clear polarization dependence was observed; for example, from the area of the nanophotonic code located in the center, a high-contrast signal intensity distribution was obtained with polarizations around 80 degree.

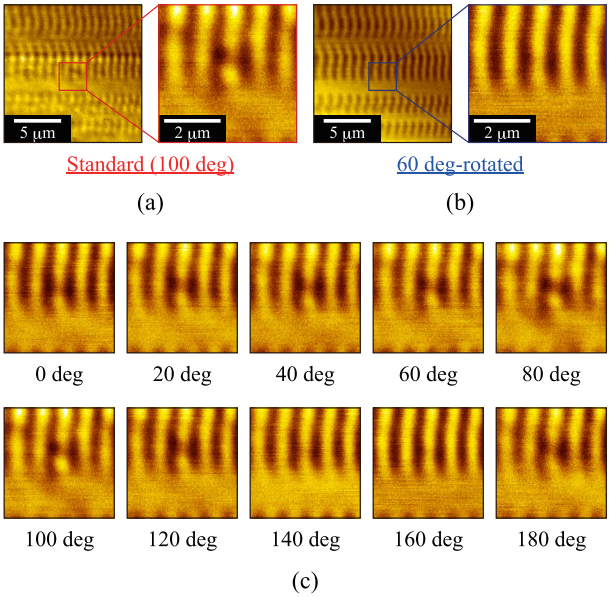

Fig. 6. Observed NOM images of optical intensity distributions of retrieved nanophotonic code embedded in environmental structures with (a) a standard polarization and (b) 60 deg-rotated polarization, and (c) NOM images observed by irradiating light with various polarizations.

To quantitatively evaluate the polarization dependency of the embedded nanophotonic code, we investigated two kinds of intensity distribution profiles from the NOM images observed. One is a horizontal intensity profile along the dashed line in Fig. 8(a), which crosses the area of the nanophotonic code, denoted by $I(x)$, where x represents the horizontal position. The other was also an intensity distribution as a function of horizontal position x; however, at every position x, we evaluated the average intensity along the vertical direction within a range of 2.5 μm, denoted by $\langle I(x)\rangle_{\mathrm{env}}$, which indicates the environmental signal distribution. When a higher intensity is obtained selectively from the area of the nanophotonic code, the difference between

#121248 - $15.00 USD Received 9 Dec 2009; revised 18 Feb 2010; accepted 25 Mar 2010; published 26 Mar 2010

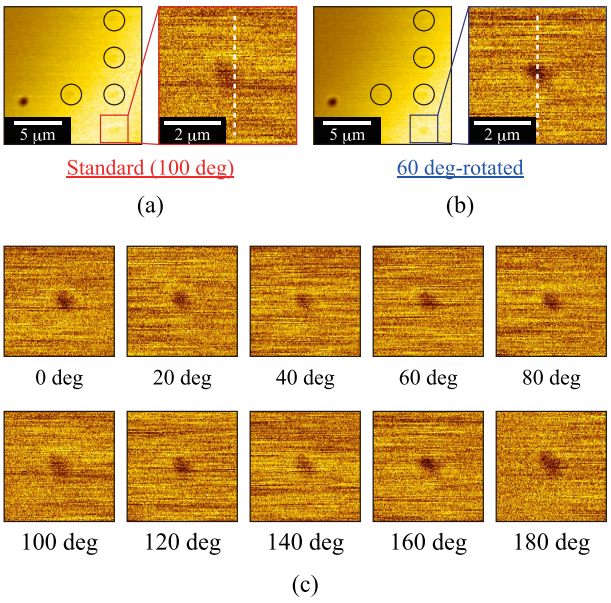

Fig. 7. Observed NOM images of optical intensity distributions of retrieved isolated nanophotonic code with (a) a standard polarization and (b) 60 deg-rotated polarization, and (c) NOM images observed by irradiating light with various polarizations.

$I(x)$ and $\langle I(x)\rangle_{\mathrm{env}}$ can be large. On the other hand, if the intensity distribution is uniform along the vertical direction, the difference between $I(x)$ and $\langle I(x)\rangle_{\mathrm{env}}$ should be small. Thus, the difference of $I(x)$ and $\langle I(x)\rangle_{\mathrm{env}}$ indicates the recognizability of the nanophotonic code. We define an experimental recognizability R_{exp} as

$$R_{\mathrm{exp}} = \sum_{x} \left| I(x) - \langle I(x)\rangle_{\mathrm{env}} \right|. \tag{2}$$

Figure 8(b) shows an example of $I(x)$ and $\langle I(x)\rangle_{\mathrm{env}}$ obtained from the NOM image of the nanophotonic code embedded in the hologram with the standard input light polarization (corresponds to Fig. 6(a)). Figures 8(c) and 8(d) show R_{exp} as a function of input light polarization based on the NOM results shown in Figs. 6(c) and 7(c), respectively. The nanophotonic code embedded in the hologram exhibited much greater polarization dependency, as shown in Fig. 8(c), where the maximum R_{exp} was obtained at 80-degree input polarization, whereas only slight polarization dependency was observed with the isolated nanophotonic code, as shown in Fig. 8(d). Such polarization dependence in retrieving the nanophotonic code agrees well with the results of the simulations in Figs. 2 and 3.

5. Summary

In this paper, we described the basic concept of a nanophotonic code embedded in a hologram as an implementation of a hierarchical hologram, and we demonstrated its features by numerical simulations, experimental fabrication of prototype devices, and optical characterization. One of the most notable characteristics of our proposed approach is embedding a nanophotonic code within the patterns of a hologram composed of one-dimensional grating structures; it yields clear polarization dependence compared with an isolated nanophotonic code that is not embedded within a grid structure. These features were successfully demonstrated both nu-

#121248 - $15.00 USD Received 9 Dec 2009; revised 18 Feb 2010; accepted 25 Mar 2010; published 26 Mar 2010

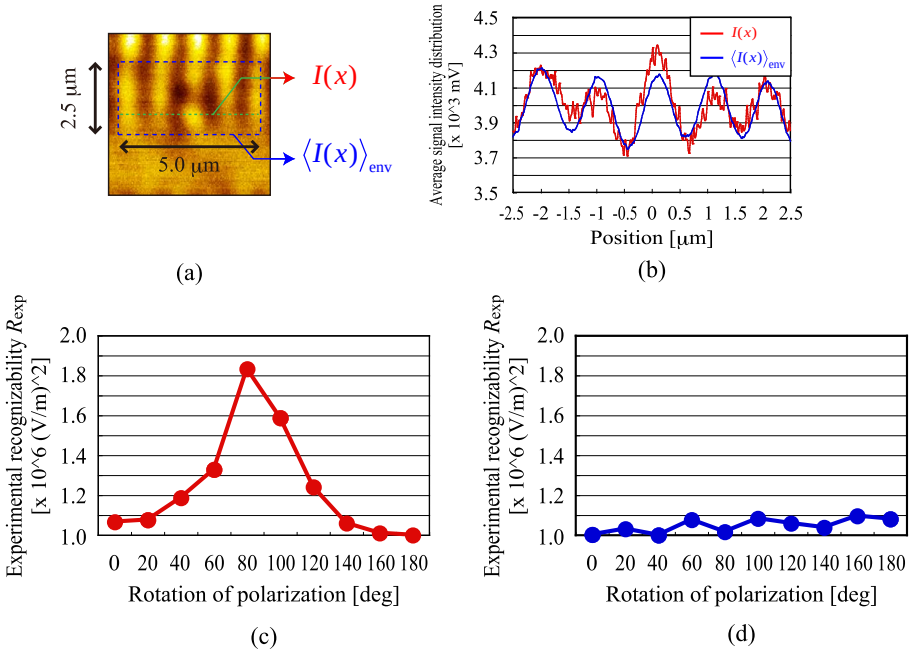

Fig. 8. (a) Schematic diagram explaining definition of $I(x)$ and $\langle I(x)\rangle_{\mathrm{env}}$, and (b) their plotted results. (c) Calculated experimental recognizability R_{exp} of embedded nanophotonic code and (d) that of isolated nanophotonic code. Evident recognizability and polarization dependency were exhibited.

merically and experimentally. Also, because embedding and retrieval of a nanophotonic code requires highly advanced technical know-how, this approach can also improve the strength of anti-counterfeiting measures.

Our results indicated that the environmental structure provides interesting polarization dependency, and more interestingly, facilitates the retrieval of near-field information. In our further research, we may understand the relation between the retrieved optical intensity distributions and the design of the nanometric structures, including their environmental conditions. Such insights should allow us to propose, for instance, an optimized strategy for implementing nanophotonic codes, or a strategy robust to errors that possibly occur in the fabrication and/or retrieval processes [7]. Moreover, a simpler method for retrieving the nanophotonic code is required without using optical fiber probe tips [8]. These aspects are currently being investigated by the authors.

Acknowledgement

This work was supported in part by a comprehensive program for personnel training and industry–academia collaboration based on projects funded by the New Energy and Industrial Technology Organization (NEDO), Japan, the Global Center of Excellence (G-COE) gSecure-Life Electronicsh project, and Special Coordination Funds for Promoting Science and Technology sponsored by the Ministry of Education, Culture, Sports, Science and Technology (MEXT), Japan.

#121248 - $15.00 USD Received 9 Dec 2009; revised 18 Feb 2010; accepted 25 Mar 2010; published 26 Mar 2010

Self-assembly method of linearly aligning ZnO quantum dots for a nanophotonic signal transmission device

T. Yatsui,[1,2,a)] Y. Ryu,[1] T. Morishima,[1] W. Nomura,[1,2] T. Kawazoe,[1,2] T. Yonezawa,[3] M. Washizu,[1] H. Fujita,[4] and M. Ohtsu[1,2]
[1]*School of Engineering, University of Tokyo, Bunkyo-ku, Tokyo 113-8656, Japan*
[2]*The Nanophotonics Research Centre, University of Tokyo, Bunkyo-ku, Tokyo 113-8656, Japan*
[3]*Faculty of Engineering, Hokkaido University, Sapporo, Hokkaido 060-8628, Japan*
[4]*Institute of Industrial Science, University of Tokyo, Meguro-ku, Tokyo 153-8505, Japan*

(Received 12 February 2010; accepted 4 March 2010; published online 30 March 2010)

We report a self-assembly method that aligns nanometer-sized quantum dots (QDs) into a straight line along which photonic signals can be transmitted by optically near-field effects. ZnO QDs were bound electrostatically to DNA to form a one-dimensional QD chain. The photoluminescence intensity under parallel polarization excitation along the QDs chain was much greater than under perpendicular polarization excitation, indicating an efficient signal transmission along the QD chain. As optical near-field energy can transmit through the resonant energy level, nanophotonic signal transmission devices have a number of potential applications, such as wavelength division multiplexing using QDs of different sizes. © *2010 American Institute of Physics*.
[doi:10.1063/1.3372639]

Innovations in optical technology are required for the continued development of information processing systems. One potential innovation, the increased integration of photonic devices, requires a reduction in both the size of the devices and the amount of heat they generate. Chains of closely spaced metal nanoparticles that can convert the optical mode into nonradiating surface plasmonic waves have been proposed as a way to meet these requirements.[1,2] However, one disadvantage is that they cannot break the plasmon diffraction limit. To overcome this difficulty, we developed nanophotonic signal transmission (NST) devices consisting of semiconductor quantum dots (QDs).[3–5] These NST devices operate using excitons generated in the QDs by optical near-field interactions between closely spaced QDs as the signal carrier. The exciton energy is transferred to adjacent QDs through resonant exciton energy levels, and therefore the optical beam spot may be decreased to the size of the QD. Moreover, NST devices using semiconductor QDs have higher transmission efficiency because QDs hardly couple with the lattice vibrational modes as opposed to transmission in metallic waveguides. This lattice vibration is the principal cause of large propagation losses in plasmonic waveguides. Here we report a self-assembly method that aligns nanometer-sized QDs into a straight line along which photonic signals can be transmitted by optically near-field effects.

The NST device fabrication process requires the following:

(A) Small size dispersion of QDs: it is estimated that to fabricate an NST device consisting of 5 nm QDs and an efficiency equivalent of 97%, the size dispersion must be as small as ±0.5 nm.[3]
(B) Subnanometer scale controllability in the separation between QDs: because the optical near-field coupling efficiency between adjacent QDs is determined by a Yukawa type function,[6] the separation between QDs should be controlled to a subnanometer scale.

To meet these requirements, we developed a new technique for positioning and aligning QDs that yields precise separation. Figure 1 illustrates our approach to a self-assembling NST device with angstrom-scale spacing controllability among QDs using silane-based molecular spacers and deoxyribonucleic acid (DNA).[7,8] First, ZnO QDs 5 nm in diameter were synthesized using the sol-gel method.[9,10] Typical transmission electron micrographic (TEM) images of synthesized ZnO dots are presented in Figs. 2(a) and 2(b). The dark areas indicated by the dashed ellipses correspond to the ZnO QD. These images reveal lattice spacing matches for the c-plane (0.26 nm) and m-plane (0.28 nm) of wurtzite ZnO. These results confirmed that the fabricated ZnO QDs had high-quality single-crystal crystallinity. An average ZnO QDs diameter of 5.2 nm with a standard deviation (σ) of 0.5 nm was determined from TEM images [Fig. 2(c)] and meets the first requirement (A).

Second, the surfaces of QD were coated with a silane coupling agent $N^+(CH_3)_3(CH_2)_3Si(OCH_3)_3$ with 0.6 nm in length. To avoid particle aggregation, we added small

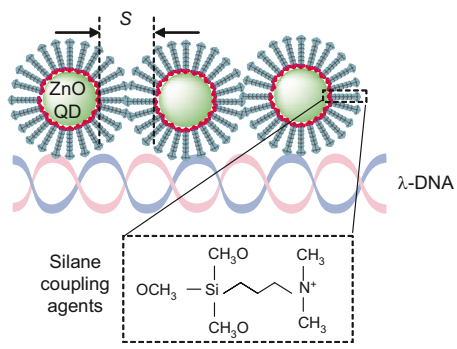

FIG. 1. (Color online) Schematic of ZnO QD alignment along the λ DNA. *S*: separation between QDs.

a)Electronic mail: yatsui@ee.t.u-tokyo.ac.jp.

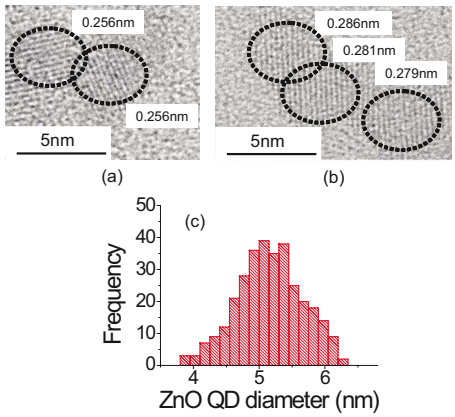

FIG. 2. (Color online) TEM analysis of fabricated ZnO QDs. [(a) and (b)] Typical TEM pictures of the ZnO QDs. (c) ZnO QD diameter distribution.

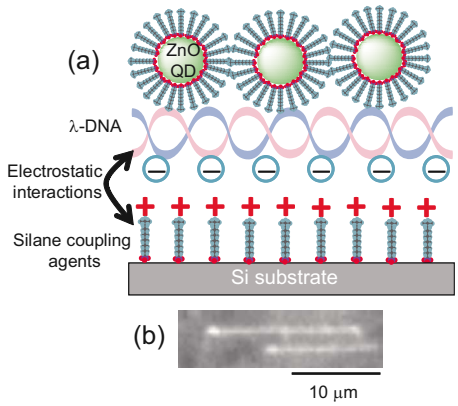

FIG. 4. (Color online) Schematic of the molecular combing technique. (a) Schematic of the alignment of the DNA with QDs on the cationic silicon substrate. (b) Charge-coupled device image of the stretched λ DNA.

amounts of the agent into the ZnO QD colloidal dispersion. The agent maintains the spacing between QDs and, because of its cationic nature, acts as an adhesive for the anionic DNA. Third, we used λ DNA (number of base pairs =48 000, stretched length=16.4 μm) as the template to align the QDs so that the QDs were self-assembled onto the DNA by electrostatic interactions when they were mixed. As shown in the TEM image [Fig. 3(a)], dense packing of the ZnO QDs along the DNA was realized, in which the diameter of the DNA with the QDs was 15 nm. Considering a QD size of 5 nm and the DNA diameter of 2 nm, four QDs were attached around the DNA [see Figs. 3(b) and 3(c)]. The 1.2 nm separation between QDs (S) was determined from the TEM image [Fig. 3(d)] and was in good agreement with twice the length of the silane coupling agents. Because the length of the silane coupling agents can be controlled by changing the number of CH_2 by 0.15 nm, this technique meets the second requirement (B). Despite the electrostatic repulsion between ZnO QDs, such high-density packing is due to the quaternary ammonium group of the silane coupling agent.[7] Quaternary ammonium groups and these QDs have highly condensed positive electrical changes on their particle surfaces. Because of these condensed charges, the QDs were densely adsorbed on the oppositely charged surfaces when their intervals were fixed by the stabilizer length.

To observe the optical properties of the NST, we stretched and straightened the QD-immobilized DNA on the silicon substrate using the molecular combing technique [Fig. 4(a)].[11] First, the silicon substrate was terminated with the silane coupling agent so that the anionic DNA was adsorbed on the cationic silicon substrate. Second, the solution including the DNA and the QDs was dropped onto the cationic silicon substrate. Finally, the glass substrate was slid over the droplet. To check the alignment of DNA-QDs alignment, we obtained an emission image of the cyanine dye attached to the DNA using its 540 nm emission peak under halogen lamp illumination. As shown in the optical image taken with a charge-coupled device camera [Fig. 4(b)], the DNA with QDs stretched in the direction determined by the slide direction of the glass substrate; also, these stretched DNA were found to be isolated.

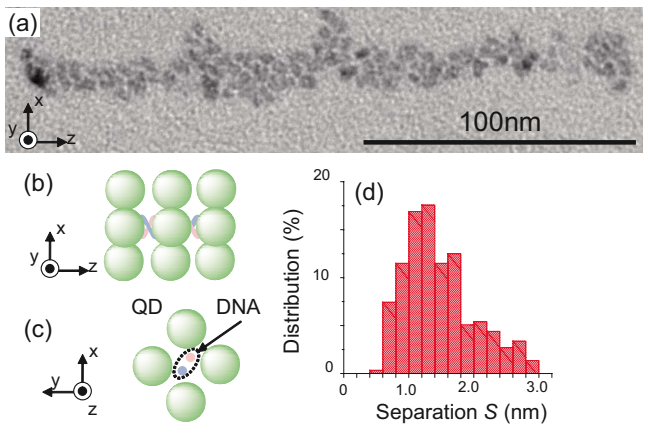

FIG. 3. (Color online) TEM analysis of aligned ZnO QDs. (a) TEM image of the aligned ZnO QDs. [(b) and (c)] Schematics of the QD alignment along the DNA. (d) Separation (S) distribution.

Using the linearly aligned ZnO QDs, we evaluated the photoluminescence (PL) polarization dependence. A fourth-harmonic of a Q-switched Nd:YAG laser (neodymium-doped yttrium aluminum garnet; Nd:$Y_3Al_5O_{12}$ laser, λ=266 nm) with a spot size of approximately 2 mm was used to excite the ZnO QDs at various polarization angles [Fig. 5(a)]. From the polarization dependence of the PL at a wavelength of 350 nm [Fig. 5(b)], corresponding to the ground state of 5 nm ZnO QDs, stronger PL emission was obtained by exciting the parallel polarization along the QD chains (E_0) than was obtained under the perpendicular polarization [E_{90}; Fig. 5(c)]. Since the decay time of ZnO QDs is more than 20 times longer than the energy transfer time to adjacent QDs,[10] it is possible that the dipoles between adjacent QDs were coupled by an optical near-field interaction, indicating that the signals were transmitted through the QD chain. Furthermore, QD chains have great dipolar strength [see the inset of Fig. 5(c)] that can be realized when the QDs are coherently coupled.[12,13] If M QDs are coherently coupled and the coherent length along the z-axis is N times greater than that along the x-axis, the equivalent total dipolar strength is given by $Me \times d$ [E_{90}; see Fig. 5(d)] and $Me \times Nd$ [E_0; see Fig. 5(e)], where e is the electrical charge excited in the QD and d is the coherent length along the x-axis, which is equivalent to the width of the QD chain. The resulting emission intensities are $(Me \times d)^2$ and $(Me \times Nd)^2$ for E_{90} and E_0, respectively. Therefore, we obtained N^2 times greater PL intensity with E_0 than with E_{90}. To evaluate the number of coherently coupled QDs, N, we fit the polarization intensity dependence PL(θ) using

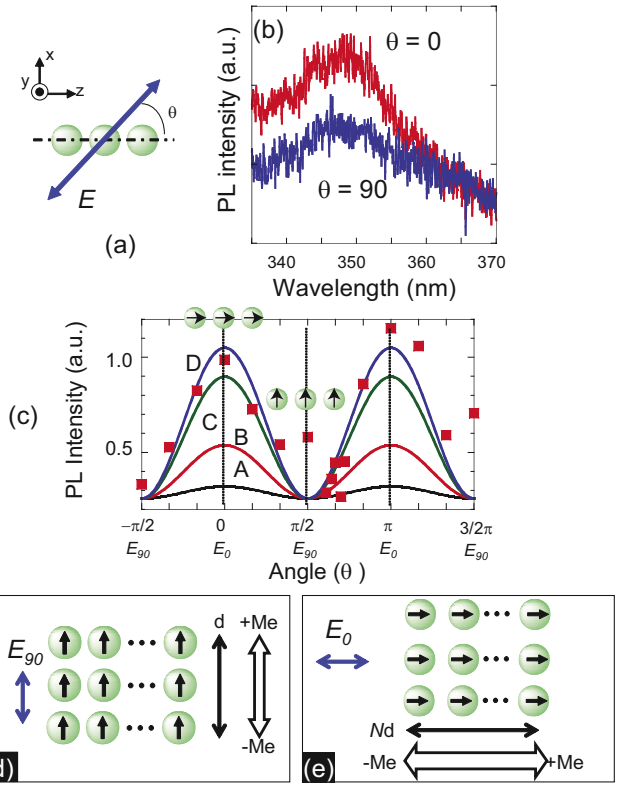

FIG. 5. (Color online) Polarization dependence of the linearly aligned QD chain. (a) Incident light polarization dependence of PL intensity. θ: Polarization angle with respect to the direction along the QD chains (x-axis). (b) Typical PL spectra obtained at $\theta=0$ and 90. (c) Incident light polarization dependence of the PL intensity obtained at $\lambda=350$ nm. Curves A to D correspond to $N=3$, 6, 9, and 10, respectively. Schematics of the equivalent total dipole strength under (d) E_{90} and (e) E_0.

$$\mathrm{PL}(\theta) = k(\sin^2\theta + N^2\cos^2\theta) + \text{const.}, \quad (1)$$

where k is a proportionality constant. As shown by the solid curves in Fig. 5(c) (curves A to D correspond to N=3, 6, 9, and 10, respectively), the polarization dependence of the PL intensity was fitted using Eq. (1), and the value of N was estimated to be 10, indicating that the coherent length along the z-axis was ten times greater than the width of the QD chain. Since the QD chain was 15 nm wide [see Fig. 3(a)], the coherent length along the QD chain was 150 nm. This value is five times larger than that in bulk ZnO.[14] This large coherent length along the QD chains originates from the reduction in phonon scattering in the QDs due to the decrease in the propagation length through ZnO for QDs.

In conclusion, we developed a self-assembly method for linearly aligning QDs to realize a NST device. The polarization-dependent PL from the QD chain revealed that the coherent length along the QDs chain was 150 nm, indicating efficient signal transmission through the QD chain. As optical near-field energy can transmit through the resonant energy level, NST devices have a number of potential applications, such as wavelength division multiplexing using QDs of different sizes.

Tetsu Yonezawa is grateful for the Grant-in-Aid for Priority Area "Strong Photon-Molecule Coupling Fields for Chemical Reactions (470)" from MEXT, Japan (Grant No. 21020010), which provided partial financial support. This work is partially supported by The University of Tokyo Global COE Program "Secure-Life Electronics."

[1]S. A. Maier, P. G. Kik, H. A. Atwater, S. Meltzer, E. Harel, B. E. Koel, and A. A. G. Requicha, Nature Mater. **2**, 229 (2003).
[2]W. Nomura, M. Ohtsu, and T. Yatsui, Appl. Phys. Lett. **86**, 181108 (2005).
[3]W. Nomura, T. Yatsui, T. Kawazoe, and M. Ohtsu, J. Nanophotonics **1**, 011591 (2007).
[4]M. Ohtsu, T. Kawazoe, T. Yatsui, and M. Naruse, IEEE J. Sel. Top. Quantum Electron. **14**, 1404 (2008).
[5]C.-J. Wang, L. Huang, B. A. Parviz, and L. Y. Lin, Nano Lett. **6**, 2549 (2006).
[6]M. Ohtsu, K. Kobayashi, T. Kawazoe, S. Sangu, and T. Yatsui, IEEE J. Sel. Top. Quantum Electron. **8**, 839 (2002).
[7]T. Yonezawa, S. Onoue, and N. Kimizuka, Chem. Lett. **31**, 1172 (2002).
[8]M. G. Warner and J. E. Hutchison, Nature Mater. **2**, 272 (2003).
[9]E. A. Meulenkamp, J. Phys. Chem. B **102**, 5566 (1998).
[10]T. Yatsui, H. Jeong, and M. Ohtsu, Appl. Phys. B: Lasers Opt. **93**, 199 (2008).
[11]H. Oana, M. Ueda, and M. Washizu, Biochem. Biophys. Res. Commun. **265**, 140 (1999).
[12]M. Tammer, L. Horsburgh, A. P. Monkman, W. Brown, and H. Burrows, Adv. Funct. Mater. **12**, 447 (2002).
[13]M. Campoy-Quiles, Y. Ishii, H. Sakai, and H. Murata, Appl. Phys. Lett. **92**, 213305 (2008).
[14]B. Gil and A. V. Kavokin, Appl. Phys. Lett. **81**, 748 (2002).

Appl Phys B (2010) 99: 75–78
DOI 10.1007/s00340-009-3797-0

Applied Physics B
Lasers and Optics

Repairing nanoscale scratched grooves on polycrystalline ceramics using optical near-field assisted sputtering

W. Nomura · T. Yatsui · Y. Yanase · K. Suzuki · M. Fujita · A. Kamata · M. Naruse · M. Ohtsu

Received: 2 October 2009 / Published online: 1 November 2009

Abstract We propose an optical near-field assisted sputtering method for repairing scratches on the surface of polycrystalline ceramics in a self-assembling manner. An Al_2O_3 source was sputtered on substrates with laser radiation of wavelength 473 nm. The average depth of the scratched grooves on polycrystalline Al_2O_3 ceramic substrate decreased from 3.2 nm to 0.79 nm. Using a Hough transform, we also confirmed the selective repair of scratches.

PACS 81.16.Mk · 81.15.Cd

1 Introduction

Recently, optical transmission loss in polycrystalline ceramics has been dramatically decreased to levels as low as those in single crystals. As a result, these transparent ceramics are attracting interest for applications in optical technology [1–4] for use as gain media for solid state lasers or optical windows [5–7]. To realize larger lasing efficiency or to reduce the scattering loss in optical windows, further decreases in the surface roughness are required. To meet this requirement, chemical–mechanical polishing (CMP) has been employed on single crystalline and amorphous optical materials [8]. However, this method is difficult to apply to polycrystalline ceramics because of their anisotropic interaction with the polishing medium. A key problem with CMP is that it may cause scratches because of collisions with the abrasive grains in the slurry. Furthermore, the CMP may cause bumps on the surface, due to the difference in etching rates between adjacent grains in the polycrystal.

To solve these problems, we propose a novel method that makes use of the optical near field. Its outstanding advantage is not only its high spatial resolution, which is beyond the diffraction limit, but also its self-assembling reaction capability. Because localized optical near fields are generated preferably on a surface with nanoscale curvature, they can be induced on fine scratches, contributing to repair them. In addition, the repairing process stops automatically after the scratches disappear. Such selective self-assembling optical near-field interactions previously have been used for depositing nanoparticles, sputtering, and photochemical etching [9–11]. Here, we employ this novel technique to repair the scratches on polycrystalline Al_2O_3 ceramics.

2 Experimental technique

Figure 1 shows a schematic of our method. As a result of preliminary polish of the Al_2O_3 ceramic, its surface contains nanoscale scratched grooves. Because the edges of the grooves have larger surfaces areas than the flat surface, the sputtered Al_2O_3 particles have a higher deposition rate at the edge after migration on the surface [12, 13]. As shown in Fig. 1(a), it therefore is expected that Al_2O_3 will be

W. Nomura (✉) · T. Yatsui · M. Naruse · M. Ohtsu
School of Engineering, The University of Tokyo, 2-11-16, Yayoi, Bunkyo-ku, Tokyo 113-8656, Japan
e-mail: nomura@nanophotonics.t.u-tokyo.ac.jp

W. Nomura · T. Yatsui · M. Naruse · M. Ohtsu
The Nanophotonics Research Center, The University of Tokyo, 2-11-16, Yayoi, Bunkyo-ku, Tokyo 113-8656, Japan

Y. Yanase · K. Suzuki · M. Fujita · A. Kamata
Core Technology Center, Covalent Materials Corporation, 30, Soya, Hadano-shi, Kanagawa, 257-8566, Japan

M. Naruse
National Institute of Information and Communications Technology, 4-2-1 Nukui-kita, Koganei, Tokyo 184-8795, Japan

deposited preferentially at the edges of scratched grooves, which will not help to repair the scratches. To avoid extra deposition on the edge of the grooves and to repair the scratches, we used optical near-field desorption [10]. Because the optical near field (i.e., the dressed photon) can excite coherent phonons in the nanoscale structure, a virtual exciton–phonon–polariton (EPP) is generated on the substrate. A multistep transition via the EPP can accelerate the photochemical reaction although the photon energy is lower than the absorption band edge energy of the material [14]. When the ceramic is irradiated, a highly localized optical near field is generated at the edges of scratches, causing the photodesorption of depositing Al_2O_3 nanoparticles. As shown in Fig. 1(b), if the light has a lower energy than the absorption band edge of the nanoparticles, effective deposition will decrease at the edge, and Al_2O_3 will accumulate on the bottom of the groove [10]. This process automatically stops after the scratches disappear, so that the optical near field can no longer be generated.

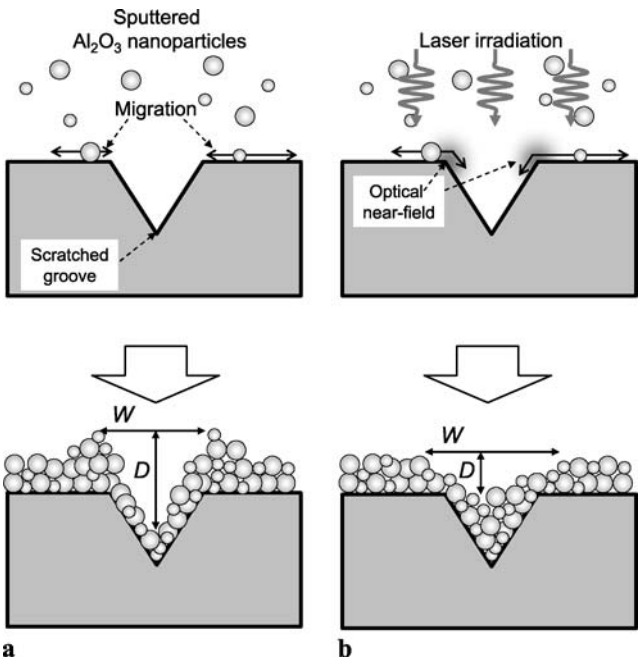

Fig. 1 Schematics of deposition on the scratched substrate surface (**a**) without and (**b**) with irradiation during the sputtering. *D* is the depth and *W* is the width of the scratched groove

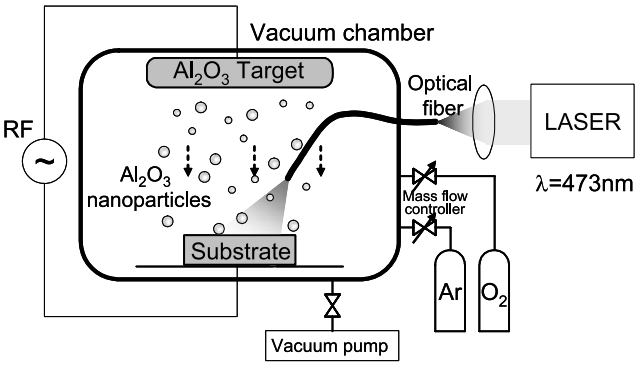

Fig. 2 Schematic of the experimental setup

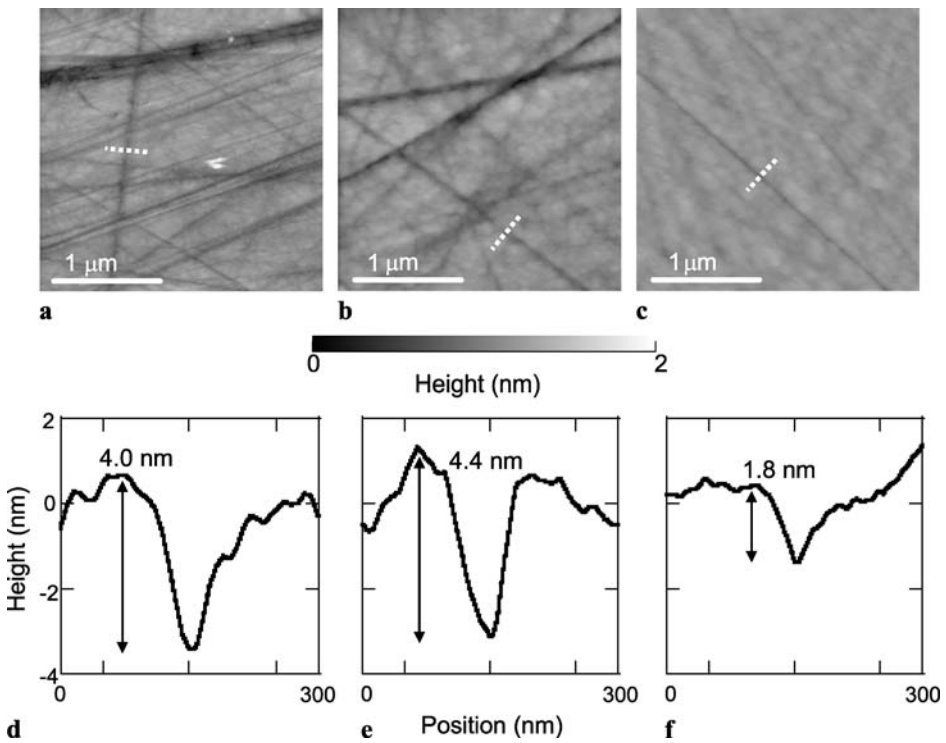

Fig. 3 AFM images of substrates (**a**) before sputtering (substrate *A*), (**b**) after sputtering without irradiation (substrate *B*), and (**c**) after sputtering with irradiation (substrate *C*). (**d**), (**e**), and (**f**) Cross-sectional profiles along the white *dashed lines* in (**a**), (**b**), and (**c**), respectively

We performed optical near-field assisted sputtering to repair the scratches on the surface of the translucent Al_2O_3 ceramic SAPPHAL®.[1] Figure 2 shows a schematic of the experimental setup. Planar surfaces of SAPPHAL® substrate were prepared by polishing using diamond abrasive grains with a diameter of 0.5 μm. The Al_2O_3 was deposited using radio-frequency (RF) magnetron sputtering (RF power: 300 W; frequency: 13 MHz). The total gas pressure was 7×10^{-1} Pa, with a gas flow of 16 sccm Ar and 1.2 sccm O_2 [15]. We also used SAPPHAL® as the target material for sputtering. The CW second harmonic of a Nd:YAG laser with a wavelength of $\lambda = 473$ nm was used as the light source for optical near-field generation. During the sputtering process, the surface was irradiated with light with an optical power density of 2.7 W cm^{-2}. As stated previously, the photon energy of this laser was lower than the absorption band edge energy of Al_2O_3 ($\lambda = 250$ nm) [16]. The light was introduced to the ceramic surface through a multimode optical fiber. After 30 min of sputtering, the thickness of the deposited Al_2O_3 layer was about 100 nm. We observed the surface of the substrates using an atomic force microscope (AFM).

3 Results and discussion

Figures 3(a), (b), and (c) show typical AFM images of SAPPHAL® surfaces before sputtering, after sputtering without irradiation, and after sputtering with irradiation, respectively. Figures 3(d), (e), and (f) show the cross-sectional profiles of typical scratches along the white dashed lines in Figs. 3(a), (b), and (c), respectively. The depth of the scratched grooves in Fig. 3(e) is 4.4 nm, which is deeper than that in Fig. 3(d) (4.0 nm). This was caused by the extra deposition at the edges of the scratch due to the low surface potential, as described in Fig. 1(a). In contrast, Fig. 3(f) shows that the depth decreased to 1.8 nm without extra deposition at the edges of scratches after sputtering with irradiation. For more quantitative evaluation, we calculated the surface roughness *Ra*. The R_a values over the AFM images of Figs. 3(a)–(c) were $Ra_A = 1.3$ nm, $Ra_B = 1.1$ nm, and $Ra_C = 0.49$ nm, respectively. These results indicated that the repair of scratched grooves by optical near-field desorption at the edge of the scratches resulted in a drastic decrease in the surface roughness.

To selectively evaluate the profiles of the scratched grooves, we used the Hough transform [17]. After the AFM image of Fig. 4(a) was leveled by a least squares-method and binarized, the linear features of scratches were automatically extracted using a Hough transform; see Fig. 4(b).

[1] A product of the Covalent Materials Corporation: http://www.covalent.co.jp/.

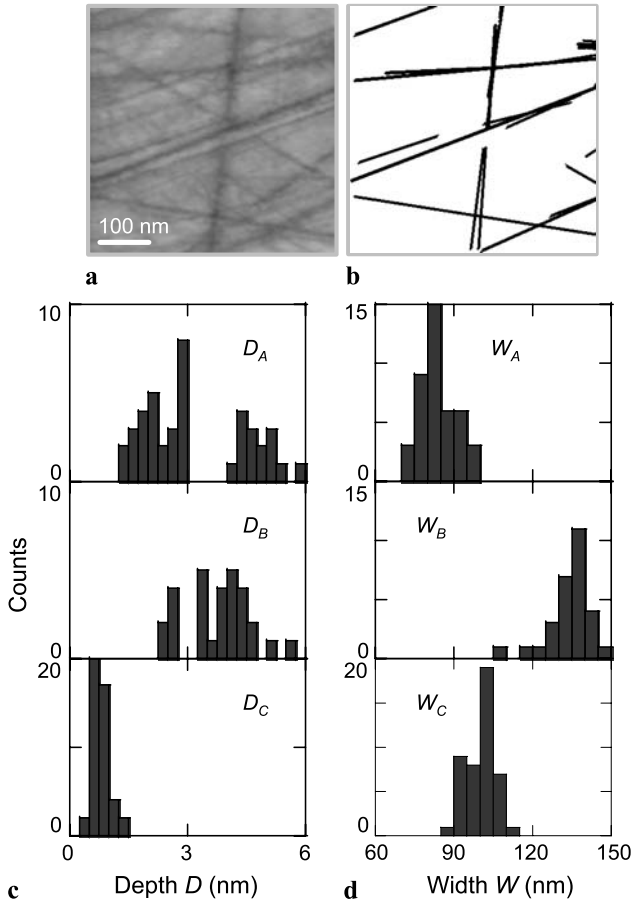

Fig. 4 (**a**) An AFM image is leveled by a least-squares method. (**b**) Schematic of the Hough transform. *Straight lines* of the scratches are detected using the Hough transform of (**a**). (**c**) Histograms of depths, D_n. (**d**) Widths (W_n) of scratches on alumina ceramics substrates; *A* (before sputtering), *B* (after sputtering without irradiation), and *C* (after sputtering with irradiation)

Through this method we obtained the depth D and width W of the detected scratches. Figures 4(c) and (d) show statistical analyses of D and W obtained from the images in Figs. 3(a), (b), and (c), respectively. As shown in Fig. 4(c), the average values of D were $\overline{D_A} = 3.2$ nm, $\overline{D_B} = 3.8$ nm, and $\overline{D_C} = 0.79$ nm, respectively, which confirmed that the depth of the scratches was drastically decreased using near-field assisted sputtering. Figure 4(d) shows that the width of the scratches after the sputtering without irradiation (W_B) was increased beyond the original value W_A, which also supports our deposition model; see Fig. 1(a). In addition, the width W_C also increased in comparison to W_A, supporting the model of Fig. 1(b). Further decreases in the width could be achieved by optimizing laser and sputtering conditions.

4 Conclusion

In conclusion, we proposed an optical near-field assisted sputtering method for repairing the scratched grooves on a

translucent polycrystalline Al_2O_3 ceramic surface. We confirmed that the depth of the grooves was decreased by RF sputtering of Al_2O_3 with laser irradiation at a wavelength of $\lambda = 473$ nm. We found a drastic decrease in surface roughness and obtained an average depth of 0.79 nm. Furthermore, we analyzed the surface profile using a Hough transform. This approach clearly revealed the effects of the optical near-field assisted sputtering, which selectively repaired the scratched grooves. We believe our technique is applicable to a variety of substrates, including ceramic and crystal substrates. Furthermore, this method is compatible with mass production.

Acknowledgement This work was supported by the New Energy and Industrial Technology Development Organization (NEDO) Special Courses: A comprehensive activity for personnel training and industry-academia collaboration based on NEDO projects, and NEDO under the Research and Development Program of Innovative Energy Efficiency Technology.

References

1. A. Ikesue, I. Furusato, J. Am. Ceram. Soc. **78**, 225 (1995)
2. A. Ikesue, T. Kinoshita, K. Kmata, K. Yoshida, J. Am. Ceram. Soc. **78**, 1033 (1995)
3. J. Lu, J. Son, M. Prabhu, J. Xu, K. Ueda, H. Yagi, T. Yanagitani, A. Kudryashov, Jpn. J. Appl. Phys. **39**, L1048 (2000)
4. N. Tanaka, Bull. Ceram. Soc. Jpn. **38**, 967 (2003)
5. A. Krell, P. Blank, H. Ma, T. Hutzler, J. Am. Ceram. Soc. **86**, 12 (2003)
6. J. Lu, K. Ueda, H. Yagi, T. Yanagitani, Y. Akiyama, A.A. Kaminskii, J. Alloys Compd. **341**, 220 (2002)
7. A. Ikesue, Opt. Mater. **19**, 183 (2002)
8. L.M. Cook, J. Non-Cryst. Solids **120**, 152 (1990)
9. T. Yatsui, W. Nomura, M. Ohtsu, IEICE Trans. Electron. **E88-C**, 1798 (2005)
10. T. Yatsui, W. Nomura, M. Ohtsu, Nano Lett. **5**, 2548 (2005)
11. T. Yatsui, K. Hirata, W. Nomura, Y. Tabata, M. Ohtsu, Appl. Phys. B **93**, 55 (2008)
12. F.J. Himpsel, J.E. Ortega, G.J. Mankey, R.F. Willis, Adv. Phys. **47**, 511 (1998)
13. E.J. Menke, Q. Li, R.M. Penner, Nano Lett. **4**, 2009 (2004)
14. T. Kawazoe, K. Kobayashi, S. Takubo, M. Ohtsu, J. Chem. Phys. **122**, 024715 (2005)
15. J.B. Wachtman, A.R. Haber, *Ceramic Films and Coatings* (William Andrew Publishing/Noyes, New York/Norwich, 1993)
16. F. Benabid, M. Notcutt, V. Loriette, L. Ju, D.G. Blair, J. Phys. D **33**, 589 (2000)
17. R.O. Duda, P.E. Hart, Commun. ACM **15**, 11 (1972)

Appl Phys B (2010) 98: 685–689
DOI 10.1007/s00340-009-3772-9

Applied Physics B
Lasers and Optics

Transcription of optical near-fields by photoinduced structural change in single crystal metal complexes for parallel nanophotonic processing

N. Tate · H. Tokoro · K. Takeda · W. Nomura · T. Yatsui · T. Kawazoe · M. Naruse · S.-i. Ohkoshi · M. Ohtsu

Received: 29 September 2009 / Published online: 18 October 2009

Abstract Exploiting the unique attributes of nanometer-scaled optical near-field interactions in a completely parallel manner is important for nanophotonics for enhancing the throughput in obtaining two-dimensional information on the nanometer scale, as well as for developing more practical and easy characterization or utilization of optical near-fields. In this paper, we propose *transcription* of optical near-fields, whereby their effects are spatially magnified so as to be detected in optical far fields. By utilizing cyano-bridged metal complexes that exhibit photoinduced structural changes, transcription at the nanometric scale can be realized. We synthesized single crystals of such metal complexes and observed their photoinduced phase changes. We experimentally achieved photoinduced structural changes via optical near-fields, which is the fundamental process in their transcription.

PACS 42.79.Ta · 78.67.-n · 87.64.mt

N. Tate (✉) · W. Nomura · T. Yatsui · T. Kawazoe · M. Naruse · M. Ohtsu
Department of Electrical Engineering and Information Systems, School of Engineering, The University of Tokyo, 2-11-16 Yayoi, Bunkyo-ku, Tokyo 113-8656, Japan
e-mail: tate@nanophotonics.t.u-tokyo.ac.jp

N. Tate · W. Nomura · T. Yatsui · T. Kawazoe · M. Naruse · M. Ohtsu
Nanophotonics Research Center, School of Engineering, The University of Tokyo, 2-11-16 Yayoi, Bunkyo-ku, Tokyo, 113-8656, Japan

H. Tokoro
PRESTO, Japan Science and Technology Agency, 4-1-8 Honcho Kawaguchi, Saitama, 332-0012, Japan

H. Tokoro · K. Takeda · S.-i. Ohkoshi
Department of Chemistry, School of Science, The University of Tokyo, 7-3-1 Hongo, Bunkyo-ku, Tokyo, 113-0033, Japan

M. Naruse
National Institute of Information and Communications Technology, 4-2-1 Nukui-kita, Koganei, Tokyo 184-8795, Japan

1 Introduction

Nanophotonics is a novel technology that utilizes the optical near-field, which is the electromagnetic field that mediates the interactions between closely separated nanometric matter [1, 2]. By exploiting optical near-field interactions, nanophotonics has broken the diffraction limit of light, and realized *quantitative* and *qualitative* innovations, especially in the fields of optical fabrication and measurement technologies [3, 4].

One of the most important technological vehicles that have contributed to the study of nanophotonics so far is the development of a high-quality optical near-field probing tip for retrieval of optical near-fields. However, methods using probing tips to characterize one-dimensional (1D) scanning processes severely limit the throughput in obtaining two-dimensional (2D) information on the nanometer scale. Additionally, precision technologies are indispensable in fabricating probe tips and also in controlling their position during measurement; such technologies are large obstacles to developing more practical and easy characterization or utilization of optical near-fields. Therefore, eliminating one-dimensional scanning processes, or in other words, *probe-free nanophotonics*, is an important step toward further exploiting the possibilities of light-matter interactions on the nanometer scale.

In this paper, we apply nanophotonics to the field of information processing and describe the basics of *probe-free retrieval* to implement spatially parallel processing in an optical nanometric system. We propose transcription and spatial-magnification of optical near-fields as preprocessing of the retrieving process. Its implementation using metal complexes exhibiting photoinduced phase transitions is experimentally and numerically demonstrated.

2 Concept of spatially parallel processing based on nanophotonics

Figure 1 shows a schematic diagram that represents the basic concept of probe-free nanophotonics. Generally, the two-dimensional distribution of optical near-fields in the vicinity of the surface of a nanostructure in response to far-field light irradiation can be measured by one-dimensional scanning of an optical near-field probe tip, as shown in the upper half of Fig. 1. The idea of the work presented here is to spatially magnify the distribution of optical near-fields so that their effects can be detected in optical far-fields, as schematically shown in the lower half of Fig. 1. In other words, we transcribe the optical near-field distribution to another layer with a certain magnification factor.

The process of transcription is crucial for the implementation of such a concept, and it should originate from the physical attributes associated with the material used. In our proposal, it is necessary to spatially magnify an optical near-field from the nanometric scale to the sub-micrometer scale in the resultant transcribed pattern so that it is observable in the optical far-field. It turns out that the magnification factor in the transcription should be 10–100. Once the spatial pattern is detectable in the far-field, various concepts and technologies common in parallel processing will be applicable, such as fully parallel processing [5], so-called smart pixels, or parallel processing VLSI devices [6].

Several properties of optical near-field sources and transcription media can contribute to spatial patterns of transcription. Therefore, it can be said that our proposal retrieves not only the existence or nonexistence of optical near-fields, but also several of their characteristics, such as energy transfer [7] and hierarchy [8]. From this point of view, our proposal is fundamentally different from other recording and retrieving methods, including near-field holography [9], which is concerned only with structural changes in the media.

3 Transcription of optical near-fields

3.1 Photoinduced phase transition of metal complexes

A photoinduced phase transition has been observed in several cyano-bridged metal complexes [10]. They exhibit bistable electronic states at room temperature. The energy barrier between these bistable states maintains a photoproduced state even after photo-irradiation is terminated. Also, the state can easily be reset either via optical irradiation or temperature control. Moreover, typical phase transitions are excited in a cascaded manner, meaning that they exhibit high quantum efficiencies.

Concerning the applicability of these features of cyano-bridged metal complexes to the transcription discussed previously, we chose a rubidium manganese hexacyanoferrate [11] as a suitable material for the transcription medium. Compounds in this series show a charge-transfer phase transition from Mn^{II} ($S = 5/2$)–NC–Fe^{III} ($S = 1/2$) as the high-temperature (HT) phase to Mn^{III} ($S = 2$)–NC–Fe^{II} ($S = 0$) as the low-temperature (LT) phase [12, 13]. The LT phase is a ferromagnet because of ferromagnetic coupling between the MnIII sites ($S = 2$ at the Mn^{III} sites), but the PI phase, which has a similar valence state to the HT phase, is an antiferromagnet ($S = 5/2$ at the Mn^{II} sites and $S = 1/2$ at the Fe^{III} sites). Figure 2(a) shows the scheme for reversible

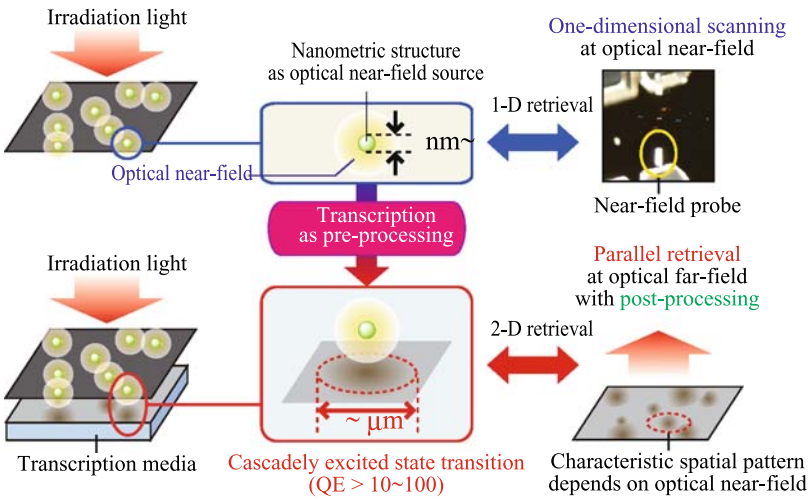

Fig. 1 Basic concept of spatially parallel processing based on the transcription of optical near-fields. Our fundamental idea is to spatially magnify the distribution of an optical near-field from the nanometric scale to the sub-micrometer scale in the resultant transcribed pattern so that it is observable in the optical far-field

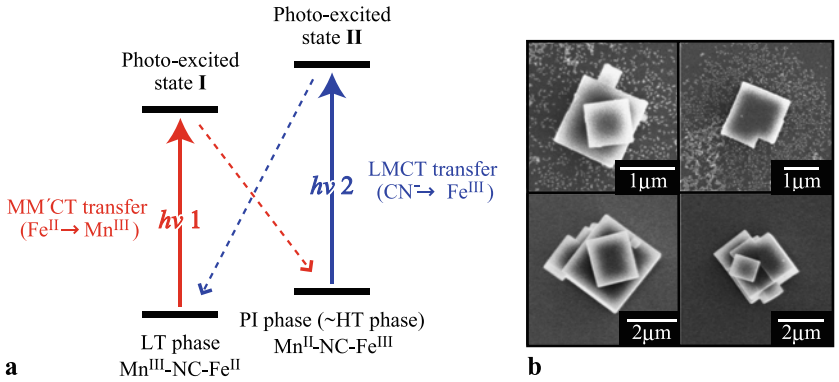

Fig. 2 (**a**) Schematic illustration of the visible-light-induced reversible photo-magnetic effect in rubidium manganese hexacyanoferrate. The charge-transfer phase transition is accompanied by a structural change from a cubic to a tetragonal structure due to Jahn–Teller distortion of Mn^{III}. (**b**) Observed SEM images of rubidium manganese hexacyanoferrate in the single crystal state

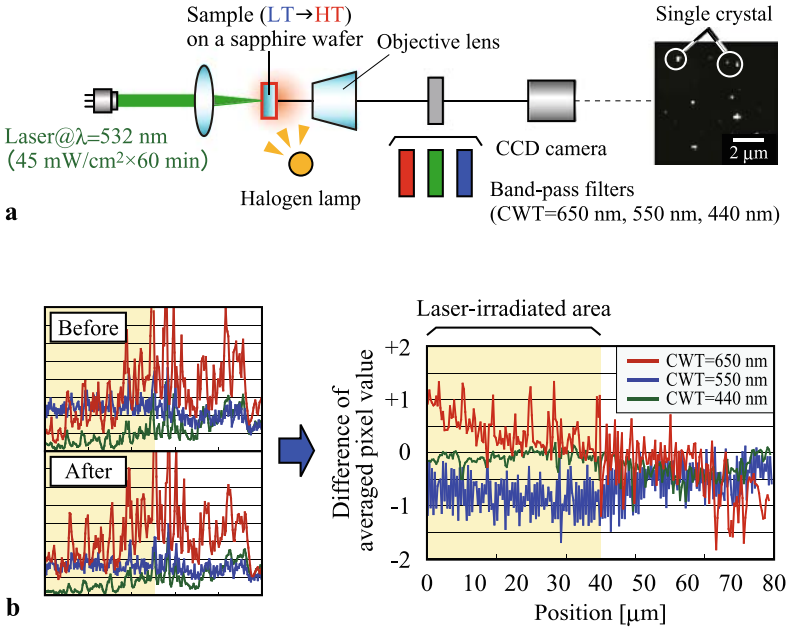

Fig. 3 (**a**) Schematic diagram of experimental setup for microspectroscopic detection of photoinduced phase transition. (**b**) Qualitative comparison of optical responses before and after irradiation. The change of the response at each wavelength, particularly at the wavelengths of 440 and 650 nm, in the irradiated area can be clearly observed, whereas the response remains unchanged in the unirradiated area

charge transfer between the Mn^{III}–NC–Fe^{II} and Mn^{II}–NC–Fe^{III} states and the spin ordering for the LT and HT phases. This charge-transfer phase transition is accompanied by a structural change from a cubic to a tetragonal structure due to Jahn–Teller distortion of Mn^{III}. The maximum value of the quantum efficiency of this type of material has found to be more than 30 [14].

In their typical optical characterizations, these materials are prepared in bulk form. However, for our transcription purposes, especially for the proof-of-principle experiments shown earlier, it is important to spatially distribute these materials so that we can evaluate the optical responses individually from each material. Therefore, in this paper, we mixed the materials with a dispersant based on an ester surfactant and dispersed the materials as single crystals in the solution. Scanning electron microscope (SEM) images of single crystals are shown in Fig. 2(b). The mean size of the single crystals was 1 μm (horizontal) × 1 μm (vertical) × 500 nm (thickness).

3.2 Proof-of-principle experiments

For experimental confirmation of the photoinduced phase transitions, we first measured microscopic optical responses of these single crystals on a sapphire substrate. Figure 3(a) shows the experimental setup. A green laser light source, emitting light at a wavelength of 532 nm with a power density of 45 mW/cm^2, was employed for inducing the phase transition from the LT to the HT phase [11]. The optical responses of the materials were obtained by a CCD camera (Apogee, AltaU260) before and after 60 minutes of irradiation. In the characterization processes, the materials were irradiated with a halogen lamp. We alternately inserted three types of band-pass filters to evaluate the spectral responses before and after irradiation. The center wavelengths of the band-pass filters were 650, 550, and 440 nm, and the bandwidth of each filter was 20 nm.

To compare the differences in the images observed before and after irradiation, we calculated average pixel val-

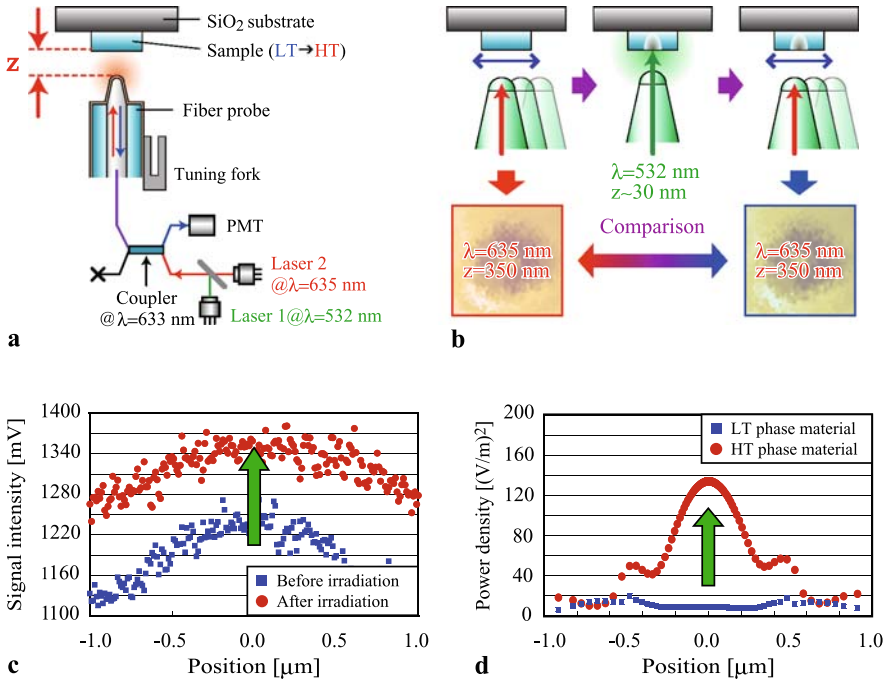

Fig. 4 Schematic diagrams of (**a**) setup and (**b**) process for the experimental demonstration of the amplified transcription. (**c**) Experimental results and (**d**) numerically simulated results. The signal intensity in the near-field is increased by the irradiation in both cases

ues in the horizontal direction and plotted each value along the vertical direction. Figure 3(b) shows the difference of the two results, before and after the irradiation. The shaded area in the profiles corresponds to the laser-irradiated area. We can clearly observe the change of the response at each wavelength, in particular at the wavelengths of 440 nm and 650 nm, in the irradiated area, whereas the responses remained unchanged in the unirradiated area. Such changes in the optical response correspond to changes of the dielectric constant found in previous research with bulk materials [11]. The results indicate that the phase transition of each single crystal could be successfully observed as a change of optical response at an appropriate wavelength.

To experimentally demonstrate the transcription of optical near-fields with the materials introduced previously, we employed a near-field optical microscope (NOM) setup, as shown in Fig. 4(a). It was operated in an illumination-collection setup using an optical fiber probe with a tip radius of 50 nm. A change in the material was induced by laser light with a wavelength of 532 nm (L1). The optical responses from the samples were evaluated microspectroscopically using laser illumination with a wavelength of 635 nm (L2). The power of L2 was kept as low as possible in order to avoid any unintended transitions during observation. The fiber probe tip was positioned close to the target crystal only when L1 was radiated for inducing a transition in the sample. Scattered light from the sample was detected with a photomultiplier tube (PMT) via a fiber probe, and an optical image was constructed from the detected signal. The spatial distributions evaluated with L2 illumination were obtained before and after 15-minute irradiation with L1. From these distributions, we compared the differences (Fig. 4(b)); Fig. 4(c) shows the results. The detected signal intensity in the near-fields was obviously increased by the L1 irradiation. The increase nicely corresponds to the results of microspectroscopic imaging at the wavelength of 650 nm, which is shown in Fig. 3(b).

Furthermore, for numerical proof, we simulated the difference of the optical response between the LT- and HT-phase materials using finite-difference time-domain based electromagnetic simulation. We used Poynting for Optics, a product of Fujitsu, Japan. A nanometric fiber probe with a radius of 50 nm and an illumination light source with an operating wavelength of 635 nm were also included in the calculation model. The electric field intensity was evaluated at the surface of each material. The results are shown in Fig. 4(d). The power density at the surface of the HT-phase material was much stronger than that of the LT-phase material. This change is similar to the NOM result in Fig. 4(c). These results also indicate that the increase of scattered light intensity is attributed to the structural change in the rubidium manganese hexacyanoferrate material. From these results, we believe that we have successfully demonstrated the fundamental principle of the transcription of optical near-fields at the scale of a single crystal by using a nanometric fiber probe.

4 Conclusion

In summary, we proposed the concept of transcription of optical near-field distributions for parallel nanophotonic

processing, and we experimentally demonstrated its principle with nanometric light irradiation of a single crystal of a metal complex exhibiting a structural change that affects the change in its optical response. Specifically, we employed rubidium manganese hexacyanoferrate as the transcription medium, and we experimentally confirmed that the phenomenon could be induced on the scale of a single crystal. The transcription of optical near-fields that we demonstrated here will be one of the key techniques for implementation of proposed parallel nanophotonics processing systems.

Our idea is not only a technique having the traditional meaning of transcription but is also a technique that reveals several nanometric phenomena of optical near-fields. Further advances, including the introduction of postprocessing after the transcription and developing an original coding theorem that utilizes several features of nanophotonics, might yield highly integrated, real-time information processing at the scale of optical near-fields. This work is currently underway in our laboratory.

Acknowledgements This work was supported in part by a comprehensive program for personnel training and industry–academia collaboration based on NEDO projects funded by the New Energy and Industrial Technology Organization (NEDO), Japan, and the Global Center of Excellence (G-COE) "Secure-Life Electronics" project sponsored by the Ministry of Education, Culture, Sports, Science and Technology (MEXT), Japan.

References

1. M. Ohtsu, K. Kobayashi, T. Kawazoe, S. Sangu, T. Yatsui, IEEE J. Sel. Top. Quantum Electron. **8**, 839 (2002)
2. M. Naruse, T. Miyazaki, T. Kawazoe, K. Kobayashi, S. Sangu, F. Kubota, M. Ohtsu, IEICE Trans. Electron. **E88-C**, 1817 (2005)
3. T. Kawazoe, M. Ohtsu, Y. Inao, R. Kuroda, J. Nanophotonics **1**, 011595 (2007)
4. U. Maheswari Rajagopalan, S. Mononobe, K. Yoshida, M. Yoshimoto, M. Ohtsu, Jpn. J. Appl. Phys. **38**, 6713 (1999), part 1
5. J. Tanida, Y. Ichioka, Appl. Opt. **27**, 2926 (1988)
6. M. Ishikawa, A. Morita, N. Takayanagi, in *Proc. Int. Conf. on Intelligent Robots and Systems*, vol. 373 (1992)
7. M. Ohtsu, T. Kawazoe, T. Yatsui, M. Naruse, IEEE J. Sel. Top. Quantum Electron. **14**, 1404 (2008)
8. M. Naruse, T. Yatsui, W. Nomura, N. Hirose, M. Ohtsu, Opt. Exp. **13**, 9265 (2005)
9. B. Lee, J. Kang, K.-Y. Kim, Proc. SPIE **4803**, 220 (2002)
10. O. Sato, S. Hayami, Y. Einaga, Z.Z. Gu, Bull. Chem. Soc. Jpn. **76**, 443 (2003)
11. H. Tokoro, T. Matsuda, T. Nuida, Y. Morimoto, K. Ohoyama, E.D.L.D. Dangui, K. Boukheddaden, S. Ohkoshi, Chem. Mater. **20**, 423 (2008)
12. S. Ohkoshi, H. Tokoro, M. Utsunomiya, M. Mizuno, M. Abe, K. Hashimoto, J. Phys. Chem. B **106**, 2423 (2002)
13. H. Tokoro, S. Ohkoshi, T. Matsuda, K. Hashimoto, Ignor. Chem. **43**, 5231 (2004)
14. H. Tokoro, T. Matsuda, K. Hashimoto, S. Ohkoshi, J. Appl. Phys. **97**, 10M508 (2005)

Appl Phys B (2010) 98: 283–289
DOI 10.1007/s00340-009-3762-y

Applied Physics B
Lasers and Optics

Nonadiabatic multi-step excitation for the blue–green light emission from dye grains induced by the near-infrared optical near-field

H. Fujiwara · T. Kawazoe · M. Ohtsu

Received: 1 September 2009 / Published online: 2 October 2009

Abstract Blue–green light emission (wavelength range: 460–520 nm) from coumarin dye grains due to near-infrared excitation (CW, $\lambda_{ex} = 808$ nm), based on the nonadiabatic excitation process induced by an optical near-field, was observed. A maximum frequency up-shift of 1.17 eV was confirmed. Based on the excitation intensity dependence, a light emission mechanism originating from a nonadiabatic three-step excitation was confirmed for the first time. The lifetime of the intermediate excited state was approximately 1.1–1.9 ps, and thus realization of frequency up-conversion with a rapid response can be expected.

PACS 78.67.-n · 78.47.J- · 33.80.Wz

1 Introduction

Light in the infrared region has been increasingly used in environmental and security applications, and there is a growing demand for infrared photodetectors. Among these, photodiodes using the inter-band transition due to light absorption have high industrial potential because of their relatively rapid response [1]. However, because an infrared photodetector utilizes material with a narrow band gap, which easily produces noise by thermal excitation, a cooler for cooling the photodetector is required in order to realize a sufficiently high S/N ratio for detection. As a solution to these problems, there is a method in which the incident light is frequency up-converted (to a shorter wavelength) and a photodetector having detection sensitivity for visible light, with less noise, is used [2]. In using IR-phosphor for the frequency up-conversion, excitation to a triplet state from the ground state by another excitation method, such as ultraviolet excitation, is required, and thus, a slow response and an unstable conversion efficiency of the measurement light become problematic [3].

In order to solve these problems, we have been investigating a novel method for the frequency up-conversion: a method in which emission of visible light is obtained by multi-step excitation of a dye molecule's vibrational states using an optical near-field with a near-infrared frequency, thereby inducing transition of electrons into the electronically excited state [4]. Excitation of the molecular vibrational state is not possible with propagating light because it is optically forbidden. However, if an optical near-field is considered as a photon dressed with material excitations (a *dressed photon*), the optical near-field excites a coherent phonon at the molecular particle surface, creating a coupled state with the coherent phonon (exciton–phonon–polariton (EPP)) [5]. Therefore, molecules in the area where the optical near-field is present are excited by the phonon into higher vibrational states, via which they are electronically excited by the dressed photon. In contrast to the conventional optical excitation using propagating light, which is adiabatic and excites only the electronic system, the method described above

H. Fujiwara (✉)
Central Research Laboratories, Hamamatsu Photonics K.K., Hirakuchi 5000, Hamakita-ku, Hamamatsu 434-8601, Japan
e-mail: fujiwara@crl.hpk.co.jp
Fax: +81-53-5850673

T. Kawazoe · M. Ohtsu
Department of Electrical Engineering and Information Systems, Graduate School of Engineering, The University of Tokyo, 2-11-16 Yayoi, Bunkyo-ku, Tokyo 113-8656, Japan

T. Kawazoe · M. Ohtsu
Nanophotonics Research Center, Graduate School of Engineering, The University of Tokyo, 2-11-16 Yayoi, Bunkyo-ku, Tokyo 113-8656, Japan

is referred to as nonadiabatic because the optical near-field excites the molecular vibration. This nonadiabatic excitation has been applied to, for example, chemical vapor deposition [6–8], lithography [9, 10], and chemical etching [11].

In our previous work, we have discovered a novel light emission process using the nonadiabatic excitation [4]. We have observed emission of visible light through the near-infrared excitation of dye grains, such as 4-Dicyanmethylene-2-methyl-6-(p-dimethylaminostyryl)-4H-pyran (DCM) and Benzoic Acid, 2-[6-(ethylamino)-3-(ethylimino)-2,7-dimethyl-3H-xanthen-9-yl]-ethyl ester, monohydrochloride (Rhodamine 6G). These dyes are transparent to near-infrared light; however, individual protrusions of dye grains contribute to generating the optical near-field. Inside the dye grains in the vicinity, dye molecules are excited to a higher vibrational state as an intermediate excited state due to the nonadiabatic excitation, thus causing light emission from the dyes.

However, detailed properties of the intermediate excited state in the nonadiabatic excitation process have not been elucidated. In addition, with these types of dyes, wavelength conversion has been limited to one from approximately $\lambda =$ 805 nm to 650 nm, that is, 0.37 eV in terms of the frequency up-shift. This is because the excitation wavelength and the fluorescence wavelength are close, and the excitation to electrically excited states occurs only by the one- and two-step nonadiabatic excitation processes. A larger up-shift is needed for detector applications, which would be effectively achieved by using a nonadiabatic excitation process involving two or more steps. Also, realizing blue-green light emission without using ultraviolet light as an excitation light source shows great promise for applications such as displays.

Therefore, in the present study, experiments were conducted involving switching the types of dyes to ones that have fluorescence properties toward shorter wavelengths. The dyes used were 2,3,5,6-1H,4H-Tetrahydro-8-methylquinolizino-[9,9a,1-gh]-coumarin (Coumarin 480) and 2,3,5,6-1H,4H-Tetrahydro-8-trifluormethylquinolizino-[9,9a,1-gh]-coumarin (Coumarin 540A), materials that generate fluorescence of $\lambda = 460$ nm and 570 nm, respectively, when excited by light of a shorter wavelength than the absorption-edge wavelength used in the conventional adiabatic excitation [12]. Using these dye grains as samples, emission of visible light due to the near-infrared excitation was measured, and the emitted light spectral properties, excitation intensity dependence, and lifetime of the intermediate excited state were investigated.

2 Principles and sample preparation

We now describe the principles of light emission by nonadiabatic optical near-field excitation of dye grains. Figure 1

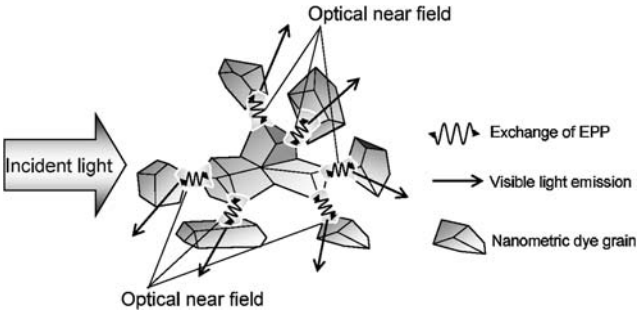

Fig. 1 Overview of light emission from dye grains induced by the nonadiabatic excitation

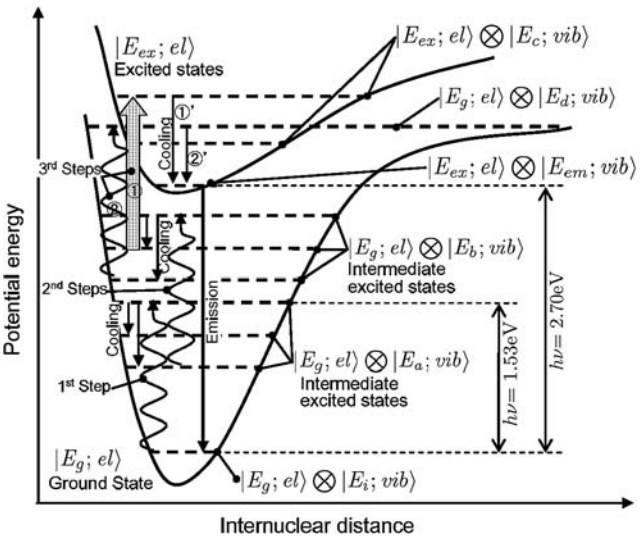

Fig. 2 Potential curves of an electron in a molecular orbital

is an overview of light emission from dye grains induced by the nonadiabatic optical near-field excitation (Fig. 2(c) of [4]). When near-infrared light whose wavelength is longer than the absorption-edge wavelength of the dyes is incident on the dye grains, an optical near-field is generated at the surface of the dye grains, and it is especially pronounced at sharp protrusions. The generated optical near-field excites a coherent phonon at the surface of the dye grains, creating a coupled state with it (exciton–phonon–polariton (EPP)) [5]. Therefore, dye molecules in the dye grains in the area in which the optical near-field is generated are excited into a higher energy state by a phonon of the EPP. Because the higher vibrational state serves as the intermediate excited state, the dye molecules are further excited by multiple phonons to an even higher energy state through multi-step excitation, eventually resulting in an electronically excited state. Subsequently, visible light is emitted by the electronic transition.

Figure 2 shows an overview of light emission by a multi-step nonadiabatic optical near-field excitation, resulting in transition of electrons in the dye molecules to an electronically excited state [4]. In Fig. 2, a three-step excitation to the

electronically excited state is shown; however, a light emission process involving two steps [4] or four or more steps is possible depending on the energy difference between the excitation wavelength and the dye absorption-edge wavelength. Figure 2 is an electronic potential curve in the configuration coordinates of the dye molecules in the phonon mode coupled with the optical near-field.

$|E_\alpha; \mathrm{el}\rangle$ and $|E_\beta; \mathrm{vib}\rangle$ indicate the electronic state and molecular vibrational state, respectively. E_α denotes the energy of the electronic state, where the subscript α indicates the ground state ($\alpha = \mathrm{g}$) and the excited state ($\alpha = \mathrm{ex}$). E_β denotes the energy of the molecular vibrational state, where the subscript β indicates respective characteristic vibrational states ($\beta = i, a, b, c, d, em$).

(1) First step: The optical near-field is generated at the surface of the dye grains by the incident excitation light. The dye molecules in the nearby dye grains are excited by the nonadiabatic excitation process from the ground state, $|E_\mathrm{g}; \mathrm{el}\rangle \bigotimes |E_i; \mathrm{vib}\rangle$, to a higher vibrational state, $|E_\mathrm{g}; \mathrm{el}\rangle \bigotimes |E_a; \mathrm{vib}\rangle$ (indicated by the wavy arrow in Fig. 2; the first step of the nonadiabatic excitation process). Because molecules in the excited vibrational state seek stable thermal equilibrium, they are relaxed (cooled) to a lower vibrational state.

(2) Second step: The vibrational state relaxing toward thermal equilibrium, following the first step, serves as the intermediate excited state, causing a second excitation by a nonadiabatic excitation process to an even higher energy state: a transition from $|E_\mathrm{g}; \mathrm{el}\rangle \bigotimes |E_a; \mathrm{vib}\rangle$ to $|E_\mathrm{g}; \mathrm{el}\rangle \bigotimes |E_b; \mathrm{vib}\rangle$ (indicated by the wavy arrow in Fig. 2; the second step of the nonadiabatic excitation process). The molecules in the vibrational state resulting from the two steps of the nonadiabatic excitation process relax (cool) to a lower energy state.

(3) Third step: Excitation to the electronically excited state via the two transition routes described below is possible when the energy of the vibrational state relaxing toward thermal equilibrium (intermediate excited state) is equal to or greater than 1.17 eV, i.e., the difference between the energy of the electronically excited state (for example, light emission wavelength of Coumarin 480; $h\nu = 2.70$ eV, $\lambda = 460$ nm) and the photon energy of the excitation light (for example, $h\nu = 1.53$ eV, $\lambda_\mathrm{ex} = 808$ nm). The first route (excitation ①) is an excitation from $|E_\mathrm{g}; \mathrm{el}\rangle \bigotimes |E_b; \mathrm{vib}\rangle$ to $|E_\mathrm{ex}; \mathrm{el}\rangle \bigotimes |E_c; \mathrm{vib}\rangle$ by adiabatic excitation using propagating light (indicated by the thick arrow in Fig. 2). The other route (excitation ②) is an excitation to an even higher vibrational state, from $|E_\mathrm{g}; \mathrm{el}\rangle \bigotimes |E_b; \mathrm{vib}\rangle$ to $|E_\mathrm{g}; \mathrm{el}\rangle \bigotimes |E_d; \mathrm{vib}\rangle$ by the nonadiabatic excitation (indicated by the wavy arrow in Fig. 2; the third step of the nonadiabatic excitation process). This energy is greater than the initial state $|E_\mathrm{ex}; \mathrm{el}\rangle \bigotimes |E_\mathrm{em}; \mathrm{vib}\rangle$ for light emission. Molecules relax from the states in these two transition routes, $|E_\mathrm{ex}; \mathrm{el}\rangle \bigotimes |E_c; \mathrm{vib}\rangle$ or $|E_\mathrm{g}; \mathrm{el}\rangle \bigotimes |E_d; \mathrm{vib}\rangle$, to the initial state for light emission, $|E_\mathrm{ex}; \mathrm{el}\rangle \bigotimes |E_\mathrm{em}; \mathrm{vib}\rangle$.

Following excitation by the above three steps, radiative relaxation occurs from the initial state for light emission, $|E_\mathrm{ex}; \mathrm{el}\rangle \bigotimes |E_\mathrm{em}; \mathrm{vib}\rangle$, to the ground state, $|E_\mathrm{g}; \mathrm{el}\rangle \bigotimes |E_i; \mathrm{vib}\rangle$. Since the excitation in the third step is an adiabatic excitation whose transition probability is about 10^6 times greater than that of the nonadiabatic excitation [4, 6], the probability of light emission that occurs in this transition route is limited by the nonadiabatic excitation probability, and the emitted light intensity has a squared dependence on the incident light intensity ($I \propto E^2$) (this excitation process is referred to as a two-step nonadiabatic excitation process since two nonadiabatic steps contribute to the excitation). The nonadiabatic excitation ② in the third step, on the other hand, has a probability equal to the nonadiabatic excitation probabilities of the first and second steps. The emitted light intensity of the dyes due to this excitation is the origin of the cubed dependence on the incident light ($I \propto E^3$) (this excitation process is referred to as a three-step nonadiabatic excitation process since three nonadiabatic steps contribute to the excitation).

As experimental samples, two types of dyes (Coumarin 480 and 540A) were prepared. When these dyes are dissolved in solution, the absorption-edge wavelengths are approximately 440 nm for Coumarin 480 and 500 nm for Coumarin 540A, and they do not absorb near-infrared light of wavelengths around 808 nm [12]. These dyes were dissolved in acetone, then dripped into water to recrystallize [13]. The dye grains were obtained by evaporating the solution in quartz cells. The total thickness of the dye grains in the quartz cells was 1 mm. SEM images of the dye grains are shown in Fig. 3. Coumarin 480 dye grains take a rod-like shape of approximately 2 μm in diameter and 50 μm in length (Fig. 3a). Coumarin 540A dye grains take a granular shape with dimensions of approximately 5 μm × 5 μm × 5 μm (Fig. 3b). The optical near-field is generated at the surface of the dye grains by incident excitation light, and it is especially pronounced at sharp protrusions. Coumarin 540A dye grains, which have smaller crystal grain size and a greater number of protrusions per unit volume, have a higher optical near-field generation efficiency, and thus are expected to show a higher nonadiabatic light emission efficiency (Figs. 2 and 3 in [4]).

3 Experimental results and discussions

3.1 Comparison between fluorescence and nonadiabatically emitted spectra

The solid curve in Fig. 4a indicates the emitted blue light spectrum of Coumarin 480 dye grains obtained by near-

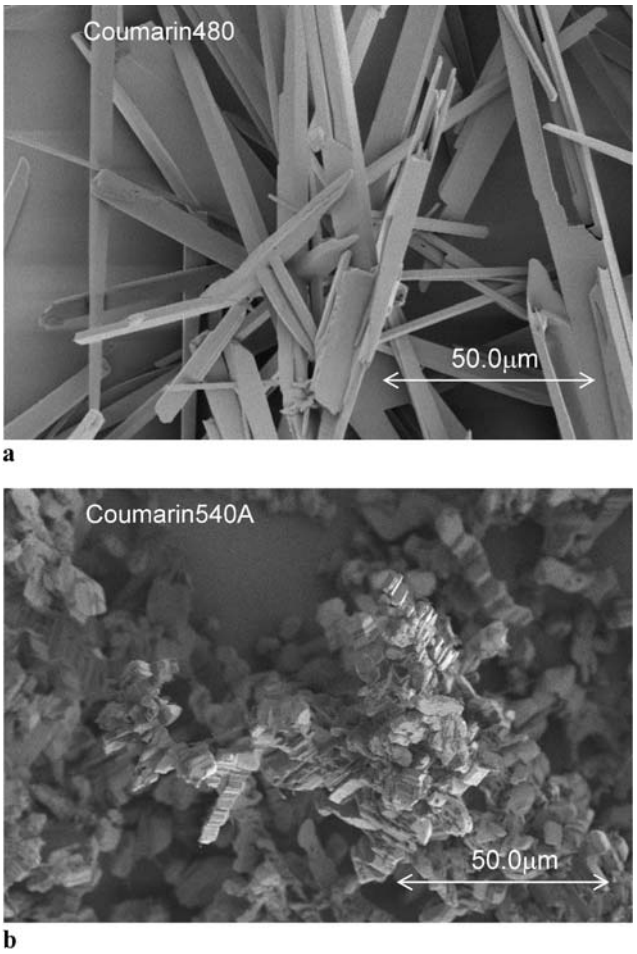

Fig. 3 SEM images of the dye grains. **a** Coumarin 480. **b** Coumarin 540A

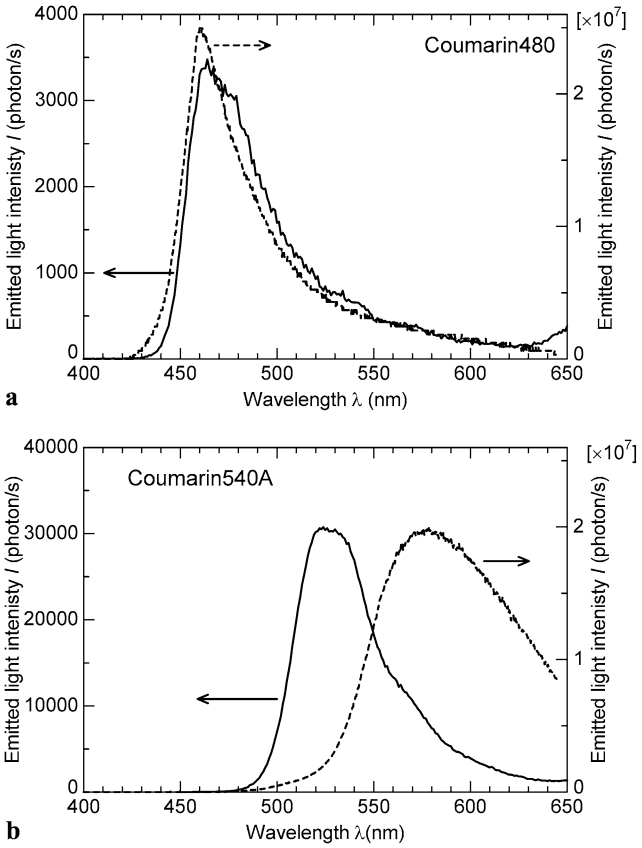

Fig. 4 Spectral profiles of the visible light emitted from Coumarin 480 **a** and Coumarin 540A **b**. *Solid* and *broken curves* represent the spectra obtained with near-infrared and ultraviolet excitation, respectively

infrared excitation. A CW laser diode (center wavelength = 808 nm) was used as the near-infrared excitation light source. Its excitation power was 1050 mW. The broken curve in Fig. 4a indicates the fluorescence spectrum obtained by conventional adiabatic excitation using an ultraviolet HeCd laser (center wavelength = 326 nm, power = 0.5 mW) as the excitation light source. Peak wavelengths of the two curves agree closely, suggesting that the light emission by near-infrared excitation is due to light emission from the electronically excited state. The frequency shift between the emitted and the excitation light was approximately 1.17 eV. The solid curve in Fig. 4b indicates the emitted green light spectrum obtained by exciting Coumarin 540A dye grains using the same near-infrared light source as above. It was shifted about 54 nm toward shorter wavelengths as compared with the ultraviolet-excitation fluorescence spectrum (the broken curve). The reason for this blue shift is currently under investigation.

We will now discuss the origin of light emission in Fig. 4a and b. Comparing peak intensities of emission spectra in the cases of near-infrared excitations, the peak intensity of the light emitted from the Coumarin 540A dye grains was approximately 10 times greater than that of the Coumarin 480 dye grains. As shown in Fig. 3a and b, comparing the shapes and sizes of the two dye grains, the nonadiabatic excitation process is suggested to be the origin of the observed difference in the emitted visible light intensities.

3.2 Excitation intensity dependence

Figure 5 shows the dependence of emitted light intensity I on the excitation intensity E at $\lambda = 460$ nm (Coumarin 480) and 520 nm (Coumarin 540A). The emitted light intensity I was least-squares fitted by the third-order function $I = aE + bE^2 + cE^3$. The values a, b, and c for the fitting obtained by the nonlinear Levenberg–Marquardt method [14] were:

For Coumarin 480: $a = (1.19 \pm 0.85) \times 10^{-17}$, $b = (1.71 \pm 0.10) \times 10^{-34}$, $c = (3.51 \pm 1.43) \times 10^{-54}$; and for Coumarin 540A: $a = (2.09 \pm 0.20) \times 10^{-16}$, $b = (1.42 \pm 0.02) \times 10^{-33}$, $c = (9.20 \pm 0.39) \times 10^{-53}$.

The results of fittings are shown by the solid curves in Fig. 5. In addition, the broken lines indicate the excitation intensity dependence of each order. The coefficient ratio c/b

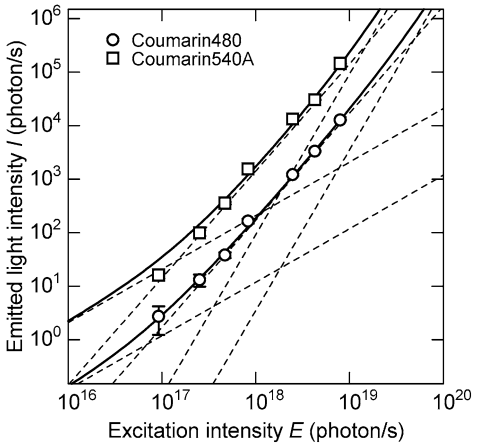

Fig. 5 Dependence of the emitted light intensity I on the excitation light intensity E

of the second and the third orders was approximately 2×10^{-20} to 6×10^{-20}.

According to the EPP model, the coefficient ratio c/b of the two-step and the three-step nonadiabatic excitation processes is represented by [6]

$$\frac{c}{b} = \frac{\hbar}{2\pi} \frac{I}{|\gamma_m|^2 E} \left(\frac{v_p'^2}{u_p'^2} \right) \left(\frac{\mu^{\mathrm{el}}}{\mu^{\mathrm{nucl}}} \right)^2. \quad (1)$$

The theoretical value of (1) was approximately 7×10^{-20}, when the measured value of Coumarin 540A at a low excitation intensity $I \approx aE = 14.8$ photons/s and the excitation light intensity $E = 9.2 \times 10^{16}$ photons/s $= 22.6$ mW were used, and additionally, $\mu^{\mathrm{nucl}} = 1$ Debye, $\mu^{\mathrm{el}} = 10^3$ Debye (the electronic and lattice vibrational dipole moments), $\gamma_m = 10^{-1}$ eV (the linewidth of the electronic and vibrational states), and $v_p'/u_p' = 0.1$ (the conversion efficiency from the incident photon to EPP) were used as other parameters. This theoretical value is nearly equal to the fitted value based on the experimental value; therefore, the EPP model is applicable to the excitation intensity dependence.

Only the coefficient a was larger than the theoretical value. This is likely caused by difficulties in estimating the first-order coefficient a. That is, the observed deviation of the coefficient a from the theoretical value is likely to be an experimental error, explained as follows: In the case of the dye samples used in this experiment, there is a large energy difference between the emitted light ($\lambda = 460$–520 nm) and the infrared excitation light ($\lambda = 808$ nm); therefore, energy needed for excitation cannot be secured in the one-step nonadiabatic excitation process (and also in the adiabatic excitation), resulting in a small proportional contribution to the light emission. As a result, the measured value aE becomes close to the detection limit (1 photons/s) of the photodetector (H7421-40 Hamamatsu Photonics KK).

Based on these experimental results and comparisons with theoretical values, it can be concluded that the visible light emission process in Coumarin 480 and 540A dye grains based on the near-infrared excitation was generated by the two- and three-step nonadiabatic excitation, with the excited vibrational level of the dye grains as the intermediate excited state. Light emission by the three-step nonadiabatic excitation was confirmed for the first time in this experiment.

3.3 Lifetime of the intermediate excited state

In the two- and three-step nonadiabatic excitation of Coumarin 480 and 540A dye grains confirmed in this experiment, the intermediate excited state shown in Fig. 2 is the vibrational state of the dye grains. The average lifetime of this intermediate excited state can be measured by pump-probe spectroscopy. More specifically, the measurement method was as follows. As the excitation light, a femtosecond pulse from a mode-locked Ti:sapphire laser was used ($\lambda = 805$ nm, pulse duration $= 100$ fs, repetition frequency $= 80$ MHz). The light pulse was split into two and made incident on a single point on a dye grain after passing through different optical paths. The length of one optical path was made variable to control the difference in the incident time of the two light pulses reaching the experimental sample. The relationship between the difference in the incident time for the two light pulses to reach the experimental sample, the delay time Δt, and the emitted light intensity (the emitted light intensity at the spectral peak wavelength of the near-infrared excitation) was examined. The results are shown in Fig. 6. The vertical axis is the increment of the emitted light intensity ΔI, defined as follows: From the nonadiabatically emitted light intensity obtained at $\Delta t = 0$, the sum of nonadiabatically emitted light intensities obtained for the two light pulses when they were separately made incident on the sample was subtracted and the difference was normalized. The increment of the emitted light intensity ΔI at the delay time $\Delta t = t$ is proportional to $\exp(-t/\tau)$, and the time constant τ is the lifetime of the intermediate excited state, explained as follows: The number of dye molecules in the intermediate state excited by the pumping light pulse decreases with time constant τ because their vibrational energies are much higher than the thermal energy determined by the sample temperature [15–17]. Also, ΔI at $\Delta t = t$ is proportional to the number of dye molecules excited by the probing light pulse from this intermediate excited state to the electronically excited state for light emission. The probability of this excitation is proportional only to the number of the intermediately excited dye molecules at $\Delta t = t$, because it is proportional to both the probing light pulse intensity and the number of the intermediately excited dye molecules. (The former was regulated (constantly) at 3.2 W/cm^2 in the experiment.) Therefore, the time constant τ, i.e., the lifetime of the intermediate excited state in the dye molecules, could be measured from the

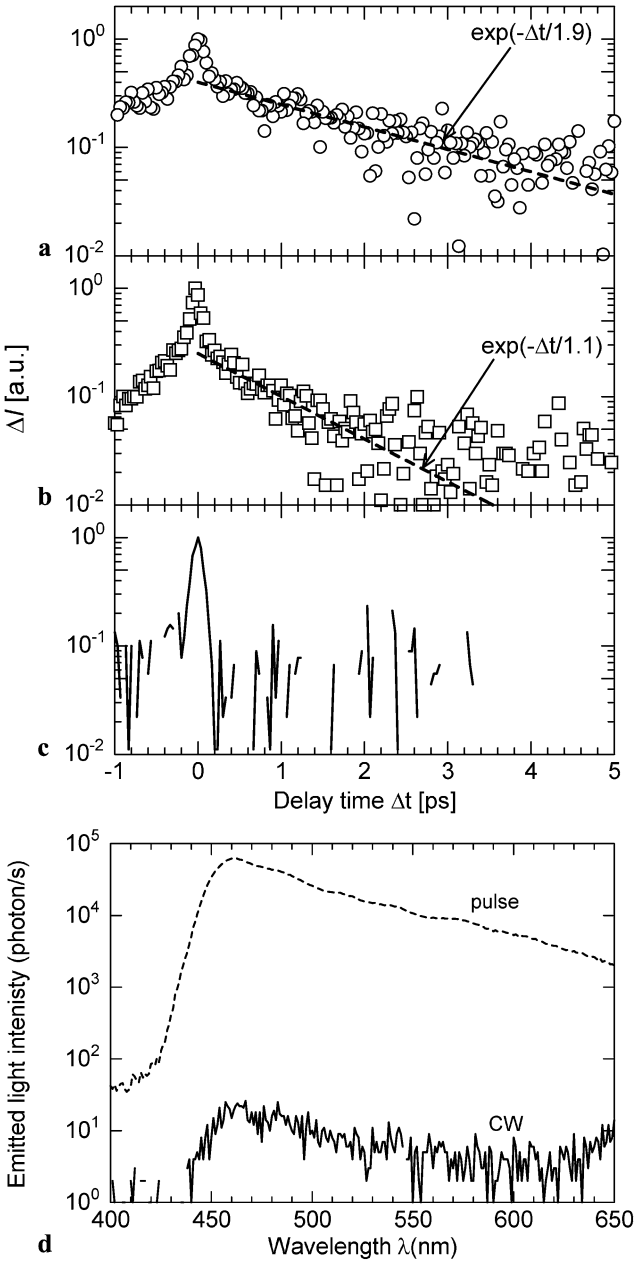

Fig. 6 Measured temporal behavior of the increment of the light intensity ΔI emitted from grains of Coumarin 480 **a**, grains of Coumarin 540A **b**, and Coumarin 540A in acetone solution **c**. **d** *Solid* and *broken curves* represent the spectral intensity emitted from Coumarin 480 grains with pulsed and CW laser excitation, respectively

dependence ΔI on the delay time Δt between the pumping and probing light pulses, if the time constant τ is longer than the pumping light pulse duration.

The decay time of ΔI was approximately 1.9 ps for Coumarin 480 dye grains (Fig. 6a), suggesting that the lifetime of their intermediate excited state was 1.9 ps. Figure 6b shows that the decay time is approximately 1.1 ps for Coumarin 540A dye grains, suggesting that the lifetime of their intermediate excited state is 1.1 ps.

For the purpose of comparison, the same measurements were carried out using a dye acetone solution (Coumarin 540A) without dye grain precipitation. The results are shown in Fig. 6c. With this sample, light emission occurred only by the two-photon excitation using propagating light. The intermediate excited state of the two-photon excitation light emission is based on a two-step excitation via a virtual level; therefore, the emitted light intensity increases only when the two excitation light pulses show a temporal overlap. As a result, the profile of the temporal behavior of ΔI corresponds to the autocorrelation waveform of the excitation light pulse. Unlike Fig. 6c, the results for the dye grains (Fig. 6a and b) suggest that their intermediate excited states are real levels whose lifetimes are longer than the duration of the light pulses.

In Fig. 6d, the CW Ti:sapphire laser was used to excite Coumarin 480 dye grains and the obtained emitted light spectral intensity was compared to that of the pulse excitation. The intensity ratio of the pulse excitation to the CW excitation was approximately 3×10^3:1, which is two orders of magnitude smaller than the ratio of peak intensities (approximately 1×10^5:1). It can also be concluded from this result that the intermediate excited states are real levels whose lifetimes are longer than the durations of the light pulses.

Blue light emission by near-infrared excitation was observed from dye grains of (2,2′-([1,1′-Biphenyl]-4,4′-diyldi-2,1-ethenediyl)-bis-benzenesulfonic acid (Stilben 420), prepared by the same method as for Coumarin 480 and Coumarin 540A. The emitted light wavelength was approximately 460 nm. The results of pump-probe spectroscopy are shown in Fig. 7a. The lifetime of the intermediate excited state for Stilben 420 was approximately 2.5 ps.

The relaxation (cooling) time for relaxing toward thermal equilibrium from an excited vibrational state ranges from a few ps to 10 ps for organic dye molecules and GaAs semiconductors [15–17], closely agreeing with our experimental results. Therefore, it can be concluded that the lifetime of the intermediate excited state observed in this experiment is the average lifetime of the intermediate excited state for the dye molecules that contributes to nonadiabatic light emission. Figure 7b shows the relationships between emitted light intensities of Stilben 420, Coumarin 480, and Coumarin 540A obtained under equal excitation conditions, and the lifetime of the intermediate excited states obtained in the experiment. The emitted light intensities decreased as the lifetime of the intermediate excited states became longer. The cooling time constant represents the phonon generation efficiency, and the smaller the cooling time constant is, the higher the phonon generation efficiency becomes. Therefore, the efficiency of the conversion from incident photon to EPP, v'_p/u'_p, is also likely higher, and it is speculated that dye grains whose intermediate excited state lifetime is shorter

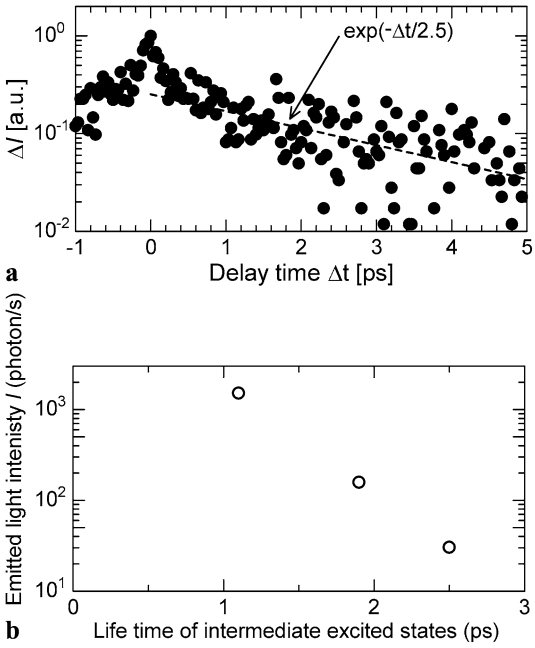

Fig. 7 Measured temporal behavior of the increment of the light intensity ΔI emitted from grains of Stilben 420 **a**, and the relations between the lifetime of the intermediate excited state and emitted light intensity for grains of Stilben 420, Coumarin 480, and Coumarin 540A

have a greater efficiency of nonadiabatic light emission. The lifetime of the intermediate excited state is expected to be closely related to the dimensions and shape of grains, and detailed experiments should be carried out for quantitative evaluation.

As described above, the average lifetime of the intermediate excited state of dye molecules excited by the nonadiabatic excitation was 1.1–1.9 ps, which is extremely short. Therefore, a frequency up-shifting mechanism using nonadiabatic light emission has great promise for photodetector applications since it can realize a very rapid response time. In addition, realizing blue-green light emission without using an ultraviolet light source or a pulse laser with a high peak intensity [18] as excitation light can be effective in such areas as display applications.

4 Conclusions

The blue-green light emission ($\lambda = 460$–520 nm) by near-infrared excitation (CW, $\lambda_{ex} = 808$ nm) was observed from coumarin dye grains. This phenomenon was based on the nonadiabatic excitation. A maximum frequency up-shift of 1.17 eV was confirmed. Based on the excitation intensity dependence, manifestation of a light emission mechanism by the three-step nonadiabatic excitation was confirmed for the first time.

The average lifetime of the intermediate excited state was shown to be 1.1–1.9 ps. The frequency up-shifting mechanism based on the nonadiabatic excitation in the dye grains is very promising for application to fast-response infrared photodetectors.

Acknowledgements A part of this work was supported by the NEDO project on a comprehensive activity for personal training and industry–academia collaboration.

References

1. A. Rogalski, K. Adamiec, J. Rutkowski, in *Narrow-Gap Semiconductor Photodiodes* (Society of Photo Optical, 2000), p. 187
2. H.J. Baker, J.J. Bannister, T.A. King, E.S. Mukhtar, Appl. Opt. **18**, 2136 (1979)
3. P.W. Atkins, *Physical Chemistry*, 6th Ed. (Oxford University Press, London, 1998), p. 497
4. T. Kawazoe, H. Fujiwara, K. Kobayashi, M. Ohtsu, J. Sel. Top. Quantum Electron. **15** (2009, in press)
5. M. Ohtsu, K. Kobayashi, T. Kawazoe, T. Yatsui, M. Naruse, in *Principle of Nanophotonics* (CRC Press, Boca Raton, 2008), p. 19
6. T. Kawazoe, K. Kobayashi, S. Takubo, M. Ohtsu, J. Chem. Phys. **122**, 024715 (2005)
7. T. Kawazoe, Y. Yamamoto, M. Ohtsu, Appl. Phys. Lett. **79**, 1184 (2001)
8. T. Kawazoe, K. Kobayashi, M. Ohtsu, Appl. Phys. B **84**, 247 (2006)
9. H. Yonemitsu, T. Kawazoe, K. Kobayashi, M. Ohtsu, J. Lumin. **122–123**, 230 (2007)
10. T. Kawazoe, M. Ohtsu, Y. Inao, R. Kuroda, J. Nanophoton. **1**, 011595 (2007)
11. T. Yatsui, K. Hirata, W. Nomura, M. Ohtsu, Y. Tabata, Appl. Phys. B **93**, 55 (2008)
12. U. Brackmann, *Lambdachrome Laser Dyes* (LAMBDA PHYSIK)
13. F.M. Lee, C.E. Stoops, L.E. Lahti, J. Cryst. Growth **32**, 363 (1976)
14. D.W. Marquardt, J. Soc. Ind. Appl. Math. **11**, 431 (1963)
15. F. Laermer, T. Elsaesser, W. Kaiser, Chem. Phys. Lett. **156**, 381 (1989)
16. H.J. Polland, W.W. Rühle, K. Ploog, C.W. Tu, Phys. Rev. B **36**, 7722 (1987)
17. Y. Rosenwaks, M.C. Hanna, D.H. Levi, D.M. Szmyd, R.K. Ahrenkiel, A.J. Nozik, Phys. Rev. B **48**, 14675 (1993)
18. G.S. He, R. Signorini, P.N. Prasad, Appl. Opt. **37**, 5720 (1998)

Appl Phys B (2010) 98: 5–11
DOI 10.1007/s00340-009-3680-z

Applied Physics B
Lasers and Optics

Evaluation of the dynamic range and spatial resolution of nonadiabatic optical near-field lithography through fabrication of Fresnel zone plates

T. Kawazoe · T. Takahashi · M. Ohtsu

Received: 9 July 2009 / Published online: 8 August 2009

Abstract Fresnel zone plates (FZPs) were fabricated in order to evaluate the performance of nonadiabatic photolithography by exploiting the localized nature of optical near fields. This novel photolithography scheme could realize FZPs with structures smaller than the wavelength of the light source used for exposure. The FZP for 325-nm-wavelength UV light could focus the incident light to a spot size of 590 nm. An FZP for focusing soft X-rays was also fabricated and, compared to conventional adiabatic photolithography, showed higher-contrast zones over the whole area of the FZP. This method exhibits a high dynamic range and good spatial resolution, and it was free from artifacts due to the interference of the residual propagating exposure light transmitted through the aperture of the photomask.

PACS 82.50.Nd · 81.16.Nd · 42.79.Ci

1 Introduction

A variety of advanced diffractive optical devices, including fiber Bragg gratings [1], two-dimensional beam splitters [2], periodically poled waveguides [3], and Fresnel zone plates (FZPs) have recently been developed. The FZP is attractive, as it has advantages over conventional convex lenses such as a solid immersion lens [4] due to its high focusing capability, planar device configuration, negligible absorption loss in the ultraviolet (UV) region, and low coma aberration for the tilted light incidence [5]. FZPs have been used in several applications, including visible optofluidic microscopy [6] and soft X-ray microscopy [7].

Electron beam lithography (EBL) and focused ion beam (FIB) techniques have been used for fabricating FZPs [8, 9]; however, these methods are not compatible with mass production because they involve raster scanning. Photolithography is the dominant technique for mass production of semiconductor devices, but the spatial resolution is too low, as it is diffraction limited. In order to solve these problems, we have developed a prototype high-resolution near-field photolithography system for industrial applications [10]. The major advantage of near-field photolithography is that it is applicable for nonadiabatic photochemical reactions [11–15], which enables the patterning of a UV-sensitive photoresist and an optically inactive resist film using a visible light source [16]. In our previous experimental and theoretical work, this reaction was described by a multistep excitation via molecular vibrational modes, based on the exciton–phonon polariton model (i.e., the dressed photon model) [11–15]. In this paper, near-field photolithography using a nonadiabatic photochemical reaction is termed *nonadiabatic photolithography* [16, 17], whereas that using a conventional adiabatic reaction [18] is called *adiabatic photolithography*. In comparison with other conventional fabrication methods, nonadiabatic photolithography has a greater potential for practical use because short-wavelength light sources are not required and it is compatible with mass production.

In order to demonstrate the advantages of nonadiabatic photolithography, we fabricated, as the first step, a typi-

T. Kawazoe (✉) · T. Takahashi · M. Ohtsu
Department of Electrical Engineering and Information Systems, Graduate School of Engineering, The University of Tokyo, 2-11-16 Yayoi, Bunkyo-ku, Tokyo 113-8656, Japan
e-mail: kawazoe@ee.t.u-tokyo.ac.jpp
Fax: +81-3-5841-1140

T. Kawazoe · M. Ohtsu
Nanophotonic Research Center, Graduate School of Engineering, The University of Tokyo, 2-11-16 Yayoi, Bunkyo-ku, Tokyo 113-8656, Japan

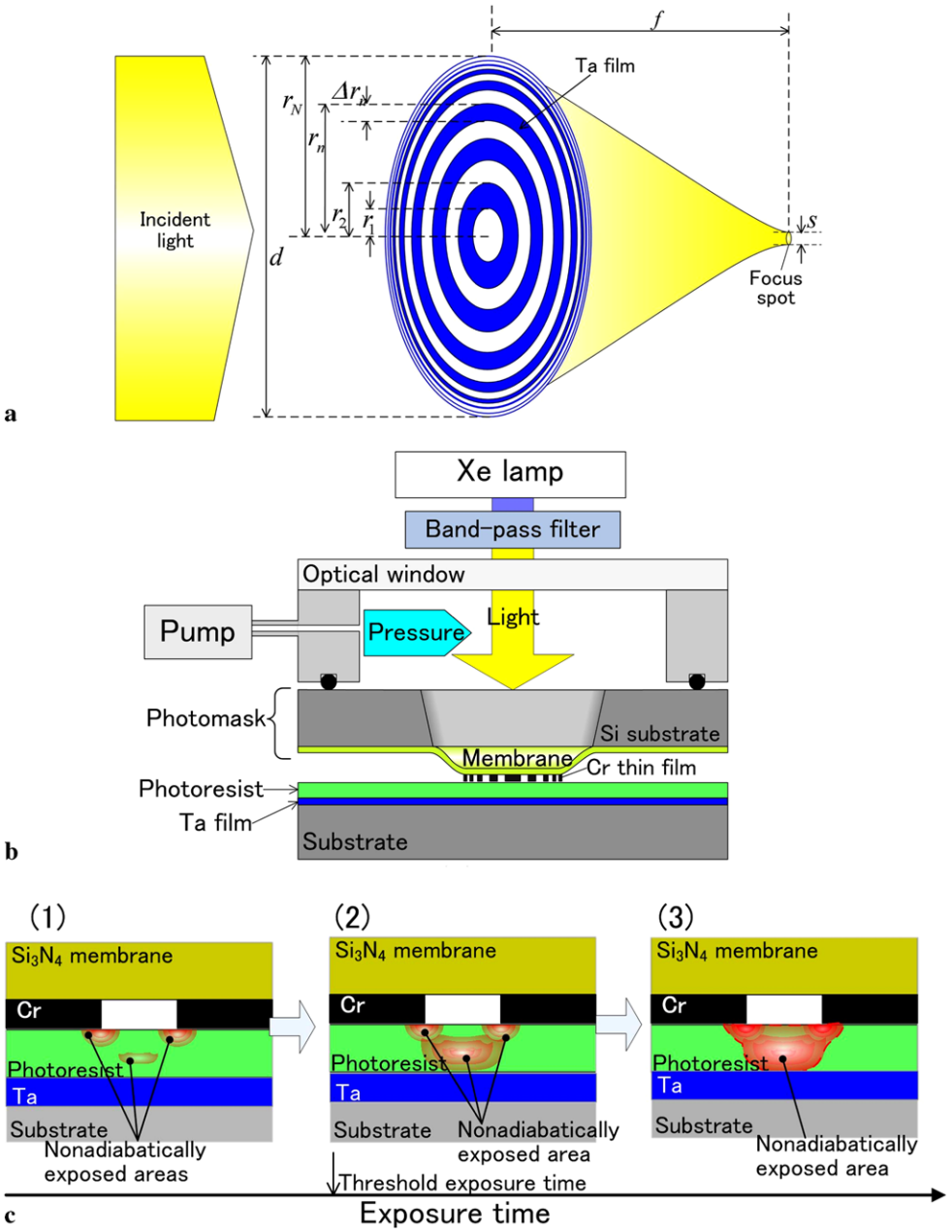

Fig. 1 **a** Structure of a two-level Fresnel zone plate (FZP). **b** Exposure setup, **c** schematic illustrating the time evolution of the exposed regions in the photomask due to nonadiabatic photochemical reaction. (1), (2), and (3) represent the exposed region before, during, and after the threshold exposed time, respectively

cal two-level FZP with a focal length, $f = 516$ μm and spot size $s = 463$ nm for incident light with a wavelength $\lambda = 325$ nm. These values are equivalent to those used for the imaging system in the visible region [6]. As the second step, we fabricated an FZP for the soft X-ray region in order to evaluate the high dynamic range and spatial resolution capabilities of nonadiabatic photolithography.

Figure 1a shows a two-level FZP, which was fabricated by pattering a Ta film with concentric circular zones on a substrate. The radius r_n of the nth order zone was

$$r_n = \sqrt{nf\lambda + \left(\frac{n\lambda}{2}\right)^2}. \quad (1)$$

The bandwidth Δr_n of the nth order is given by $\Delta r_n = r_n - r_{n-1}$. This means that the Δr_n of even-order zones (i.e., $\Delta r_{2m} : m = 1, 2, 3, \ldots$) is the bandwidth of the Ta ring used for blocking the incident light. The odd-order Δr_n is that of the light transmission zone. The spot size, s, of the light at the focal point was 1.03 Δr_N, where N is the highest order, i.e., the order of the outermost zone [19]. Based on these formulae, the number of the zones (i.e., N), the outermost radius $r_{n=N}$, and the outermost bandwidth $\Delta r_{n=N}$ are derived as 231 μm, 200 μm, and 450 nm, for $\lambda = 325$ nm, $f = 516$ μm, and $s = 463$ nm, respectively. Thus, the diameter, $d = 2r_{n=N}$, of the FZP was 400 μm. In such a configuration, the ratio between the diameter of the innermost

light transmission disk and the bandwidth of the outermost light transmission zone ($2\Delta r_1/\Delta r_N$) is as large as 60. This means that a high dynamic range of fabrication is required, i.e., wide and narrow bandwidths must be simultaneously fabricated in the inner and outer regions of the FZP, respectively, under the same exposure conditions. Furthermore, a high spatial resolution is required for fabrication because the outermost bandwidth of the soft X-ray FZP is as narrow as 190 nm (refer to Sect. 3.3), which is less than the wavelength of the exposure light.

In this paper, we report the fabrication of FZPs using nonadiabatic photolithography, evaluations of their light focusing properties, and evaluation of the cross-sectional profiles of the zones. From these results, we conclude that nonadiabatic photolithography has a high dynamic range and high spatial resolution, and that it is a promising method for fabricating FZPs.

2 Nonadiabatic photolithography

Figure 1b shows the exposure setup used for the nonadiabatic photochemical reaction induced by the optical near field. The photomask was composed of a Si substrate, a deformable Si_3N_4 membrane, and a patterned Cr thin film. During exposure, the Cr thin film was brought to within 20 nm of the photoresist by deforming the membrane by increasing the air pressure. Details of this procedure are described elsewhere [10].

Nonadiabatic photolithography is based on a novel photochemical reaction caused by the coupling between the dressed photons and coherent phonons around the edge of the photomask [11–15]. As a result, the light can be used for exposure even though its wavelength is longer than the absorption-edge wavelength of the photoresist. Although the incident propagating light can transmit through the aperture of the photomask while generating the optical near fields at the aperture, the photoresist is not sensitive to such a long-wavelength propagating light. Thus, the nonadiabatic photochemical reaction is induced only by the optical near field.

Because the nonadiabatic photochemical reaction depends on the degree of localization of the dressed photons, our previous works have employed the spatial distribution of the quantity $I(r) \cdot dI(r)/dr$ in finite difference time domain (FDTD) simulations in order to estimate the spatial extent of the exposed region of photoresist, where $I(r)$ and $dI(r)/dr$ are the light intensity and spatial gradient, respectively [16, 17]. From this, it was found that $I(r) \cdot dI(r)/dr$ took large values around the edge of the aperture of the photomask and at the region inside the photoresist film (Fig. 1c (1)). These two regions expand with increasing exposure time and merge together at a threshold exposure time (Fig. 1c (2)). After this threshold exposure time, the exposed region becomes deeper with further increase of the exposure time (Fig. 1c (3)).

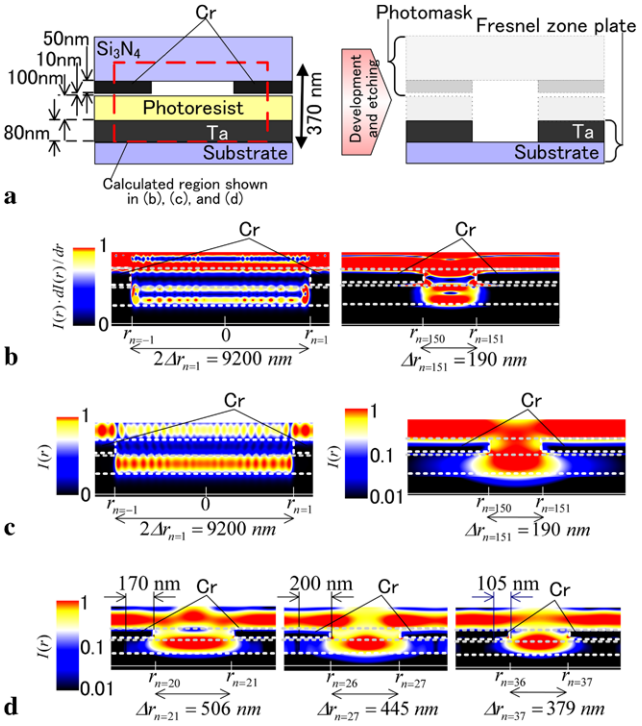

Fig. 2 **a** Cross-sectional profiles of the Cr photomask, photoresist, and Ta film, two-dimensional FDTD simulations of which were carried out assuming the linear aperture. **b** and **c** represent the calculated spatial distributions of $I(r) \cdot dI(r)/dr$ and $I(r)$ around the apertures of the photomask for patterning the innermost light transmission disk (diameter $2\Delta r_1 = 9200$ nm) and the highest-order ($n = 151$: $\Delta r_{151} = 190$ nm) light transmission zone under the same exposure conditions. The light intensity under the 151st order aperture is low because the aperture is very narrow, and so this distribution is displayed using a logarithmic scale to facilitate detailed discussions. **d** Calculated result of $I(r)$ for the aperture of the 27th order, with bandwidth ($\Delta r_n = 455$ nm) close to the wavelength of the exposure light (450 nm). For comparison, results for the neighboring apertures are also given, for which $\Delta r_n = 506$ nm with $n = 21$, and $\Delta r_n = 379$ nm with $n = 37$

Based on the results of the previous works, the possibility of high dynamic range capability is discussed. Figure 2a represents the detailed cross-sectional profiles of the Cr mask, photoresist, and a Ta film, and two-dimensional FDTD simulations were carried out for the linear aperture and assuming that the exposure time was longer than threshold. The thicknesses of the mask, photoresist, and Ta film were the same as those in the experiments for fabricating the soft X-ray FZP (refer to Sect. 3.3). Figure 2b shows the calculated spatial distributions of $I(r) \cdot dI(r)/dr$ around the apertures of the mask, for patterning the innermost light transmission disk ($2\Delta r_1 = 9200$ nm) and the highest-order ($n = 151$, $\Delta r_{151} = 190$ nm) light transmission zone under the same exposure conditions. The widths of the distributions were equal to the widths of the apertures irrespective

of the orders of zones, which means that the pattern on the mask can be faithfully transcribed to the photoresist, and both wide and narrow bandwidths can be simultaneously patterned in the inner and outer regions of the FZP, respectively, under the same exposure conditions. In other words, a high dynamic range is expected.

Figure 2c shows the results of the FDTD simulation of adiabatic photolithography. Here, the spatial distribution $I(r)$ was calculated, to which the contribution from the residual propagating light transmitted through the aperture is not negligible [10, 18]. The most important feature of this distribution is that the width is greater than that of the narrow aperture order ($\Delta r_{151} = 190$ nm), and this originates from the diffraction of the residual propagating light transmitted through the aperture. This wide distribution over-exposes the photoresist under the mask, so that a fraction of the Ta film is removed, which makes narrow-bandwidth patterning difficult. A high dynamic range is not expected.

Figure 2d shows the calculated $I(r)$ for the aperture when $n = 27$. The bandwidth was 445 nm, which is close to the wavelength of the light used for exposure ($\lambda = 450$ nm). For comparison, results for the neighboring apertures are also given, in which the values of Δr_n are 506 nm ($n = 21$) and 379 nm ($n = 37$), and they deviated from the wavelength. From these results, one can see that the light of $n = 27$ penetrates into the photoresist under the mask in an intensity-modulated manner. This originates from the resonantly enhanced interference between the scattered and propagating light transmitted through the adjacent apertures because Δr_{27} is close to λ. The penetration length is as long as 200 nm, which is longer than those of $n = 21$ and $n = 37$. The photoresist under the mask is over-exposed so that a fraction of the Ta films is removed, decreasing its thickness.

From Figs. 2c and d, it can be expected that adiabatic photolithography is not suitable for fabricating high-contrast patterns homogeneously over the whole area of an FZP. The results of these FDTD simulations will be compared with the experimental results in Sect. 3.3.

3 Experimental results and discussion

3.1 Fabrication of a membrane photomask and a Fresnel zone plate

A membrane photomask was fabricated for the 325-nm FZP with the focal length of 516 μm and the spot size of 463 nm, as described in Sect. 1, with Fig. 3a showing the fabrication procedure. We used a Si substrate with a 500-nm-thick Si_3N_4 layer. The 50-nm-thick Cr thin film and SiO_2 layer were deposited by sputtering, followed by electron beam resist (ZEP520A, Zeon Co.) deposition using spin coating (Fig. 3a (1)), and the FZP was defined using EBL

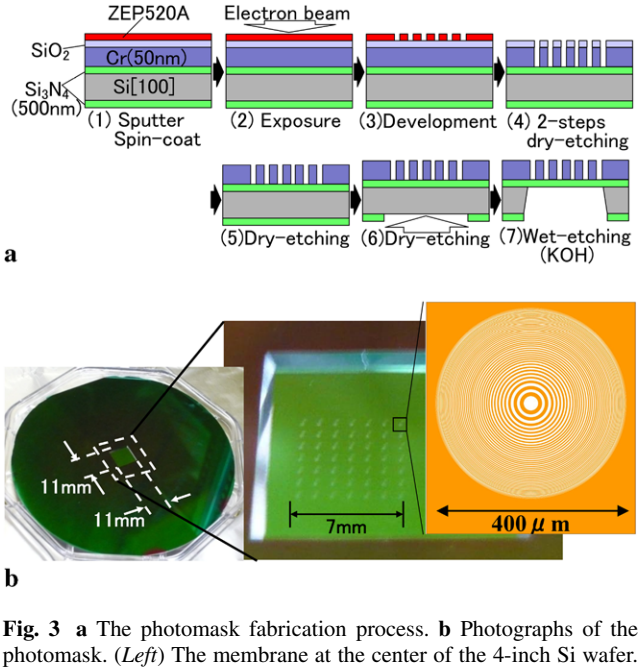

Fig. 3 **a** The photomask fabrication process. **b** Photographs of the photomask. (*Left*) The membrane at the center of the 4-inch Si wafer. (*Center*) Photomask for 49 two-dimensionally aligned FZPs. (*Right*) The profile of the photomask for the single FZP

(Fig. 3a (2)). After development of the resist, the SiO_2 and Cr thin films were etched using CHF_3/SF_6 and Cl_2/O_2 gases (Fig. 3a (3) and (4)). The SiO_2 hard mask was then removed using CHF_3/SF_6 (Fig. 3a (5)). To fabricate the deformable Si_3N_4 membrane, the central part of the Si_3N_4 layer on the back side of the photomask was removed by dry etching (Fig. 3a (6)), and the Si substrate was removed by wet etching in a solution of KOH. Figure 3a (7) shows the finished photomask with the patterned Cr thin film on the deformable Si_3N_4 membrane.

Figure 3b shows photographs of the membrane photomask. The 11 mm × 11 mm deformable Si_3N_4 membrane is seen at the center of the 4-inch Si wafer (left photograph). Because the effective contact area for nonadiabatic photolithography was larger than 7 mm × 7 mm at a typical air pressure of 7 KPa, the maximum number of 400-μm FZPs that could be fabricated in a single exposure was 100, with a center-to-center separation between adjacent FZPs of 300 μm, which suggests the possibility of mass production of the FZP. The center photograph in Fig. 3b shows the photomask for 49 two-dimensionally aligned FZPs. The right photograph shows the whole profile of the photomask for a single FZP.

An FZP was fabricated on a 200-μm-thick synthetic fused silica substrate using the photomask described above. Figure 4a shows the fabrication process. A 65-nm-thick Ta film was deposited by sputtering, and a Si-containing photoresist (FH-SP-3CL, Fuji Film Electronic Materials Co. Ltd.; long-wavelength cut-off of the absorption is 500 nm) was spun on, resulting in a 100-nm-thick film (Fig. 4a (1)). The FZP

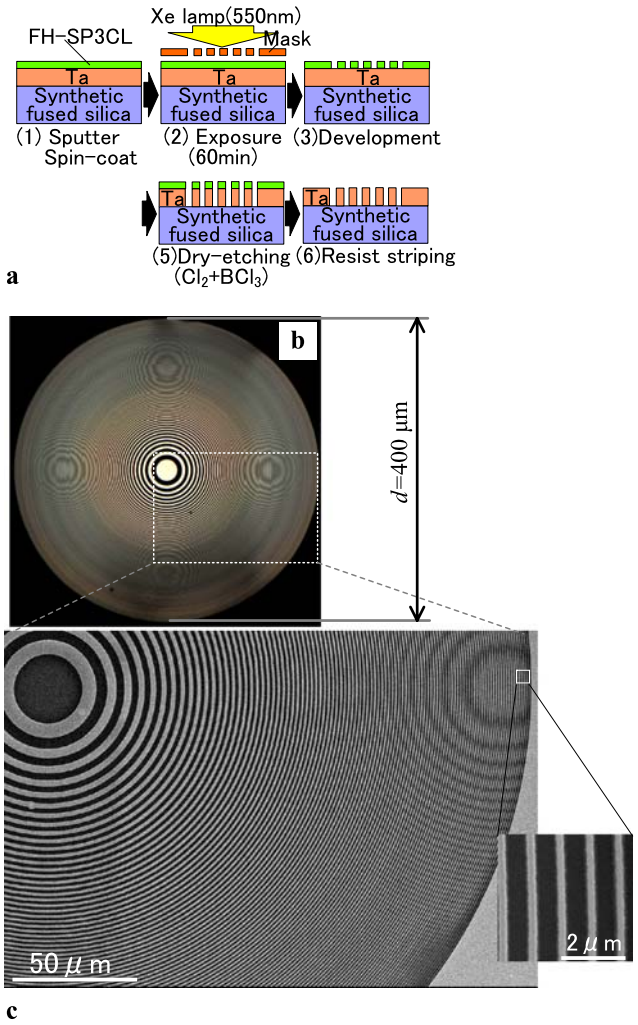

Fig. 4 **a** Fabrication procedure. **b** Microphotograph of the fabricated FZP. **c** SEM image of the fabricated FZP

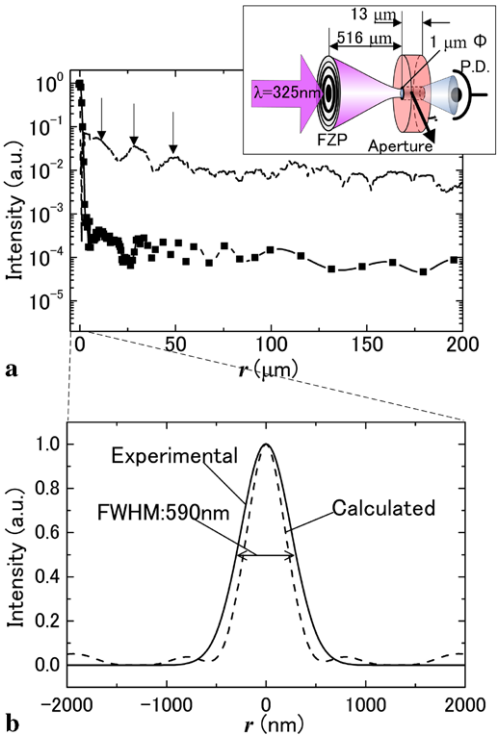

Fig. 5 **a** Cross-sectional intensity profile of the UV light on the focal plane ($f = 516$ μm). The *horizontal axis* is the displacement, r, from the center of the beam spot. The *closed squares* connected by a *solid curve* show the experimental results, and the *broken curve* is the simulated data. Experimental and calculated values are normalized to unity at $r = 0$. The *inset* represents the scanned aperture (1 μm in diameter and 13 μm thick) used for measurements. **b** Magnified cross-sectional profiles of the experimental and calculated results around $r = 0$

patterns were transcribed from the photomask to the photoresist using nonadiabatic photolithography (Fig. 4a (2)); a Xe lamp was used as a light source. The wavelength was 550 nm with a bandwidth of 80 nm, which is outside the absorption band of the photoresist. The exposure time was 60 minutes, and the optical power density 100 mW/cm^2. After development, the Ta film was patterned by etching using Cl_2/BCl_2 (Fig. 4a (3) and (4)), and finally, the photoresist was removed (Fig. 4a (5)).

Figure 4b shows a microphotograph of the FZP acquired by illuminating the specimen from behind. The concentric Ta rings are clearly visible for the whole area of the FZP. A scanning electronic microscope (SEM) image of the FZP is shown in Fig. 4c. High-contrast patterns of the Ta rings are clearly seen without any defects, even in the outermost area of the disk.

3.2 Optical properties of the Fresnel zone plate

Figure 5 shows a cross-section of the intensity profile of UV light from a 325-nm He–Cd laser focused onto the focal plane ($f = 516$ μm), with the calculated profile from diffraction optics under Fresnel approximation overlaid [19]. It should be noted that this curve is an envelope of the large number of peaks of the narrow and sharp side lobes of the diffraction pattern. Experimental and calculated values are normalized at $r = 0$. The ratio between the experimental values at the peak ($r = 0$) and at the tail ($r \geq 50$ μm) was larger than 1×10^3, and the ratio of the calculated values was about 1×10^2. The difference between the experimental and calculated ratios is attributed to the guiding effect of the focused light beam transmitting through a long, narrow aperture used for the experiments, which was not included in the calculation. However, the positions of the local maxima are in agreement, as shown by downward arrows in Fig. 5a, which implies that the fabricated FZP exhibits the good focusing performance expected at the design stage.

Figure 5b shows the magnified cross-sectional profiles around $r = 0$. The Stokes correction [20] was employed for deconvolution using the TE_{00} mode function in the

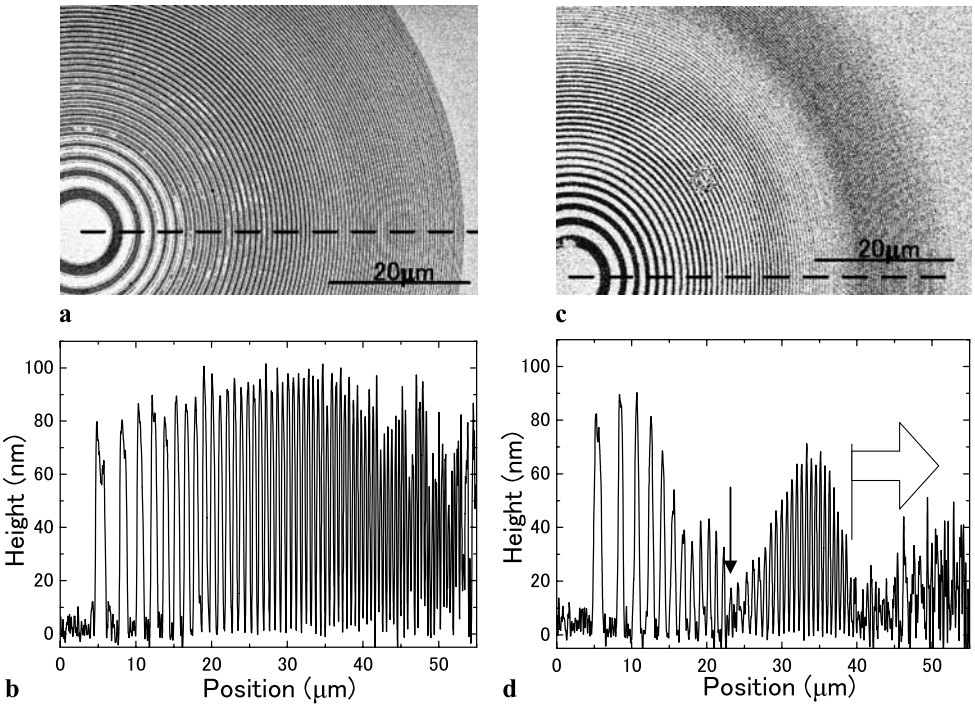

Fig. 6 **a** SEM image of the soft X-ray FZP fabricated using nonadiabatic photolithography. **b** Cross-sectional profile along the broken line in **a**. **c** SEM image of the FZP fabricated using conventional adiabatic photolithography. **d** Cross-sectional profile along the broken line in **c**

narrow and thick apertures. The estimated spot size was 590 nm (FWHM), which is close to the design spot size of 463 nm [19]. The efficiency of the collecting the light was about 30%, which was defined by the ratio between the light power at the center of the spot ($-s/2 \leq r \leq s/2$) and the total light power incident at the FZP. This performance is as good as can be expected from a conventionally fabricated FZP [21].

3.3 Comparison between adiabatic and nonadiabatic photolithographies

FZPs were fabricated to focus much shorter wavelengths, i.e., soft X-rays with $\lambda = 0.42$ nm, using both nonadiabatic photolithography and adiabatic photolithography. By comparing the resulting FZP structures, it was possible to evaluate the relative dynamic range and spatial resolution capabilities of the two techniques. The focal length was 50 mm and the spot size 196 nm, which meets the requirements for a typical soft X-ray microscope [5, 7]. Based on the design criteria in (1), the numbers of zones N, the outermost radius $r_{n=N}$, and the bandwidth $\Delta r_{n=N}$ were 151 μm, 56 μm, and 190 nm, respectively, and so the diameter of the FZP was 112 μm.

A 200-nm-thick Si_3N_4 layer on a Si wafer was used as the substrate material for the soft X-ray FZP. An 80-nm-thick Ta film was deposited by sputtering, and a 100-nm-thick Si-containing photoresist (FH-SP-3CL) was spun on. The concentric rings were transcribed from the photomask to the photoresist using the procedure described in Fig. 3a. Using nonadiabatic photolithography, the light source was a Xe lamp with a wavelength of 550 nm and bandwidth of 80 nm, which was outside the absorption band of the photoresist. The exposure time was 13 minutes, and optical power density was 100 mW/cm^2. Using conventional adiabatic photolithography, an Hg lamp with a wavelength of 450 nm and bandwidth of 40 nm was used, which was inside the absorption band of the photoresist. The exposure time was 4 s, and the optical power density was 100 mW/cm^2. After development, the Ta film was patterned by dry etching in Cl_2/BCl_2. In order to fabricate a thin Si_3N_4 membrane for efficient transmission of the soft X-rays, the central part of the Si_3N_4 layer was removed from the back side of the photomask using dry etching, and the Si substrate was removed by wet etching in KOH. Finally, the FZP for soft X-rays was fabricated with the patterned Ta film on the Si_3N_4 membrane.

Figure 6a shows an SEM image of the soft X-ray FZP fabricated with nonadiabatic photolithography. Figure 6b shows the cross-sectional profile along the broken line in Fig. 6a, measured using a laser confocal microscope (VK-9700 Keyence Co.) with lateral and vertical resolutions of 130 nm and 1 nm, respectively. Even though the bandwidth of the outermost ring ($\Delta r_{N=151} = 190$ nm) was narrower than the 550-nm-wavelength of the light source used in the photolithography, the concentric rings are clearly seen over the whole area of the FZP. This result is consistent with the calculated result of Fig. 2b, showing good dynamic range and a high spatial resolution.

For comparison, Fig. 6c shows an SEM image of the FZP fabricated by conventional adiabatic photolithography. Figure 6d shows the cross-sectional profile along the broken

line in Fig. 6c. The rings in the outer region (indicated by the white arrow) are less visible than are those in Figs. 6a and b, which is consistent with the calculated results in Fig. 2c and shows that this FZP has a lower dynamic range. The height of the ring indicated by the black arrow in this figure is very low due to interference, because the bandwidth ($\Delta r_n = 450$ nm) is equal to the wavelength of the light, which is consistent with the calculated results in Fig. 2d.

These experimental results confirmed the advantages of nonadiabatic photolithography. Although experiments using soft X-ray irradiation have not yet been carried out, high performance through focusing the soft X-rays is expected based on our previous experiments involving soft X-ray irradiation of a diffraction grating, fabricated using the same nonadiabatic photolithography process [22].

4 Summary

We have reported the fabrication of 400-μm diameter FZPs using optical near-field nonadiabatic photolithography. 325-nm UV light was focused onto a 590-nm spot size, and the collection efficiency was as high as 30%. Soft X-ray ($\lambda = 0.42$ nm) FZPs were fabricated, with the outermost bandwidth, Δr_N, of 190 nm. A high-contrast pattern was accurately transcribed from the fine-structured photomask due to the high dynamic range and high spatial resolution of nonadiabatic photolithography.

For comparison, conventional adiabatic photolithography was used to fabricate soft X-ray FZPs, and the contrast was low and suffered from interference effects due to the residual propagating exposure light. This demonstrates that the high dynamic range and high spatial resolution capabilities were due to the nonadiabatic photolithography process.

References

1. P. Cheben, E. Post, S. Janz, J. Albert, A. Laronche, J.H. Schmid, D. Xu, B. Lamontagne, J. Lapointe, A. Delâge, A. Densmore, Opt. Lett. **33**, 2647 (2006)
2. D. Gong, Z. Zhoua, H. Liua, J. Wanga, H. Gao, Opt. Lasers Eng. **47**, 662 (2009)
3. A.C. Busacca, E. D'Asaro, A. Pasquazi, S. Stivala, G. Assanto, Appl. Phys. Lett. **93**, 121117 (2008)
4. S.M. Mansfield, G.S. Kino, Appl. Phys. Lett. **57**, 2615 (1990)
5. H. Sakai, M. Fujisawa, K. Iida, I. Ito, H. Kudo, N. Nakamura, K. Shinoe, T. Tanaka, Phys. Rev. Spec. Top. Accel. Beams **10**, 042801 (2007)
6. J. Wu, X. Cui, L.M. Lee, C. Yang, Opt. Express **16**, 15595 (2008)
7. Y. Suzuki, A. Takeuchi, H. Takano, K. Uesugi, T. Oka, K. Inoue, Rev. Sci. Instrum. **75**, 1155 (2004)
8. J. Kima, K. Jalhadi, S.-Y. Lee, D.C. Joy, J. Vac. Sci. Technol. B **25**, 1771 (2007)
9. A. Surpi, S. Valizadeh, K. Leifer, S. Lagomarsino, J. Micromech. Microeng. **17**, 617 (2007)
10. Y. Inao, S. Nakasato, R. Kuroda, M. Ohtsu, Microelectron. Eng. **84**, 705 (2007)
11. T. Kawazoe, Y. Yamamoto, M. Ohtsu, Appl. Phys. Lett. **79**, 1184–1186 (2001)
12. T. Kawazoe, K. Kobayashi, S. Takubo, M. Ohtsu, J. Chem. Phys. **122**, 024715 (2005)
13. T. Kawazoe, K. Kobayashi, M. Ohtsu, Appl. Phys. B, Lasers Opt. **84**, 247 (2006)
14. T. Yatsui, K. Hirata, W. Nomura, M. Ohtsu, Y. Tabata, Appl. Phys. B, Lasers Opt. **93**, 55–57 (2008)
15. T. Kawazoe, H. Fujiwara, K. Kobayashi, M. Ohtsu, J. Sel. Top. Quant. Electron. (2009, in press)
16. H. Yonemitsu, T. Kawazoe, K. Kobayashi, M. Ohtsu, J. Lumin. **122–123**, 230 (2007)
17. T. Kawazoe, M. Ohtsu, Y. Inao, R. Kuroda, J. Nanophoton. **1**, 011595 (2007)
18. M. Naya, I. Tsuruma, T. Tani, A. Mukai, S. Sakaguchi, S. Yasunami, Appl. Phys. Lett. **86**, 201113 (2005)
19. F.L. Pedrotti, L.S. Pedrotti, in *Introduction to Optics*, 2nd edn. (Prentice Hall, New Jersey, 1993), pp. 366–390
20. T. Ungár, J. Gubicza, G. Ribárik, A. Borbély, J. Appl. Cryst. **34**, 298 (2001)
21. K. Kodate, T. Kamiya, Y. Okada, H. Takenaka, Jpn. J. Appl. Phys. **25**, 223 (1986)
22. M. Koike, S. Miyauchi, K. Sano, T. Imazono, in *Nanophotonics and Nanofabrication*, ed. by M. Ohtsu (Wiley-VCH, Weinheim, 2009), pp. 179–192

Appl Phys B (2009) 97: 825–828
DOI 10.1007/s00340-009-3654-1

Applied Physics B
Lasers and Optics

Observation of quantum confinement in ZnO nanorods fabricated using a two-temperature growth method

K. Kitamura · T. Yatsui · M. Ohtsu

Received: 3 April 2009 / Revised version: 15 June 2009 / Published online: 5 August 2009

Abstract We observed a quantum confinement effect in vertically well-aligned ultrafine ZnO nanorods using polarized excitation photoluminescence measurements. Room-temperature and low-temperature photoluminescence spectra revealed that free excitons were confined in the nanorods. The magnitude of the energy shift due to the quantum confinement in the ultrafine ZnO nanorods was 6 meV at room temperature, which corresponded to the luminescence from ZnO nanorods 12.8 nm in diameter. The diameter estimated from the spectra was comparable to the value measured from SEM images.

PACS 81.05.Dz · 81.07.Vb

1 Introduction

One-dimensional semiconductors, such as nanowires and nanorods, are attracting great interest as promising candidate materials for optical and electrical device applications. Among them, zinc oxide (ZnO) nanorods have attracted much attention because of the large exciton binding energy [1] and large oscillator strength [2]. ZnO also has great potential as a material for room-temperature nanoscale photonic devices [3], and nanophotonic switches and energy up-conversion have been demonstrated using a ZnO nanorod with double-quantum-well structures [4, 5]. Further novel functional devices can be realized using the radial quantum confinement effect of ZnO nanorods. For application to photonic and electric devices, high-quality ZnO nanorods have been fabricated using catalyst-free metalorganic vapor phase epitaxy (MOVPE) [6]. With this method, the growth temperature controls the diameter of the nanorods: a higher growth temperature results in a smaller diameter. Although ultrafine ZnO nanorods have been reported to exhibit blueshifted photoluminescence (PL) emission due to the quantum confinement effect, they grow along random directions [7]. To fabricate vertically aligned ultrafine ZnO nanorods, we developed a two-temperature growth method and succeeded in fabricating vertically well-aligned ultrafine ZnO nanorods [8]. In this paper, we report the polarized PL from ultrafine ZnO nanorods grown using the two-temperature growth method and the observation of blueshifted PL due to quantum confinement in the nanorods.

2 Experimental technique

ZnO nanorods were grown on a sapphire (0001) substrate using a catalyst-free MOVPE system. Diethylzinc and oxygen were used as the reactants, with argon as the carrier gas. The pressure inside the reactant chamber was maintained at 5 Torr. The substrate temperature was controlled using a thermocouple thermometer and radio-frequency-heated carbon susceptor. Two samples were prepared for measurement: one sample had ultrafine nanorods (sample 1, Fig. 1(a)) and the other sample had thick nanorods for reference (sample 2, Fig. 1(b)). The ultrafine ZnO nanorods of sample 1 were grown using the two-temperature growth method, which consisted of lower-temperature growth of vertically aligned thick ZnO nanorods and subsequent

K. Kitamura (✉) · T. Yatsui · M. Ohtsu
Department of Electrical Engineering and Information Systems, School of Engineering, The University of Tokyo, Tokyo 113-8656, Japan
e-mail: kitamura@nanophotonics.t.u-tokyo.ac.jp

M. Ohtsu
Nanophotonics Research Center, The University of Tokyo, Tokyo 113-8656, Japan

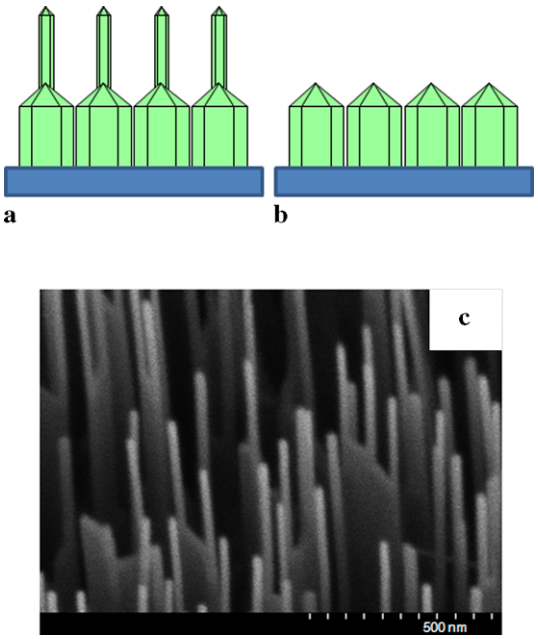

Fig. 1 Schematic images of samples (**a**) 1 and (**b**) 2, with (**c**) a SEM image of (**a**)

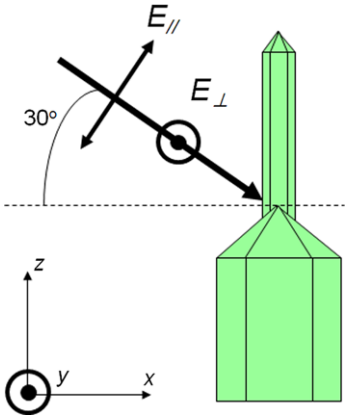

Fig. 2 Schematic images of the nanorods and excitation polarization

higher-temperature growth to fabricate vertically aligned ultrafine nanorods. In the first step, vertically well-aligned ZnO nanorods were grown at 450°C for 30 min. In the second step, ultrafine nanorods structures were grown from the tips of the preformed thick nanorods at 750°C for 10 min. Sample 1 had thick nanorods at the bases of the ultrafine nanorods. Further details of the growth method have been reported in [8]. Sample 2 was grown at 450°C for 30 min.

3 Result and discussion

Figure 1(c) shows a scanning electron microscopy (SEM) image of the ultrafine nanorods of sample 1. It confirmed that the ultrafine nanorods were well aligned vertically to the substrate. Transmission electron microscopy and electron diffraction measurement revealed that the nanorods grew along the c-axis, as reported in [8]. The average diameters of the ultrafine (second step) and thick (first step) nanorods determined using SEM were 17.7 and 124.4 nm, respectively.

We measured polarized excitation PL spectra of the ZnO nanorods at room temperature and low temperature (5 K). A He–Cd laser ($\lambda = 325$ nm) was used as the excitation light source. To obtain the polarization dependence of the PL spectra, the laser irradiated the sample at 30° to the x-axis (see Fig. 2). The polarization of the incident light was controlled with a $\lambda/2$ waveplate. We compared the PL spectra between $E_{\parallel}$ [polarization parallel to the axis of the nanorods (z-axis)] and $E_{\perp}$ (perpendicular to the axis of the nanorods).

Figure 3(a) shows the polarized excited PL spectra of sample 1 (with ultrafine and thick nanorods) at room temperature. Curves $RT1_{\parallel}(E_{\parallel})$ and $RT1_{\perp}(E_{\perp})$ show the room-temperature PL with the PL peak energy at 3.298 and 3.292 eV, respectively. Figure 3(b) shows the PL spectra of sample 2. No difference is seen in the peak energy for each polarization with sample 2. The peak at 3.292 eV is the emission from free excitons in the bulk ZnO. Here, the thick base nanorods can be approximated as the bulk because they grew at high density and their separations were narrow. Therefore, the blueshifted PL of sample 1 originated from the ultrafine ZnO nanorods. Figure 4 shows the polarized excited PL spectra of sample 1 at low temperature (5 K); no difference is seen between the peak energies of $LT1_{\parallel}$ and $LT1_{\perp}$, which indicates that the energy shift at room temperature did not originate from the polarization dependence of excitons (A, B, and C excitons).

The origin of the blueshifted PL of sample 1 is explained by considering the excitation polarization dependence and quantum confinement in the ultrafine nanorods. Previous studies on the excitation polarization dependence of nanorods of ZnO [9] and other materials [10] revealed that the PL under parallel excitation ($E_{\parallel}$) is much greater than that under perpendicular polarization ($E_{\perp}$) due to the absorption anisotropy. Under parallel polarization, the ultrafine nanorods could be excited because the nanorods have strong optical absorption of $E_{\parallel}$, whereas they could not be excited strongly by $E_{\perp}$. Therefore, PL from the ultrafine nanorods appeared under parallel polarization, allowing observation of the quantum confinement of excitons in the ultrafine nanorods. At low temperature, we obtained PL from the recombination of neutral donor-bound excitons, while the PL from the recombination of free excitons was obtained at room temperature because the increase in the thermal energy caused the bound excitons to decompose into free excitons. Furthermore, neutral donor-bound excitons cannot be confined because the excitons are bound to a neutral donor. Therefore, no energy shift was observed at low temperature. The successful observation of the quantum confinement effect in the ZnO nanorods was due to the good alignment of

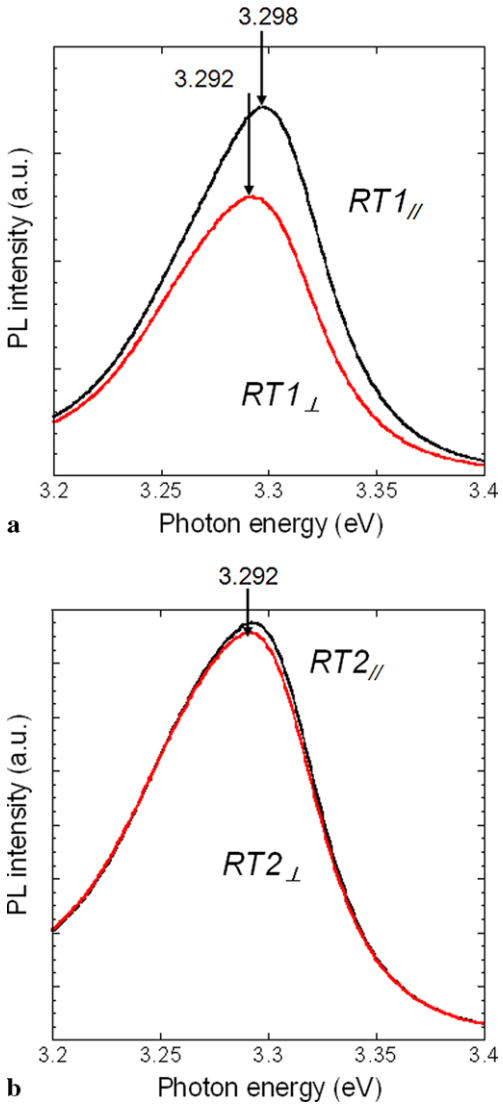

Fig. 3 Room-temperature PL spectra. (**a**) $RT1_{\parallel}$ and $RT1_{\perp}$ show the PL from sample 1 with $E_{\parallel}$ (parallel to the ZnO axis) and $E_{\perp}$ (perpendicular to the ZnO axis), respectively. (**b**) $RT2_{\parallel}$ and $RT2_{\perp}$ show the PL from sample 2 with $E_{\parallel}$ and $E_{\perp}$, respectively

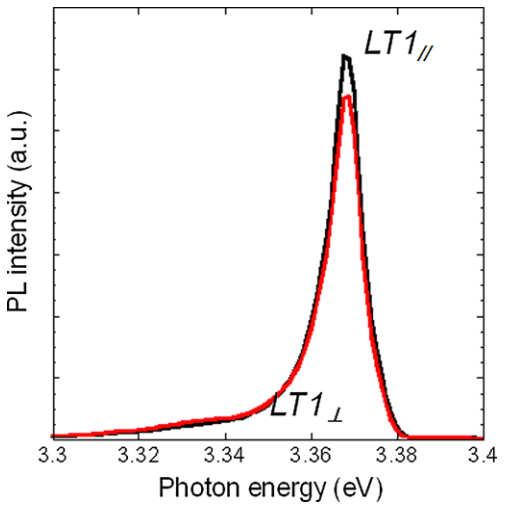

Fig. 4 Low-temperature (5 K) PL spectra of sample 1. $LT1_{\parallel}$ and $LT1_{\perp}$ show the PL from sample 1 with $E_{\parallel}$ (parallel to the ZnO axis) and $E_{\perp}$ (perpendicular to the ZnO axis), respectively

the ZnO nanorods, which resulted in the large optical absorption.

We estimated the diameter of the nanorods from the magnitude of the energy shift of 6 meV, given in Fig. 4(a). For this estimation, an infinitely deep cylindrical-well model was used while assuming that the magnitude of the energy shift corresponded to the degree of quantum confinement in the nanorods. The exciton in the nanorods is weakly confined because the Bohr radius of excitons (∼1.8 nm [11]) is sufficiently smaller than the diameter of the nanorods. The increase in energy is expressed as [12]

$$E_{n,l} = \frac{\hbar^2 j_{n,l}^2}{2Ma^2}, \tag{1}$$

where $\hbar$ is Planck's constant; $j_{n,l}$ is the Bessel function, which vanishes at zero; M is the effective mass of an exciton; and a is the diameter of a cylinder. The effective masses of the electron and hole were assumed to be $m_e = 0.28m_0$ and $m_h = 0.78m_0$, respectively [13]. As a result, the calculated diameter of the ultrafine nanorods was 12.8 nm, which is comparable to the diameter measured from SEM images (17.3 nm). We assumed that the PL peak shift depended only on ultrafine nanorods. To eliminate the emission from the thick nanorods, it is required to reduce the length of thick nanorods. Detailed dependences of the length of thick nanorods are currently under studied and will be published elsewhere.

4 Conclusions

We observed a blueshifted (6 meV) PL peak from the ultrafine ZnO nanorods at room temperature that originated from the quantum confinement. Room-temperature and low-temperature photoluminescence spectra revealed that free excitons were confined in the nanorods. The successful observation of the quantum confinement effect in the ZnO nanorods was due to the good alignment of the ultrafine ZnO nanorods. We believe that the resulting structure with radial quantum confinement allows its use in the nanophotonic devices.

Acknowledgements The authors thank Prof. Yi of Pohang University of Science and Technology for helpful discussions. This work was supported by the Special Coordination Funds for Promoting Science and Technology, Japan.

References

1. E.-S. Jang, J.Y. Bae, J. Yoo, W.I. Park, D.-W. Kim, G.-C. Yi, T. Yatsui, M. Ohtsu, Appl. Phys. Lett. **88**, 023102 (2006)
2. D.C. Reynolds, D.C. Look, B. Jogai, C.W. Litton, G. Cantwell, W.C. Harsch, Phys. Rev. B **60**, 2340 (1999)
3. M. Ohtsu, T. Kawazoe, T. Yatsui, M. Naruse, IEEE J. Sel. Top. Quantum Electron. **14**, 1404 (2008)
4. T. Yatsui, S. Sangu, T. Kawazoe, M. Ohtsu, S.J. An, J. Yoo, G.-C. Yi, Appl. Phys. Lett. **90**, 223110 (2007)
5. T. Yatsui, S. Sangu, K. Kobayashi, T. Kawazoe, M. Ohtsu, J. Yoo, G.-C. Yi, Appl. Phys. Lett. **94**, 083113 (2009)
6. W.I. Park, D.H. Kim, S.-W. Jung, G.-C. Yi, Appl. Phys. Lett. **80**, 4232 (2002)
7. W.I. Park, J. Yoo, G.-C. Yi, J. Korean Phys. Soc. **46**, L1067 (2005)
8. K. Kitamura, T. Yatsui, M. Ohtsu, G.-C. Yi, Nanotechnology **19**, 175305 (2008)
9. Z. Fan, P. Chang, J.G. Lu, E.C. Walte, R.M. Penner, C. Lin, H.P. Lee, Appl. Phys. Lett. **85**, 6128 (2004)
10. J. Wang, M.S. Gudiksen, X. Duan, Y. Cui, C.M. Lieber, Science **293**, 1455 (2001)
11. G. Lu, Z.Z. Ye, J.Y. Huang, L.P. Zhu, B.H. Zhao, Z.L. Wang, Sz. Fujita, Appl. Phys. Lett. **88**, 063110 (2006)
12. J.H. Davies, *The Physics of Low-Dimensional Semiconductors: An Introduction* (Cambridge University Press, Cambridge, 1997), p. 136
13. B.P. Zhang, N.T. Binh, K. Wakatsuki, C.Y. Liu, Y. Segawa, N. Usami, Appl. Phys. Lett. **86**, 032105 (2005)

Appl Phys B (2009) 97: 375–378
DOI 10.1007/s00340-009-3757-8

Applied Physics B
Lasers and Optics

RAPID COMMUNICATION

Increased spatial homogeneity in a light-emitting InGaN thin film using optical near-field desorption

T. Yatsui · S. Yamazaki · K. Ito · H. Kawamura · M. Mizumura · T. Kawazoe · M. Ohtsu

Received: 4 September 2009 / Published online: 14 October 2009

Abstract We report a self-assembly method that produces greater spatial uniformity in InGaN thin films using optical near-field desorption. Spatial homogeneity in the In fraction was reduced by introducing additional light during the photo-enhanced chemical vapor deposition of InGaN. Near-field desorption of InGaN nanoparticles, upon addition depended on the In content of the film, and the photon energy of the illumination source determined the energy of the emitted photons. Since this deposition method is based on a photo-desorption reaction, it can easily be applied to other deposition techniques and used with other semiconductor systems.

PACS 68.43.Tj · 81.16.Dn

1 Introduction

The control of light-emitting-diode (LED) color is important in many applications, including the generation of white light [1] and optical communications [2]. The photon energy, $h\nu_{\mathrm{em}}$, emitted from a composite semiconductor can be tailored by adjusting its composition. White light-emitting diodes (WLEDs) were developed using gallium nitride (GaN)-based LEDs because the $h\nu_{\mathrm{em}}$ from GaN can be shifted from 400 nm to 1.5 μm by adjusting the indium (In) content in $\mathrm{In}_x\mathrm{Ga}_{1-x}\mathrm{N}$ from $x = 0$ to 1, respectively [1, 3]. Although some commercial WLEDs combine the emission of three colored LEDs, the resulting color-rendering index over a broad spectrum is low due to the low spatial uniformity of In. As a result, this type of WLED has yet to replace fluorescent lamps in many applications. Here we report a self-assembly method that yields greater spatial uniformity of In in InGaN thin films using optical near-field desorption. The spatial heterogeneity of the In fraction was reduced by introducing an additional light source (i.e., a desorption light source) during the photo-enhanced chemical vapor deposition (PECVD) of InGaN, thereby causing near-field desorption of InGaN nanoparticles. The degree of nanoparticle desorption depended on In content of the film, and the photon energy of the desorption light source ultimately determined the emitted photon energy of the thin film.

2 Controlling the thin film composition using the optical near field

Figures 1a and b illustrate the approach to obtaining a more spatially uniform device composition using optical near-field effects. During the initial stages of $\mathrm{In}_{x1}\mathrm{Ga}_{1-x1}\mathrm{N}$ nanoparticle growth (bandgap energy E_{x1}), a lattice vibrational mode can be excited by far-field light originating from an optical near field caused by coupling of exciton-polaritons and phonons (Fig. 1a) [4]. If the nanoparticles are

T. Yatsui (✉) · S. Yamazaki · T. Kawazoe · M. Ohtsu
School of Engineering, The University of Tokyo, Bunkyo-ku, Tokyo 113-8656, Japan
e-mail: yatsui@ee.t.u-tokyo.ac.jp

T. Yatsui · T. Kawazoe · M. Ohtsu
Nanophotonic Research Center, Graduate School of Engineering, The University of Tokyo, Bunkyo-ku, Tokyo 113-8656, Japan

K. Ito · H. Kawamura
Central Research and Development Centre, Nitto Optical Co., Ltd., Senboku-gun, Akita 019-140, Japan

M. Mizumura
Research and Development Department, V-Technology Co., Ltd., Yokohama, Kanagawa 240-0005, Japan

concurrently illuminated by a desorption source with photon energy of $h\nu_{x2}$ ($<E_{x1}$), a strong optical absorption due to a multistep excitation of lattice vibrational modes induces desorption of a fraction of the nanoparticle population [5]. The absorption is enhanced by increasing the In content. As the deposition proceeds with desorption source illumination, the growth is governed by a trade-off between In deposition (where the In content $x < x_1$) and In desorption (where $x > x_1$). Thus, the resulting In content in the film is a function of $h\nu_{x2}$, and both spatial heterogeneity of the In fraction and spectral broadening (Fig. 1b) are avoided.

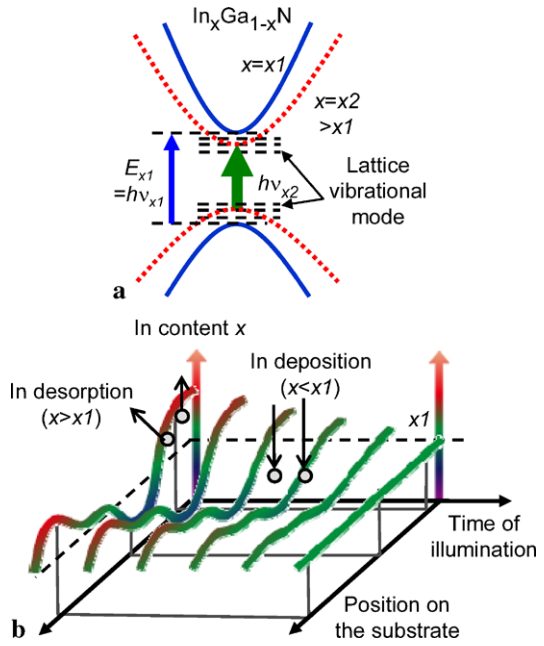

Fig. 1 Controlling the thin film composition using the optical near field. **a** A schematic diagram shows the energy dispersion and the generation of lattice vibrational modes induced by an optical near field on InGaN nanoparticles. **b** Spatial distributions of x are shown as a function of deposition time for $In_xGa_{1-x}N$ whilst illuminated with the desorption light source

3 Experiment

A spectral change was observed upon introduction of the desorption light source during PECVD of InGaN at room temperature [6] in which $h\nu_{em}$ was determined by the photon energy $h\nu_{x2}$. A 5th-harmonic, Q-switched Nd:YAG laser ($h\nu_{depo} = 5.82$ eV, $\lambda = 213$ nm) was used to excite and photodissociate trimethylgallium (TMG), triethylindium (TEI) and ammonia (NH_3, 99.999%). The choice of laser was based on the strong photo-absorptions of gas-phase TMG ($E_g > 4.59$ eV), TEI ($E_g > 4.77$ eV) and NH_3 ($E_g > 5.66$ eV), respectively [7, 8]. The desorption light source was introduced through an optical window, and H_2 gas was introduced around the window to prevent GaN deposition onto the window. The substrate was placed at the center of the reaction chamber and irradiated with a 2-mm spot size of excitation light. The total pressure in the reaction chamber was 5.4 Torr, and the deposition time was 60 min.

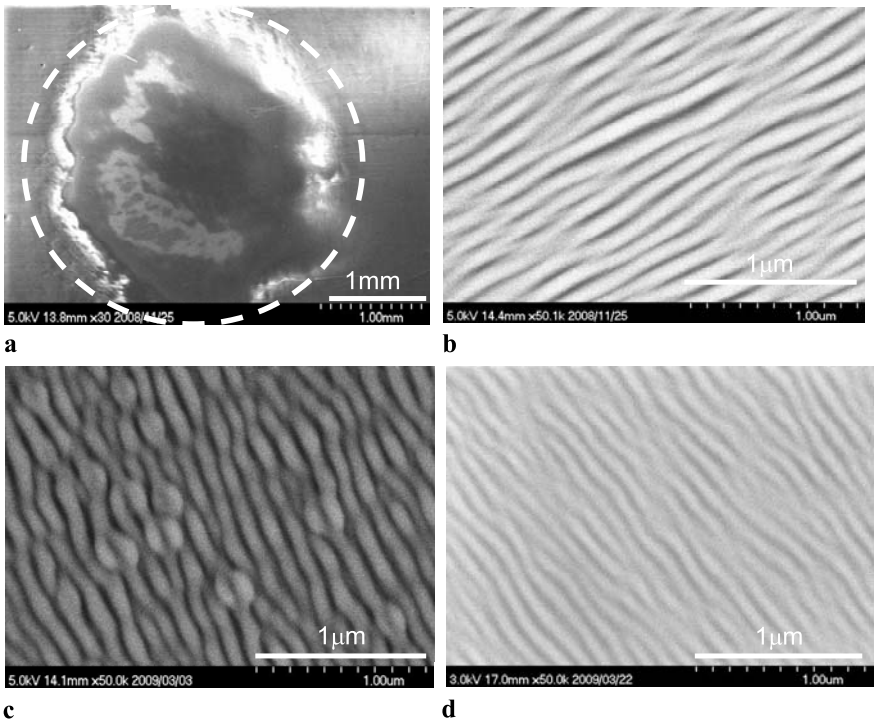

Fig. 2 SEM images of fabricated InGaN thin films. The overall image is shown in (**a**). Magnified images show films fabricated with $r_{TEI} = 0$ (**b**), 2.5×10^{-3} (**c**), 5.0×10^{-3} (**d**) sccm

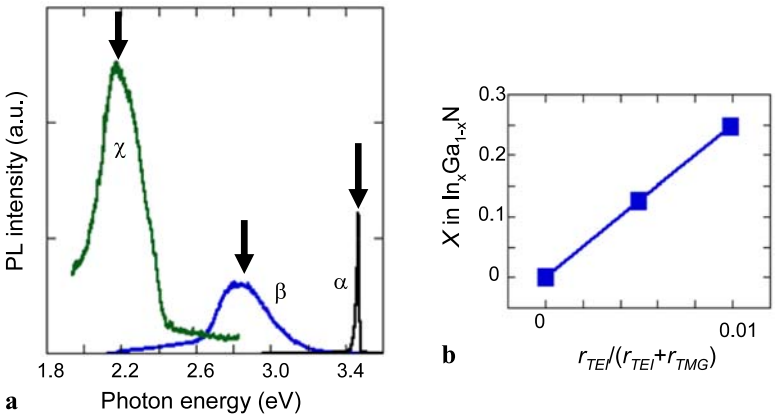

Fig. 3 Spectral control by adjusting the TEI flow rate, r_{TEI}, at room temperature. **a** PL spectra obtained at 5 K were acquired following room-temperature film deposition with $r_{\mathrm{TEI}} = 0$ (α), 2.5×10^{-3} (β), 5.0×10^{-3} (χ) sccm with $r_{\mathrm{TMG}} = 0.5$ sccm. **b** The indium content of InGaN shown as a function, r_{TEI}

4 Results and discussion

The morphology of the GaN sample was investigated with a scanning electron microscope (SEM). Figure 2a shows the overall SEM image of the InGaN film on the substrate. Figures 2b through d show magnified SEM images from within the white dashed circle in Fig. 2a. Similar morphologies, consisting of 100-nm lines, were observed at different TEI flow rates, r_{TEI}. The relative atomic compositions of indium, gallium and nitrogen were obtained by monitoring photoluminescence (PL) induced by a continuous wave He–Cd laser (3.81 eV, $\lambda = 325$ nm), in which the PL peak was shifted by changing r_{TEI} (Fig. 3a). The In content, x, was determined according to

$$E = 3.42 - 4.95x, \tag{1}$$

where E refers to the PL peak energy [9]. Figure 3b shows that x was a linear function of r_{TEI}, which agrees with results obtained using low-temperature metal-organic chemical vapor deposition (MOCVD) [10].

Based on the above results, a spectral shift was induced by introducing desorption light during PECVD. InGaN was grown with $r_{\mathrm{TEI}} = 2.5 \times 10^{-3}$ sccm and under illumination with a desorption light source of $h\nu_{x2} = 2.71$ eV. As shown in Fig. 4a, the PL intensity in the region $h\nu_{\mathrm{em}} < h\nu_{x2}$ (curve X′) decreased relative to that observed in the absence of desorption light (curve X). The difference in PL intensity, I_{diff}, between X and X′ (Fig. 4b) clearly shows the decrease in the PL intensity of X′ at energies less than $h\nu_{x2}$, indicating near-field desorption as described in Fig. 1a.

Using a desorption light source with $h\nu_{x2} = 2.33$ eV, which is lower in energy than the peak PL of deposited InGaN (2.5 eV) in the absence of desorption light, similar decreases in PL intensity were observed for $r_{\mathrm{TEI}} = 2.5 \times 10^{-3}$ sccm and $r_{\mathrm{TEI}} = 5.0 \times 10^{-3}$ sccm (curves Y′ and Z′ in Fig. 5a, respectively). The difference in PL between Y and Y′, and Z and Z′, as indicated by curves Y″ and Z″ in Fig. 5b, respectively, shows that the PL intensity of both Y′ and Z′ decreased at energies below $h\nu_{x2} = 2.33$ eV. In addition, Fig. 5b shows that higher levels of r_{TEI} (curve Z″) resulted in increased I_{diff} values at $h\nu_{x2} > 2.33$ eV relative to those obtained at lower r_{TEI} (curve Y″). This further indicates In desorption. This result confirms that the use of the desorption light source during film deposition did not permit additional In doping other than that determined by the pho-

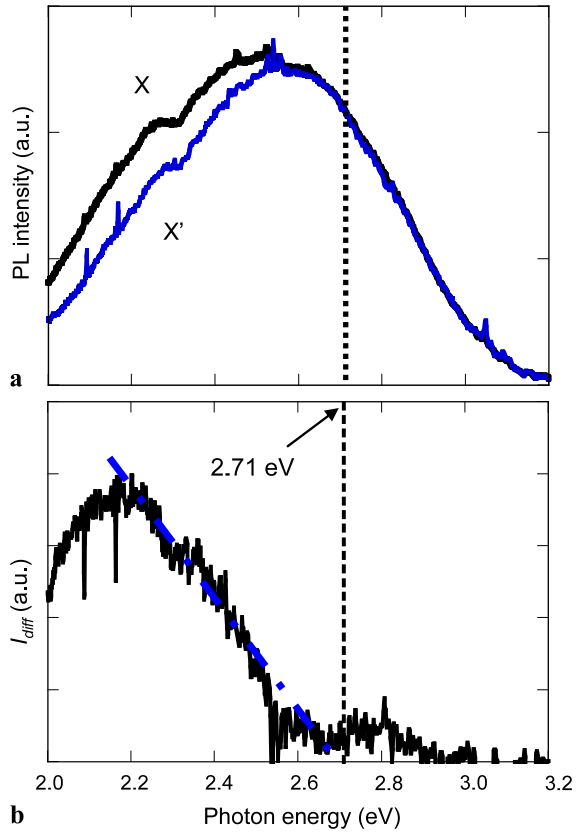

Fig. 4 Spectral changes induced by desorption light illumination at 2.71 eV during PECVD. **a** PL spectra were obtained at 5 K using room-temperature PECVD with $r_{\mathrm{TEI}} = 2.5 \times 10^{-3}$ (curves X and X′) and a desorption source energy of $h\nu_{x2} = 2.71$ eV. **b** The difference spectrum shown for X–X′

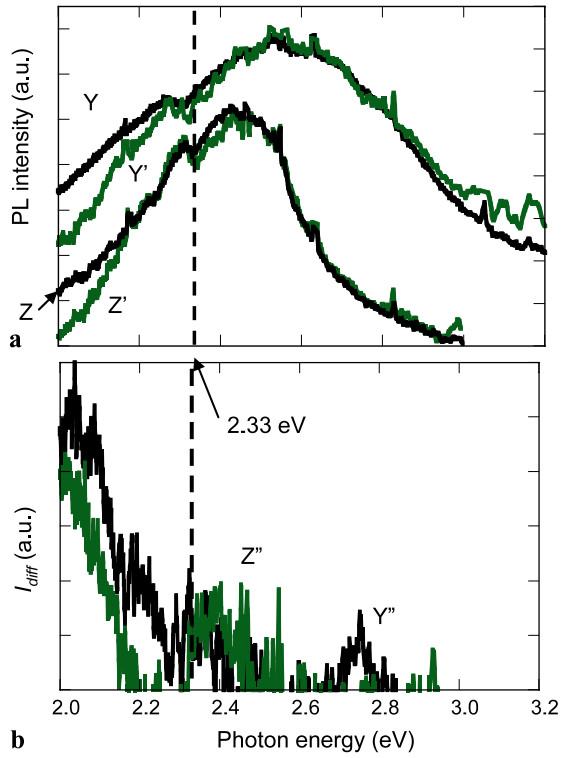

Fig. 5 Spectral changes induced by desorption light illumination at 2.33 eV during PECVD. **a** PL spectra were obtained at 5 K using room-temperature PECVD with $r_{\mathrm{TEI}} = 2.5 \times 10^{-3}$ (curves Y and Y′) and 5.0×10^{-3} (curves Z and Z′) sccm and a desorption source energy of $h\nu_{x2} = 2.33$ eV. **b** The PL difference spectra shown for Y–Y′ (curve Y″) and Z–Z′ (curve Z″)

ton energy of the desorption light source itself. This effect resulted in a film with a more spatially uniform In content.

5 Conclusion

Since the deposition method described herein is based on a photo-desorption reaction, it can be applied with other deposition techniques, such as MOCVD [1], molecular beam epitaxy [11] and pulsed-laser depositions [12], and can also be applied with other compound semiconductors such as InGaAs [13].

References

1. S. Nakamura, Science **281**, 956 (1998)
2. K.J. Vahala, Nature **424**, 839 (2003)
3. S. Nizamoglu, T. Ozel, E. Sari, H.V. Demir, Nanotechnology **18**, 065709 (2007)
4. T. Kawazoe, K. Kobayashi, S. Takubo, M. Ohtsu, J. Chem. Phys. **122**, 024715 (2005)
5. T. Yatsui, W. Nomura, M. Ohtsu, Nano Lett. **5**, 2548 (2005)
6. S. Yamazaki, T. Yatsui, M. Ohtsu, Appl. Phys. Exp. **1**, 061102 (2008)
7. H. Okabe, M.K. Emadi-Babaki, V.R. McCrary, J. Appl. Phys. **69**, 1730 (1991)
8. K. Watanabe, J. Chem. Phys. **22**, 1564 (1954)
9. M.D. McCluskey, C.G. Van de Walle, C.P. Master, L.T. Romano, N.M. Johnson, Appl. Phys. Lett. **72**, 2725 (1998)
10. A. Koukitu, H. Seki, Jpn. J. Appl. Phys. **35**, L1638 (1996)
11. R. Singh, D. Doppalapudi, T.D. Moustakas, L.T. Romano, Appl. Phys. Lett. **70**, 1089 (1997)
12. A. Kobayashi, J. Ohta, H. Fujioka, J. Appl. Phys. **99**, 123513 (2006)
13. K. Akahane, N. Ohtani, Y. Okada, M. Kawabe, J. Cryst. Growth **245**, 31 (2002)

Journal of Luminescence 129 (2009) 1912–1915

Contents lists available at ScienceDirect

Journal of Luminescence

journal homepage: www.elsevier.com/locate/jlumin

Observation of energy transfer between InAs quantum dots by pump-and-probe micro-photoluminescence measurement

K. Nishibayashi [a,*], T. Kawazoe [a], M. Ohtsu [a], K. Akahane [b], N. Yamamoto [b]

[a] Department of Electronics Engineering, University of Tokyo, 2-11-16, Yayoi, Bunkyo-ku, Tokyo 113-8656, Japan
[b] National Institute of Information and Communications Technology, Koganei, Tokyo 184-8795, Japan

ARTICLE INFO

Available online 21 May 2009

PACS:
78.55.−m
78.55.Cr
78.67.Hc

Keywords:
Quantum dot
Energy transfer
Pump-and-probe micro-photoluminescence
Nonlinear photoluminescence

ABSTRACT

Using pump-and-probe micro-photoluminescence measurement, we observed the nonlinear photoluminescence (PL) of multilayer InAs quantum dots (QDs), which originated from energy transfer between dots. In double- and five-layered InAs QDs, the differential PL intensity, $\Delta I/I_{probe}$, became negative at certain pump intensity. With changes in the pump intensity, $\Delta I/I_{probe}$ decreases or increases. This is explained by the generation of a non-radiative path and the saturation of non-radiative sites by the pump pulses. Our experimental results suggest that InAs QDs can act as AND- and NOT-gates by using suitable thresholds and control lights.

1. Introduction

To achieve high levels of integration, photonic devices must be reduced in size. However, this miniaturization is thought to be limited at the sub-micron level due to the light propagation diffraction limit. Nanophotonic switches [1], which use excitation energy transfer among optically coupled semiconductor quantum dots (QDs), have the potential to reduce the size of devices to less than 100 nm. Since excitation energy transfer occurs among QDs via an optical near-field interaction whose interaction length corresponds to the size of the QDs, the energy transfer length in a nanophotonic switch is on the order of several tens of nanometers [2,3]. So far, we have demonstrated nanophotonic AND- and NOT-gate operation using coupled CuCl quantum dots distributed randomly in a NaCl matrix [4,5]. However, randomness (size, position) makes it difficult to realize a nanophotonic device. In contrast, the fabrication process for self-assembled InAs QD systems allows the size and density of the QDs to be controlled, rendering InAs QD systems as one of the most promising materials for this application. In this letter, we describe our observations of the nonlinear photoluminescence (PL) of double- and five-layered InAs QDs, originating in the energy transfer which is the most important mechanism for nanophotonic device operation.

2. Experiment

The two samples used here were grown by molecular beam epitaxy in Stranski-Krastanov mode on (0 0 1)-oriented GaAs substrates. After growing a 155-nm-thick $Al_{0.5}Ga_{0.5}As$ barrier layer on a 150-nm-thick GaAs barrier layer, a five-monolayer InAs layer was deposited to fabricate the first QD layer. A 20.0-nm-thick $Al_{0.5}Ga_{0.5}As$ layer was then deposited on the QDs as a barrier layer. The second and fifth dot layers of the double- and five-layered QD sample were uncapped on the surface. The average diameter and height of the InAs QDs in both samples were estimated using atomic force microscopy to be 28 and 5 nm, respectively. The average QD density was 10^{11} cm^{-2}.

We carried out pump-and-probe micro-(μ-) PL measurements to confirm the difference in the PL intensity with and without the pump pulse laser. The sample was set in a microstat (Oxford Instruments) and kept at 10 K. A He–Ne laser (1.958 eV) generated excitons in the QDs (the probe beam). A picosecond mode-locked Ti:sapphire laser of 1.377 eV, E_{pump}, resonantly excited the QDs (the pump pulse) with various intensities from zero to the maximum in our experimental setup. An optical fiber guided two beams into a microscope focused on the sample through a $\times 50$ objective lens. The focal spot diameters were 6 and 3 μm for the double- and five-layered QD samples, respectively. A CCD camera (710M-T1FW; DVC Company) detected the two-dimensional PL images from the sample. A spectral filter dispersed the detection energy of the pump-and-probe measurements, E_{det}, in the range of 1.401–1.417 eV. The detection time for the PL image

* Corresponding author.
E-mail addresses: nishib@isl.titech.ac.jp, nishib@nanophotonics.t.u-tokyo.ac.jp (K. Nishibayashi).

0022-2313/$ - see front matter © 2009 Elsevier B.V. All rights reserved.
doi:10.1016/j.jlumin.2009.04.095

was 10 s. To confirm the nonlinear component of the PL operation of InAs QDs, we investigated the differential PL intensity $\Delta I/I_{\text{probe}}$, defined in the range of E_{det} as

$$\Delta I/I_{\text{probe}} = (I_{\text{pump \& probe}} - I_{\text{pump}} - I_{\text{probe}})/I_{\text{probe}}$$

where, $I_{\text{pump \& probe}}$, I_{pump} and I_{probe} are the integrated PL intensity in the focal spot with the pump-and-probe, pump, and probe laser, respectively.

3. Results and discussion

Fig. 1 shows the macro-PL spectrum of the double-layered QDs at 10 K. The PL peak of ~1.37 eV originated from the InAs QDs, and the GaAs buffer layer and/or the substrate contributed to the PL peak of 1.48 eV. To investigate the optical property of the individual QDs, we measured the PL spectra of single QDs by a near-field spectroscopy. A He–Ne laser (1.958 eV) was used as an excitation source. The aperture size of the near-field probe was 50 nm. The inset in Fig. 1 shows two typical near-field PL spectra of QDs obtained from different scanning areas. Regardless of density, we observed fewer PL lines from the single QDs in each scanning area. This resulted from the large distribution of non-radiative QDs (QDs-B) on the surface, as the near-field probe coupled to the surface (near) dots more than to the embedded (far) dots. The average linewidth of the near-field PL was in the range 1–2 meV. This value was larger than the typical value in the range 10–400 μeV as reported in Ref. [6]. This broad linewidth is attributed to the decoherence of excitons due to fluctuating charge distribution and defects on the surface and the fast relaxation of the excitons through coupling to non-radiative states on the surface. After reducing the number of QDs by processing the upper part of the sample to 200-nm-wide lines through a non-adiabatic photochemical process [7], we achieved a pump-and-probe μ-PL measurement at 10 K. Fig. 2 shows the pump intensity dependence of $\Delta I/I_{\text{probe}}$. Without mode-locked pump pulses, $\Delta I/I_{\text{probe}}$ was zero. When the pump pulse was injected, $\Delta I/I_{\text{probe}}$ became negative, with a minimum value of −0.04 at 10 μJ/cm^2. As the pump intensity increased, $\Delta I/I_{\text{probe}}$ returned to zero at 42 μJ/cm^2 and then became positive. Since E_{pump} was lower than E_{det}, one might expect the energy relaxation of the carriers from the energy state at E_{det} to that at E_{pump} to be restricted due to the filling effect by resonantly excited carriers of the energy state located at E_{pump}. However, such saturation would only increase $\Delta I/I_{\text{probe}}$.

Thus, we must use another mechanism to interpret the negative $\Delta I/I_{\text{probe}}$. We propose that the decreasing $\Delta I/I_{\text{probe}}$ originates from the generation of a non-radiative path of radiative QDs via resonant energy transfer to non-radiative QDs by the pump pulses [5].

Without the pump, the number of radiative QDs (QDs-A) and non-radiative QDs in the focal spot determines the μ-PL intensity of the QDs. QDs-B have an impurity state at the lower energy side of the exciton state that is coupled to the non-radiative site. With pump pulses (Fig. 1(a) inset), the resonantly excited carriers in this

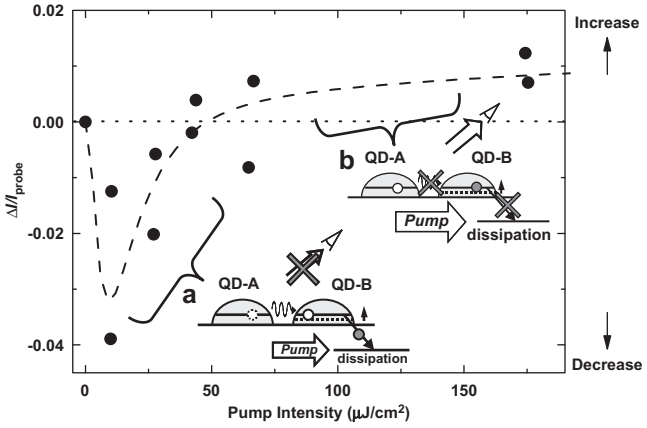

Fig. 2. Pump intensity dependence of the integrated differential PL intensities. Insets show a schematic explanation of the negative (a) and positive (b) differential PL intensity.

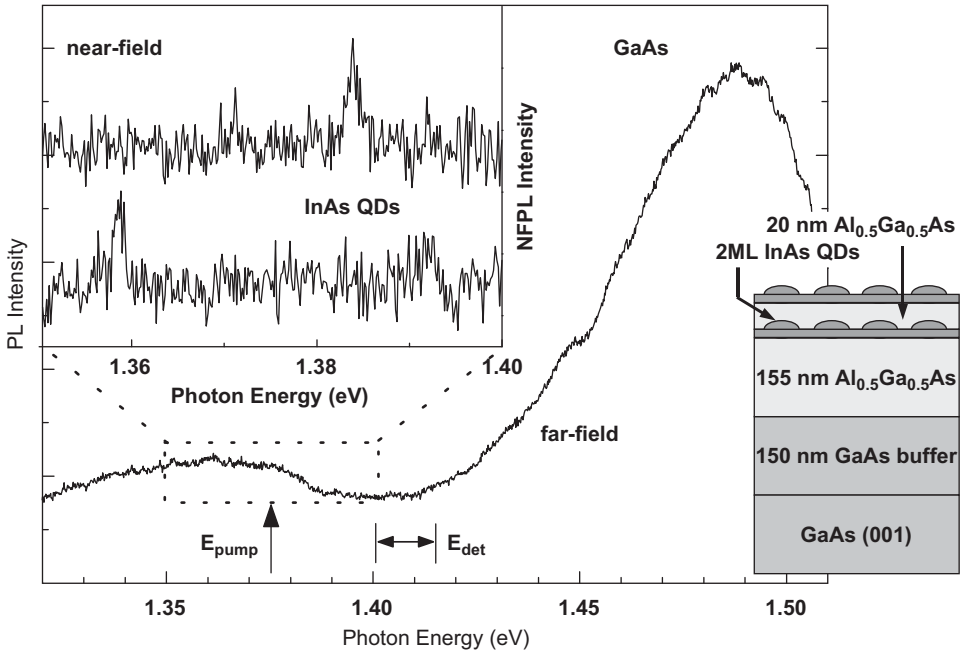

Fig. 1. (a) PL spectrum of the double-layered InAs QD sample. Insets show the schematic structure of the sample (right) and the two near-field PL spectra of the InAs QDs at 10 K (left).

impurity state cause an energy shift and broadening of the exciton state of QDs-B by electrostatic interaction. When the energy of the exciton state of QDs-B overlaps QDs-A through this energy modulation, resonant energy transfer occurs between them via an optical near-field interaction. As a result, the exciton energy of QDs-A dissipates, due to this energy transfer and to the non-radiative state in QDs-B. This causes the decrease of $\Delta I/I_{probe}$ in the observed area. At high pump intensity (Fig. 1(b) inset), the impurity state of QDs-B is saturated by resonantly excited carriers. This restricts the energy relaxation to the non-radiative state and increases $\Delta I/I_{probe}$.

We simulated the pump intensity dependence of $\Delta I/I_{probe}$ using a simple model. We assumed that QDs-A and QDs-B are non-resonant at an initial state with small energy differences. We used a log-normal distribution of the number of non-radiative paths of QDs-A due to resonant coupling with QDs-B, which was induced by the pump pulses, proportional to the negative $\Delta I/I_{probe}$. We also used the square root dependence of the pump intensity as the saturation effect of the non-radiative sites because these sites are considered to spread three dimensionally around QDs-B. In spite of the roughness of the model, the fitted result agrees well with our experimental results.

Next, we investigated the nonlinear PL of five-layered QDs. The sample was processed into square blocks using electron beam lithography to identify the observation area. Each block was $1.0\,\mu m \times 1.0\,\mu m$. Fig. 3 shows the macro-PL spectrum and the inset shows an image of the processed surface. The experimental setup was the same as for the μ-PL measurement of the double-layered QDs. The pump intensity dependence of $\Delta I/I_{probe}$ is shown in Fig. 4. Without pump pulses, $\Delta I/I_{probe}$ was zero. $\Delta I/I_{probe}$ increased at low pump intensity ($59\,\mu J/cm^2$). With increasing pump intensity, $\Delta I/I_{probe}$ decreased, down to a negative value at intermediate pump intensity ($285\,\mu J/cm^2$), then increased again up to a slightly positive value at high pump intensity ($660\,\mu J/cm^2$). The insets in Fig. 4 show two-dimensional images of the differential μ-PL. Ignoring the initial increase in $\Delta I/I_{probe}$ at low pump intensity, the dependence of $\Delta I/I_{probe}$ on the pump intensity exhibited the same behavior as displayed by the double-layered QD system. Thus, we consider that the same mechanism causes the pump intensity dependence of five-layered QDs. A fitting curve from the model that we applied to the double-layered QDs is also shown in Fig. 4 (solid line). These results indicate that the nonlinear component of μ-PL intensity of QDs is decided by competition between the generation of a non-radiative path and the saturation of non-radiative sites by pump pulses.

It is difficult to say whether lateral or transverse energy transfer contributes most to the nonlinear PL due to the high density of the QDs. In the lateral direction, the QDs are close to each other, permitting easy optical coupling. Additionally, the small PL intensities of the macro-spectra of the two samples indicate that the non-radiative sites also exist in the embedded dots. However, we recently observed the interlayer energy transfer between InAs QDs with a 24-nm-thick spacer layer and estimated transfer times to be as fast as 75 ps at 15 K [8]. Thus, the effective energy transfer in the transverse direction was not negligible in these two samples. Further investigation is necessary. Our results of nonlinear PL indicate that multilayer InAs QDs will act as AND- and NOT-gates with suitable thresholds and control lights.

4. Conclusions

We observed nonlinear PL of multilayer InAs QDs using pump-and-probe μ-PL measurement. The differential PL intensity decreased and increased with changes in pump intensity. This behavior is explained by the generation of a non-radiative path via energy transfer between the radiative and non-radiative QDs and the saturation of non-radiative sites. Our experimental results suggest that multilayer InAs QD systems will act as AND- and NOT-gates with suitable control lights.

This paper belongs to "Innovative Nanophotonics Components Development project" which OITDA contracted with The New

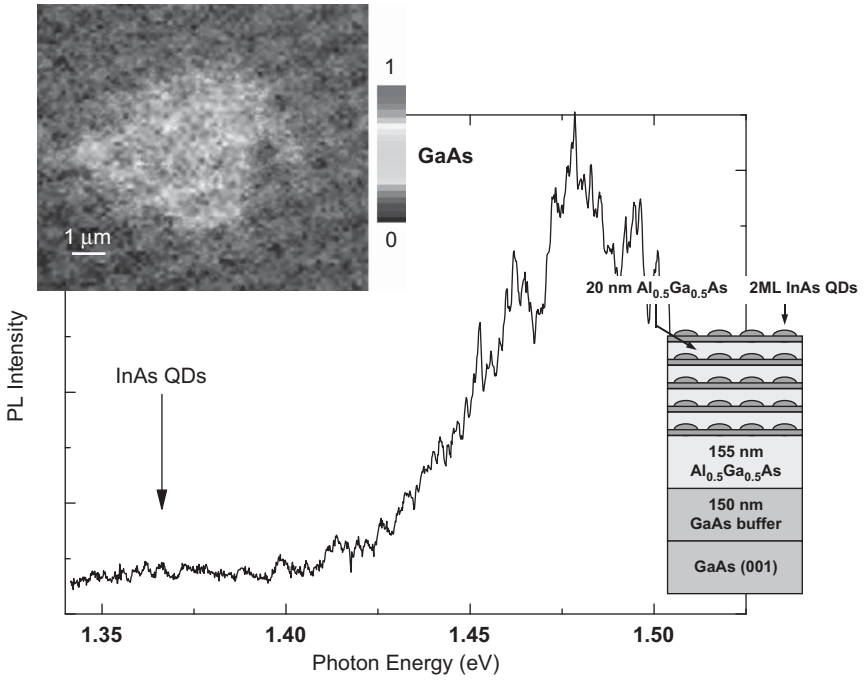

Fig. 3. PL spectrum of the five-layered InAs QD sample. Insets show the schematic structure of the sample (right) and a scanning electron microscopic image of the processed sample (left). The bright area indicates the focal spot of the probe beam.

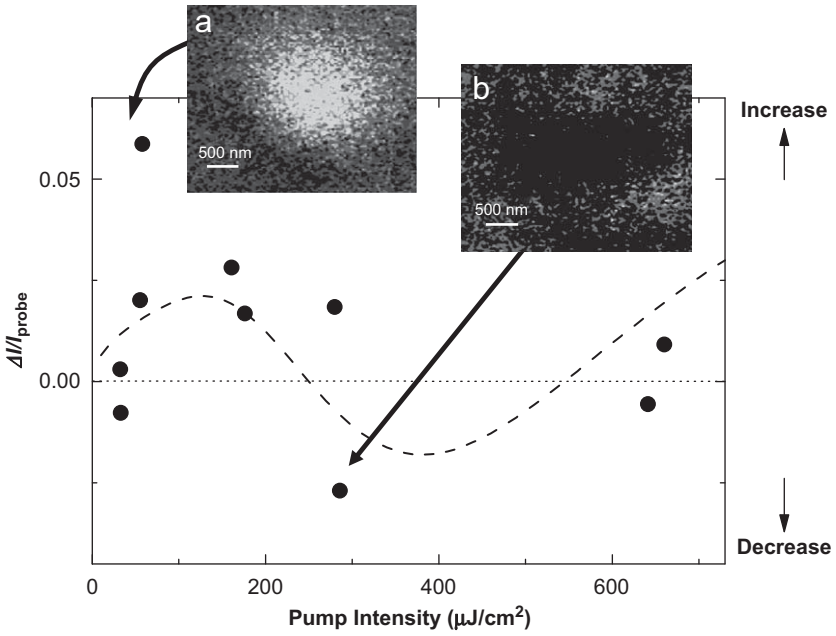

Fig. 4. Pump intensity dependence of the integrated differential PL intensity. Insets show a two-dimensional image of differential PL.

Energy and Industrial Technology Development Organization (NEDO) since 2006.

References

[1] M. Ohtsu, K. Kobayashi, T. Kawazoe, S. Sangu, T. Yatsui, IEEE J. Sel. Top Quantum Electron. 8 (2002) 839.
[2] S. Sangu, K. Kobayashi, A. Shojiguchi, M. Ohtsu, Phys. Rev. B 69 (2004) 115334.
[3] T. Kawazoe, K. Kobayashi, J. Lim, Y. Narita, M. Ohtsu, Phys. Rev. Lett. 88 (2002) 067404.
[4] T. Kawazoe, K. Kobayashi, S. Sangu, M. Ohtsu, Appl. Phys. Lett. 82 (2003) 2957.
[5] T. Kawazoe, K. Kobayashi, K. Akahane, M. Naruse, N. Yamamoto, M. Ohtsu, Appl. Phys. B 84 (2006) 243.
[6] I. Favero, G. Cassabois, R. Ferreira, D. Darson, C. Voisin, J. Tignon, C. Delalande, G. Bastard, Ph. Roussignol, J.M. Gérard, Phys. Rev. B 68 (2003) 233301.
[7] T. Kawazoe, K. Koabayashi, M. Ohtsu, Appl. Phys. B 84 (2006) 247.
[8] K. Nishibayashi, T. Kawazoe, K. Akahane, N. Yamamoto, M. Ohtsu, Appl. Phys. Lett. 93 (2008) 042101.

Visible Light Emission From Dye Molecular Grains via Infrared Excitation Based on the Nonadiabatic Transition Induced by the Optical Near Field

Tadashi Kawazoe, Hiroyasu Fujiwara, Kiyoshi Kobayashi, *Member, IEEE*, and Motoichi Ohtsu, *Senior Member, IEEE*

***Abstract*—We observed light emission in the visible wavelength range ($\lambda = 600$–690 nm) from aggregated 4-dicyanomethylene-2-methyl-6-*p*-dimethylaminostyryl-4H-pyran (DCM) dye molecule grains excited by infrared light ($\lambda_{ex} = 805$ nm). The domains of visible light emission were localized at the surface and edges of the dye grains, where the optical near field was strengthened. The emitted visible light intensity decayed exponentially according to the time constants $\tau_1 = 0.45$ ns and $\tau_2 = 1.37$ ns, which were equivalent to those of conventional fluorescence excited by visible light at $\lambda_{ex} = 402$ nm. The emitted light intensity increased with the infrared excitation intensity, in agreement with the theoretical results of the exciton–phonon polariton model. This confirmed that the visible light emission originated from the nonadiabatic transition process due to optical near-field features. The frequency upconversion efficiency for excitation from infrared ($\lambda_{ex} = 805$ nm) to visible ($\lambda = 600-690$ nm) in the film of the DCM molecular grains was experimentally estimated to be higher than that of the second harmonic generation (SHG) from a potassium dihydrogen phosphate (KDP) crystal. In particular, it was higher when the fundamental light power density was lower than 100 W/cm^2. Visible light emission from the grains of the rhodamine 6G (N-{2-[2-(2-aminoethoxy)ethoxy]ethyl} rhodamine 6G-amide bis[trifluoroacetate]) dye molecule was also observed in the infrared light ($\lambda_{ex} = 805$ nm). Our results demonstrated the universality of the nonadiabatic transition process.**

***Index Terms*—Nonadiabatic photochemical reaction, optical near field, upconversion.**

I. Introduction

FREQUENCY upconversion of infrared light is advantageous for many applications, such as expanding the effective bandwidth of photodetectors or imaging sensors. Although second harmonic generation (SHG) [1] and phosphorescence using a multistep transition [2] are popular alternatives, SHG requires a high-power and coherent incident light or an expensive built-up cavity for high efficiency. Phosphorescence suffers from problems with saturation of the emitted light intensity. To avoid saturation, an additional light source is required to excite the electrons into the optically forbidden triplet state, which is the first transition state for the phosphorescence. However, in this case, a problem occurs. A high-power reference light is required, from which additional light is usually emitted.

The frequency upconversion efficiency can be increased and the aforementioned problems avoided, if a novel, highly efficient process for excitation to the optically forbidden state is discovered. One possible approach is to utilize the molecular vibrational state. Transition from the lowest molecular vibrational state to higher ones of energy larger than a few hundred meV is usually optically forbidden for excitation by the propagating light due to the Hermitian nature of optically forbidden wave functions. However, the optical near-field (ONF) excitation can make this transition optically allowed due to the nonadiabatic response of the molecule. The nonadiabatic response and transition have been found in the photochemical reaction of organic molecules induced by the ONF [3]–[9]. They have been theoretically described by the exciton–phonon polariton (EPP) model, in which the ONF efficiently excites the optically forbidden molecular vibrational state with the help of the coherent phonon. Thus, even though the photon energy of the ONF is lower than the activation energy of the molecule, the electronic states of the molecule can be excited due to a multistep transition via the molecular vibrational state. Because this excitation can induce successive photodissociations or photochemical reactions, it has been applied to nanometric fabrication, e.g., ONF chemical vapor deposition [3]–[6], lithography [7], [8], and chemical polishing [9]. It is also applicable to the highly efficient frequency upconversion of infrared light because the ONF nonadiabatic transition can excite the optically forbidden state efficiently, and the molecule that is photoactivated by the ONF can relax electronically to the initial state by emitting a photon.

We demonstrated visible light emission from grains of 4-dicyanomethylene-2-methyl-6-*p*-dimethylaminostyryl-4H-pyran (DCM) and N-{2-[2-(2-aminoethoxy)ethoxy]ethyl} rhodamine 6G-amide bis(trifluoroacetate) (rhodamine 6G) dye molecules using infrared excitation due to the nonadiabatic ONF transition. We discuss possible applications for efficient frequency upconversion.

II. Nonadiabatic Transition Process

Fig. 1(a) shows the potential of an electron in a molecular orbital as a function of the internuclear distance of the relevant chemical bond [10]. The energy levels of the molecular vibrational states are indicated by the horizontal lines (*Vi*:$i = 0$, 1,

Manuscript received December 22, 2008; revised January 24, 2009. Current version published October 7, 2009.

T. Kawazoe, K. Kobayashi, and M. Ohtsu are with the Electrical Engineering and Information Systems, University of Tokyo, Tokyo 113-8656, Japan (e-mail: kawazoe@ee.t.u-tokyo.ac.jp; kkoba@nanophotonics.t.u-tokyo.ac.jp; ohtsu@ee.t.u-tokyo.ac.jp).

H. Fujiwara is with Central Research Laboratory, Hamamatsu Photonics KK, Hamakita, Hamamatsu, 434-8601, Japan (e-mail: fujiwara@crl.hpk.co.jp).

Digital Object Identifier 10.1109/JSTQE.2009.2014781

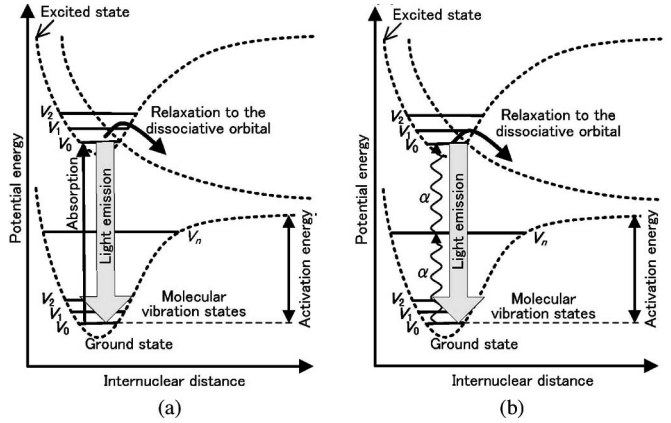

Fig. 1. Potential curves of an electron in a molecular orbital. The energy levels of the molecular vibrational states are indicated by the horizontal lines. (a) and (b) show schematics of the conventional adiabatic transition and novel nonadiabatic transition for the light emission, respectively.

. . . n) in each potential curve. When light is absorbed by the electron, the transition to the excited state (indicated by the upward arrow in Fig. 1[a]) triggers a photochemical reaction and light emission [2]. It is a conventional adiabatic transition that follows the Franck–Condon principle. When the ONF is involved, however, a multistep transition via the molecular vibrational states (indicated by the upward wavy arrows α in Fig. 1[b]) can also excite the electron, inducing a photochemical reaction [3]–[9] and light emission, even though the intermediate transition is optically forbidden. This is a novel nonadiabatic transition that deviates from the Franck–Condon principle. Thus, it allows infrared to be used as a light source because the energy of the transition between the molecular vibrational states (the wavy arrow α) is much lower than that of the electronic transition. This process has been described by the EPP model, in which the ONF is described as a quasiparticle, i.e., an exciton polariton trailing the coherent phonon [4], [5]. Thus, the ONF is able to couple the transition between the molecular vibrational states, even though it is optically forbidden. The name "nonadiabatic" is used because coupling between the electronic and nuclear systems is involved in the transition. The nonadiabatic transition can be used for frequency upconversion because the photon energy of the emitted light is higher than that of the excitation light. When DCM dye molecules are used, red light can be emitted via an infrared light for excitation.

III. Samples

We prepared three samples of the DCM molecules.

A. Sample 1

After the DCM molecules were dispersed in ethanol in a quartz glass cell, the ethanol was evaporated to deposit a film of aggregated DCM crystalline grains onto an inner wall of the glass cell of less than 100 μm thickness. A scanning electron microscope (SEM) image of sample 1 is shown in Fig. 2(a). The grains were inhomogeneous, with a size distribution in the range between 10 nm and several microns. The ONF was generated

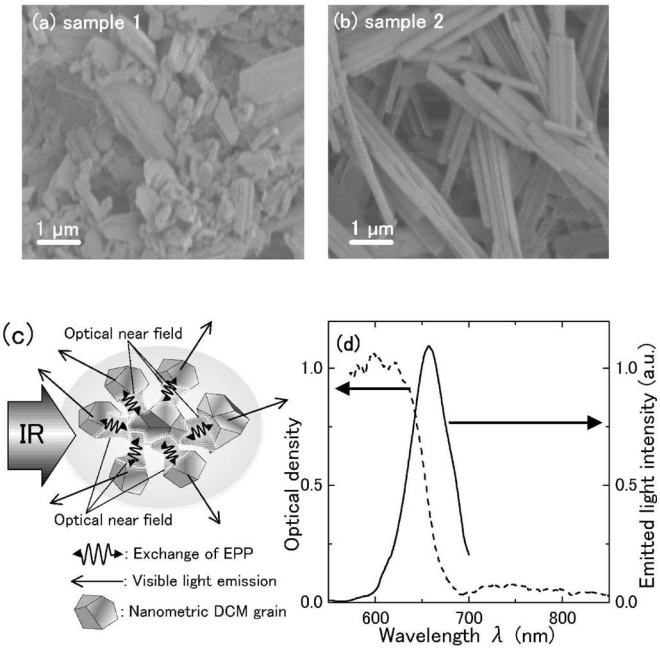

Fig. 2. SEM images of samples 1(a) and 2(b) using DCM molecules. (c) Schematic explanation of the generation of the optical near field and the exciton–phonon polariton. (d) Light emission (solid curves) and optical density (broken curves) spectra of sample 1 measured using the visible light ($\lambda_{\rm ex} = 532$ nm) for excitation.

on the surfaces of the DCM grains under irradiation by the excitation light and was enhanced on their sharp edges.

B. Sample 2

After the DCM molecules were dissolved in an acetone solvent, we grew recrystallized grains by dropping water into the solution [11]. The solvent (acetone and water) was evaporated to deposit a film of aggregated rod-shaped crystalline DCM molecules onto an inner wall of the glass cell of less than 100 μm thickness. The SEM images of sample 2 are shown in Fig. 2(b). The average diameter and length of the rods were 200 nm and 5 μm, respectively. The forms and sizes of the rods were more homogenous than those of the grains in sample 1. Furthermore, the volume density of the rods was lower than that of the grains. These comparisons confirmed that the number of sharp edges for enhancing the ONF intensity was larger in sample 1 than that in sample 2.

C. Sample 3

Sample 3 was a suspension of DCM molecular grains in ethanol.

Fig. 2(c) is a schematic of the ONF generation and nonadiabatic transition with successive visible light emission. When infrared light hit the aggregated grains, an ONF was generated on their surfaces and enhanced at their edges. ONF energy was exchanged between the neighboring grains via the EPPs, and the coherent phonon component of the EPP induced a transition via molecular vibrational states, as indicated by the wavy arrows α in Fig. 1(b). Finally, the electronic system was excited

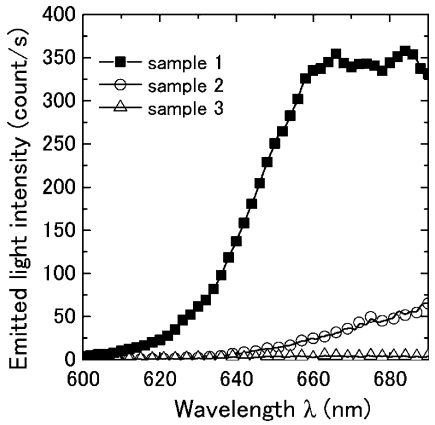

Fig. 3. Light emission spectra in the visible wavelength range ($\lambda = 600-690$ nm) from the three samples of DCM molecules. A CW Ti:sapphire laser was used as the infrared light source ($\lambda_{ex} = 805$ nm) for excitation. The excitation laser powers were 260 mW for samples 1 and 2, and 1 W for sample 3.

and visible light was emitted by the electronic transition (downward arrow in Fig. 1[b]). Sample 1 was the most appropriate for inducing the nonadiabatic transition because the size (volume density) of the grains was much smaller (higher) there than in the other samples.

The solid and broken curves in Fig. 2(d) represent the spectra of the light emitted from sample 1 and its optical density measured using a propagating light ($\lambda_{ex} = 532$ nm) as an excitation source. For wavelength $\lambda > 660$ nm, the optical density was sufficiently low, which came only from scattering by the aggregated DCM grains. Thus, the absorption was negligible. The spectral peak of the emitted light appeared at $\lambda = 655$ nm, which corresponded to that of the conventional fluorescence spectrum. These curve features confirmed that degradation of the DCM dye molecules due to impurities or molecular dissociation was avoided and the optical properties of the DCM molecules were maintained sufficiently even after sample preparation.

IV. Experimental Results and Discussion

Fig. 3 shows the light emission spectra from the three samples using a continuous wave (CW) Ti:sapphire laser as the infrared light source for the excitation ($\lambda_{ex} = 805$ nm). The excitation laser powers were 260 mW for samples 1 and 2, and 1 W for sample 3. Samples 1 and 2 emitted visible light in the 600–690 nm range, even by infrared light excitation. Although the light emission extended to wavelengths longer than 690 nm, our spectral measurements were limited to wavelengths below this value to avoid artifact signals caused by the excitation laser scattering. We confirmed that the visible light emission was not due to the second harmonic (SH) nonlinearity of the DCM molecules because SH light ($\lambda_{SH} = 403$ nm) could not be observed even using highly sensitive photomultipliers (H7421-40 and R3809U-52: Hamamatsu Photonics KK). The light intensity emitted from sample 1 was approximately ten times higher than that from sample 2, and visible light emission from sample 3 could not be observed. The buoyant density of the DCM grain in sample 3 was too low to couple the grains via ONF,

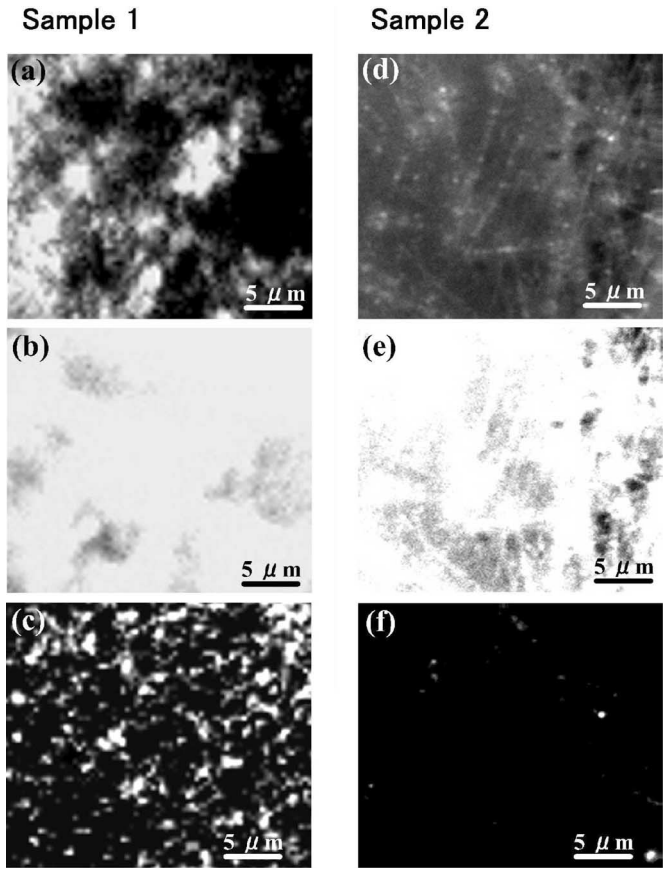

Fig. 4. (a) Optical morphology of sample 1. (b) Distribution of light intensity ($\lambda = 650$ nm) emitted from sample 1 using a blue light source ($\lambda_{ex} = 402$ nm) for excitation. (c) Emitted light ($\lambda = 650$ nm) distribution of sample 1 using an infrared light source ($\lambda_{ex} = 805$ nm) for excitation. (d) Optical morphology of sample 2. (e) Distribution of light intensity ($\lambda = 650$ nm) emitted from sample 2 using a blue light source ($\lambda_{ex} = 402$ nm) for excitation. (f) Emitted light ($\lambda = 650$ nm) distribution of sample 2 using an infrared light source ($\lambda_{ex} = 805$ nm) for excitation.

as shown in Fig. 2(c). These results strongly suggested that the origin of the visible light emission from samples 1 and 2 was the nonadiabatic transition process described in Section III.

In the nonadiabatic transition process, the area of visible light emission must be localized on the surfaces of DCM molecular grains and its intensity should be high at their edges. To confirm spatially localized visible light emission, we observed its two-dimensional distribution using an optical microscope with spatial resolution of 1 μm. Fig. 4(a) shows the morphology of sample 1 imaged by white light, which was not clearly resolved due to the low spatial resolution of the microscope. Fig. 4(b) shows the conventional fluorescence intensity distribution ($\lambda = 650$ nm) observed using a blue light source ($\lambda_{ex} = 402$ nm) for the excitation. It indicates that almost all of the DCM grains fluoresced, and thus, the whole area of the image was homogenously bright. Fig. 4(c) shows the intensity distribution of the visible light emission ($\lambda = 650$ nm) observed using an infrared light source ($\lambda_{ex} = 805$ nm) for excitation. Numerous small bright spots on a dark background are visible, even though the sample was homogeneously illuminated by the infrared light.

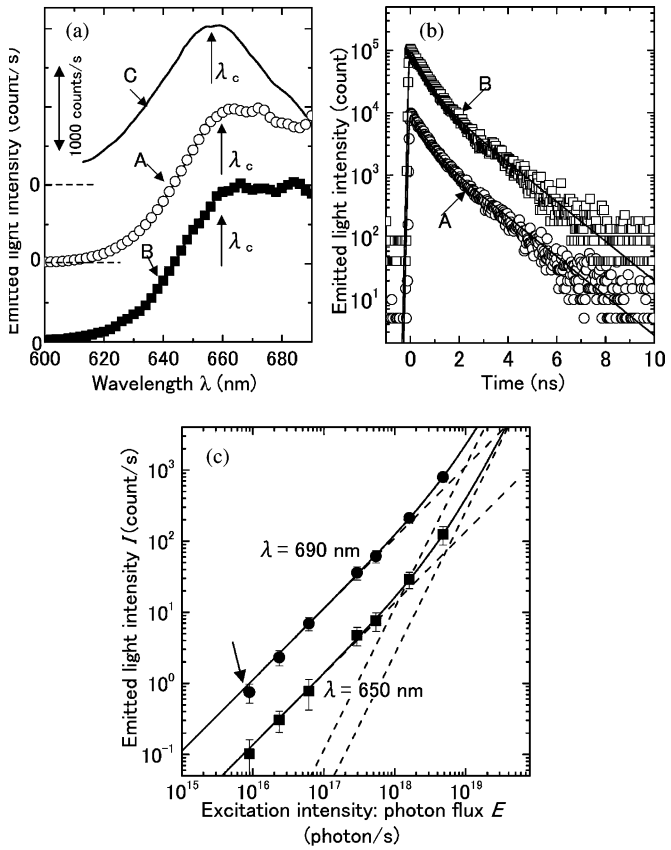

Fig. 5. (a) Spectra of light intensity emitted from sample 1. Curves A and B correspond to the spectra of light emitted using infrared light of wavelength $\lambda_{\rm ex} = 753$ and 805 nm, respectively, for the excitations. Curve C shows the conventional fluorescence spectra emitted using visible light of $\lambda_{\rm ex} = 402$ nm for excitation. (b) Open circles and squares indicate the time evolution of emitted light measured by the infrared ($\lambda_{\rm ex} = 805$ nm) and visible ($\lambda_{\rm ex} = 402$ nm) excitation light from a mode-locked Ti:sapphire laser and its SH, respectively. The solid curves A and B show the fitted results. (c) Dependence of the emitted light intensities I at $\lambda = 650$ nm (closed squares) and 690 nm (closed circles) on the excitation intensity E of the infrared light ($\lambda_{\rm ex} = 805$ nm). The solid curves were fitted by the second-order function $I = a_\lambda E + b_\lambda E^2$.

Fig. 4(d)–(f) shows images of sample 2, corresponding to Fig. 4(a)–(c), respectively. The morphology of the crystalline rod could barely be seen (Fig. 4[d]). In the case of $\lambda_{\rm ex} = 402$ nm excitation (Fig. 4[e]), the spatial distribution of the fluorescence intensity was strongly correlated with that of Fig. 4(d). However, in the case of $\lambda_{\rm ex} = 805$ nm excitation (Fig. 4[f]), only a few bright spots are visible. Comparing the detailed morphology of samples 1 (Fig. 2[a]) and 2 (Fig. 2[b]) obtained by SEM measurements, assuming that the visible light was emitted from the surfaces of the DCM molecular grains is reasonable, especially since intensity is highest at their edges. This was because sample 1 had more edges than sample 2. These experimental results support the hypothesis that the origin of the visible light emission was the nonadiabatic transition process.

From here, we focus on sample 1 because of its high intensity of emitted visible light. Curves A and B in Fig. 5(a) show the spectra of the light emitted from sample 1 using the infrared light of wavelength $\lambda_{\rm ex} = 753$ and 805 nm, respectively, for excitation. As a reference, curve C shows the conventional fluorescence spectrum emitted using the SH of a mode-locked Ti:sapphire laser ($\lambda_{\rm ex} = 402$ nm) for excitation. The spectral profiles of curves A and B agreed closely with each other, confirming that artifacts due to the excitation laser were avoided in these measurements. The spectral peaks of curves A and B were redshifted from those of curve C. In other words, curves A and B had a short-wavelength cutoff of $\lambda_c = 660$ nm, which was approximately 5 nm longer than that of curve C. This difference came from the reabsorption of the emitted light: infrared light was absorbed by the whole DCM grains deposited on the inner wall of the glass cell. This was due to the low optical density of the DCM grains, as shown in Fig. 2(d). Thus, the reabsorption of the emitted light of curves A and B occurred selectively for $\lambda < 660$ nm. In the case of curve C, however, the visible light for excitation was absorbed only at the surface of the aggregated DCM grains due to its high optical density.

We measured the decay times of the emitted light intensity to identify the origin of the emission process. In Fig. 5(b), the open circles and squares show the experimental results under excitation by infrared and visible light of wavelength $\lambda_{\rm ex} = 805$ and 402 nm using a mode-locked Ti:sapphire laser and its SH, respectively. In both cases, the experimental values were fitted by two exponential decay components with time constants of $\tau_1 = 0.45$ ns and $\tau_2 = 1.37$ ns, as shown by curves A and B in Fig. 5(b). This confirmed that the emitted light originated from the electronic transition from the first excited state to the ground state [12], [13].

Fig. 5(c) shows the dependence of the emitted light intensities I at $\lambda = 650$ nm (closed squares) and 690 nm (closed circles) on the excitation intensity E of the infrared light ($\lambda_{\rm ex} = 805$ nm). They were least-square fitted by the second-order function $I = a_\lambda E + b_\lambda E^2$. The values (a_λ, b_λ) for the fitting and the variance with the weight factor $\delta_\lambda^2 / I_\lambda(E)$, obtained by the nonlinear Levenberg–Marquardt method [14], were $a_{650\ \rm nm} = (1.37 \pm 0.33) \times 10^{-17}$, $b_{650\ \rm nm} = (2.61 \pm 0.92) \times 10^{-36}$ and $\delta^2_{650\ \rm nm}/I_{650\ \rm nm}(E) = 0.0238$ for $\lambda = 650$ nm and $a_{690\ \rm nm} = (1.12 \pm 0.09) \times 10^{-16}$, $b_{690\ \rm nm} = (1.17 \pm 0.25) \times 10^{-35}$ $\delta^2_{690\ \rm nm}/I_{690\ \rm nm}(E) = 0.0814$ for $\lambda = 690$ nm. The results are shown by the solid curves in Fig. 5(c).

The nonadiabatic transition can explain the origin of the visible light emission by infrared-light excitation ($\lambda_{\rm ex} = 805$ nm) and its excitation intensity dependence, which is shown in Fig. 5(c). It can be explained by a two-step transition, as shown in Fig. 6, where, $|E_\alpha; el\rangle$and $|E_\beta; vib\rangle$represent molecular electronic and vibrational (phonon) states, respectively. In addition, $E_\alpha (\alpha = g, ex)$ and $E_{\beta;} (\beta = i, a, b, c, em)$ represent the molecular electronic and vibrational energies, respectively.

1) The first-step transition: After the excitation light generates an ONF at the surfaces of DCM grains (see Fig. 2[c]), the ONF induces a transition from $|E_g; el\rangle \otimes |E_i; vib\rangle$to $|E_g; el\rangle \otimes |E_a; vib\rangle$ coherently, due to a nonadiabatic transition (see the wavy arrow in Fig. 6).
2) The second-step transition: After the first step, the excited coherent phonon, described by the EPP model, relaxes to the lower phonon energy levels that are equivalent in the phonon energy distribution to the molecular

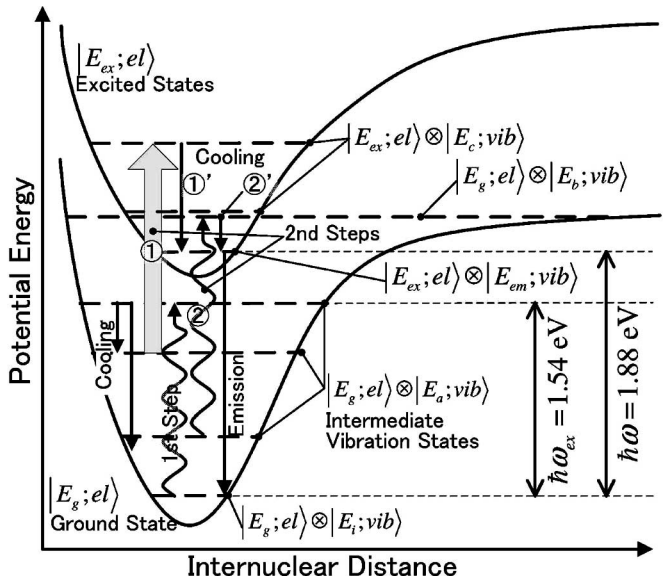

Fig. 6. Schematic explanation of the origin of the visible light emission by a two-step transition based on the nonadiabatic transition and EPP model.

temperature due to cooling, as shown by the downward arrows in Fig. 6. This relaxation rate (the cooling rate) is about 100 meV/ps, which has been experimentally confirmed [15]. If the energy of the redistributed phonon $|E_g; el\rangle \otimes |E_a; vib\rangle$ exceeds the energy difference of 0.34 eV between the electronic excited state in a molecule ($\hbar\omega = 1.88$ eV; $\lambda = 660$ nm) and the photon energy of the excitation light ($\hbar\omega = 1.54$ eV; $\lambda_{\rm ex} = 805$ nm), the transition occurs via two possible routes. One route is from $|E_g; el\rangle \otimes |E_a; vib\rangle$ to $|E_{\rm ex}; el\rangle \otimes |E_c; vib\rangle$ (as shown by the thick arrow ① in Fig. 6) due to the conventional photo-excited process. The other is from $|E_g; el\rangle \otimes |E_a; vib\rangle$ to $|E_g; el\rangle \otimes |E_b; vib\rangle$,which is of higher energy than $|E_{\rm ex}; el\rangle \otimes |E_{\rm em}; vib\rangle$ (as shown by the wavy arrow ② in Fig. 6). After the transition ① or ②, both$|E_{\rm ex}; el\rangle \otimes |E_c; vib\rangle$ and $|E_g; el\rangle \otimes |E_b; vib\rangle$ relax to $|E_{\rm ex}; el\rangle \otimes |E_{\rm em}; vib\rangle$ due to cooling or the coupling of the degenerated phonon and electronic states [16], [17], respectively (as shown by the respective downward arrows ①' and ②' in Fig. 6).

After the two-step transitions described before, visible light is emitted due to the transition from $|E_{\rm ex}; el\rangle \otimes |E_{\rm em}; vib\rangle$to $|E_g; el\rangle \otimes |E_i; vib\rangle$. Since the transition ① in the second step transition 2) is a conventional adiabatic transition, its probability is more than 10^6 times that of the first-step transition [4], [5]. Furthermore, the probability of visible light emission by infrared excitation is governed only by the nonadiabatic transition of the first step, because the second-step transition easily saturates. This is the origin of the linear intensity dependence ($I \propto E$) seen in Fig. 5(c). Because the transition ② in the second step transition 2) is nonadiabatic, its probability of occurrence is equal to that of the first step transition 1). This is origin of the squared dependence ($I \propto E^2$) seen in Fig. 5(c). The nonadiabatic transition is not a thermal effect because the aforementioned energy difference (0.34 eV) corresponds to temperatures as high as 4000 K.

According to the EPP model [4], [5] of the nonadiabatic transition process, the ratio between the expansion coefficients a_λ and b_λ is given by

$$\frac{b_\lambda}{a_\lambda} = \frac{\hbar}{2\pi} \frac{a_{\lambda 0}}{|\gamma_m|^2 E_{\lambda 0}} \left(\frac{v_p'^2}{u_p'^2}\right) \left(\frac{\mu^{\rm el}}{\mu^{\rm nucl}}\right)^2. \quad (1)$$

For sample 1, this ratio was calculated to be $\simeq 10^{-19}$. Here, we used the experimental values of $a_{690\ {\rm nm}0} E_{690\ {\rm nm}0} = 0.75$ counts/s and $E_{690\ {\rm nm}0} = 8.9 \times 10^{15}$ photons/s, as shown by an arrow in Fig. 5(c). Reasonable values of $\mu^{\rm nucl} = 1$ Debye, $\mu^{\rm el} = 10^{-3}$ Debye (the electronic and vibrational dipole moments), $\gamma_m = 10^{-1}$ eV (the linewidth of the vibrational and electronic states), $v'_{p^2}/u'_{p^2} = 0.01$ (the ratio between transformations of phonon and EPP), and $d = 30$ nm (the expected mean edge radius of DCM grains contributing to the nonadiabatic transition) were also used for this estimation. However, the values of the ratio for $\lambda = 650$ and 690 nm were found to be $b_{650\ {\rm nm}}/a_{650\ {\rm nm}} \simeq b_{690\ {\rm nm}}/a_{690\ {\rm nm}} \simeq 10^{-19}$ from the fitted curves in Fig. 5(c). They agreed closely with the theoretical estimated value given before. This agreement indicated that the EPP model and the nonadiabatic transition were able to describe the visible light emission by the infrared excitation.

The inset of Fig. 7(a) shows an image of the DCM grains in sample 1 in the glass cell under infrared excitation ($\lambda_{\rm ex} = 805$ nm) taken by a CCD camera though a bandpass filter for visible light. The excitation beam diameter was 2 mm, represented by a white circle in this figure. The bright spot at the center of this circle represents the beam spot of visible light emitted from the DCM grains. This visible emission intensity was used to estimate the frequency upconversion efficiency C of the 100-μm-thick film of the aggregated DCM grains from infrared ($\lambda_{\rm ex} = 805$ nm) to visible light (λ = 600–690 nm). The closed squares and solid curve in Fig. 7(a) represent the experimental and least-square-fitted results based on (1). The least-square fitted results were represented by $C_{\rm DMC} = (2.77 \pm 0.22) \times 10^{-11} + (2.03 \pm 0.43) \times 10^{-13} \times P$, where the error range was obtained from the nonlinear Levenberg–Marquardt method [14] with 0.95 accuracy. For comparison, the broken line represents the theoretical efficiency C of the SHG (λ = 403 nm) emitted from a 100-μm-thick potassium dihydrogen phosphate (KDP) crystal [1], given by $C_{\rm KDP} = 1.50 \times 10^{-13} \times P$, where P is the power density (W/cm^2) of the fundamental light ($\lambda_{\rm ex} = 805$ nm). Comparison of $C_{\rm DCM}$ and $C_{\rm KDP}$ shows that the efficiency of the present light emission was higher than that of the SHG over the entire range of excitation intensity in Fig. 7(a). Furthermore, because $C_{\rm DCM}$ was much higher than $C_{\rm KDP}$ for fundamental power densities lower than 100 W/cm^2 due to the contribution of the constant term in $C_{\rm DCM}$, an application to practical frequency upconversion devices for low incident light power is anticipated.

Finally, to confirm the universality of the new visible emission process, we prepared a sample using rhodamine 6G molecules in the same way as sample 1 to measure the visible light emission caused by infrared excitation ($\lambda_{\rm ex} = 805$ nm). As a result, the sample of rhodamine 6G also emitted visible light with λ = 600 and 680 nm, as shown in Fig. 7(b). Hence the universality of

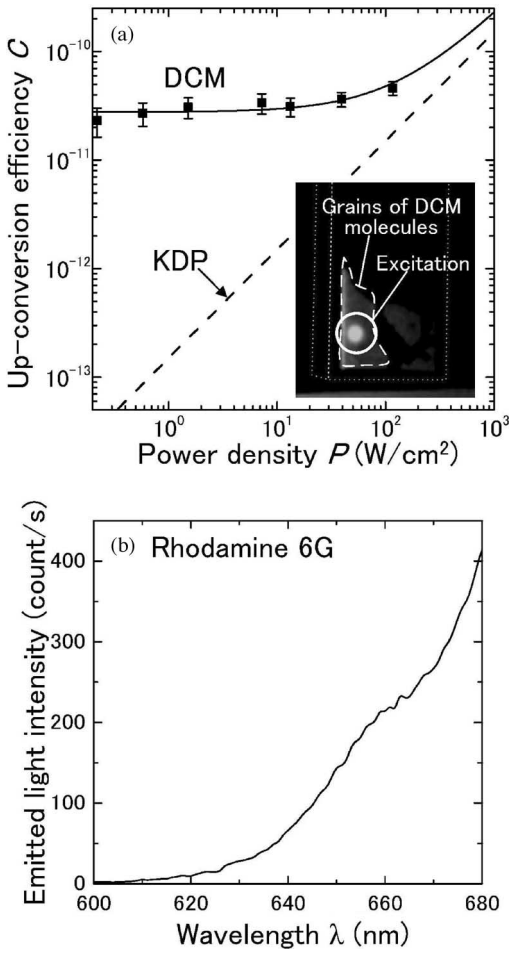

Fig. 7. (a) Comparison of the frequency upconversion efficiencies from infrared to visible light between sample 1 and a KDP crystal. The closed squares indicate the experimental results, and the solid curve shows the fitted result. The broken line denotes the SHG conversion efficiency calculated for a 100-μm-thick KDP crystal. (b) Spectrum of the visible light emission from the grains of rhodamine 6G between 600 and 680 nm observed by the infrared excitation ($\lambda_{ex} = 805$ nm).

the visible light emission process was confirmed. Detailed experimental results for the rhodamine 6G sample will be reported elsewhere.

V. Conclusions

We demonstrated visible light emission by infrared light excitation ($\lambda_{ex} = 805$ nm) from DCM grains in the 600–690 nm wavelength range and from rhodamine 6G grains in the 600–680 nm range. The origin of this emission and dependence of the emitted light intensity on the excitation light intensity were attributable to a nonadiabatic transition by the ONF, which was generated on the surface of the dye molecular grains. The dependence on the excitation intensity agreed closely with a theoretical estimation using an EPP model. The frequency upconversion efficiency of the present light emission was higher than that of the SHG from a KDP crystal. Such a high efficiency is applicable to devices such as sensitive infrared photodetectors and highly efficient illuminating sources.

References

[1] A. Yariv, "Second-harmonics generation and parametric oscillation," in *Introduction to Optical Electronics*, 1st ed. New York, Holt: Rinehert and Winston, 1985, ch. 8, pp. 177–221.

[2] P. W. Atkins, "Spectroscopy 2: Electronic transitions," in *Physical Chemistry*, 6th ed. Oxford, U.K.: Oxford Univ. Press, 1998, ch. 17, pp. 497–526.

[3] T. Kawazoe, Y. Yamamoto, and M. Ohtsu, "Fabrication of a nanometric Zn dot by nonresonant near-field optical chemical-vapor deposition," *Appl. Phys. Lett.*, vol. 79, no. 8, pp. 1184–1186, Aug. 2001.

[4] T. Kawazoe, K. Kobayashi, S. Takubo, and M. Ohtsu, "Nonadiabatic photodissociation process using an optical near field," *J. Chem. Phys.*, vol. 122, no. 2, pp. 024715-1–024715-5, Jan. 2005.

[5] M. Ohtsu, K. Kobayashi, T. Kawazoe, T. Yatsui, and M. Naruse, "Principle of nanofabrication using optical near field," in *Principle of Nanophotonics*, E. R. Pike and R. G. W. Brown, Series, Eds Boca Raton, FL/London/New York: CRC Press, Taylor & Francis, 2008, ch. 2, pp. 19–107.

[6] T. Kawazoe, K. Kobayashi, and M. Ohtsu, "Near-field optical chemical vapor deposition using $Zn(acac)_2$ with a non-adiabatic photochemical process," *Appl. Phys. B: Lasers Opt.*, vol. 84, no. 1–2, pp. 247–251, Jul. 2006.

[7] H. Yonemitsu, T. Kawazoe, K. Kobayashi, and M. Ohtsu, "Nonadiabatic photochemical reaction and application to photolithography," *J. Lumin.*, vol. 122–123, pp. 230–233, Jan.–Apr. 2007.

[8] T. Kawazoe, M. Ohtsu, Y. Inao, and R. Kuroda, "Exposure dependence of the developed depth in nonadiabatic photolithography using visible optical near fields," *J. Nanophoton.*, vol. 1, no. 1, pp. 011595-1–011595-9, Dec. 2007.

[9] T. Yatsui, K. Hirata, W. Nomura, M. Ohtsu, and Y. Tabata, "Realization of an ultra-flat silica surface with angstrom-scale average roughness using nonadiabatic optical near-field etching," *Appl. Phys. B: Lasers Opt.*, vol. 93, no. 1, pp. 55–57, Oct. 2008.

[10] R. L. Jackson, "Vibrational energy of the monoalkyl zinc product formed in the photodissociation of dimethyl zinc, diethyl zinc, and dipropyl zinc," *J. Chem. Phys.*, vol. 96, no. 8, pp. 5938–5951, Apr. 1992.

[11] F.-M. Lee, C. E. Stoops, and L. E. Lahti, "An investigation of nucleation and crystal growth mechanism of urea from water–alcohol solutions," *J. Cryst. Growth*, vol. 32, no. 3, pp. 363–370, Mar. 1976.

[12] W. Cao, P. Palffy-Muhoray, B. Taheri, A. Marino, and G. Abbate, "Lasing thresholds of cholesteric liquid crystals lasers," *Mol. Cryst. Liq. Cryst.*, vol. 429, pp. 101–110, May 2005.

[13] S. K. Pal, D. Sukul, D. Mandal, S. Sen, and K. Bhattacharyya, "Solvation dynamics of DCM in micelles," *Chem. Phys. Lett.*, vol. 327, no. 1–2, pp. 91–95, Sep. 2000.

[14] D. W. Marquardt, "An algorithm for least-squares estimation of nonlinear parameters," *J. Soc.*, vol. 11, no. 2, pp. 431–441, Jun. 1963.

[15] F. Laermer, T. Elsaesser, and W. Kaiser, "Ultrashort vibronic and thermal relaxation of dye molecules after femtosecond ultraviolet excitation," *Chem. Phys. Lett.*, vol. 156, no. 4, pp. 381–386, Apr. 1989.

[16] H. Sumi, "Dynamic defect reactions induced by multiphonon nonradiative recombination of injected carriers at deep levels in semiconductors," *Phys. Rev. B*, vol. 29, no. 8, pp. 4616–4630, Apr. 1984.

[17] M. S. Miao, S. Limpijumnong, and W. R. L. Lambrecht, "Stacking fault band structure in 4H-SiC and its impact on electronic devices," *Appl. Phys. Lett.*, vol. 79, no. 26, pp. 4360–4362, Dec. 2001.

Tadashi Kawazoe was born in Kochi, Japan, on April 5, 1967. He received the B.E., M.E., and Ph.D. degrees in physics from the University of Tsukuba, Tsukuba, Japan, in 1990, 1993, and 1996, respectively.

He has studied optical nonlinearities in semiconductor quantum dots at the Institute of Physics, University of Tsukuba. In 1996, he joined the Faculty of Engineering, Yamagata University, Japan, as a Research Associate, where he was engaged in research on nonlinear optical materials and devices. He was with Japan Science and Technology Corporation, Japan, in 2000. Since 2000, he has studied optical devices and fabrication based on an optical near-field interaction. In 2007, he joined the University of Tokyo as a projected Associated Professor. His current research interests include the nanophotonic devices.

Dr. Kawazoe is a member of the Japan Society of Applied Physics and the Physical Society of Japan.

Hiroyasu Fujiwara received the B.S. and M.S. degrees from the Department of Physics, Nagoya University, Nagoya, Japan, in 1995 and 1997, respectively.

He joined Hamamatsu Photonics KK, Shizuoka, Japan, in April 1997, where he is engaged in the research and development of nanophotonic devices as well as high-power industrial lasers.

Mr. Fujiwara is a member of the Physical Society of Japan and the Japan Society of Applied Physics.

Kiyoshi Kobayashi (M'94) was born in Okayama, Japan, on November 25, 1953. He received the D.S. degree in physics from the University of Tsukuba, Tsukuba, Japan, in 1982.

After receiving the degree, he joined IBM Japan as a Researcher at Tokyo Research Laboratory, Tokyo, Japan. In 1998, he became a Theoretical Group Leader of the "Localized Photon" project for Exploratory Research for Advanced Technology (ERATO) at the Japan Science and Technology Agency (JST). In 2004, he became a Professor with the 21st Century Center of Excellence Program, Nanometer-Scale Quantum Physics, Department of Physics, Tokyo Institute of Technology, Tokyo. He joined Nanophotonics Group at the University of Tokyo in 2008, and became a Professor at the University of Yamanashi in 2009. His current research interests include quantum optical near-field theory and its application to nano/atom photonics.

Prof. Kobayashi is a Member of the Japan Society of Applied Physics, the Physical Society of Japan, the American Physical Society, and the Optical Society of Japan.

Motoichi Ohtsu (M'88–SM'90) received the B.E., M.Eng., and Dr. Eng. degrees in electronics engineering from the Tokyo Institute of Technology, Tokyo, Japan, in 1973, 1975, and 1978, respectively.

In 1978, he was appointed a Research Associate, and in 1982, he became an Associate Professor at the Tokyo Institute of Technology. From 1986 to 1987, while on leave from the Tokyo Institute of Technology, he joined the Crawford Hill Laboratory, AT&T Bell Laboratories, Holmdel, NJ. In 1991, he became a Professor at the Tokyo Institute of Technology. In 2004, he moved to the University of Tokyo as a Professor. He has been the leader of the "Photon Control" project (1993–1998: the Kanagawa Academy of Science and Technology, Kanagawa, Japan), the "Localized Photon" project (1998–2003: Exploratory Research for Advanced Technology Organization [ERATO], Japan Science and Technology Corporation [JST], Japan), "Terabyte Optical Storage Technology" project (2002–2006: New Energy and Industrial Technology Development Organization [NEDO], Japan), and "Near-field optical lithography system" project (2004–2006: Ministry of Education, Japan). He is concurrently the leader of the "Nanophotonics" team (2003–present: Solution Oriented Research for Science and Technology [SORST], JST, Japan), "Innovative Nanophotonics Components Development" project (2006–present: NEDO, Japan), and "Nanophotonics Total Expansion: Industry–University Cooperation and Human Resource Development" project (2006–present: NEDO, Japan). He has written 426 papers and holds 87 patents. He is the author, coauthor, or editor of 51 books, including 22 in English, titled *Near-Field Nano/Atom Optics and Technology* (Springer Verlag, 1998), *Near-Field Nano-Optics* (Kluwer Academic/Plenum Publishers, 1999), *Progress in Nano Electro-Optics I–V* (Springer Verlag, 2002–present), *Optical Near Fields* (Springer Verlag, 2004), *Principles of Nanophotonics* (Taylor & Francis, 2008), etc. His current research interests include the nanophotonics and atom photonics.

Prof. Ohtsu is a Fellow of the Optical Society of America, a Fellow of the Japan Society of Applied Physics, a Senior Member of IEEE, a Member of the Institute of Electronics, Information and Communication Engineering of Japan, and a Member of the American Physical Society. He is also a Tandem Member of the Science Council of Japan. In 1999, he was the Vice President of the IEEE/LEOS Japan Chapter, and in 2000, he was appointed as the President. Since 2000, he is an Executive Director of the Japan Society of Applied Physics. He served as a Technical Program Cochair for the 4th Pacific Rim Conference on Lasers and Electro-Optics(CLEO/PR01), 2001. He has been a Tutorial Lecturer of the Society of Photo-Optical Instrumentation Engineers (SPIE) and the Optical Society of America (OSA). He has been awarded 14 prizes from academic institutions, including the Issac Koga Gold Medal of URSI in 1984, the Japan IBM Science Award in 1988, two awards from the Japan Society of Applied Physics in 1982 and 1990, the Inoue Science Foundation Award in 1999, the Japan Royal Medal with a Purple Ribbon from the Japanese Government in 2004, H. Inoue Award from JST in 2005, and the Distinguished Achievement Award from the Institute of Electronics, Information and Communication Engineering of Japan in 2007.

Optimal mixture of randomly dispersed quantum dots for optical excitation transfer via optical near-field interactions

Makoto Naruse,[1,2] Tadashi Kawazoe,[2] Ryuichi Ohta,[2] Wataru Nomura,[2] and Motoichi Ohtsu[2]
[1]*National Institute of Information and Communications Technology, 4-2-1 Nukui-kita, Koganei, Tokyo 184-8795, Japan*
[2]*Department of Electrical Engineering and Information Systems and Nanophotonics Research Center, School of Engineering, The University of Tokyo, 2-11-16 Yayoi, Bunkyo-ku, Tokyo 113-8656, Japan*
(Received 2 June 2009; revised manuscript received 26 July 2009; published 22 September 2009)

We theoretically and experimentally investigated a system composed of a mixture of different-sized quantum dots involving optical near-field interactions to effectively induce optical excitation transfer. We demonstrated that the ratio of the number of smaller quantum dots to larger ones can be optimized using a density-matrix formalism so that excitons generated in the smaller ones are efficiently transferred to the larger ones. We also describe experimental demonstrations based on a mixture of 2 nm- and 2.8 nm-diameter CdSe/ZnS quantum dots dispersed on the surface of a silicon photodiode, where the increase in induced photocurrents due to optical excitation transfer is maximized at a certain quantum dot mixture which agrees with theoretical calculations.

DOI: 10.1103/PhysRevB.80.125325 PACS number(s): 74.25.Gz, 78.67.Bf, 73.63.Kv

I. INTRODUCTION

There have been in-depth theoretical and experimental efforts to reveal and exploit light-matter interactions on the nanometer scale[1–3] because of their potential impact in a wide range of applications. Since they are based on optical near-field interactions, quantitative breakthroughs have been achieved, such as in overcoming the integration restrictions posed by conventional propagating light.[4] Moreover, qualitative innovations are made possible by the unique attributes of optical near-field interactions which are unachievable by their conventional counterparts.[1,5]

One such unique function is the optical excitation transfer between nanoscale matter via optical near-field interactions.[6] The localized nature of optical near fields at the surface of nanoscale matter could free us from conventional optical selection rules, meaning that optical excitation could be excited to energy levels that are conventionally dipole forbidden.[1] This unique behavior of optical near-field interactions has been theoretically formulated as the dressed photon model.[1,7,8] Also, it has already been demonstrated experimentally in CuCl quantum dots,[6] InAs quantum dots,[9] and ZnO nanorods.[10] Its application to logic devices[11,12] and information and communication systems[5] has also been demonstrated. The process of optical excitation transfer has also been extensively studied in artificial photosynthesis systems.[13,14]

Besides the versatile applications mentioned above, we found that the input light wavelength is downconverted, or redshifted, at the output through such optical excitation transfers, as discussed shortly in Sec. II. This redshift may also be useful in various applications; for instance, it would effectively improve the sensitivity of a photodetector if the input wavelength could be shifted to longer wavelengths at which the photodetector is more sensitive. Applications to solar cells would also be one possibility.

In this paper, we describe our theoretical and experimental investigation of a system composed of a mixture of different-sized quantum dots involving optical near-field interactions so that such a wavelength conversion is effectively induced. Based on a density-matrix formalism, we formulate the dynamics of a mixed quantum dot system where excitons generated in the smaller ones are transferred to larger ones via optical near-field interactions. We demonstrate that the ratio of the number of small quantum dots to large ones can be optimized so that the input light energy is efficiently transformed to the output energy. Experimental demonstrations are also shown using a mixture of 2 nm- and 2.8 nm-diameter CdSe/ZnS core/shell quantum dots randomly dispersed on a silicon photodiode surface where the effect of wavelength conversion is evaluated as induced photocurrents.

This paper is organized as follows. In Sec. II, we theoretically deal with a multiple quantum dot system composed of smaller and larger quantum dots. Section III summarizes our experimental demonstrations. Section IV concludes the paper.

II. OPTICAL EXCITATION TRANSFER IN MIXED SYSTEM OF DIFFERENT-SIZED QUANTUM DOTS: THEORY AND SIMULATION

We begin with the interaction Hamiltonian between an electron-hole pair and an electric field, which is given by

$$\hat{H}_{\mathrm{int}} = -\int d^3r \sum_{i,j=e,h} \hat{\psi}_i^{\dagger}(\boldsymbol{r}) e\boldsymbol{r}\cdot\boldsymbol{E}(\boldsymbol{r})\psi_j(\boldsymbol{r}), \tag{1}$$

where e represents a charge, $\hat{\psi}_i^{\dagger}(\boldsymbol{r})$ and $\hat{\psi}_j(\boldsymbol{r})$ are, respectively, creation and annihilation operators of either an electron $(i,j=e)$ or a hole $(i,j=h)$ at $\boldsymbol{r}$, and $\boldsymbol{E}(\boldsymbol{r})$ is the electric field.[15] In usual light-matter interactions, $\boldsymbol{E}(\boldsymbol{r})$ is a constant since the electric field of diffraction-limited propagating light is homogeneous on the nanometer scale. Therefore, we can derive optical selection rules by calculating the dipole transition matrix elements. As a consequence, in the case of spherical quantum dots, for instance, only transitions to states specified by $l=m=0$ are allowed, where l and m are the orbital

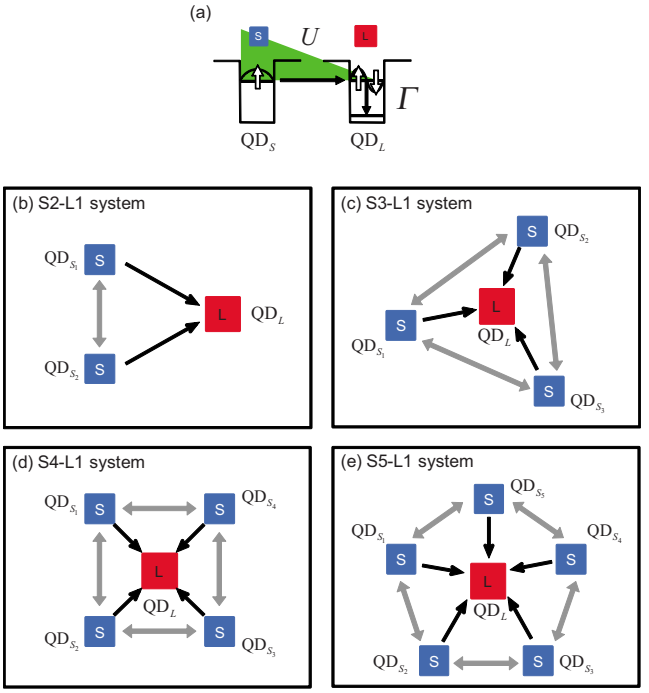

FIG. 1. (Color online) (a) Optical excitation transfer from a smaller quantum dot (QD_S) to a larger one (QD_L). (b) Three-dot system composed of two QD_Ss and one QD_L (S2-L1 system). (c) Four-dot system composed of three QD_Ss and one QD_L (S3-L1 system). (d) Five-dot system composed of four QD_Ss and one QD_L (S4-L1 system). (e) Six-dot system composed of five QD_Ss and one QD_L (S5-L1 system).

angular momentum quantum number and magnetic quantum number, respectively. In the case of optical near-field interactions, on the other hand, due to the large spatial inhomogeneity of the localized optical near fields at the surface of nanoscale material, an optical transition that violates conventional optical selection rules is allowed. Detailed theory can be found in Ref. 1.

Here we assume two spherical quantum dots whose radii are R_S and R_L, which we call QD_S and QD_L, respectively, as shown in Fig. 1(a). The energy eigenvalues of states specified by quantum numbers (n,l) are given by

$$E_{nl} = E_g + E_{\text{ex}} + \frac{\hbar^2 \alpha_{nl}^2}{2MR^2} \quad (n = 1,2,3,\ldots), \tag{2}$$

where E_g is the band gap energy of the bulk semiconductor, E_{ex} is the exciton binding energy in the bulk system, M is the effective mass of the exciton, and α_{nl} are determined from the boundary conditions, for example, as $\alpha_{n0}=n\pi$, $\alpha_{11}=4.49$. According to Eq. (2), there exists a resonance between the level of quantum number (1,0) of QD_S and that of quantum number (1,1) of QD_L if $R_L/R_S=4.49/\pi\approx 1.43$. Note that the (1,1) level of QD_L is a dipole-forbidden energy level. However, optical near fields allow this level to be populated by excitation. Therefore, an exciton in the (1,0) level in QD_S could be transferred to the (1,1) level in QD_L. In QD_L, due to the sublevel energy relaxation with a relaxation constant Γ, which is faster than the near-field interaction, the exciton relaxes to the (1,0) level, from where it radiatively decays. Also, the radiation lifetime of quantum dots is inversely proportional to their volume.[16] Therefore, finally we find unidirectional optical excitation transfer from QD_S to QD_L. Here, we regard the optical excitation generated in QD_S as the *input* of the system and the radiation from QD_L as the *output*. Due to the energy dissipation (sublevel energy relaxation) in QD_L, the wavelength of the output light is redshifted relative to the input one.

We also consider a quantum dot system where multiple smaller dots (QD_S) can be coupled with one large dot (QD_L). Such a system composed of two QD_Ss and one QD_L, denoted by "S2-L1 system," is shown in Fig. 1(b). Figure 1 also shows multiple quantum dot systems denoted by "S3-L1 system" [Fig. 1(c)], "S4-L1 system" [Fig. 1(d)], and "S5-L1 system" [Fig. 1(e)], which are respectively composed of three, four, and five QD_Ss connected to one QD_L. As schematically shown in Figs. 1(b)–1(e), we also assume interdot interactions between adjacent smaller quantum dots; that is, (i) QD_{S_i} interacts with $QD_{S_{i+1}}$ $(i=1,\ldots,N-1)$ and (ii) QD_{S_N} interacts with QD_{S_1}, where N is the number of QD_Ss. We consider that such a ringlike arrangement of QD_Ss surrounding one QD_L is a reasonable assumption that represents a mixed system of multiple QD_S and one QD_L.

Now, what is of interest is maximizing the flow of excitons from these QD_Ss to the QD_L so that the wavelength conversion is effectively induced by controlling the mixture of QD_Ss and QD_L. We deal with such a problem theoretically based on a density-matrix formalism as described in the following.

We take the S2-L1 system [Fig. 1(b)] to describe the theoretical treatment. Figure 2(a) shows representative parametrizations associated with the S2-L1 system, where the two smaller dots are, respectively, QD_{S_1} and QD_{S_2}, and the larger dot is QD_L. The (1,0) levels in QD_{S_i} $(i=1,2)$ are denoted by S_i and the (1,1) level in QD_L is denoted by L_2. These three levels are resonant with each other and are connected by interdot interactions between QD_{S_i} and QD_L, denoted by U_{S_iL}, as well as interactions between the smaller dots QD_{S_1} and QD_{S_2}, denoted by $U_{S_1S_2}$ in Fig. 2(a). The lower level in QD_L, namely, the (1,0) level, is denoted by L_1, which could be filled via the sublevel relaxation denoted by Γ from L_2. The radiations from the S_1, S_2, and L_1 levels are, respectively, represented by the relaxation constants γ_{S_1}, γ_{S_2}, and γ_L. We call the inverse of those relaxation constants the radiation lifetime in the following.

We suppose that the system initially has two excitons in S_1 and S_2; namely, the initial state of the system is represented by $|\phi_{S_1S_2}\rangle=|1\rangle_{S_1}|0\rangle_{L_2}|0\rangle_{L_1}|1\rangle_{S_2}$, which is graphically represented in Fig. 2(b). With such an initial state, we can prepare a total of eleven bases, as summarized in Fig. 2(c), where zero, one, or two exciton(s) occupy the energy level(s) among S_1, S_2, L_1, and L_2. All bases are connected by either interdot interactions, radiative relaxations, or sublevel relaxations.

From the initial state, through the interdot interactions between the energy levels of [S_1 and L_2] and [S_2 and L_2], the excitons in S_1 and S_2 could respectively be transferred to L_2. Also the exciton in S_1 could be transferred to S_2 through the

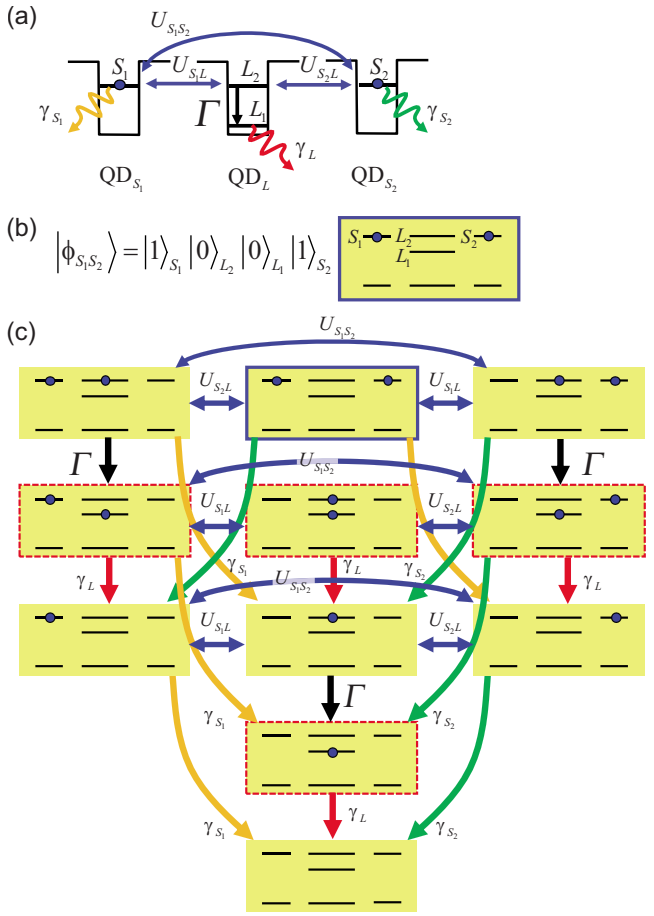

FIG. 2. (Color online) (a) Three-dot system composed of two smaller quantum dots (QD_{S_1} and QD_{S_2}) and a larger one QD_L. The (1,0) level of QD_{S_i}(denoted by S_i) and the (1,1) level of QD_L(denoted by L_2) are resonant and coupled by optical near-field interactions indicated by U_{S_iL}. The interaction between smaller dots is denoted by $U_{S_iS_j}$. The radiations from S_i and L_2 are denoted by γ_{S_i} and γ_L. The sublevel relaxation from L_2 to L_1, the (1,0) level of QD_L, is marked by Γ. (b) A graphical representation of the state of the system when the energy levels of S_1 and S_2 are respectively occupied with an exciton. (c) Total of 11 states where zero, one, or two exciton(s) occupy the energy level(s) in the system. Those states are interconnected via relaxations and interdot interactions.

interdot interaction between the smaller quantum dots and vice versa. Correspondingly, we can derive quantum master equations in the density-matrix formalism.[1,17,18] The Hamiltonian regarding the two-exciton states, $|\phi_{S_1S_2}\rangle$, and $|\phi_{S_2L_2}\rangle$ is given by

$$H = \hbar \begin{pmatrix} \Omega_{S_1} + \Omega_{L_2} & U_{S_1L_2} & U_{S_1S_2} \\ U_{S_1L_2} & \Omega_{S_1} + \Omega_{S_2} & U_{S_2L} \\ U_{S_1S_2} & U_{S_2L} & \Omega_{S_2} + \Omega_{L_2} \end{pmatrix}, \quad (3)$$

where $\hbar U_{S_iL}$ is the near-field interaction between QD_{S_i} and QD_L, $\hbar U_{S_1S_2}$ is that between QD_{S_1} and QD_{S_2}, and $\hbar\Omega_{S_i}$ represents the eigenenergies of QD_{S_i} $(i=1,2)$. The relaxation regarding those three states is given by

$$N_\Gamma = \begin{pmatrix} \frac{\gamma_{S_1}+\Gamma}{2} & 0 & 0 \\ 0 & \frac{\gamma_{S_1}+\gamma_{S_2}}{2} & 0 \\ 0 & 0 & \frac{\gamma_{S_2}+\Gamma}{2} \end{pmatrix}. \quad (4)$$

The Liouville equation for the system is then given by

$$\frac{d\rho(t)}{dt} = -i[H,\rho(t)] - N_\Gamma\rho(t) - \rho(t)N_\Gamma + \rho(t)P_\Gamma, \quad (5)$$

where P_Γ represents the relaxations that increase the corresponding population.[17] (P_Γ is an empty matrix in the particular case described above.) Similarly, we can derive Liouville equations regarding the two-exciton states, one of which excitons fills L_1, namely, $|\phi_{S_1L_1}\rangle$, $|\phi_{L_2L_1}\rangle$, and $|\phi_{S_2L_1}\rangle$, and also with one-exciton states $|\phi_{S_1}\rangle$, $|\phi_{L_2}\rangle$, and $|\phi_{S_2}\rangle$. Finally, we can calculate the population of the lower level of QD_L, which we regard as the output signal, as the summation of the populations of $|\phi_{S_1L_1}\rangle$, $|\phi_{S_2L_1}\rangle$, $|\phi_{L_2L_1}\rangle$, and $|\phi_{L_1}\rangle$, which correspond to states indicated by the dashed boxes in Fig. 2(c). In the numerical calculation, we assume $U_{S_iL}^{-1}=200$ ps, $U_{S_iS_j}^{-1}=100$ ps, $\Gamma^{-1}=10$ ps, $\gamma_L^{-1}=1$ ns, and $\gamma_{S_i}^{-1}=(R_L/R_S)^3 \times \gamma_L^{-1} \approx 2.92$ ns as a typical parameter set for the CdSe/ZnS quantum dots used for our experiments. The radiation lifetime of CdSe/ZnS quantum dots with a diameter of 2.8 nm, which is also used in the experiment in Sec. III, was measured to be 2.1 ns in Ref. 19, which is close to the above parametrization of radiation lifetimes. Also, the interaction time between smaller and larger quantum dots via optical near fields was estimated to be 135 ps in Ref. 19. Together with the fact that the interaction between the two dipole-allowed levels of the same-sized quantum dots, $(U_{S_iS_j})$, is stronger than that between smaller and larger dots, (U_{S_iL}),[1] we adopted the above parametrization for the interdot interactions. Finally, the calculated output population is represented by the curve A in Fig. 3(a).

Following the same procedure as described above, we can also derive quantum master equations for the S3-L1 system shown in Fig. 1(c), the S4-L1 system in Fig. 1(d), and the S5-L1 system in Fig. 1(e), with their initial states in which all smaller quantum dots have excitons. We can derive the evolution of the population of the lower level of the larger dot, that is, the output signal. We assume the same parameter sets in those systems as in the case of the S2-L1 system described above. The curves B–D in Fig. 3(a) respectively indicate the populations of the output signals from the S3-L1, S4-L1, and S5-L1 systems.

As the number of smaller quantum dots, or equivalently initial excitons, increases, the decay time of the output population from QD_L gets longer to accommodate multiple excitons initially located at QD_S. However, due to the limited radiation lifetime of QD_L ($\gamma_L^{-1}=1$ ns), not all of the initial excitons can be successfully transferred to QD_L due to the state filling of the lower level of QD_L. Therefore, part of the

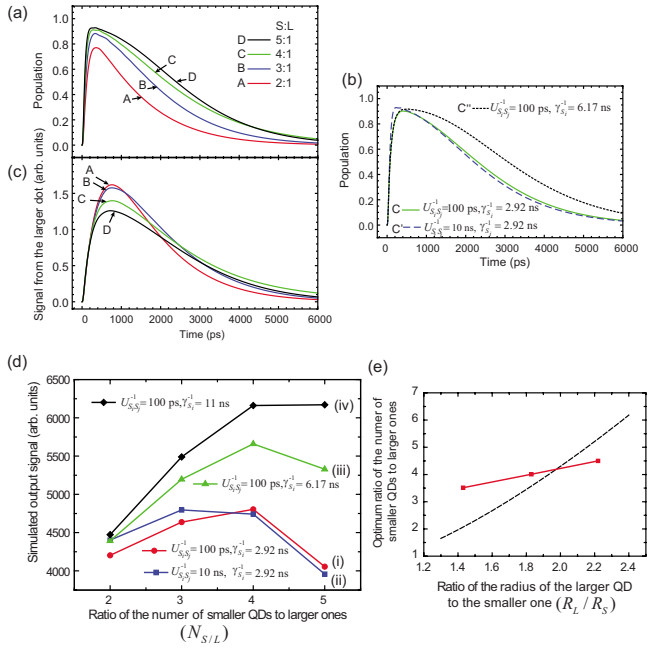

FIG. 3. (Color online) (a) Evolutions of the populations of the lower level of QD_L for the S2-L1, S3-L1, S4-L1, and S5-L1 systems in their initial states with all smaller dot(s) occupied by exciton(s). (b) Dependence of the output population on the interaction time between smaller dots ($U_{S_iS_j}^{-1}$) and the radiation lifetime of smaller dot ($\gamma_{S_i}^{-1}$). (c) Evolution of the output signals obtained by multiplying the population of the S*N*-L1 system obtained in (a) by a factor $\alpha/(N+1)$ so that the density of all quantum dots is kept constant. (d) Integrated signal levels obtained in (c) as a function of the ratio of the number of smaller QDs to larger ones (red circles). Their dependence on the interactions between smaller dots and the radiation lifetime of the smaller dots is also shown. (e) Optimal ratio of the number of smaller QDs to larger ones as a function of the ratio of the radius of the larger QD to the smaller one.

input populations must be decayed at QD_S, which results in loss in the conversion from the input to output.

One way of decreasing such loss is to increase the interdot interactions between smaller quantum dots, namely, $U_{S_iS_j}$, in order for an exciton to be transferred to neighboring smaller dots before being radiatively decayed. The curves C and C′ in Fig. 3(b), respectively, indicate the output populations from two kinds of S4-L1 systems, in which $U_{S_iS_j}^{-1}$ is 100 ps and 10 ns. We find that the decay time of the output gets slightly longer with the greater interactions between smaller dots, $(U_{S_iS_j}^{-1}=100$ ps), than with weaker ones, $(U_{S_iS_j}^{-1}=10$ ns). In addition, the interactions between smaller dots play another interesting role in the system, tolerating system errors, as will be discussed shortly.

Another way of decreasing such loss is to give a longer radiation lifetime for the smaller dots ($\gamma_{S_i}^{-1}$), for instance, by decreasing the size of the smaller quantum dots while maintaining the conditions for optical excitation transfer from the smaller dots to the larger one. For instance, $\alpha_{12}=5.76$ in Eq. (2) satisfies the condition between the (1,0) level of QD_S and (1,2) level of QD_L when the size ratio of the quantum dots is given by $R_L/R_S=5.76/\pi\approx 1.83$. Such a configuration provides a longer radiation lifetime for QD_L, given by $\gamma_{S_i}^{-1}=(R_L/R_S)^3\times\gamma_L^{-1}\approx 6.17$ ns. This allows input excitons in QD_S to effectively wait until they can be transferred to the larger dot. The curve C″ in Fig. 3(b) indicates the output population with $\gamma_{S_i}^{-1}=6.17$ ns, where we can clearly observe a substantially enhanced output signal. Even smaller sizes for QD_S, such as corresponding to the condition $\alpha_{13}=6.99$ and $R_L/R_S=6.99/\pi\approx 2.22$, provide longer radiation lifetime of 11.0 ns, resulting in an enhanced output signal.

Now we consider quantum dot systems composed of different ratios of the number of smaller dots to larger ones while maintaining the total density of quantum dots constant. For this purpose, we multiply the output population from the S*N*-L1 system by a factor $\alpha/(N+1)$, where N represents the number of smaller quantum dots connected to one larger dot. The factor α indicates the number of quantum dots, regardless of their size (smaller or larger), in a given unit area. Figure 3(c) shows the resulting signals from S*N*-L1 systems, each of which was already obtained as shown in Fig. 3(a). The unit on the vertical axis in Fig. 3(c) is arbitrary; we assumed $\alpha=10$ in Fig. 3(c).

By integrating the time evolutions of these output signals between 0 and 20 ns, the resultant signal (that is, the integrated output signal) can be compared as shown by the circles (i) in Fig. 3(d). They exhibit their maximum when the ratio of the number of smaller dots to the larger one, which we denote as $N_{S/L}$, is 4. We can clearly see that increasing the number of smaller quantum dots does not necessarily contribute to increased output signal. Besides the ratio of the number of smaller dots to larger ones, the output signal also depends on the interactions between the smaller dots and the radiation lifetime of the smaller dots, as already discussed above. Figure 3(d) also includes the estimated output signal level with a $U_{S_iS_j}^{-1}$ value of 10 ns, as indicated by the squares (ii), where the optimal mixture of QD_S and QD_L that yields the highest output signal, or equivalently, that most efficiently induces the wavelength conversion, is obtained when $N_{S/L}$ is 3. With longer radiation lifetime of the smaller quantum dots, $\gamma_{S_i}^{-1}=6.17$ ns and $\gamma_{S_i}^{-1}=11.0$ ns, the output signal levels are greatly improved, as respectively indicated by the triangles (iii) and diamonds (iv) in Fig. 3(d).

Two remarks should be made regarding these theoretical calculations. First, the optimal ratios of the number of smaller quantum dots to larger ones in the cases $R_L/R_S=1.43$ [circles (i)] and $R_L/R_S=1.83$ [triangles (iii)] are both obtained when $N_{S/L}$ is 4, as shown in Fig. 3(d). However, with the larger quantum dot size ratio R_L/R_S of 1.83, that is $\gamma_{S_i}^{-1}=6.17$ ns, the output signal remains larger even when $N_{S/L}$ is 5. For the case of $R_L/R_S=2.22$ [diamonds (iv)], the output signal is nearly equal when $N_{S/L}$ is both 4 and 5. In order to account for this tendency, we evaluate the optimal $N_{S/L}$ by calculating the weighted center with respect to $N_{S/L}$ that yields output signals greater than 0.9 of the maximum. Then, we can clearly observe that the optimal ratio of the number of smaller QDs to larger ones increases as the ratio of the radius of the larger QD to the smaller one (R_L/R_S) increases, as indicated by the squares in Fig. 3(e).

We can understand these phenomena from the following reasoning. The larger quantum dot could accommodate multiple input excitations from smaller quantum dots as long as

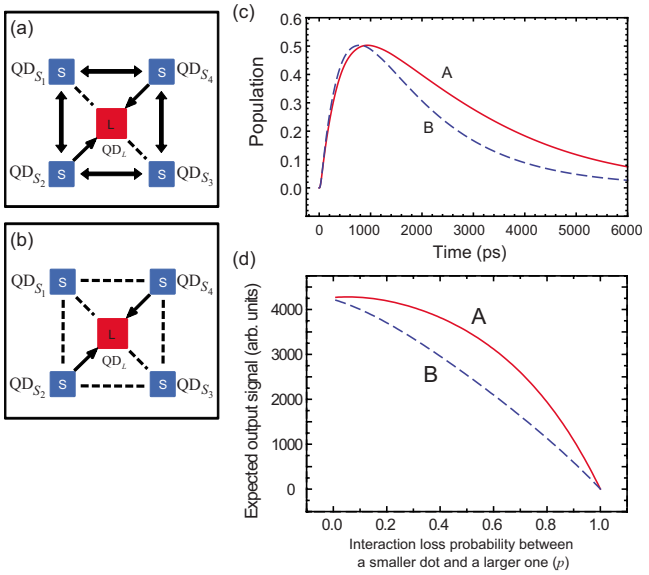

FIG. 4. (Color online) (a) A S4-L1 system in which the interactions between [QD_{S_1} and QD_L] and [QD_{S_3} and QD_L] are degraded. (b) A S4-L1 system where the interactions between smaller dots are also degraded. (c) Evolution of populations of the radiation from the larger dot in the system shown in (a) [curve A] and (b) [curve B]. (d) Expected output signal from S4-L1 systems with and without inter-smaller-dot interactions as a function of interaction-loss probability between a smaller dot and a larger one.

the input excitation can effectively wait at the smaller quantum dot. Therefore, the larger quantum dot could ideally accommodate multiple excitations, at most $\gamma_S^{-1}/\gamma_L^{-1}=(R_L/R_S)^3$. However, due to the finite interaction time between QD_S and QD_L (U_{SL}^{-1}), it is approximately limited by $\gamma_S^{-1}/(\gamma_L^{-1}+NU_{SL}^{-1})$, where N represents the number of excitations in the smaller quantum dots. Therefore, the number of smaller quantum dots whose excitations are all accommodated in the larger one will be approximately given by solving the equation

$$N=\frac{\gamma_S^{-1}}{\gamma_L^{-1}+NU_{SL}^{-1}}=\frac{(R_L/R_S)^3\gamma_L^{-1}}{\gamma_L^{-1}+NU_{SL}^{-1}}. \tag{6}$$

The dashed curve in Fig. 3(e) depicts N obtained by solving Eq. (6) as a function of R_L/R_S, assuming $\gamma_L^{-1}=1$ ns and $U_{SL}^{-1}=200$ ps, which agrees with the optimal ratio of the number of the smaller QDs to large ones indicated by the squares in Fig. 3(e), which are obtained via the numerical evaluations shown in Fig. 3(d).

The second remark is to highlight another function of the interactions between smaller dots. Figure 4(a) schematically represents an S4-L1 system where four smaller dots surround one larger dot and there are interdot interactions between adjacent smaller dots. Here, we suppose that some of the interactions between the smaller dots and the larger one are degraded or lost. Such a weak interaction could physically correspond to situations, for instance, where the distance between the smaller dot and the larger one is very large, or the size or the shape of the quantum dots deviates from the required conditions for energy transfer, or other reasons. In Fig. 4(a), we suppose that QD_{S_1} and QD_{S_3} have extremely weak interactions with QD_L; the dashed lines in Fig. 4(a) schematically indicate those weak interactions. Also, Fig. 4(b) represents another S4-L1 system where *all* of the interactions between smaller dots are assumed to be negligible, in addition to the weak interactions assumed in the system in Fig. 4(a). What is of interest is to evaluate the impact of the interactions between smaller dots on the energy transfer from the smaller dots to the larger one as a total system. In the following analysis, we assume degraded interactions that are 100 times weaker than the normal ones.

The curves A and B in Fig. 4(c), respectively, represent the evolutions of the population of the radiation from the larger dot in the system shown in Figs. 4(a) and 4(b), where the former exhibits a higher population compared with the latter. In the system shown in Fig. 4(a), thanks to the interactions between smaller dots, the excitations in QD_{S_1} and QD_{S_3} can be successfully transferred to QD_L by way of the adjacent smaller dots. On the other hand, it is hard for the excitations in QD_{S_1} and QD_{S_3} in Fig. 4(b) to be transferred to QD_L due to the weak interactions with the surrounding dots. From a system perspective, the interactions among smaller dots provide *robustness* to degradation of the excitation transfer from the smaller dots to larger ones.

To quantitatively evaluate such robustness, here we introduce the probability that an interaction between a smaller dot and a larger one suffers interaction degradation or loss; we denote it by p $(0\leq p\leq 1)$. Accordingly, we assume that the probability of the existence of interaction between a smaller and a larger one is given by $1-p$. We consider that although modeling of the loss in such an interaction is simple, that is, the probability p indicates the loss/existence of the interactions, one can clearly grasp the role of interactions in the following discussion. We can calculate the probability of all possible resulting system configurations as a function of p; for instance the probability of the system shown in Fig. 4(a) is given by $p^2(1-p)^2$. Also, we calculate the evolution of the population and its integral as the output signal for each of the system configurations. Finally, we can derive the expected output signal level as a function of p, given by

$$E(p)=\sum_i P(C_i)L(C_i), \tag{7}$$

where C_i indicates each system configuration, $P(C_i)$ means the probability of resulting in system C_i, and $L(C_i)$ means the output signal level from system C_i.

The curves A and B in Fig. 4(d), respectively, represent the expected output signals corresponding to systems with and without interactions between smaller dots as a function of the interaction loss probability between a smaller dot and a larger one. We can clearly observe that the expected output signal levels remain higher thanks to the existence of interactions between smaller dots, even though they suffer a larger p; this is a manifestation of the improved robustness of the system provided by the interactions between smaller dots.

III. EXPERIMENTS

In order to verify the effect of wavelength conversion via different sized quantum dots involving near-field interactions

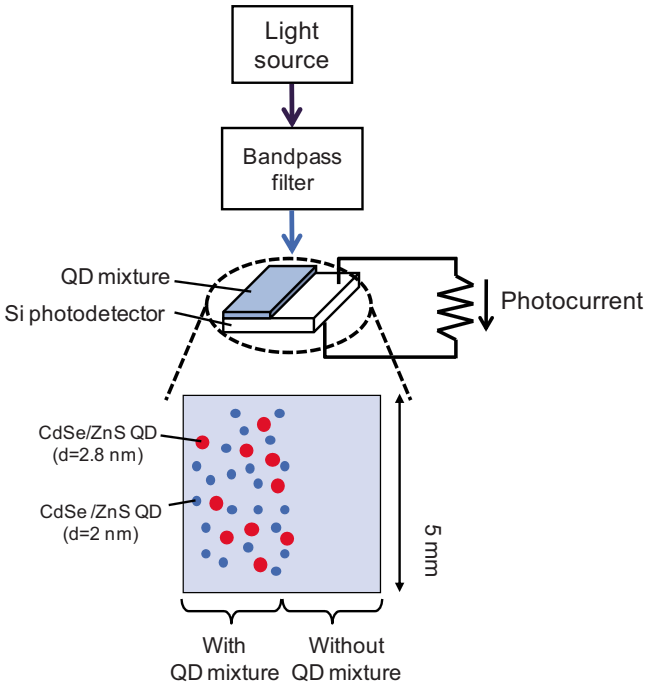

FIG. 5. (Color online) Experimental devices and setups used for the characterization of induced photocurrents.

and its impact on the increased sensitivity in light detection, we experimentally fabricated a composition of quantum dots formed on the surface of a photodiode by the following procedure.

Two kinds of quantum dots, QD_S and QD_L, were both CdSe/ZnS core/shell quantum dots (Evident Technologies, Inc., Core Shell EviDots). The diameters of QD_S and QD_L were respectively 2.0 nm and 2.8 nm. Note that the ratio of the radii of those dots is 1.43, which is the condition discussed in Sec. II. The quantum dots were dispersed in a matrix composed of toluene and ultraviolet curable resin and coated on the surface of a silicon photodiode whose aperture was 5.8 mm$\times$5.8 mm (Hamamatsu Photonics K.K., Si Photodiode S2368). The mean density of the quantum dots was kept constant so that the mean distance between quantum dots was around 40 nm. As schematically shown in Fig. 5, half of the surface of the photodiode was spin-coated by an ultraviolet-curable resin with a mixture of quantum dots and cured by ultraviolet radiation for 10 min, whereas the other half of the surface was coated by the same resin without the quantum dot mixture. Input light was selectively radiated onto each area to evaluate the difference in the generated photocurrent.

The light source was composed of a deuterium lamp and a halogen lamp. The emitted light was spectrally filtered in 2 nm wavelength intervals using a grating installed in a spectrometer and was radiated onto the sample. The diameter of the light spot on the sample was around 1 mm. The induced photocurrent was measured with a lock-in amplifier connected in parallel to an external load resister of the photodiode. The experiment was performed at room temperature.

The ratio of the increased photocurrent at each wavelength between 300 and 400 nm is evaluated as $[I_w(\lambda) - I_{wo}(\lambda)]/I_{wo}(\lambda)$, where $I_w(\lambda)$ and $I_{wo}(\lambda)$, respectively, indicate the photocurrents induced by input light with wavelength λ irradiating the areas with and without the mixture of quantum dots. Here we attribute the increase in such a metric to optical excitation transfer between quantum dots by which the input wavelength is redshifted to wavelengths where the photodetector is more sensitive.

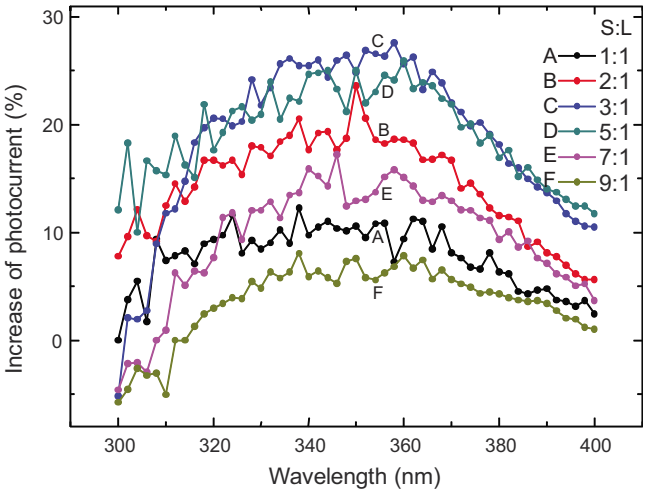

FIG. 6. (Color online) Increase in the photocurrent with different mixtures of smaller and larger quantum dots as a function of input light wavelength.

Figure 6 shows the increase in the induced photocurrent as a function of the input light wavelength. The ratio of the number of QD_S to QD_L was controlled to be $N_{S/L}=1$, 2, 3, 5, 7, and 9, which are respectively indicated by the curves A–F in Fig. 6, while the total density of the quantum dots was kept constant. The increase in the photocurrent was observed to be higher when the ratio of the number of QD_S to QD_L was 3:1. The squares in Fig. 7 represent the average increase in the photocurrent between 340 and 360 nm in Fig. 6, showing a maximum when the ratio of the number of QD_S to QD_L was 3:1. This agrees with the theoretical optimal ratio of the

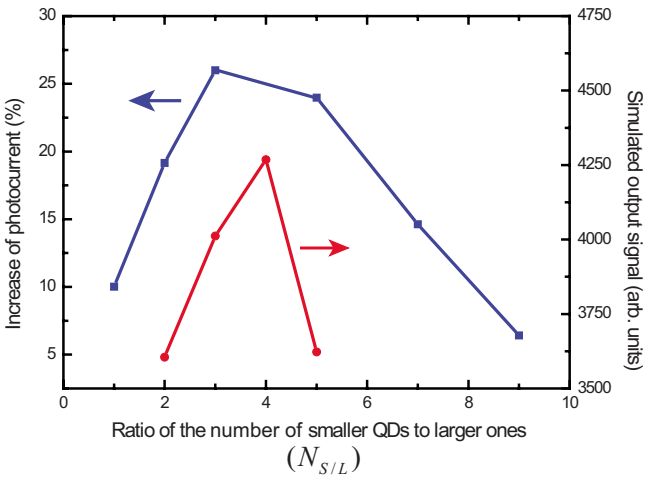

FIG. 7. (Color online) The average increase in photocurrent as a function of the ratio of the number of smaller quantum dots to larger ones (squares), which agrees with theoretical calculations (circles).

number of smaller quantum dots to larger ones discussed in Sec. II, indicated by the circles in Fig. 7, with parameters $U_{S_iS_j}^{-1}=100$ ps, $U_{S_iL}^{-1}=200$ ps, $\gamma_L^{-1}=1$ ns, and $\gamma_{S_i}^{-1}=2.92$ ns, which is also shown by the circles (i) in Fig. 3(d). More detailed investigation of each of the parameters, such as the radiation lifetime of CdSe quantum dots reported for instance in Refs. 20 and 21, could result in better agreement. Nevertheless, as demonstrated by the squares in Fig. 3(e), the optimal ratio of smaller dots to larger ones should be around 4, which agrees with the experimental data shown in Fig. 7.

IV. CONCLUSION

We theoretically and experimentally investigated a system composed of a mixture of different-sized quantum dots involving optical near-field interactions so that optical excitation transfer is effectively induced. Based on the density-matrix formalism, we formulated a quantum dot mixture in which excitons generated in the smaller ones are transferred to the larger one. The evolution of the population was evaluated as a function of the number of smaller quantum dots interacting with a larger one. We demonstrated that the ratio of the number of smaller quantum dots to larger ones could be optimized so that the input light energy was efficiently transferred to the output. The effects of interactions between smaller dots and the radiation lifetime of the smaller dots were also analyzed. We also demonstrated that the interactions between smaller quantum dots provide robustness against degradation of the interactions between the larger and the smaller dots. Experimental demonstrations are shown based on a mixture of CdSe/ZnS core-shell quantum dots dispersed on the surface of a silicon photodiode. The induced photocurrent was maximized when the ratio of the number of smaller quantum dots to larger ones was 3, which agrees with theoretical calculations.

We will seek further theoretical and experimental insights regarding such optical excitation transfer which is enabled uniquely by optical near-field interactions, in order to allow a wide range of system applications, as well as a deeper understanding of light-matter interactions on the nanometer scale.

ACKNOWLEDGMENTS

The authors would like to thank Kiyoshi Kobayashi of the University of Yamanashi and Masaru Tsukada and Hiroyuki Tamura of Tohoku University for helpful discussions on the theory of optical excitation transfer. This work was partially supported by the New Energy and Industrial Technology Development Organization (NEDO) under the program of comprehensive activity for personnel training and industry-academia collaboration based on NEDO projects.

[1] M. Ohtsu, K. Kobayashi, T. Kawazoe, T. Yatsui, and M. Naruse, *Principles of Nanophotonics* (Taylor & Francis, Boca Raton, 2008).
[2] P. Vasa, R. Pomraenke, S. Schwieger, Yu. I. Mazur, V. Kunets, P. Srinivasan, E. Johnson, J. E. Kihm, D. S. Kim, E. Runge, G. Salamo, and C. Lienau, Phys. Rev. Lett. **101**, 116801 (2008).
[3] *Semiconductor and Metal Nanocrystals*, edited by V. I. Klimov (Marcel Dekker, New York, 2003).
[4] *Near Field Optics*, edited by D. W. Pohl and D. Courjon (Kluwer Academic, Dordrecht, 1993).
[5] M. Naruse, T. Kawazoe, T. Yatsui, S. Sangu, K. Kobayashi, and M. Ohtsu, in *Progress in Nano-Electro-Optics V*, edited by M. Ohtsu (Springer, Berlin, 2006).
[6] T. Kawazoe, K. Kobayashi, J. Lim, Y. Narita, and M. Ohtsu, Phys. Rev. Lett. **88**, 067404 (2002).
[7] M. Ohtsu, T. Kawazoe, T. Yatsui, and M. Naruse, IEEE J. Sel. Top. Quantum Electron. **14**, 1404 (2008).
[8] Y. Tanaka and K. Kobayashi, J. Microsc. **229**, 228 (2008).
[9] T. Kawazoe, K. Kobayashi, K. Akahane, M. Naruse, N. Yamamoto, and M. Ohtsu, Appl. Phys. B: Lasers Opt. **84**, 243 (2006).
[10] T. Yatsui, H. Jeong, and M. Ohtsu, Appl. Phys. B: Lasers Opt. **93**, 199 (2008).
[11] T. Kawazoe, K. Kobayashi, S. Sangu, and M. Ohtsu, Appl. Phys. Lett. **82**, 2957 (2003).
[12] T. Yatsui, S. Sangu, T. Kawazoe, M. Ohtsu, S. J. An, J. Yoo, and G.-C. Yi, Appl. Phys. Lett. **90**, 223110 (2007).
[13] H. Imahori, J. Phys. Chem. B **108**, 6130 (2004).
[14] S. Kang, T. Umeyama, M. Ueda, Y. Matano, H. Hotta, K. Yoshida, S. Isoda, M. Shiro, and H. Imahori, Adv. Mater. **18**, 2549 (2006).
[15] H. Haug and S. W. Koch, *Quantum Theory of the Optical and Electronic Properties of Semiconductors* (World Scientific, Singapore, 2004).
[16] T. Itoh, M. Furumiya, T. Ikehara, and C. Gourdon, Solid State Commun. **73**, 271 (1990).
[17] H. J. Carmichael, *Statistical Methods in Quantum Optics 1* (Springer-Verlag, Berlin, 1999).
[18] M. Naruse, T. Miyazaki, F. Kubota, T. Kawazoe, K. Kobayashi, S. Sangu, and M. Ohtsu, Opt. Lett. **30**, 201 (2005).
[19] W. Nomura, T. Yatsui, T. Kawazoe, and M. Ohtsu, J. Nanophotonics **1**, 011591 (2007).
[20] S. A. Crooker, T. Barrick, J. A. Hollingsworth, and V. I. Klimov, Appl. Phys. Lett. **82**, 2793 (2003).
[21] O. Labeau, P. Tamarat, and B. Lounis, Phys. Rev. Lett. **90**, 257404 (2003).

Information theoretical analysis of hierarchical nano-optical systems in the subwavelength regime

Makoto Naruse,[1,2,*] Hirokazu Hori,[3] Kiyoshi Kobayashi,[3] Masatoshi Ishikawa,[4] Kenji Leibnitz,[5] Masayuki Murata,[1,5] Naoya Tate,[2] and Motoichi Ohtsu[2]

[1]*National Institute of Information and Communications Technology, 4-2-1 Nukui-kita, Koganei, Tokyo 184-8795, Japan*

[2]*Department of Electrical Engineering and Information Systems and Nanophotonics Research Center, School of Engineering, The University of Tokyo, 2-11-16 Yayoi, Bunkyo-ku, Tokyo 113-8656, Japan*

[3]*Interdisciplinary Graduate School of Medicine and Engineering, University of Yamanashi, Kofu, Yamanashi 400-8511, Japan*

[4]*Department of Information Physics and Computing, School of Information Science and Technology, The University of Tokyo, 7-3-1 Hongo, Bunkyo-ku, Tokyo 113-8656, Japan*

[5]*Department of Information Networking, Graduate School of Information Science and Technology, Osaka University, 1-5 Yamadaoka, Suita, Osaka 565-0871, Japan*

**Corresponding author: naruse@nict.go.jp*

Received May 11, 2009; revised July 20, 2009; accepted July 27, 2009; posted July 29, 2009 (Doc. ID 111228); published August 24, 2009

Optical near-field interactions exhibit a hierarchical response, which is one of the most unique attributes of light–matter interactions occurring locally on the nanometer scale. It allows hierarchical nano-optical systems that break through the integration restrictions posed by the diffraction limit of conventional propagating light and offers multiple hierarchical functionalities at different physical scales in the subwavelength regime. Here we demonstrate an information theoretical approach to such nano-optical systems while assessing their electromagnetic and logical aspects via angular-spectrum analysis. Mutual information at each level of the hierarchy reveals quantitatively the relation between the physical effects associated with the hierarchy in the optical near-fields, as well as possible environmental disturbances affecting the system locally or globally, and the system's capabilities for information processing and communication.

OCIS codes: 260.2110, 200.3050, 110.3055.

1. INTRODUCTION

Optical devices and systems are increasingly exploiting physical fundamentals based on optical near-field interactions that occur locally at the nanometer-scale [1–6], not just those based on conventional diffraction-limited propagating light. The need for such nanometer-scale optical systems comes from the demands for higher integration density in applications such as optical memories [7], sensors [8], nanofabrication [9], and so forth. In addition, disruptive innovations are also expected in nanophotonic systems such their extremely low power dissipation [10], novel functional memories [11], trust and security applications [12,13], and more. The theoretical basis of light–matter interactions at the nanometer scale have been deepened [14–17] through the development of, e.g., dressed photon models [16] or angular-spectrum analysis [17]. Experimental technologies, both in fabrication and characterization of nanostructures, have also seen rapid progress such as in geometry-controlled quantum dots [18], metal nanostructures [19,20], and advanced spectroscopy [21,22].

Besides those physical insights and experimental methodologies, it is important in developing practical systems to grasp the fundamental properties from the viewpoint of information and communication [23]. In optical communications, for instance, insights gained from information theory are indispensable in assessing and improving the performance figures [24]. Information theoretic analysis also sheds light on the behavior of a wide range of optical devices and systems [25,26]. As in similar disciplines, fundamental limits in optical components have also been studied [27]. The application of information theoretic methods to nanotechnologies is found, for instance, in molecular communications based on material transfer [28] and molecular biology [29].

For nano-optical systems, on the other hand, while their physical understanding has been extensively deepened [1], their information theoretic aspects are, to the best of our knowledge, completely unknown. If the unique attributes enabled by optical near-fields, which conventional propagating light does not offer, are properly defined as an information and communication system, it would provide critical knowledge and guidelines in designing concrete applications.

The hierarchical property in optical near-field interactions, meaning that the interaction depends on the physical scale involved, as schematically shown in Fig. 1(a), is one of the attributes that differentiates them most from conventional diffraction-limited far-field light [30]. In [30], we have demonstrated that the optical near-fields can be distributed independently at different scales of observation by exploiting the nature that the high spatial-frequency terms in optical near-fields are rapidly decayed with a decay rate that is spatial-frequency dependent. As

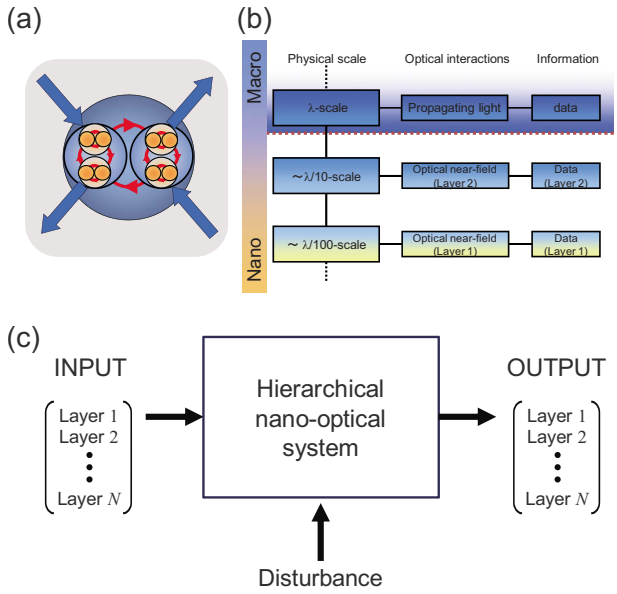

Fig. 1. (Color online) Hierarchy in optical near-fields at the subwavelength scale and its application to information and communications. (a) Optical near-field interactions and their scale-dependence. (b) Hierarchical nano-optical system where different functionalities are associated with each of the physical scales involved. (c) System diagram to study information theoretic aspects of hierarchical nano-optical systems.

introduced in Section 2 below, it is convenient, in discussing such a hierarchical property in optical near-fields, to represent the electric fields as a superposition of plane waves with complex wave vector, called the angular spectrum. This approach clearly unifies the fine/coarse structures and their associated decay of the optical near-fields.

Such a hierarchical property leads to versatile novel functions in nano-optical systems; for example, multiple functionalities could be associated with each of the physical scales in the subwavelength regime, as illustrated in Fig. 1(b). This has already had an impact on a wide range of applications [11–13,31]. This also implies that, whereas the time-domain behavior is crucial in conventional optical communications [24], space-domain properties dominate the unique behavior observed in nano-optical systems and these should be analyzed from the viewpoint of information theory.

In this paper, we take an information theoretic approach to analyzing such nano-optical systems while assessing their electromagnetic and logical aspects via angular-spectrum analysis. As schematically shown in Fig. 1(c), the hierarchical nano-optical system is modeled as a communication medium that connects input and output symbols and also suffers from environmental disturbances. Concrete applications represented by such a model will include, for instance, optical storage systems where the input and output respectively correspond to the write and retrieve processes. Here, at each level of the hierarchy, we formulate mutual information that quantitatively reveals the relation between the physics associated with the hierarchy in optical near-fields, as well as possible environmental disturbances affecting the system locally or globally, and the capabilities of the system for information processing and communications. In other words, here we intend to grasp the hierarchical structure of nano-optical systems from a cross-cutting standpoint, including their electromagnetic, logical, and information theoretic aspects.

This paper is organized as follows: In Section 2, we start by discussing the hierarchical properties in optical near-fields based on angular-spectrum analysis and its logical responses as a hierarchical system. In Section 3, we formulate hierarchical nano-optical systems from the viewpoint of information theory and reveal their layer- and disturbance-dependent mutual information. Section 4 concludes the paper.

2. HIERARCHICAL NANO-OPTICAL SYSTEMS BASED ON OPTICAL NEAR-FIELDS

A. Electromagnetic Hierarchy in Nano-Optical Systems

We first introduce an electromagnetic theory to describe hierarchy in optical near-fields. The angular spectrum representation of the electromagnetic field [17,32] is useful in discussing the hierarchy in optical near-fields [30]. It allows an analytical treatment while giving an intuitive picture of the localization of optical near-fields, and represents relevance in optical near-field interactions at different scales of observation, since it describes electromagnetic fields as a superposition of evanescent waves with different decay lengths and corresponding spatial frequencies assuming planar boundary conditions.

Suppose that there is an oscillating electric dipole, $\boldsymbol{d}^{(k)}=(d^{(k)}\cos\varphi^{(k)},0)$, on the xz plane, oriented parallel to the x axis. Note that those dipoles are oscillating; the orientations of the dipoles, specified by $\varphi^{(i)}$, physically correspond to the absolute phase of the electric fields. Also note that the physical scales under study are smaller than the wavelength of light, but larger than the scales governed by the electron interactions, typically around 1 nm.

Now, consider the electric field of radiation observed at a position displaced from the dipole by $\boldsymbol{R}^{(k)}=(r_{\parallel}^{(k)}\cos\phi^{(k)},z^{(k)})$. Assuming the planar boundary as the xy plane, the angular spectrum representation of the z-component of the optical near-field is given by

$$E_z(\boldsymbol{R})=\left(\frac{iK^3}{4\pi\varepsilon_0}\right)\int_1^{\infty}\mathrm{d}s_{\parallel}\frac{s_{\parallel}}{s_z}f_z(s_{\parallel},\boldsymbol{d}^{(1)},\ldots,\boldsymbol{d}^{(N)}), \tag{1}$$

where

$$f_z(s_{\parallel},\boldsymbol{d}^{(1)},\ldots,\boldsymbol{d}^{(N)})=\sum_{k=1}^{N}d^{(k)}s_{\parallel}\sqrt{s_{\parallel}^2-1}\cos(\varphi^{(k)}-\phi^{(k)})J_1(Kr_{\parallel}^{(k)}s_{\parallel})\exp(-Kz^{(k)}\sqrt{s_{\parallel}^2-1}), \tag{2}$$

where N represents the number of dipoles, and $\boldsymbol{R}$ indicates the observation position. Here, $s_{\parallel}$ is the spatial frequency of an evanescent wave propagating parallel to the x axis, and $J_n(x)$ represents Bessel functions of the first kind. The term $f_z(s_{\parallel},\boldsymbol{d}^{(1)},\ldots,\boldsymbol{d}^{(N)})$ is called the angular spectrum of the electric field, where the spatial frequency-dependent exponential decay is clearly represented. Details of the theory can be found in [30].

In the following, a two-layer system is introduced where (i) at locations closer to the dipoles, two items of *first-layer* information are retrieved, and (ii) at a location relatively far from the dipoles, one item of *second-layer* information is retrieved. What should be noted here is that a coarser scale structure can affect the optical responses relatively far from the structure thanks to the longer decay length of the optical near-fields, while a finer scale structure can only affect the optical responses closer to the structure due to the rapidly decaying nature of higher spatial frequency terms in optical near-fields. Therefore, as will be introduced shortly below, the optical near-field amplitude can be distributed independently at different scales of observation; in other words, arbitrary logical combinations are possible at the first layer and the second layer.

In order to clearly represent such a situation, we introduce a model composed of two closely spaced dipole pairs [$\boldsymbol{d}^{(1)}$ and $\boldsymbol{d}^{(2)}$] and [$\boldsymbol{d}^{(3)}$ and $\boldsymbol{d}^{(4)}$], whose positions are specified as shown in Fig. 2(a). The fractional numbers in the figure indicate the distances in units of optical wavelength. The fine-scale structures, affecting the first layer response, are represented by each of those pairs, whereas the coarse-scale structures, affecting the second-layer response, depend on the relation between those pairs. In other words, the mixture of the coarse-scale and the fine-scale structures is represented by those four dipoles, which are precisely described theoretically in the following manner based on the angular spectrum representation.

First, we assume that the dipoles $\boldsymbol{d}^{(1)}$ and $\boldsymbol{d}^{(2)}$ are oriented in the same direction, namely, $\varphi^{(1)}=\varphi^{(2)}=0$, and that the other dipoles, $\boldsymbol{d}^{(3)}$ and $\boldsymbol{d}^{(4)}$, are both oriented oppositely to $\boldsymbol{d}^{(1)}$ and $\boldsymbol{d}^{(2)}$, namely, $\varphi^{(3)}=\varphi^{(4)}=\pi$. At a position close to the x axis equidistant from $\boldsymbol{d}^{(1)}$ and $\boldsymbol{d}^{(2)}$, such as at the position $F^{(1)}$ in Fig. 2(a), the electric field is weak (logical ZERO) since the angular spectrum contributions originating from $\boldsymbol{d}^{(1)}$ and $\boldsymbol{d}^{(2)}$ cancel each other, and the electric field originating from $\boldsymbol{d}^{(3)}$ and $\boldsymbol{d}^{(4)}$ is small. In fact, as shown by the dashed curve in Fig. 2(b), since the angular spectrum at position $F^{(1)}$ oscillates equally around the x axis, the integral of the angular spectrum, which is related to the field intensity at that point, will be low.

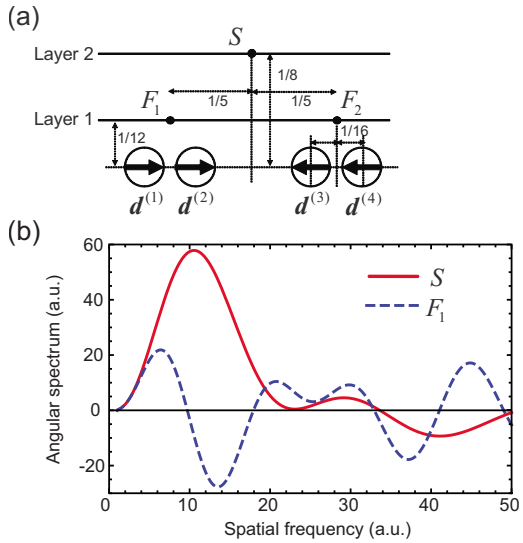

Fig. 2. (Color online) Angular spectrum analysis of a hierarchical nano-optical system. (a) Physical model for a hierarchical nano-optical system consisted of four oscillating dipoles ($\boldsymbol{d}^{(1)}$,$\boldsymbol{d}^{(2)}$,$\boldsymbol{d}^{(3)}$,$\boldsymbol{d}^{(4)}$). The optical response at the first layer ($F^{(1)}$ and $F^{(2)}$) and the second layer (S) are evaluated. (b) Angular spectrum evaluated at the first layer (dashed curve) and the second layer (solid curve) from an array of dipoles whose phase arrangement is specified in (a), which indicates that the optical near-fields are localized in the second layer, whereas they are not localized in the first layer.

For the second layer, consider the observation at an intermediate position between the dipole pairs, such as the position S in Fig. 2(a). From this position, the four dipoles effectively appear to be two dipoles that are oriented in opposite directions to each other. Particularly with the present system conditions, the second-layer signal at S is dominated by the arrangement of the two center dipoles. As shown by the solid curve in Fig. 2(b), the angular spectrum exhibits a single peak, indicating that the electric field in the xy-plane is localized to a degree determined by its spectral width, so that a logical ONE is retrievable at position S. Meanwhile, the angular spectrum observed at position $F^{(2)}$ shown in Fig. 2(a) is identical to that observed at position $F^{(1)}$, meaning that the electric field at $F^{(2)}$ is also at a low level.

B. Logical Hierarchy in Nano-Optical Systems

As described above, one of the two first-layer signals, the electric field at $F^{(1)}$, primarily depends on the dipole pair $\boldsymbol{d}^{(1)}$ and $\boldsymbol{d}^{(2)}$, and the other, the electric field at $F^{(2)}$, is dominated by the dipole pair $\boldsymbol{d}^{(3)}$ and $\boldsymbol{d}^{(4)}$. The second-layer signal is determined by those two pairs of dipoles. These dependence structures are schematically shown in Fig. 3(a). With such a hierarchical mechanism, a total of eight different signal combinations, or symbols, can be achieved by appropriately orienting the four dipoles [30], as summarized in Fig. 3(b) where the eight symbols are denoted by a_i ($i=0,\ldots,7$), each of which refers to a three-bit sequence whose first element represents the digit obtained at the second layer (S), and whose second and third elements respectively refer to the digits obtained at the first layer ($F^{(1)}$ and $F^{(2)}$). A corresponding dipole orientation is also indicated in the right-hand side of Fig. 3(b).

Figure 4 represents examples of simulated electric field distributions obtained through finite-difference time-domain methods to visualize hierarchical electromagnetic structures. Four silver nanoparticles (radius of 15 nm) containing a virtual oscillating light source were assumed in order to simulate dipole arrays. The operating wavelength was 488 nm.

Corresponding to the angular spectrum-based theoretical analysis discussed above, Fig. 4(a) shows the z-component of the electromagnetic intensity corresponding to the dipole arrangement of the symbol a_4. The electric fields obtained at $F^{(1)}$ and $F^{(2)}$ remained low, while that at S yielded a higher level. Figure 4(b) shows another example, corresponding to the symbol a_3, exhibiting opposite responses to the former case. Figure 4(c) compares the intensity levels at the second layer for all eight

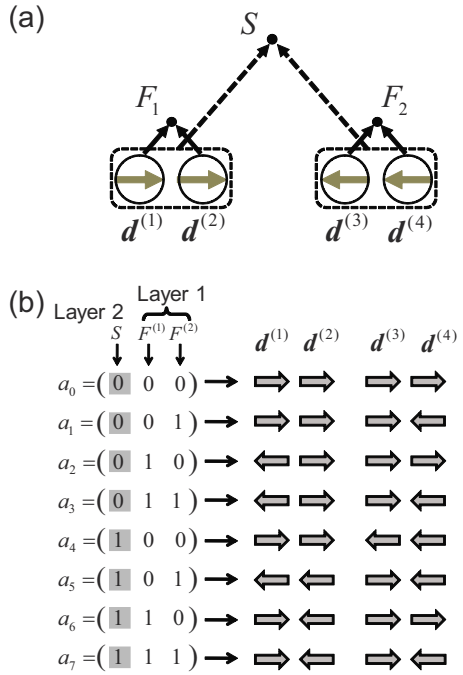

Fig. 3. (Color online) Dependence structure between the dipole pairs and the logical levels in the first and second layers. (a) Relation between dipole pairs and the logical level in each layer. (b) List of the total of eight bit-sequences, or symbols, and their corresponding dipole arrangements.

combinations, which agrees with the first bit of each symbol in Fig. 3(b) by digitizing with a threshold depicted by a dashed line in Fig. 4(c).

The relation between the electromagnetic hierarchy and its logical implications depends also on other factors at the nanometer scale, such as the intensity distributions of the sources. As mentioned earlier, the second-layer information depends on the larger scale structures; therefore, even the two dipoles located at the edges, that is, $\boldsymbol{d}^{(1)}$ and $\boldsymbol{d}^{(4)}$, can dominate the second-layer responses. For instance, suppose that the amplitude of the radiation from the peripheral dipoles is larger than that from the

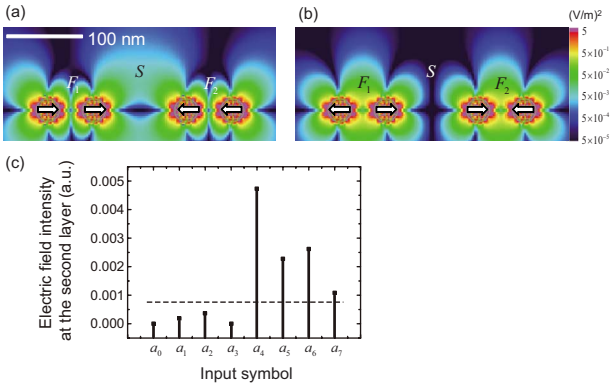

Fig. 4. (Color online) Hierarchical electromagnetic structures at the subwavelength scale. (a,b) Simulated electric field intensity distributions corresponding to the input symbols (a) a_4 and (b) a_3. (c) Simulated electric field intensity obtained at the second layer for all of the symbols that yield the intended digit for the second layer by digitizing the intensity with a threshold indicated by the dashed line.

two center ones, that is, $|\boldsymbol{d}^{(1)}|:|\boldsymbol{d}^{(2)}|:|\boldsymbol{d}^{(3)}|:|\boldsymbol{d}^{(4)}|=b:a:a:b$ where $b>a$, while keeping the total intensity $\Sigma_i|\boldsymbol{d}^{(i)}|^2$ the same. Figure 5(a) represents a case with $b/a=4$. This yields logically different behavior in the second layer; namely, the dipoles located at the periphery then dominate the second layer. For instance, with the dipole phase arrangement corresponding to the symbol a_6, the second-layer signal exhibits contrasting patterns. Figure 5(b) compares angular spectra corresponding to the uniform intensity distributions (denoted by Array 6 in Fig. 5(a)) with biased intensity pattern (denoted by Array 6′) of the four dipoles, where the latter yields poorer localization than the former. Figures 5(c) and 5(d), respectively, show calculated electromagnetic distributions corresponding to Array 6 and Array 6′, where the difference in the second layer is clearly observed.

Here we make two remarks regarding the modeling described above. First, we do not take into account the multiple scattering processes between electric polarizations in the analysis. One reason is to avoid unnecessary complexity of the discussion, since the primary concern of this paper is about the information theoretic analysis beginning in Section 3. Second is that we can apply such an angular spectrum-based approach in the same manner after considering multiple scattering processes. The essential logical flow of the discussion remains the same.

Another remark is about the physically reasonable equivalents to an array of electric dipoles used in the modeling. Shape-engineering of metal nanostructures is one approach to implement electric polarizations in designated orientations; for instance, combinations of triangular-shaped gold nanostructures exhibit hierarchical responses, as demonstrated in [33]. The difference of the amplitude of electric dipoles could then correspond to, for instance, the difference in sizes of those metal nanostructures. Also, electric polarizations induced in semiconductor nanorods [34] or geometry-controlled semiconductor quantum dots [18] could effectively correspond to the present model.

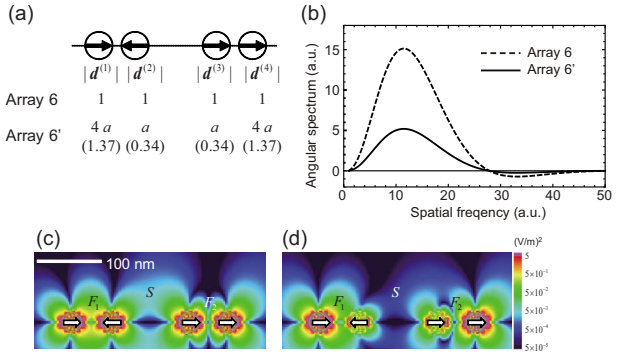

Fig. 5. (Color online) Dependence of the hierarchical electromagnetic structure to various nano-scale entities. (a) Array of dipoles, corresponding to the symbol a_6, each of which has identical radiation intensity (denoted by Array 6) and those which have biased radiation intensity while the total intensity remains the same (denoted by Array 6′). (b) Angular spectrum evaluated at the second layer for Array 6 and Array 6′, where the Array 6′ exhibits degraded light localization. Simulated electric field intensity distributions corresponding to (c) Array 6 and (d) Array 6′.

3. INFORMATION THEORETIC ANALYSIS OF HIERARCHICAL NANO-OPTICAL SYSTEMS

Here we start by analyzing the information theoretic aspects of the hierarchical nano-optical system, which is viewed as a communication medium that connects the input to the output channels while experiencing certain environmental disturbances. The input and output signals are, as introduced already, three-bit sequences; the total of eight symbols for the input and the output symbols are, respectively, denoted by $A=\{a_i\}$ and $B=\{b_i\}$, where $i=0,\ldots,7$. The output symbol b_i should represent the same three-bit sequence given by the input symbol a_i if there is no error from the input to the output. The probability of the input symbol a_i is given by $P(a_i)$. The probability of the output symbol b_i, given by $P(b_i)$, depends on the input symbol probability $P(a_i)$ and the transition matrix T that represents the relation between the input and output and is given by

$$\begin{pmatrix} P(b_0) \\ \vdots \\ P(b_7) \end{pmatrix} = T \begin{pmatrix} P(a_0) \\ \vdots \\ P(a_7) \end{pmatrix}, \tag{3}$$

where the elements of T are given by $t_{ij}=P(b_i|a_j)$, which is the probability of the output b_i conditioned on the input a_j. The matrix T is affected by environmental disturbances. We will introduce two representative disturbance models for the analysis. The first is the case where the environmental disturbance has an explicit spatial structure or what we call a *near-field* disturbance. The second is the case where the disturbance selectively couples to the dipole arrangement or what we name as a *far-field* disturbance. Here, we take into account the optical selection rule that the far-field optical radiation cannot be coupled to energy levels specified by even quantum number(s), or quadrupole(s), in considering the interactions between the disturbance and the system under study.

A. Near-Field Disturbance

We assume an environmental disturbance that modifies the status of each spatial position in the system locally. In other words, here we assume a *near-field* environmental disturbance that locally disturbs the polarizations of each of the dipoles. Suppose that the phase of at most one of the four dipoles could be flipped, that is, changed by 180°. Let the probability of such a phase flip occurring for the dipole $\boldsymbol{d}^{(i)}$ be given by p_i. In the case of input symbol a_0, for example, whose corresponding four dipoles are all in phase (See Fig. 3(b)), the phase of the first dipole $\boldsymbol{d}^{(1)}$ is flipped, which yields output symbol b_2 with probability p_1, as schematically shown in Fig. 6(a). When the second dipole $\boldsymbol{d}^{(2)}$ is flipped, the resulting output symbol is b_6. The error-free probability is given by $q=1-\Sigma_{i=1}^{4}p_i$. All transitions from input symbols to output ones are derived as schematically represented in Fig. 6(b), where possible changes from an input to an output symbol are indicated by arrows.

It is technically possible to further generalize the effects of disturbances in this model, such as arbitrary phase flips occurring in the dipoles. However, this leads to an unnecessarily complex situation and makes it hard to understand how the local change in the system affects the information capacity. As a first step, simple position-dependent errors clearly reveal the relation between the physical consequences and their impact on layer-dependent information theoretic measures, which is the primary concern of this paper.

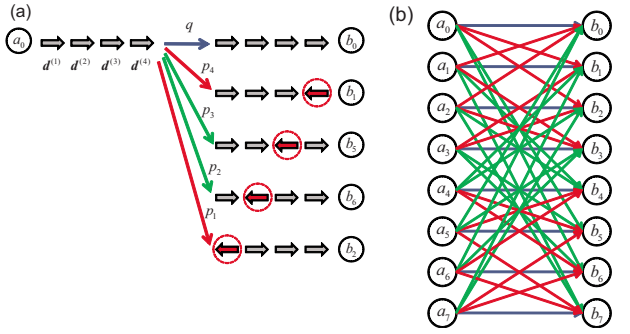

Fig. 6. (Color online) Near-field disturbances to the system. (a) Model of an environmental disturbance that locally affects each of the dipoles. The phase of dipole $\boldsymbol{d}^{(i)}$ can be flipped with probability p_i. (b) The relation between the input symbols a_i and the output ones b_j. The red and green arrows, respectively, correspond to the phase flips at the edge and at the center dipole(s). The blue ones correspond to no error.

The mutual information $I(A;B)$ represents the quantity of the data transmitted through the system, which is equal to the amount of remaining uncertainty of data A on condition that the output B is measured, namely, $I(A;B)=H(A)-H(A|B)$, where $H(A)$ is the entropy of the input and $H(A|B)$ is the entropy of the input conditioned on the output. It is calculated by

$$I(A;B)=\sum_{i=0}^{N-1}\sum_{j=0}^{N-1}P(a_i,b_j)\log_2\frac{P(a_i,b_j)}{P(a_i)P(b_j)}, \tag{4}$$

where the joint probability of input a_i and output b_j is given by $P(a_i,b_j)=t_{j,i}P(a_i)$ [35]. N indicates the number of symbols.

Here we further introduce a representative spatial structure of environmental disturbances so that the error probabilities affecting dipoles located at the edge and the center are different; that is, the error probability for the dipoles $\boldsymbol{d}^{(1)}$ and $\boldsymbol{d}^{(4)}$ is given by p_E, namely $p_1=p_4=p_E$, whereas that for $\boldsymbol{d}^{(2)}$ and $\boldsymbol{d}^{(3)}$ is given by $p_C=p_2=p_3$. The error-free probability is given by $q=1-2p_E-2p_C$. As described in Section 2, the four dipole model intends to represent the mixture of the coarse-scale structure and the fine-scale structure. In the present model, the two center dipoles dominate the second-layer information, meaning that those two play the major role in coarser scale structures. Therefore, the position-dependent errors denoted by p_C and p_E are physically associated with errors occurring in coarse-scale structures and in the fine-scale structures, respectively. As remarked at the end of Section 2, if those dipoles with designated orientations are implemented by means of shape-engineered nanostructures, the error would physically correspond to fabrication errors occurring at either coarser or finer scales.

Now, we suppose that the input symbol probability is uniform; that is, $P(a_i)=1/8$ $(i=0,\ldots,7)$. The mutual infor-

mation is evaluated as a function of p_E and p_C, as shown in Fig. 7(a). For example, $p_E=9/100$ and $p_C=1/100$ yields 1.92 bit of mutual information.

We now analyze the mutual information regarding each of the layers separately to see how the spatial structure of the local system disturbance affects the transmission capability for each of the layers.

Let the input symbols for the left-hand side of the first layer be $f_0^{(1)}$ and $f_1^{(1)}$, which respectively mean logical 0 and 1. Since $f_0^{(1)}$ and $f_1^{(1)}$ are respectively equivalent to the input symbol of either one of $F_0^{(1)}=\{a_0,a_1,a_4,a_5\}$ and $F_1^{(1)}=\{a_2,a_3,a_6,a_7\}$, the probability of input symbol $f_i^{(1)}$ is given by

$$P(f_i^{(1)}) = \sum_{a_j \in F_i^{(1)}} P(a_j). \tag{5}$$

Likewise, we denote the output symbols as $g_0^{(1)}$ and $g_1^{(1)}$, which are equivalent to either of the output symbols $G_0^{(1)}=\{b_0,b_1,b_4,b_5\}$ and $G_1^{(1)}=\{b_2,b_3,b_6,b_7\}$, respectively. The joint probability of inputs $f_i^{(1)}$ and $g_j^{(1)}$ is then derived as

$$P(f_i^{(1)},g_j^{(1)}) = \sum_{a_s \in F_i^{(1)}} \sum_{b_t \in G_j^{(1)}} P(b_t|a_s)P(a_s), \tag{6}$$

which leads to mutual information for the left-hand bit of the first layer, given by

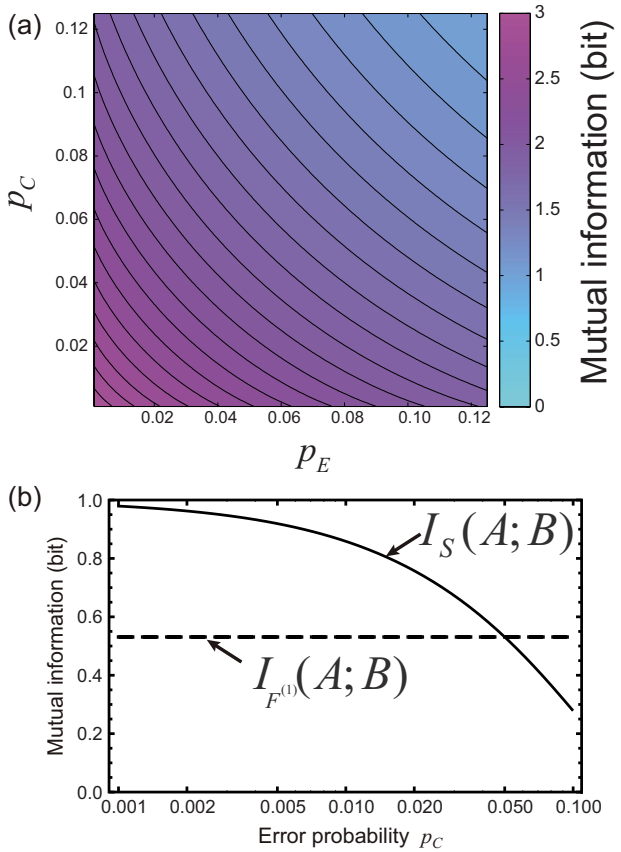

Fig. 7. (Color online) Scale-dependent mutual information. (a) Mutual information $I(A;B)$ as a function of error probabilities p_E and p_C. (b) Mutual information for the left-hand bit at the first layer ($I_{F^{(1)}}(A;B)$) and that for the second layer ($I_S(A;B)$) are evaluated as a function of error probability p_C, while keeping the total error rate p_E+p_C constant.

$$I_{F^{(1)}}(A;B) = \sum_{i=0}^{1}\sum_{j=0}^{1} P(f_i^{(1)},g_j^{(1)})\log_2 \frac{P(f_i^{(1)},g_j^{(1)})}{P(f_i^{(1)})P(g_j^{(1)})}. \tag{7}$$

Second, let the symbols of the second layer be s_0 and s_1. The symbols s_0 and s_1, respectively, correspond to either one of the input symbols $S_0=\{a_0,a_1,a_2,a_3\}$ and $S_1=\{a_4,a_5,a_6,a_7\}$. Similarly, the corresponding output symbols are defined by t_0 and t_1. The mutual information for the second layer is given by

$$I_S(A;B) = \sum_{i=0}^{1}\sum_{j=0}^{1} P(s_i,t_j)\log_2 \frac{P(s_i,t_j)}{P(s_i)P(t_j)}. \tag{8}$$

Here we quantitatively compare the mutual information given by Eqs. (7) and (8) assuming the same error probabilities. With less errors in the center and more errors at the periphery, for instance $p_C=1/100$ and $p_E=9/100$, $I_{F^{(1)}}(A;B)$ yields 0.53 bit, whereas $I_S(A;B)$ yields 0.86 bit, indicating that the second layer has larger information transmission efficiency than the first layer. On the other hand, with more errors in the center and less errors at the periphery, for instance $p_C=9/100$ and $p_E=1/100$, $I_{F^{(1)}}(A;B)$ yields 0.53 bit, whereas $I_S(A;B)$ yields 0.32 bit, showing that the quantity of information for the first layer is unchanged, whereas that for the second layer is severely degraded. With the condition that the error-free probability be kept constant at 0.8, $I_{F^{(1)}}(A;B)$ and $I_S(A;B)$ are respectively calculated as functions of p_C in Fig. 7(b), where $I_{F^{(1)}}(A;B)$ stays constant, whereas $I_S(A;B)$ takes larger values as p_C gets smaller. This is due to the fact that the second-layer information depends on the two center dipoles. On the other hand, the left-hand bit at the first layer depends on both $\boldsymbol{d}^{(1)}$ and $\boldsymbol{d}^{(2)}$; therefore, $I_{F^{(1)}}(A;B)$ yields a constant value as long as p_1+p_2 is constant.

B. Far-Field Disturbance

We now consider another type of environmental disturbance involving *far-field* radiation applied to nano-scale optical systems. Here, the optical selection rule that the far-field optical radiation cannot be coupled to energy levels specified by even quantum number(s) or quadrupole(s) [1,36] should be taken into account in considering the interactions between the disturbance and the system under study. The physical model consisting of multiple dipoles is, in fact, not directly compatible with such quantum optical properties. However, we consider that the following assumptions approximately describe their principal characteristics in order to understand its impact on information theoretic measures. They are as follows:

(i) When the phases of $\boldsymbol{d}^{(1)}$ and $\boldsymbol{d}^{(2)}$ are the same, both phases can be flipped with probability p. Similarly, the phases of $\boldsymbol{d}^{(3)}$ and $\boldsymbol{d}^{(4)}$ can be flipped with probability p when they have the same phase. The error-free probability is given by $q=1-p$. [Fig. 8(a)]

(ii) When all of the dipoles have the same phase, they can be flipped with probability p. The error-free probability is given by $q=1-p$. [Fig. 8(b)]

(iii) When the combinations of [$\boldsymbol{d}^{(1)}$ and $\boldsymbol{d}^{(2)}$] and/or [$\boldsymbol{d}^{(3)}$ and $\boldsymbol{d}^{(4)}$] have opposite phases, we assume that the

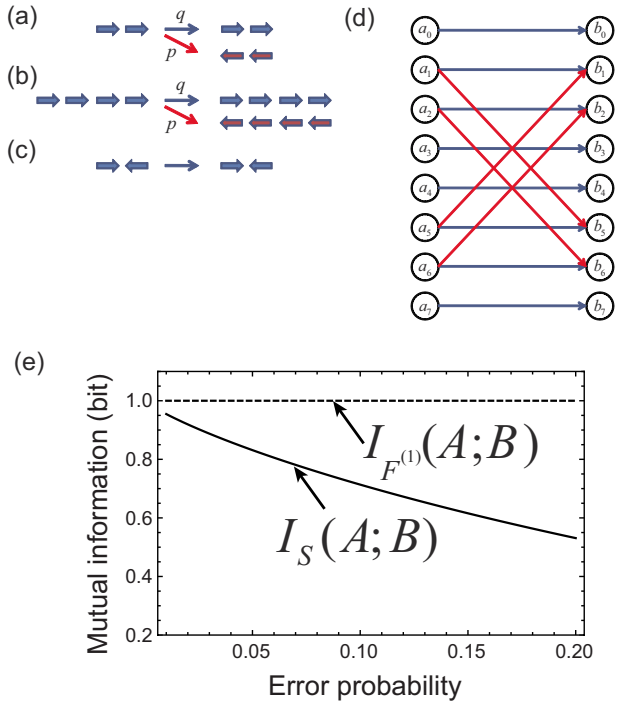

Fig. 8. (Color online) Far-field disturbance and its impact on layer-dependent mutual information. (a–c) Model of an environmental disturbance that couples to the system when arranged in a dipole manner and that does not couple to it when in a quadrupole arrangement. (a) Two closely separated dipole pairs can be flipped when they have the same phase. (b) Four dipoles can be flipped when they have the same phase. (c) The dipole pair does not suffer disturbances when they have opposite phases. (d) The relation between the input symbols a_i and the output ones b_j with those disturbances. The red (diagonal) arrows correspond to errors due to disturbances. The blue (horizontal) ones correspond to no error. (e) Mutual information for the left-hand bit at the first layer ($I_{F^{(1)}}(A;B)$) and that for the second layer ($I_S(A;B)$) as a function of error probability. $I_{F^{(1)}}(A;B)$ takes the value of 1, meaning that the first-layer information is completely resistant to such environmental disturbances.

far-field radiation serving as the system disturbance cannot be coupled to the dipoles and so no phase flips occur. [Fig. 8(c)]

For instance, for the case of input symbol a_0, all of the dipoles are arranged in the same directions, and they can all be coupled to the environmental disturbance; that is, item (ii) above will apply. However, from a logical point of view, flipping all of the dipoles does not affect the information of any bits to be retrieved at the output. In other words, the input symbol a_0 is always connected to output symbol b_0. For the case of input symbol a_1, $\boldsymbol{d}^{(1)}$ and $\boldsymbol{d}^{(2)}$ are in dipole arrangement, whereas $\boldsymbol{d}^{(3)}$ and $\boldsymbol{d}^{(4)}$ are in quadrupole arrangement. The dipoles $\boldsymbol{d}^{(1)}$ and $\boldsymbol{d}^{(2)}$ can be flipped with probability p, which results in the output symbol b_5. The relations between all input and output symbols are summarized in Fig. 8(d).

The mutual information for the first layer and the second layer are respectively evaluated following Eqs. (7) and (8). As indicated by the dashed line in Fig. 8(e), the mutual information for the first layer $I_{F^{(1)}}(A;B)$ is always 1, indicating that the system is completely resistant to the disturbances in the first layer. This is due to the fact that the environmental disturbance transforms the input symbols $F_0^{(1)}=\{a_0,a_1,a_4,a_5\}$ into the output symbols $G_0^{(1)}$, and the input symbols $F_1^{(1)}=\{a_2,a_3,a_6,a_7\}$ to $G_1^{(1)}$, where the left-hand bit at the first layer remains the same. On the other hand, the mutual information for the second layer $I_S(A;B)$ decreases as the error probability increases, as shown in the solid curve in Fig. 8(e). Since the second-layer signal depends on the pairs of dipoles, it could be disturbed in situations where the left- and the right-hand dipole pairs are a combination of a dipole arrangement and a quadrupole one.

The mutual information for the entire system can be improved by biasing the input symbol probability distribution, whose maximum is defined as the channel capacity, given by $C=\max_{p(a_i)}I(A;B)$. With the error probability $p=2/10$, the maximum mutual information, i.e., the channel capacity, is 2.68 bit when the probability distribution is given by $P(a_0)=P(a_3)=P(a_4)=P(a_7)=0.16, P(a_1)=P(a_2)=P(a_5)=P(a_6)=0.09$, which is obtained by a full search in the parameter space. On the other hand, the mutual information with a uniform input symbol distribution $P(a_i)=1/8$ $(i=0,\ldots,7)$ yields 2.64 bit. Although the higher number of bits obtained by changing the probability distribution is, in this particular case, just 0.04 bit, such consideration leads to system design strategies to fully utilize the capacity of such hierarchical systems.

4. CONCLUSION

In conclusion, we have demonstrated an information theoretic analysis of hierarchical nano-optical systems by highlighting the layer- and disturbance-dependent mutual information while assessing their electromagnetic and logical aspects with an angular-spectrum based method. Our formulation and analysis of mutual information at each level of the hierarchy reveal quantitatively the relation between the physics associated with the hierarchy in optical near-fields, as well as possible environmental disturbances affecting the system locally or globally, and the capabilities of the hierarchical nano-optical system for information processing and communications. Specifically, assuming an array of oscillating electric dipoles as a system model, we analyzed its electromagnetic and logical hierarchical structure and we quantitatively evaluated its capabilities as an information system by determining the mutual information for each level of the hierarchy; either the first or the second layer could be more resistant to environmental disturbances compared to the other one.

We believe that this paper reveals, for the first time, one fundamental aspect of nano-optical systems in the subwavelength regime from the viewpoint of information theory, which provides useful knowledge and guidelines in designing concrete applications. At the same time, however, we also believe that the unique attributes enabled by nanophotonics, which conventional propagating light does not offer, are not limited by this study. For instance, optical excitation transfer via optical near-field interactions [1], nonadiabatic processes enabled by optical near-fields [37,38], and other principles in nanophotonics may be other crucial aspects impacting the system from the viewpoint of information theory. Also, unique information strategies for nanophotonic systems such as smart coding

algorithms, for example, could be derived. We aim to further develop our understanding of the fundamentals of nanophotonic systems in future studies.

REFERENCES

1. M. Ohtsu, K. Kobayashi, T. Kawazoe, T. Yatsui, and M. Naruse, *Principles of Nanophotonics* (Taylor and Francis, 2008).
2. *Near Field Optics*, D. W. Pohl and D. Courjon, eds. (Kluwer Academic, 1993).
3. S. A. Maier, P. G. Kik, H. A. Atwater, S. Meltzer, E. Harel, B. E. Koel, and A. A. G. Requicha, "Local detection of electromagnetic energy transport below the diffraction limit in metal nanoparticle plasmon waveguides," Nature Mater. **2**, 229–232 (2003).
4. Y. Fedutik, V. V. Temnov, O. Schöps, U. Woggon, and M. V. Artemyev, "Exciton-plasmon-photon conversion in plasmonic nanostructures," Phys. Rev. Lett. **99**, 136802 (2007).
5. A. Ueda, T. Tayagaki, and Y. Kanemitsu, "Energy transfer from semiconductor nanocrystal monolayers to metal surfaces revealed by time-resolved photoluminescence spectroscopy," Appl. Phys. Lett. **92**, 133118 (2008).
6. V. I. Klimov, A. A. Mikhailovsky, S. Xu, A. Malko, J. A. Hollingsworth, C. A. Leatherdale, H.-J. Eisler, and M. G. Bawendi, "Optical gain and stimulated emission in nanocrystal quantum dots," Science **290**, 314–317 (2000).
7. T. Nishida, T. Matsumoto, F. Akagi, H. Hieda, A. Kikitsu, and K. Naito, "Hybrid recording on bit-patterned media using a near-field optical head," J. Nanophotonics **1**, 011597 (2007).
8. J. N. Anker, W. P. Hall, O. Lyandres, N. C. Shah, J. Zhao, and R. P. Van Duyne, "Biosensing with plasmonic nanosensors," Nature Mater. **7**, 442–453 (2008).
9. M. Naya, I. Tsurusawa, T. Tani, A. Mukai, S. Sakaguchi, and S. Yasutani, "Near-field optical photolithography for high-aspect-ratio patterning using bilayer resist," Appl. Phys. Lett. **86**, 201113 (2005).
10. M. Naruse, T. Miyazaki, T. Kawazoe, K. Kobayashi, S. Sangu, F. Kubota, and M. Ohtsu, "Nanophotonic computing based on optical near-field interactions between quantum dots," IEICE Trans. Electron. **E88-C**, 1817–1823 (2005).
11. M. Naruse, T. Yatsui, W. Nomura, N. Hirose, and M. Ohtsu, "Hierarchy in optical near-fields and its application to memory retrieval," Opt. Express **13**, 9265–9271 (2005).
12. M. Naruse, T. Yatsui, T. Kawazoe, Y. Akao, and M. Ohtsu, "Design and simulation of a nanophotonic traceable memory using localized energy dissipation and hierarchy of optical near-field interactions," IEEE Trans. Nanotechnol. **7**, 14–19 (2008).
13. N. Tate, H. Sugiyama, M. Naruse, W. Nomura, T. Yatsui, T. Kawazoe, and M. Ohtsu, "Quadrupole-dipole transform based on optical near-field interactions in engineered nanostructures," Opt. Express **17**, 11113–11121 (2009).
14. C. Cohen-Tannoudji, I. Dupont-Roc, and G. Grynberg, *Photons and Atoms* (Wiley, 1989).
15. H. Ishihara and K. Cho, "Nonlocal theory of the third-order nonlinear optical response of confined excitons," Phys. Rev. B **48**, 7960–7974 (1993).
16. M. Ohtsu, T. Kawazoe, T. Yatsui, and M. Naruse, "Nanophotonics: application of dressed photons to novel photonic devices and systems," IEEE J. Sel. Top. Quantum Electron. **14**, 1404–1417 (2008).
17. T. Inoue and H. Hori, "Quantum theory of radiation in optical near field based on quantization of evanescent electromagnetic waves using detector mode," in *Progress in Nano-Electro-Optics IV*, M. Ohtsu, ed. (Springer Verlag, 2005), 127–199.
18. W. Q. Ma, M. L. Hussein, J. L. Shultz, G. J. Salamo, T. D. Mishima, and M. B. Johnson, "Enhancing the in-plane spatial ordering of quantum dots," Phys. Rev. B **69**, 233312 (2004).
19. E. Ozbay, "Plasmonics: merging photonics and electronics at nanoscale dimensions," Science **311**, 189–193 (2006).
20. E. X. Jin and X. Xu, "Enhanced optical near field from a bowtie aperture," Appl. Phys. Lett. **88**, 153110 (2006).
21. K. Matsuda and T. Saiki, "Local density of states mapping of a field-induced quantum dot by near-field photoluminescence microscopy," Appl. Phys. Lett. **87**, 043112 (2005).
22. E. Runge and C. Lienau, "Near-field wave-function spectroscopy of excitons and biexcitons," Phys. Rev. B **71**, 035347 (2005).
23. C. E. Shannon, "A mathematical theory of communications," Bell Syst. Tech. J. **27**, 379–423 (1948); **27**, 623–656 (1948).
24. P. P. Mitra and J. B. Stark, "Nonlinear limits to the information capacity of optical fibre communications," Nature **411**, 1027–1030 (2001).
25. M. A. Neifeld and M. Lee, "Information theoretic framework for the analysis of a slow-light delay device," J. Opt. Soc. Am. B **25**, C31–C38 (2008).
26. P. Oittinen and H. Saarelma, "Average mutual information as a quality measure in imaging processes," J. Opt. Soc. Am. A **3**, 897–901 (1986).
27. D. A. B. Miller, "Fundamental limit for optical components," J. Opt. Soc. Am. B **24**, A1–A18 (2007).
28. A. W. Eckford, "Achievable information rates for molecular communication with distinct molecules," in *Bio-Inspired Models of Network, Information and Computing Systems 2007* (IEEE, 2007), pp. 313–315.
29. R. C. Yu, C. G. Pesce, A. Colman-Lerner, L. Lok, D. Pincus, E. Serra, M. Holl, K. Benjamin, A. Gordon, and R. Brent, "Negative feedback that improves information transmission in yeast signaling," Nature **456**, 755–761 (2008).
30. M. Naruse, T. Inoue, and H. Hori, "Analysis and synthesis of hierarchy in optical near-field interactions at the nanoscale based on angular spectrum," Jpn. J. Appl. Phys. **46**, 6095–6103 (2007).
31. M. Naruse, K. Nishibayashi, T. Kawazoe, K. Akahane, N. Yamamoto, and M. Ohtsu, "Scale-dependent optical near-fields in InAs quantum dots and their application to non-pixelated memory retrieval," Appl. Phys. Express **1**, 072101 (2008).
32. E. Wolf and M. Nieto-Vesperinas, "Analyticity of the angular spectrum amplitude of scattered fields and some of its consequences," J. Opt. Soc. Am. A **2**, 886–889 (1985).
33. M. Naruse, T. Yatsui, J. H. Kim, and M. Ohtsu, "Hierarchy in optical near-fields by nano-scale shape engineering and its application to traceable memory," Appl. Phys. Express **1**, 062004 1-3 (2008).
34. K. Kitamura, T. Yatsui, M. Ohtsu, and G.-C. Yi, "Fabrication of vertically aligned ultrafine ZnO nanorods using metal-organic vapor phase epitaxy with a two-temperature growth method," Nanotechnology **19**, 175305 (2008).
35. T. M. Cover and J. A. Thomas, *Elements of Information Theory* (Wiley, 1991).
36. Z. K. Tang, A. Yanase, T. Yasui, Y. Segawa, and K. Cho, "Optical selection rule and oscillator strength of confined exciton system in CuCl thin films," Phys. Rev. Lett. **71**, 1431–1434 (1993).
37. T. Kawazoe, K. Kobayashi, and M. Ohtsu, "Near-field optical chemical vapor deposition using Zn(acac)2 with a non-adiabatic photochemical process," Appl. Phys. B **84**, 247–251 (2006).
38. M. Naruse, T. Yatsui, W. Nomura, K. Hirata, Y. Tabata, and M. Ohtsu, "Analysis of surface roughness of optical elements planarized by nonadiabatic optical near-field etching," J. Appl. Phys. **105**, 063516 (2009).

[II] PRESENTATIONS

IN INTERNATIONAL CONFERENCES

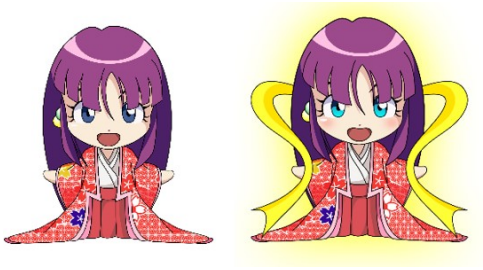

Localizing few-cycle light pulses in space and time in random dielectric media

M. Mascheck[1], S. Schmidt[1], M. Silies[1], D. Leipold[2], E. Runge[2], K. Kitamura[3], T. Yatsui[3], M. Ohtsu[3], and C. Lienau[1]

[1]*Institut für Physik, Carl von Ossietzky Universität, 26111 Oldenburg, Germany*
[2]*Institut für Physik, Technische Universität Ilmenau, 98684 Ilmenau*
[3]*School of Engineering, University of Tokyo, 113-8656, Japan*
martin.silies@uni-oldenburg.de

Abstract: We directly visualize, for the first time, the weak localization of light in both space and time in a disordered array of ZnO nanoneedles using a novel diffraction-limited second-harmonic microscope with few-cycle time resolution.

OCIS codes: (320.7110) (240.4350)

The weak localization of light due to multiple scattering in disordered nanoscale dielectric media is a particularly fascinating aspect of wave physics [1], offering a possibility to partially trap light and therefore to enhance its interaction with the medium. It is of particular importance in nano-optics, where the localization of surface plasmon polaritions in metallic nanostructures enables one to localize visible light to dimensions of 10 nm or even less and therefore to generate greatly enhanced local electromagnetic fields [2]. This combination of field localization and enhancement is currently finding a rapidly increasing number of applications such as locally-enhanced Raman spectroscopy, nano- and biosensing or ultrahigh resolution optical and electron microscopy.

So far, light localization due to wave interference has mostly been studied by macroscopic experimental techniques such as, e.g., coherent backscattering [1]. More direct studies are experimentally challenging since spatial light localization occurs on a (sub-) wavelength scale and the scattering dynamics happen on ultrashort, femtosecond time scales.

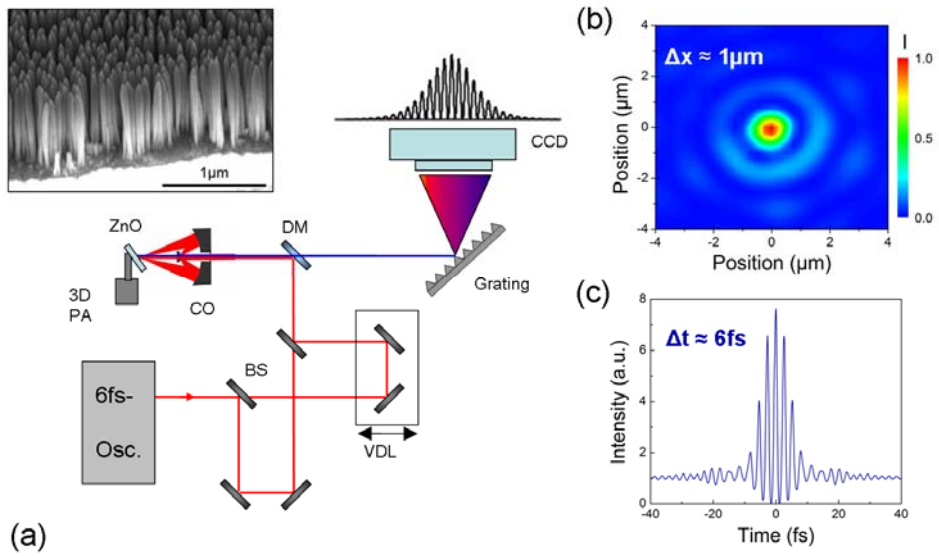

Fig. 1. (a) ZnO nanoneedle array and ultrafast second-harmonic microscope. Phase-correlated pairs of few-cycle pulses from a 6-fs-Ti:sapphire oscillator are focused onto the sample using an all-reflective Cassegrain objective and the resulting second-harmonic is spectrally dispersed and recorded using a CCD spectrometer. (b) Spatial intensity profile of the diffraction-limited focused few-cycle pulses recorded by scanning a near-field fiber probe through the focal plane. (c) Interferometric autocorrelation trace recorded in the focal plane of the objective.

Here, we demonstrate a new experimental approach, based on second-harmonic microscopy with few-cycle time resolution, to directly visualize the localization of light in random dielectric media in both space and time.

We investigate a densely packed array of zinc oxide (ZnO) nanorods fabricated by metal-organic vapor phase epitaxy with an average rod distance of about 100 nm and rod diameters down to 20 nm (Fig. 1a) [3]. Due to the large 3.4 eV bandgap of ZnO, this array is an essentially lossless random dielectric medium for near-IR light. We

make use of the large second harmonic (SH) coefficient of ZnO for probing light localization. Laser pulses with a duration of 6 fs centered around 800 nm from a Ti:Sapphire laser are focused onto the ZnO nanoneedle array to a diffraction-limited spot with a diameter of about 1 µm using an optimized all-reflective Cassegrain objective with a numerical aperture of 0.5 (Fig.1). Phase-locked pulse pairs for time-resolved measurements are created in a Michelson interferometer.

The resultant second harmonic (SH) emission is spectrally dispersed and recorded as a function of sample position using a 3D-piezo scanner. It displays pronounced spatial intensity fluctuations with local SH signals increasing by almost two orders of magnitude above the average (Fig. 2a). Since the SH intensity is proportional to the fourth power of the local field enhancement f, $I_{SH} \propto \left(f \cdot E_{loc} \right)^4$, SH emission is a highly sensitive probe of the localized light field E_{loc}. We find enhancement factors $f \approx 2-4$. These SH hot spots are spatially localized to about 0.5 µm, the resolution of our microscope.

In order to gain information about the time structure of these locally enhanced electromagnetic fields, interferometric frequency-resolved (IFROG) autocorrelation traces are recorded with sub-µm spatial resolution on selected individual hot spots (Fig. 2b). Clearly, the recorded autocorrelation traces indicate a considerable increase in pulse duration due to light scattering inside the nanoneedle array. As described elsewhere [4], the time structure of the electric field of light pulses can directly be retrieved from such IFROG traces. When being compared to the incident pulse field (Fig. 2c), the retrieved local electric field from an individual hot spot displays a clear exponential tail with a life time of about 10 – 15 fs. This shows that coherent electromagnetic fields persist for more than 20 fs in individual localization sites until multiple random scattering and/or scattering to the far field destroys the phase coherence of the localized electric field.

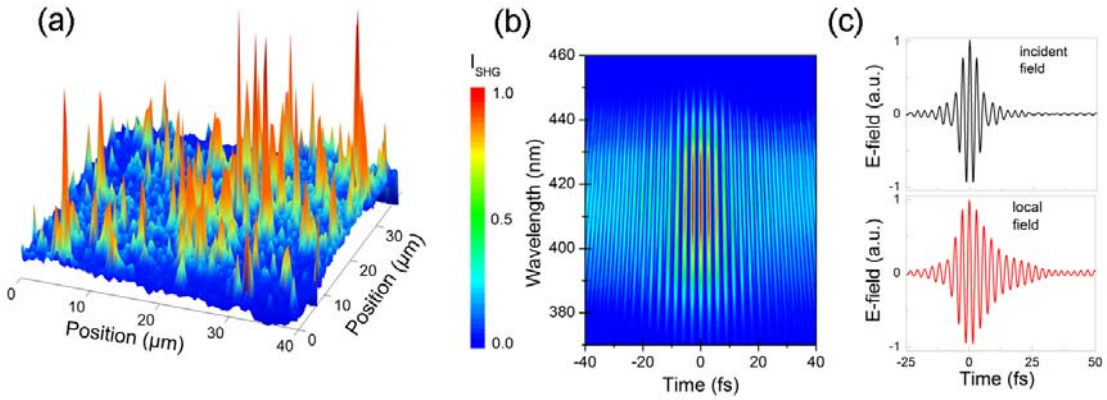

Fig. 2. Spatially-resolved SH emission from the ZnO nanoneedle array after illumination with 6-fs-pulses centered at 800nm. We find random SH enhancements by more than a factor of 100 localized to a 500-nm spot size. (b) Frequency-resolved interferometric autocorrelation (IFROG) trace recorded at an individual localization site in the ZnO nanoneedle array with a spatial resolution of 0.5 µm. (c) Time structure of the electric field of the incident pulses and of the light pulses in an individual localization site of the nanoneedle array reconstructed from spatially-resolved IFROG measurements.

First theoretical simulations clearly confirm the existence of strong resonant field localization and enhancement in random dielectric media with geometries similar to our nanorod arrays. Modelling of the lifetimes of such local fields is currently underway.

To our knowledge, we report the first direct space- and time-resolved study of light localization in a disordered dielectric medium. Key hallmarks of weak localization, in particular the existence of strong spatially localized electromagnetic fields with finite coherence times, are experimentally resolved. This gives new and direct insight into the evolution of the weak (Anderson) localization of light in disordered dielectrics. Such nanoneedle arrays therefore present a highly interesting template for exploring SPP localization in disordered metallic nanostructures as well as random lasing.

References:

[1] D.S. Wiersma, P. Bartolini, A. Lagendijk, and R. Righini, „Localization of light in a disordered medium“, Nature **390**, 671-673 (1997).
[2] M. I. Stockman, “Femtosecond Optical Responses of Disordered Clusters, Composites, and Rough Surfaces: “The Ninth Wave” Effect”, Phys. Rev. Lett. **84**, 1011 (2000).
[3] K. Kitamura, T. Yatsui, M. Ohtsu and G.C. Yi, “Fabrication of vertically aligned ultrafine ZnO nanorods using metal–organic vapor phase epitaxy with a two-temperature growth method”, Nanotechnology **19**, 175305 (2009).
[4] G. Stibenz and G. Steinmeyer, “Interferometric frequency-resolved optical gating”, Opt. Express **13**, 2617 (2005).

B-1 *Invited*

Dressed photon technology for innovative optical devices, fabrications, and systems

Motoichi Ohtsu*[,1]

[1] Department of Electrical Engineering and Information Systems, the University of Tokyo, 2-11-16 Yayoi, Bunkyo-ku, Tokyo 113-8656, Japan
*e-mail: ohtsu@ee.t.u-tokyo.ac.jp

This paper reviews the recent progress of *nanophotonics*, which was proposed by the author in the year 1993[1,2]. The key is to utilize optical near-fields in order to realize novel nanometric device operation, fabrication, and energy conversion, etc., by the control of an intrinsic interaction between nanometer-sized materials. The nature of optical near-fields was studied by regarding the optical near-field as an electromagnetic field that mediates the interaction between nanometric materials. As a result, the physically intuitive concept of a *dressed photon* was established to describe optical near-fields, *i.e.*, the interaction between nanometric materials is mediated by exchanging dressed photons[3,4]. The principles of device operation are reviewed considering the excitation energy transfer via the optical near-field interaction and subsequent relaxation[5]. The operations of logic gates, an optical nano-fountain, a nano-coupler, a pulse generator, a phonon-assisted light emitter, etc. are described as well as their single photon emission and extremely low power consumption capability.

This presentation also reviews nanophotonic fabrications based on phonon-assisted processes triggered by optical-near-field interactions. These processes represent *qualitative* innovation in photochemical vapor deposition and photolithography, suggesting that large, expensive ultraviolet light sources are no longer required, although they are indispensable for conventional adiabatic photochemical vapor deposition, photolithography, and photochemical etching. It also suggests that phonon-assisted photochemical vapor deposition can even dissociate optically inactive molecules (i.e., inactive to the propagating light), which is advantageous for environment protection because most optically inactive molecules are chemically stable and harmless. For example, optically inactive $Zn(acac)_2$ molecules have been dissociated to deposit nanometric Zn particles[6]. In addition, in the case of phonon-assisted photolithography, an optically inactive resist film for electron-beam lithography has been used to fabricate fine patterns[7].

A prototype of the commercial lithography system has been produced in collaboration with industry[8], and has been used for fabricating a diffraction grating[9] and a Fresnel zone plate[10] for the soft X-ray. Furthermore, phonon-assisted photochemical etching and sputtering were developed for realizing ultra-flat surfaces of glass and polycrystalline ceramics, respectively, in a self-organized manner[11,12]. Phonon-assisted deposition will be also reviewed in order to increasing spatial homogeneity of the mol fractional ratio of In in a light emitting InGaN film[13].

References

1) M. Ohtsu, et al., *IEEE J. Selected Topics in Quantum Electronics*, **8** (2002) 839.
2) M. Ohtsu, et al., *IEEE J. Selected Topics in Quantum Electronics*, **14** (2008) 1404.
3) M. Ohtsu and K. Kobayashi, *Optical Near Fields*, Springer-Verlag, Berlin (2003) 109.
4) M. Ohtsu, et al., *Principles of Nanophotonics*, London, England: Tailor & Francis (2008).
5) M. Ohtsu, et al., IEEE J. Selected Topics in Quantum Electron., **8** (2002) 839.
6) T. Kawazoe, et al., *Appl. Phys. B*, **84**, 247 (2006).
7) T. Kawazoe, et al., *Progress in Nano-Electro-Optics V*, (ed)M. Ohtsu, Springer-Verlag, Berlin (2006) 109.
8) Y. Inao, et al., *Microelectronic Eng.*, **84** (2007) 705.
9) M. Koike, et al., *Nanophotonics and Nanofabrication*, (ed)M. Ohtsu, Wiley-VCH, Weinhelm (2009) 179.
10) T. Kawazoe, et al., *Appl. Phys. B*, **98** (2010) 5.
11) T. Yatsui, et al., *Appl. Phys. B*, **93** (2008) 55.
12) W. Nomura, et al., Appl. Phys. B, in press.
13) T.Yatsui, et al., Appl. Phys. B, **97** (2009) 375.

Nanophotonics: Dressed photon technology for innovative devices, fabrications, and systems

M. Ohtsu[1)]

1) Dept. Electrical Eng. and Information Systems, the University of Tokyo
2-11-16 Yayoi, Bunkyo-ku ,Tokyo 113-8656, Japan
Email: ohtsu@ee.t.u-tokyo.ac.jp

Prininciples of nanophotonics, application to novel devices, fabrications, and systems will be presented in order to realize qualitative innovation of the optical technology.

This paper reviews the recent progress of *nanophotonics*, which was proposed by the author in the year 1993[1,2]. The key is to utilize optical near-fields in order to realize novel nanometric device operation, fabrication, and energy conversion, etc., by the control of an intrinsic interaction between nanometer-sized materials. The nature of optical near-fields was studied by regarding the optical near-field as an electromagnetic field that mediates the interaction between nanometric materials. As a result, the physically intuitive concept of a *dressed photon* was established to describe optical near-fields, *i.e.*, the interaction between nanometric materials is mediated by exchanging dressed photons[3,4]. The principles of device operation are reviewed considering the excitation energy transfer via the optical near-field interaction and subsequent relaxation[5]. The operations of logic gates, an optical nano-fountain, a nano-coupler, a pulse generator, a phonon-assisted light emitter, etc. are described as well as their single photon emission and extremely low power consumption capability. Experimental results using quantum dos at the room temperature are described. Using a systems-perspective approach, the principles of content-addressable memory for optical router, a multilayer memory retrieval system, etc. are demonstrated.

This presentation also reviews nanophotonic fabrications based on phonon-assisted processes triggered by optical-near-field interactions. These processes represent *qualitative* innovation in photochemical vapor deposition[6] and photolithography[7], suggesting that large, expensive ultraviolet light sources are no longer required, although they are indispensable for conventional adiabatic methods. A prototype of the commercial lithography system has been produced in collaboration with industry[8], and has been used for fabricating a diffraction grating[9] and a Fresnel zone plate[10] for the soft X-ray. Furthermore, phonon-assisted photochemical etching and sputtering were developed for realizing ultra-flat surfaces of glass and polycrystalline ceramics, respectively, in a self-organized manner[11,12]. Phonon-assisted deposition will be also reviewed in order to increasing spatial homogeneity of the mol fractional ratio of In in a light emitting InGaN film[13].

References

[1]M. Ohtsu, et al., *IEEE J. Selected Topics in Quantum Electronics*, **8**, 839 (2002).
[2]M. Ohtsu, et al., *IEEE J. Selected Topics in Quantum Electronics*, **14**, 1404 (2008).
[3]M. Ohtsu and K. Kobayashi, *Optical Near Fields*, Springer-Verlag, Berlin, 109 (2003).
[4]M. Ohtsu, et al., *Principles of Nanophotonics*, London, England: Tailor & Francis, (2008).
[5]M. Ohtsu, et al., IEEE J. Selected Topics in Quantum Electron., **8**, 839 (2002).
[6]T. Kawazoe, et al., *Appl. Phys. B*, **84**, 247 (2006).
[7]T. Kawazoe, et al., *Progress in Nano-Electro-Optics V*, (ed)M. Ohtsu, Springer-Verlag, Berlin, 109 (2006).
[8]Y. Inao, et al., *Microelectronic Eng.*, **84**, 705 (2007).
[9]M. Koike, et al., *Nanophotonics and Nanofabrication*, (ed)M. Ohtsu, Wiley-VCH, Weinhelm, 179 (2009).
[10]T. Kawazoe, et al., *Appl. Phys. B*, **98**, 5 (2010).
[11]T. Yatsui, et al., *Appl. Phys. B*, **93**, 55 (2008).
[12]W. Nomura, et al., Appl. Phys. B, in press.
[13]T.Yatsui, et al., Appl. Phys. B, **97**, 375 (2009).

Efficient and Robust Energy Transfer Network in Quantum Dot Mixtures via Optical Near-Fields Interactions

Makoto Naruse[1),2)], Tadashi Kawazoe[2)], and Motoichi Ohtsu[2)]

1) National Institute of Information and Communications Technology, 4-2-1 Nukui-kita, Koganei, Tokyo 184-8795, Japan

naruse@nict.go.jp

2) The University of Tokyo, 2-11-16 Yayoi, Bunkyo-ku, Tokyo 113-8656, Japan

Abstract: We theoretically and experimentally investigate an optimal mixture of different-sized quantum dots so that energy transfers via near-field interactions are efficiently induced. We also demonstrate the near-field interaction network provides robustness to tolerate system errors.

OCIS codes: (250.5590) Quantum-well, -wire and -dot devices, (260.2160) Energy transfer, (999.9999) Nanophotonics

There have been in-depth theoretical and experimental efforts to reveal and exploit optical near-field interactions on the nanometer scale because of their potential impact in a wide range of applications. One of the unique functions available is the optical excitation transfer between nano-scale matter [1-3] via optical near-field interactions that even allow populating energy levels that are conventionally dipole forbidden [1]. Here we assume two spherical quantum dots whose radii are R_S and R_L, which are denoted by QD_S and QD_L respectively in Fig. 1(a). The energy eigenvalues of states specified by quantum numbers (n,l) are given by $E_{nl} = E_g + E_{ex} + \hbar^2\alpha_{nl}^2 / 2MR^2$ (n=1,2,3,…) where E_g is the band gap energy of the bulk semiconductor, E_{ex} is the exciton binding energy in the bulk system, M is the effective mass of the exciton, and α_{nl} are determined from the boundary conditions. There exists a resonance between the level of quantum number (1,0) of QD_S and that of quantum number (1,1) of QD_L if $R_L / R_S = 4.49/\pi \sim 1.43$. Due to the large spatial inhomogeneity of the localized optical near-fields at the surface of nano-scale material, an optical transition to the (1,1)-level in QD_L, which is conventionally forbidden, is allowed. Therefore, an exciton in the (1,0)-level in QD_S could be transferred to the (1,1)-level in QD_L. In QD_L, due to the sublevel energy relaxation with a relaxation constant Γ, which is faster than the near-field interaction, the exciton relaxes to the (1,0)-level, from where it radiatively decays.

Here we consider a quantum dot system, as shown in Fig. 1(b), where multiple smaller dots (denoted by S1, S2, …, SN) can be coupled with one large dot (denoted by L). We also assume inter-dot interactions between adjacent smaller quantum dots; that is, (i) Si interacts with S(i+1) (i=1,…,N-1), and (ii) SN interacts with S1, where N is the number of smaller QDs. Now, what is of interest is maximizing the flow of excitons from smaller dots to larger one. We deal with this problem theoretically based on a density matrix formalism. In the case of the system shown in Fig. 1(c), composed of two smaller QDs and one larger QD, the inter-dot interactions between smaller dots and larger one are denoted by U_{SiL}, and that between the smaller dots is denoted by U_{S1S2}. The radiations from S1, S2, and L are respectively represented by the relaxation constants γ_{S1}, γ_{S2}, and γ_L. We suppose that the system initially has two excitons in S1 and S2. With such an initial state, we can prepare a total of eleven bases where zero, one, or two exciton(s) occupy the energy levels. We derive quantum master equations in the density matrix formalism. In the numerical calculation, we assume $U_{S_iL}^{-1} = 200$ ps, $U_{S_iS_j}^{-1} = 100$ ps, $\Gamma^{-1} = 10$ ps, $\gamma_L^{-1} = 1$ ns, and $\gamma_{S_i}^{-1} = (R_L / R_S)^3 \times \gamma_L^{-1}$ ~2.92 ns as a typical parameter set for the CdSe/ZnS quantum dots used for our experiments below. Following the same procedure, we also derive quantum master equations for systems consisted of three smaller QDs (N=3), four smaller QDs (N=4), and five smaller QDs (N=5) with initial states in which all smaller quantum dots have excitons. Finally, we can calculate the population of the lower level of QD L, of which time integral we regard as the output signal.

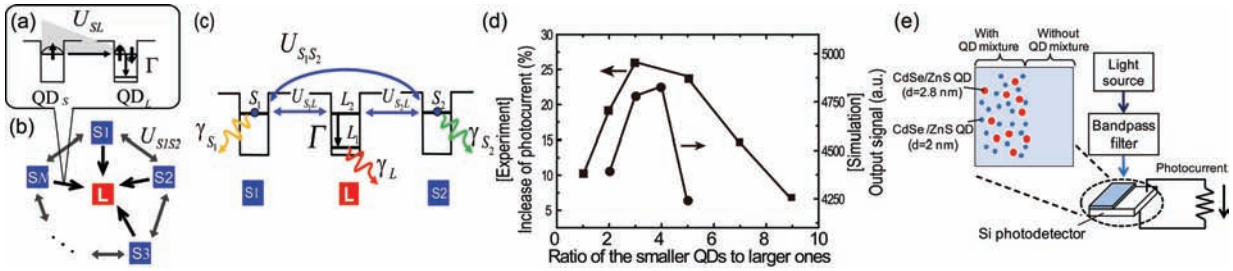

Fig. 1 (a,b,c) Optical near-field interaction network between smaller and larger QDs (d) Optical excitation transfer exhibits its maximum efficiency with an appropriate QD mixture. (e) Experimental setup for the verification of the optimal QD mixture.

We compare the output signal as a function of the ratio of the number of smaller dots to larger one assuming that the total number of QDs, regardless of their sizes (smaller or larger), in a given unit area is the same. As shown in the circles in Fig. 1(d), the most efficient transfer was obtained when the ratio of the number of smaller dots to the larger one is 4. That is, increasing the number of smaller quantum dots does not necessarily contribute to increased output signal. Because of the limited radiation lifetime of QD L, not all of the initial excitons can be successfully transferred to QD L due to the state filling of the lower level of QD L. Therefore, part of the input populations must be decayed at QD S, which results in loss in the transfers from the smaller QDs to the larger one.

Such an *optimal* mixture of smaller and larger QDs was experimentally demonstrated by using two kinds of CdSe/ZnS core/shell quantum dots whose diameters were 2.0 nm and 2.8 nm, respectively. The quantum dots were dispersed in a matrix composed of toluene and ultraviolet curable resin, and coated on the surface of a silicon photodiode (Hamamatsu Photonics K.K., Si Photodiode S2368). As schematically shown in Fig. 1(e), half of the surface of the photodiode was spin-coated by an ultraviolet-curable resin with a mixture of quantum dots and cured by ultraviolet radiation, whereas the other half of the surface was coated by the same resin without the quantum dot mixture. Input light was selectively radiated onto each area to evaluate the difference in the generated photocurrent. The increase of the induced photocurrent via the QD-coated area with input light wavelengths between 340 nm and 360 nm is shown by the square marks in Fig. 1(d). We attribute such increase to the optical excitation transfer through which the input light wavelength is red-shifted to wavelengths where the photodetector is more sensitive. The maximum increase was obtained when the ratio of the number of smaller QDs to larger QDs was 3:1. This agrees with the theoretical optimal ratio of the number of smaller quantum dots to larger ones discussed above.

Finally, we highlight another function of the interactions between smaller dots. Fig. 2(a) schematically represents systems where four smaller dots surround one larger dot. Here, we suppose that some of the interactions between the smaller dots and the larger one are degraded. Such a weak interaction could physically correspond to situations, for instance, where the distance between the smaller dot and the larger one is very large, or the size or the shape of the quantum dots deviates from the required conditions for energy transfer, or other reasons. In the System A in Fig. 2(a), QD S1 and S3 have weak interactions with QD L. In the System B in Fig. 2(a), *all* of the interactions between smaller dots are assumed to be negligible, in addition to the weak interactions assumed in System A. What is of interest is to evaluate the impact of the interactions between smaller dots on the energy transfer from the smaller dots to the larger one as a total system. The curves A and B in Fig. 2(a) respectively represent the evolutions of the population of the radiation from QD L in System A and System B, where the former exhibits a higher population compared with the latter. In System A, thanks to the interactions between smaller dots, the excitations in S1 and S3 can be successfully transferred to L by way of the adjacent smaller dots. On the other hand, it is hard for the excitations in S1 and S3 in System B to be transferred to L due to the weak interactions with the surrounding dots. From a system perspective, the interactions among smaller dots provide *robustness* to degradation of the excitation transfer from the smaller dots to larger ones. To quantitatively evaluate such robustness, we introduce the probability that an interaction between a smaller dot and a larger one suffers interaction degradation or loss; we denote it by p $(0 \le p \le 1)$. We can derive the expected output signal level as a function of p. The curves A and B in Fig. 2(b) respectively represent the expected output signals corresponding to systems with and without interactions between smaller dots as a function of the interaction loss probability between a smaller dot and a larger one. The curves A' and B' in Fig. 2(c) represent those when the number of smaller dots is five. As shown in the curves A and A', thanks to the existence of interactions between smaller dots, the expected output signal levels remain higher, even greater than the no-error situation (p=0) especially in the curve A', although they suffer a larger value of p. This is a manifestation of the improved robustness of the system provided by the interactions between smaller dots.

References

[1] M. Ohtsu, et al., Principles of Nanophotonics (Taylor and Francis, Boca Raton, 2008).
[2] V. I. Klimov ed., Semiconductor and Metal Nanocrystals (Marcel Dekker, New York, 2003).
[3] T. Franzl, T. A. Klar, S. Schietinger, A. L. Rogach, and J. Feldmann, Nano Lett. **4**, 1599 (2004).

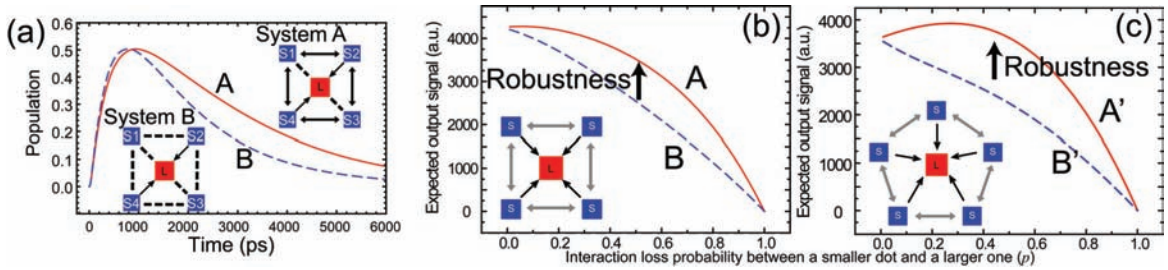

Fig. 2 (a) Output population from degrated systems (b,c) The inter-smaller-dot interactions provide *robustness* to tolerate errors

Self-organized Nonadiabatic Optical Near-field Assisted Sputtering for Repairing Surface Scratches on Al_2O_3 Ceramic Substrate

W. Nomura[1),a)], T. Yatsui[1)], Y. Yanase[2)], K. Suzuki[2)], M. Fujita[2)], A. Kamata[2)], M. Naruse[3,1)], and M. Ohtsu[1)]

1) School of Engineering, The University of Tokyo, and The Nanophotonics Research Center, The University of Tokyo, 2-11-16 Yayoi, Bunkyo-ku, Tokyo 113-8656, Japan

2) Core Technology Center, Covalent Materials Corporation, 30, Soya, Hadano-shi, Kanagawa 257-8566, Japan

3) National Institute of Information and Communications Technology, 4-2-1 Nukui-kita, Koganei, Tokyo 184-8795, Japan

a) nomura@nanophotonics.t.u-tokyo.ac.jp

The scratches on the surface of Al_2O_3 ceramics were repaired by optical near-field assisted sputtering with laser irradiation of 473-nm wavelength in a self-organized manner. Their average depth decreased from 3.2 nm to 0.79 nm.

OCIS code: (310.1860) Deposition and fabrication; (350.4238) Nanophotonics and photonic crystals;

1. Introduction

Transparent ceramics are attracting interest in optical technology applications as gain media for solid-state lasers or optical windows. To increase the lasing efficiency and reduce the scattering loss in optical windows, further decreases in the surface roughness are required. However, conventional chemical–mechanical polishing does not work well on polycrystalline ceramics because of their anisotropic interaction with the polishing medium. To solve these problems, we developed a novel method of optical near-field (ONF)-assisted sputtering, which is based on nonadiabatic photochemical reactions and near-field photodesorption [1,2]. Here, we use this method to repair the scratches on polycrystalline Al_2O_3 ceramics in a self-organized manner [3].

2. Experiment

Figure 1(a) shows a schematic of the experimental setup. Planar surfaces of SAPPHAL® [4] substrate were prepared by polishing using diamond abrasive grains with a diameter of 0.5 μm. The Al_2O_3 was deposited using radio-frequency (RF) magnetron sputtering (RF power: 300 W; frequency: 13 MHz; sputtering time: 30 min). The total gas pressure was 7×10^{-1} Pa, with a gas flow of 16 sccm Ar and 1.2 sccm O_2 [5]. We used SAPPHAL® as the sputtering target material. During the sputtering, we irradiated the sample surface with the CW second harmonic of a Nd:YAG laser with wavelength of $\lambda = 473$ nm and optical power density 2.7 W cm^{-2}.

When the ceramic substrate was irradiated, a highly localized optical near field was generated at the edges of scratches, causing the photodesorption of depositing Al_2O_3 nanoparticles. Hence, the sputtered Al_2O_3 particles

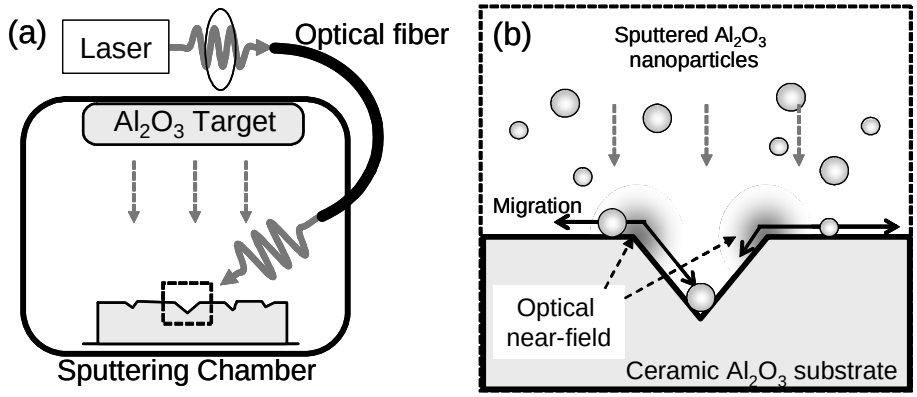

Fig. 1 (**a**) Schematic of the experimental setup. (**b**) Schematic of the ONF-assisted sputtering (magnified image of the dashed box in (a)).

migrated through the edge of scratched grooves and accumulated on the bottom of the groove (see Fig. 1(b)). As a result, the scratched grooves were selectively repaired. This process automatically stopped in a self-organized manner after the scratches were repaired, so that the optical near field could no longer be generated.

3. Result and discussion

Figures 2(a) and (b) show typical Atomic Force Microscope (AFM) images of SAPPHAL® surfaces before and after ONF-assisted sputtering, respectively. As can be seen, the scratches were repaired by the sputtering. To evaluate the scratch removal quantitatively, we used the Hough transform to extract the linear features of the scratched grooves from these AFM images [6]. We then evaluated the depth of the scratched grooves along the detected straight lines. Figures 2(c) shows statistical analyses of the depth of scratched grooves obtained from the AFM images in Figure 2(a) and (b). The average values of the depth before and after ONF-assisted sputtering were 3.2 and 0.79 nm, respectively. This confirmed that the depth of the scratches was drastically decreased using the ONF-assisted sputtering. Further decreases in the width could be achieved by optimizing laser and sputtering conditions.

4. Conclusion

We used a self-organized ONF-assisted sputtering method to repair the scratched grooves on a polycrystalline Al_2O_3 ceramic surface. We confirmed that the grooves were repaired by RF sputtering of Al_2O_3 with laser irradiation at a wavelength of λ = 473 nm. Using AFM measurement and the Hough transform, we found a drastic decrease in the average depth, from 3.2 to 0.79 nm. This approach clearly revealed the effects of the ONF-assisted sputtering, which selectively repaired the scratched grooves. We believe that our method is applicable to a variety of substrates, including ceramic and crystal substrate. Furthermore, this method is compatible with mass production.

References

[1] T. Kawazoe, K. Kobayashi, S. Takubo, M. Ohtsu, "Nonadiabatic photodissociation process using an optical near field," J. Chem. Phys. **122**, 024715 (2005).

[2] T. Yatsui, W. Nomura, and M. Ohtsu, "Self-Assembly of Size- and Position-Controlled Ultralong Nanodot Chains using Near-Field Optical Desorption," Nano Lett. **5**, 2548 (2005).

[3]] W. Nomura, T. Yatsui, Y. Yanase, K. Suzuki, M. Fujita, A. Kamata, M. Naruse and M. Ohtsu, "Repairing nanoscale scratched grooves on polycrystalline ceramics using optical near-field assisted sputtering." Appl. Phys. B, in press [DOI 10.1007/s00340-009-3797-0]

[4] A product of the Covalent Materials Corporation: http://www.covalent.co.jp/

[5] J. B. Wachtman, A. R. Haber, *Ceramic Films and Coatings* (William Andrew Publishing / Noyes, New York, Norwich 1993).

[6] R. O. Duda, P. E. Hart, "Use of the Hough transformation to detect lines and curves in pictures," Commun. ACM **15**, 11 (1972).

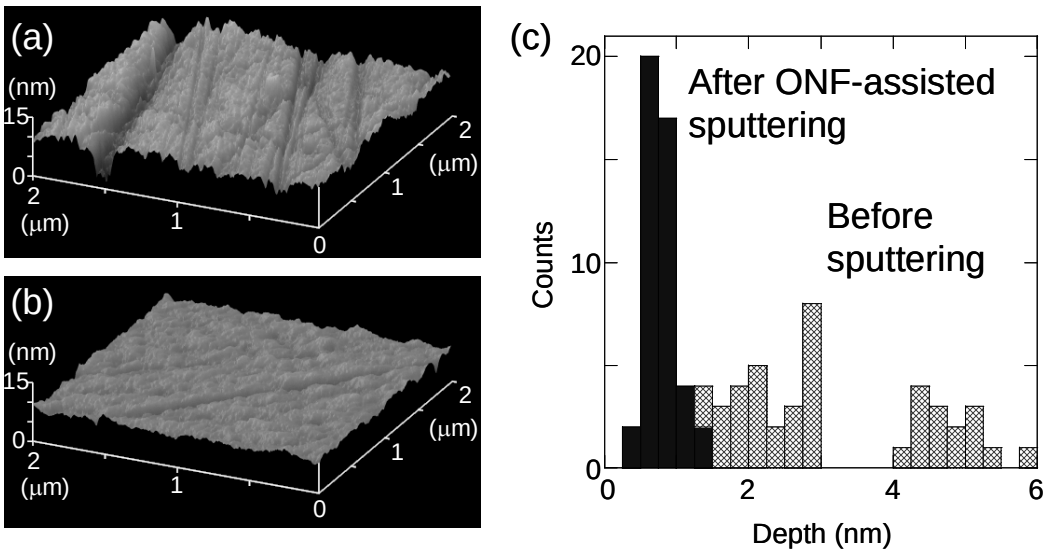

Fig. 2 AFM images of Al_2O_3 ceramic substrates (**a**) before and (**b**) after ONF-assisted sputtering. (**c**) Histograms of the depth of scratched grooves on substrates before (mesh bar) and after ONF-assisted sputtering (black bar).

Self-organized nanophotonic signal transmission device

T. Yatsui,[(1),] Y. Ryu,[(1)] T. Morishima,[(1)] W. Nomura,[(1)] T. Yonezawa,[(2)] M. Washizu,[(1)] H. Fujita,[(3)] and M. Ohtsu[(1)]

(1)School of Engineering, The University of Tokyo, 2-11-16 Yayoi, Bunkyo-ku, Tokyo, Japan 113-8656
+81 3-5841-0416, +81 3-5841-0406
(2)Graduate School of Engineering, Hokkaido University, Sapporo, Hokkaido, Japan 060-8628
(3)Institute of Industrial Science, University of Tokyo, Meguro-ku, Tokyo, Japan, 153-8505
yatsui@ee.t.u-tokyo.ac.jp

Abstract: We developed a self-assembly method for alignment of ZnO quantum dots (QDs) into a straight line. The polarization dependence of photoluminescence intensity revealed the signal transmission via an optical near-field along the QD chain.

OCIS codes: (230.5590) Quantum-well, -wire and -dot devices, (220.4241) Nanostructure fabrication

Innovations in optical technology are required for the development of future information processing systems, which includes increasing the integration of photonic devices by reducing their size and levels of heat generation. To address these requirements, it has been proposed that the chains of closely spaced metal nanoparticles can convert the optical mode into non-radiating surface plasmonic waves [1,2]. However, they have several disadvantages in that they cannot break the plasmon diffraction limit, and cannot avoid reflection at the output port. To overcome these difficulties, we proposed nanophotonic signal transmission (NST) devices that consist of semiconductor quantum dots (QDs) [3]. These NST devices are operated using excitons in QDs as the signal carrier, due to optical near-field interactions between closely spaced QDs. The exciton energy transfers to another QD when the exciton energy levels are resonant and, therefore, the optical beam spot may be decreased to be as small as the QD size. The advantages of NST devices using metal nanoparticles are as follows. 1) NST devices using semiconductor QDs have higher transmission efficiency because QDs have low coupling efficiency to lattice vibrational mode. The lattice vibration is the main cause of large propagation loss in plasmonic waveguides. 2) By introducing a larger QD as an output port in which the first excited state resonates to the ground state of the smaller QD, the energy reflection at the output QD can be avoided by energy dissipation due to the sublevel energy transmission in the larger QD. To produce the NST device, a new technique is required for positioning and alignment of QDs with precise separation.

Figure 1(a) illustrates our approach for the development of a self-assembling NST device with angstrom-scale controllability in spacing among QDs using silane-based molecular spacers and DNA [4,5]. First, ZnO QDs 5 $\pm$ 0.5 nm in diameter were synthesized using the Sol-Gel method [6,7]. Then, the surfaces of QDs were coated with a silane coupling agent ($N^{+}(CH_3)_2(CH_2)_3Si(OCH_3)_3$) 0.6 nm in length. The function of the agent is to maintain the spacing between QDs, and to be adhesive to anionic DNA, due to its cationic nature. We used λ-DNA (48kb, stretched length = 16 μm) as a template, and when the QDs are mixed, the QDs are self-assembled onto the DNA by electrostatic interactions. Dense packing of the ZnO QDs along the DNA was obtained, as shown by transmission electron micrography (TEM) (Fig. 1(b)). The separation between QDs (*S*) was determined by TEM and shown to be 1.2 nm (Fig. 1(c)), which was in good agreement with twice the length of silane coupling agents. Such a high

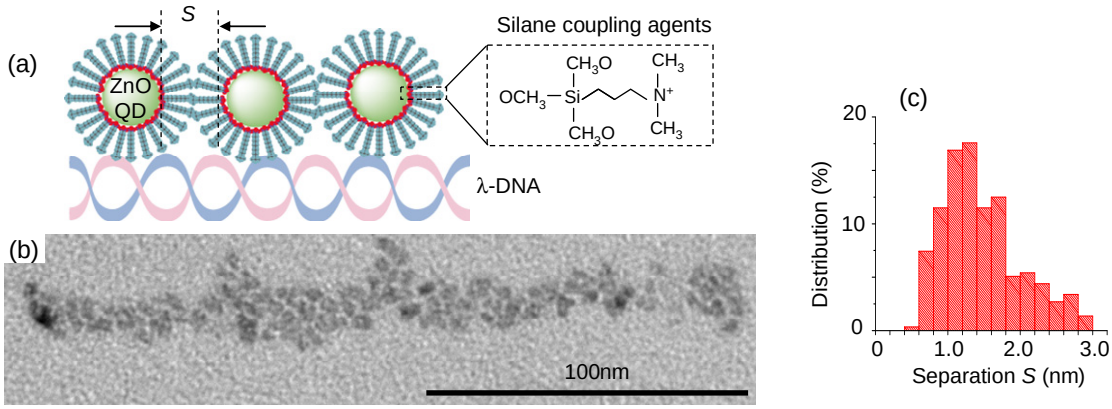

Fig. 1 Fabrication and evaluation of nanophotonic signal transmission device. (a) Schematic of ZnO QD alignment along the λ DNA. *S*: separation between QDs (b) TEM picture of the aligned ZnO QDs. (c) Separation distribution.

density of packing, despite the electrostatic repulsion between ZnO QDs, was due to the quaternary ammonium group of the silane coupling agent [4].

To observe the optical properties of the aligned ZnO QDs, the DNA with QDs was stretched and straightened on the silicon substrate using combing technique [8], where the silicon substrate was terminated with silane coupling agent and the anionic DNA was adsorbed on the cationic silicon substrate. We obtained the isolated chain of ZnO QDs (see Fig. 2(a)). From the polarization dependence of photoluminescence (PL) at a wavelength of 350 nm (Figs. 2(b) and 2(c)), corresponding to the ground state of 5-nm ZnO QDs, the strong PL emission was obtained by excitation of parallel polarization along the QD chains (E_0). Previous studies on the excitation polarization dependence of nanorods [9] indicated that the PL under parallel excitation (E_0) is much greater than that under perpendicular polarization (E_{90}), due to the absorption anisotropy. Similar polarization dependence was observed in our chained structure. It is possible that the dipoles between adjacent QDs are coupled with optical near-field interaction, and QD chains have large dipolar strength (see Fig. 2(c)), indicating that they act as an NST device along the chained QDs.

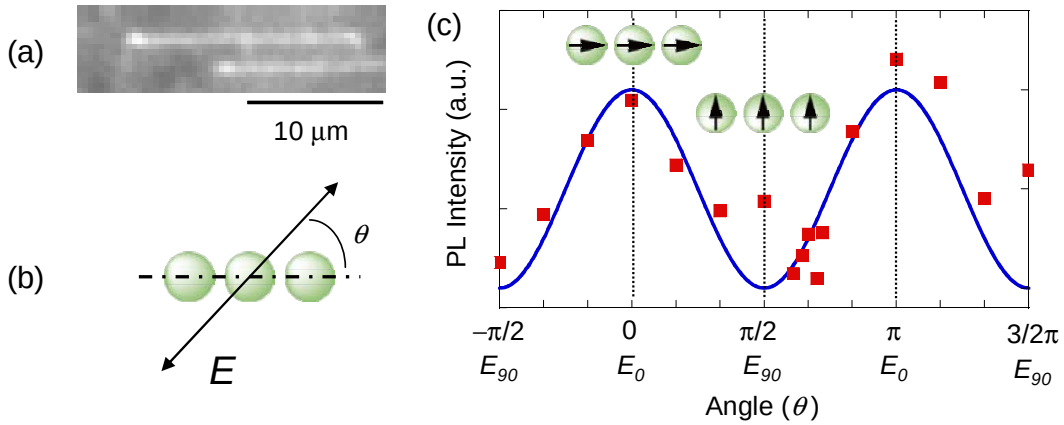

Fig.2. (a) Stretched ZnO QD chain along the λ DNA. (b) θ: Polarization angle with respect to the direction along the QD chains. (c) Incident light polarization dependence of PL intensity. A 4th-harmonic, Q-switched Nd:YAG laser (λ = 266 nm) was used to excite the ZnO QDs.

As optical near-field energy can transmit through the resonant energy level, NST devices have a number of potential applications, such as wavelength division multiplexing using QDs of different sizes.

References

1. S.A. Maier, P.G. Kik, H.A. Atwater, S. Meltzer, E. Harel, B.E. Koel, A.A.G. Requicha, "Local detection of electromagnetic energy transport below the diffraction limit in metal nanoparticle plasmon waveguides," Nature Mat. **2**, 229-232 (2003).
2. W. Nomura, M. Ohtsu, and T. Yatsui, "Nanodot coupler with a surface plasmon polariton condenser for optical far/near-field conversion," Appl. Phys. Lett. **86**, 181108 1-3 (2005).
3. M. Ohtsu, T. Kawazoe, T. Yatsui, M. Naruse, "Nanophotonics: Application of dressed photons to novel photonic devices, and systems," IEEE J. Select. Top. Quant. Electron. **14**, 1404-1417 (2008).
4. T. Yonezawa, S. Onoue, N. Kimizuka, "Metal Coating of DNA Molecules by Cationic, metastable gold nanoparticles," Chem. Lett. **31** 1172-1173 (2002).
5. M.G. Warner and J.E. Hutchison, "Linear assemblies of nanoparticles electrostatically organized on DNA scaffolds," Nature Mater. **2**, 272-277 (2003).
6. E.A. Meulenkamp, "Synthesis and growth of ZnO nanoparticles," J. Phys. Chem. B **102**, 5566-5572 (1998).
7. T. Yatsui, H. Jeong, and M. Ohtsu, "Controlling the energy transfer between near-field optically coupled ZnO quantum dots," Appl. Phys. B **93**, 199-202 (2008).
8. H. Oana, M. Ueda, M. Washizu, "Visualization of a specific sequence on a single large DNA molecule using fluorescence microscopy based on a new DNA-stretching method," Biochem. Biophys. Research Commun. **265**, 140-143 (1999).
9. J. Wang, M. S. Gudiksen, X. Duan, Y. Cui, C.M. Lieber, "Highly polarized photoluminescence and photodetection from single indium phosphide nanowires," Science **293**, 1455-1457 (2001).

Nanophotonic Devices by Dressed Photon Exchange

M. Ohtsu
School of Engineering, The University of Tokyo, 2-11-16 Yayoi, Bunkyo-ku, Tokyo, Japan 113-8656
ohtsu@ee.t.u-tokyo.ac.jp

Abstract: Nanophotonics is defined, and a physical picture of dressed photons is presented. Room-temperature nanophotonic logic gates and related devices are demonstrated. An application for an optical router system is also reviewed.

OCIS codes: (230.5590) Quantum-well, -wire and -dot devices, (250.3750) Optical logic devices

1. Introduction

Nanophotonics or "dressed photon technology" was proposed by M. Ohtsu in 1993 [1]. It is a novel method that utilizes the optical near field, which is the electromagnetic field that mediates the interaction between close nanometric particles. Nanophotonics allows “qualitative innovation” in photonic devices, fabrication techniques, and systems using novel phenomena caused by optical-near field interactions. As these interactions are impossible when conventional propagating light is used, the principles of nanophotonics are different from those of plasmonics and crystal, metamaterial, and silicon photonics. This paper reviews the principles and practice of nanophotonics, particularly its applications to novel photonic devices.

2. Principles

M. Ohtsu's 1993 proposal was motivated by the need to break the deadlock of conventional optical technology. This was necessary to realize advanced information systems with high capacities and transmission rates. To decrease the size of light below the diffraction limit, a promising method is to use the optical near field. This field is non-propagating; it is localized on the surface of the nanometric material. The localization size is equivalent to the material size and is independent of the wavelength of the incident light.

The optical near field is the virtual cloud of photons generated on the surface of an illuminated nanometric material [2]. To use the optical near field for novel device operation, a second nanometric material is installed close to the first, which allows for optical near-field energy transfer. Under illumination, virtual photon clouds are generated on the surfaces of the two materials and exchange energy. Scattered photons are also generated from the materials. The nanometric system, which consists of the two materials and their virtual photon clouds, is buried by the macroscopic system, which consists of the incident light, the scattered light, and the macroscopic material. Energy is exchanged between these systems through the absorption / emission of scattered photons and phonons. Thus, the virtual photon clouds should be represented by photons, material excitations, and relaxations.

To draw a physically intuitive picture of such a complex system, it is essential to select an appropriate base function. For this purpose, the base function of the coupled state of light and material excitation can be very useful. It expresses the optical near field as the dressed photon, i.e., the photon carrying the material excitation. As a result, the interaction between the nanometric materials can be simply described by emission, absorption, and scattering of dressed photons in a physically intuitive manner.

The magnitude of the effective interaction energy by dressed photon exchange is estimated by including the effect of the macroscopic system *via* renormalization. As a result, it is expressed as a screened potential (Yukawa function), and the range of interaction is determined by the material size.

3. Nanophotonic devices and their applications

Energy transfer to an electric dipole-forbidden state is a novel phenomenon that allows for qualitative innovation in device operations [3]. Because the range of the optical near-field interaction is equivalent to the material size and is much shorter than the optical wavelength, the long-wavelength approximation is not applied. This means that the exciton generated in the electric dipole-allowed state of a semiconductor quantum dot (QD) can be transferred to the resonant electric dipole-forbidden state of the adjacent QD by dressed photon exchange. If the transferred exciton is quickly relaxed to a lower energy level, unidirectional energy transfer from one QD to the other occurs. This has possible applications in device operation.

One example of a nanophotonic device based on this principle is the optical switch, or AND gate. Three QDs of different sizes are used as the input-, output-, and control ports of the device. Dynamic operation with a rise time of 25 ps has been confirmed using CuCl QDs embedded in a NaCl crystal at a temperature of 5 K [3]. The second example is a NOT gate, which is formed using two different-sized QDs [4]. Optical near-field

energy transfer and light-induced linewidth broadening are used in the NOT gate. Its operation has also been confirmed using CuCl QDs at 5 K.

For room temperature operation, three-layered and two-layered InAs QDs have been grown as AND and NOT gates, respectively, by size- and site-controlled molecular beam epitaxy [4]. The sides of the layers were removed using nonadiabatic nanophotonic lithography, to form two-dimensional arrays of these devices [5]. Device operation has been confirmed at 280 K.

By modifying these device operations, NOR-, OR-, and NAND gates have been formed. This allows for a complete set of logic gates to be realized. The fan-out is given by the ratio between the carrier lifetime of the QD for free photon emission and the time-constant of the optical near-field energy transfer. It has been estimated as 5 and 10 for the AND gates using InAs and CuCl QDs, respectively.

To connect the nanophotonic devices to conventional macroscopic photonic devices, an optical nano-fountain device was proposed that could transform the propagating light to the optical near field with high efficiency [6]. By the optical near-field energy transfer and subsequent relaxation from a smaller to a larger QD, the optical energy of the incident propagating light was concentrated on the largest QD with an optical spot size smaller than 10 nm. This was achieved using CuCl QDs at 5 K. Room temperature operation was achieved by InAs QDs [7].

Nanophotonic devices have unique features in their operation: (1) Low heat generation; because the heat is generated only through relaxation from the upper to lower quantized energy levels of the QD excitons, the magnitude of the generated heat is estimated to be 10^{-5} that of conventional electronic transistor devices. This suggests that the devices may be integrated extremely closely without increasing their temperature. (2) Single photon operation [8]; due to the intrinsic photon-blocking feature in the optical near-field energy transfer, 99.3 % plausibility of single photon emission has been confirmed by a photon-correlation experiment with 99.98 % accuracy. This suggests that extremely low-power devices will be possible. (3) Difficulty of non-invasive attack [9]; because the energy is dissipated only through the non-radiative relaxation, as was described in (1), non-invasive attack is extremely difficult compared to that in conventional wired electronic devices. This suggests novel information security system applications.

Because of these unique features, nanophotonic devices could allow us to develop novel display systems, optical information processing, energy conversion, and input/output interfaces. Some of these technologies have already been developed in collaboration with industry. For application to a highly integrated and low-power optical router system, content-addressable memory operation has been demonstrated (Fig. 1). For a global sum system, an optical nano-fountain has been used for three-bit digital-to-analog conversion [10]. For a broadcast system, three nanophotonic switches have been used to distribute an optical signal to three output channels [11].

4. Summary

The advantages of nanophotonic devices over conventional photonic devices are their low power consumption, small size, correlation functions, and high tamper resistance. Coupling the dressed photons with various elementary excitations, such as magnons, in a nanometric space will allow electron spin properties to be used in further novel device operations.

References

[1] M. Ohtsu, K. Kobayashi, T. Kawazoe, T. Yatsui, and M. Naruse, *Principles of Nanophotonics*, (Tailor&Francis, 2008), Preface.
[2] K. Kobayashi Sangu, H. Ito, and M. Ohtsu, "Near-field optical potential for a neutral atom", Phys. Rev.A, **63**, pp.013806 1-9 (2001).
[3] T. Kawazoe, K. Kobayashi, S. Sangu, and M. Ohtsu, "Demonstration of a nanophotonic switching operation by optical near-field energy transfer", Appl. Phys. Lett., **82**, pp.2957-2959 (2003).
[4] T. Kawazoe, K. Kobayashi, K. Akahane, M. Naruse, N. Yamamoto, and M. Ohtsu, "Demonstration of nanophotonic NOT gate using near-field optically coupled quantum dots", Appl. Phys. B, **84**,pp.243-246 (2006).
[5] H. Yonemitsu, T. Kawazoe, K. Kobayashi, and M. Ohtsu, "Nonadiabatic photochemical reaction and application to photolithography", J. Photoluminescence, **122**, pp.230-233(2007).
[6] T. Kawazoe, K. Kobayashi, and M. Ohtsu, "Optical nanofountain: A biomimetic device that concentrates optical energy in a nanometric region", Appl. Phys. Lett., **86**, pp. 103102 1-3 (2005).
[7] K. Akahane and N. Yamamoto, under preparation for publication
[8] T. Kawazoe, S. Tanaka, and M. Ohtsu, "A single-photon emitter using excitation energy transfer between quantum dots", J. Nanophotonics, **2**, pp.029502 1-6 (2008).
[9] M. Naruse, H. Hori, K. Kobayashi, and M. Ohtsu, "Tamper resistance in optical excitation transfer based on optical near-field interactions", Opt. Lett., **32**, pp.1761-1763 (2007).
[10] M. Naruse, T. Miyazaki, F. Kubota, T. Kawazoe, K. Kobayashi, S. Sangu, and M. Ohtsu, "Nanometric summation architecture based on optical near-field interaction between quantum dots", Opt. Lett., **30**, pp.201-203 (2005).
[11] M. Naruse, T. Kawazoe, S. Sangu, K. Kobayashi, and M. Ohtsu, "Optical interconnects based on optical far- and near-field interactions for high-density data broadcasting", Opt. Express, **14**, pp.306-313 (2005).

OMH2.pdf

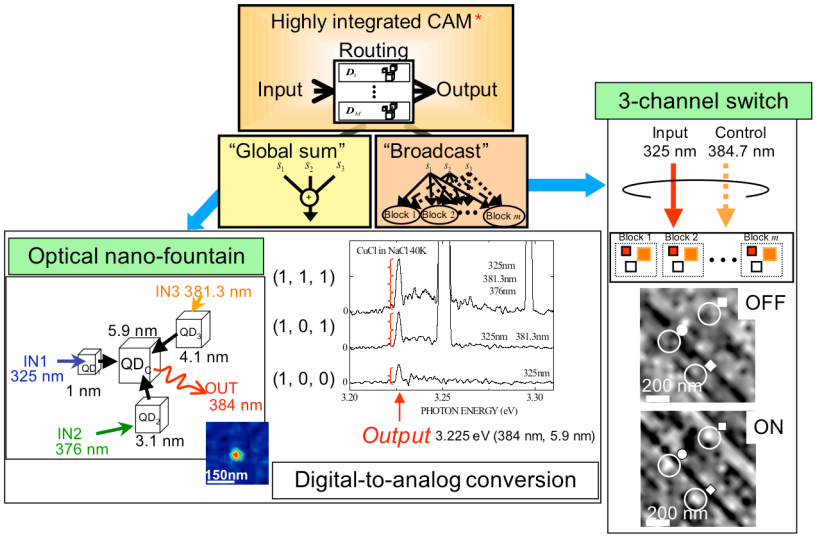

Fig. 1 Experimental demonstrations of CAM (content addressable memory) [10,11].

Phonon-assisted visible light photocatalyst using ZnO nanorods

oK. Kitamura, T. Yatsui, H. Yasuda, T. Kawazoe, and Motoichi Ohtsu

Department of Electrical Engineering and Information Systems,
School of Engineering, the University of Tokyo
2-11-16 Yayoi, Bunkyo-ku, Tokyo

Since conventional photocatalyst material of TiO_2 is activated only under UV light irradiation, the effective utilization of visible light has been one of the most important objectives. Here we report visible light photocatalyst reaction using phonon-assisted optical near-field process. Schematic of this process is shown in Fig. 1. To excite the carriers using propagating light, the higher photon energy than band gap energy is required (3.3 eV for ZnO). While, the usage of the optical near-field allows us to excite the dipole forbidden phonon state, which is called as a non-adiabatic process [1]. To realize high efficiency of the non-adiabatic excitation process, we introduced ZnO nanorods grown by MOVPE, which were used for semiconductor electrodes (Fig. 2). Optical near-field generated around the material depends on the size of material. The diameter of the ZnO nanorods is controlled by the growth temperature in MOVPE process. We prepared two samples of ZnO nanorod with the diameters D of 100 nm (sample 1) and 10nm (sample 2). Using these electrodes, water splitting reaction was performed. Current was measured under laser irradiation. The potential of the electrodes was maintained at open circuit potential under a non-irradiated condition by potentiostatically. We used bulk single crystal ZnO substrate with a flat surface as reference. Figs. 3 (a) and (b) show the dependence of current on power of UV (3.8 eV) and visible (2.6 eV) laser, respectively. Under UV laser irradiation, all samples had similar dependence. While, under visible light irradiation, more than four times higher current was measured using sample 2 than others. This result indicated that the efficient non-adiabatic excitation process due to phonon-assisted optical near field was realized by introducing the fine structure as small as 10 nm.

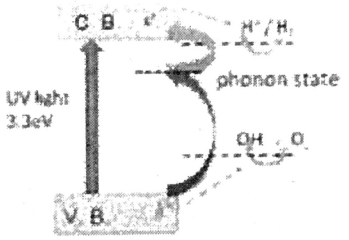

Fig. 1 Phonon-assisted non-adiabatic excitation process.

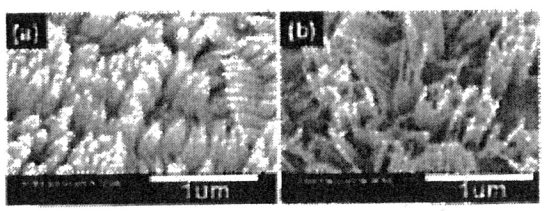

Fig. 2 SEM images of (a) Sample 1 (D = 100nm) and (b) Sample 2 (D = 10 nm).

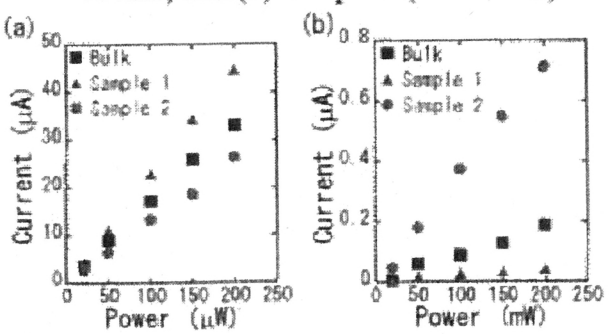

Fig. 3 Dependence of current on incident light power of (a) UV and (b) visible lasers.

References

[1]. H. Fujiwara, *et al.*, Appl. Phys. B **98** (2010) 283. [2]. K. Kitamura, *et al.*, *Nanotech.* **19** (2008) 175305.

Progress in developing nano-scale photonic devices driven by an optical near-field

Takashi Yatsui [a,b] and Motoichi Ohtsu [a,b]

[a] School of Engineering, The University of Tokyo, 2-11-16 Yayoi, Bunkyo-ku, Tokyo, Japan 113-8656
[b] Nanophotonics Research Center, The University of Tokyo, 2-11-16 Yayoi, Bunkyo-ku, Tokyo, Japan 113-8656

yatsui@ee.t.u-tokyo.ac.jp

***Abstract* — Systems of optically coupled quantum structures should be applicable to quantum information processing. Additional functional devices, i.e., nanophotonic devices can be realized by controlling the exciton excitation in quantum structures. This paper reviews the recent achievements with nanophotonic devices based on ZnO.**

***Keywords* — nanophotonics, ZnO, dipole-forbidden energy transfer.**

I. Introduction

Innovations in optical technology are required for future information processing systems. For the integration of photonic devices, it is particularly important to reduce both their size and heat generation. To reduce the size of photonic devices below the diffraction limit, we have proposed nanophotonic devices that consist of semiconductor quantum cubes [1-2], quantum dots (QD) [3,4], and quantum wells [6,7]. ZnO is a promising material for room temperature operation of a nanophotonic device, because of its large exciton binding energy [7-9] and recent achievements in the fabrication of nanorod heterostructures [10,11]. Here, we used chemically synthesized ZnO QD to realize a highly integrated nanophotonic device. We chose QD because they have a higher degree of arrangement freedom than the one-dimensional nanorod system. We observed the energy transfer from smaller ZnO QD to larger QD whose with mutually resonant energy levels. The energy transfer time and energy transfer ratio between the two QD were also calculated from the experimental results.

We considered pairs of small (QDS) and large (QDL) QD fixed at a distance closer than the dot diameter (see Fig. 1). Unidirectional energy flow was expected through this structure due to the optical near-field energy transfer and subsequent dissipation. The ground exciton energy level in the QDS (ES1) and the first excited level in the QDL (EL2) resonated with each other [1]. The input signal exciton in the QDS coupled with the QDL and excited an exciton in EL2, which relaxed to the ground state of the QDL (EL1). This dissipation prevented reflection of the exciton energy to the QDS. The level EL2 was a dipole-forbidden state, which could only be excited through energy transfer from adjacent QDS.

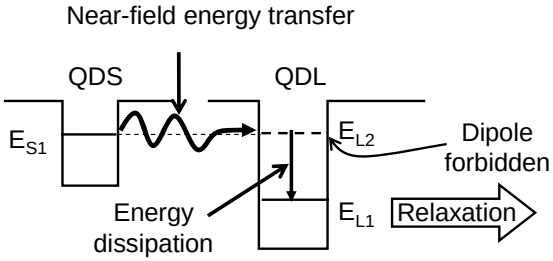

Fig. 1. Schematic of the energy diagram between the QDS and the QDL.

II. ZnO dot synthesis using the sol-gel method

ZnO QD were prepared using the sol-gel method [12,13].

(i) A sample of 1.10g (5 mmol) of $Zn(Ac)_2 \cdot 2H_2O$ was dissolved in 50 mL of boiling ethanol at atmospheric pressure, and the solution was then immediately cooled to 0 ^oC. A sample of 0.29g (7 mmol) of LiOH•H2O was dissolved in 50mL of ethanol at room temperature in an ultrasonic bath and cooled to 0 oC. The hydroxide-containing solution was then added dropwise to the $Zn(Ac)_2$ suspension with vigorous stirring at 0 ^oC. The reaction mixture became transparent after approximately 0.1 g of LiOH had been added. The ZnO sol was stored at 0 °C to prevent particle growth.

(ii) A mixed solution of hexane and heptane, with a volume ratio of 3:2, was used to remove the reaction products (LiAc and H_2O) from the ZnO sol.

(iii) To initiate the particle growth, the ZnO solution was warmed to room temperature. The mean diameter of ZnO QD was determined from the growth time, T_g.

Figure 2(a) shows a transmission electron microscopy (TEM) image of synthesized ZnO dots after the second step. Dark areas inside the white dashed circles correspond to the ZnO QD. This image suggested that mono-dispersed single crystalline particles were obtained.

To check the optical properties and diameters of our ZnO QD, we measured the photoluminescence (PL) spectra using He-Cd laser (λ = 325 nm) excitation at 5 K. We compared the PL spectra of ZnO QD with T_g = 0 and T_g = 42 h (solid and dashed curves in Fig. 2(b),

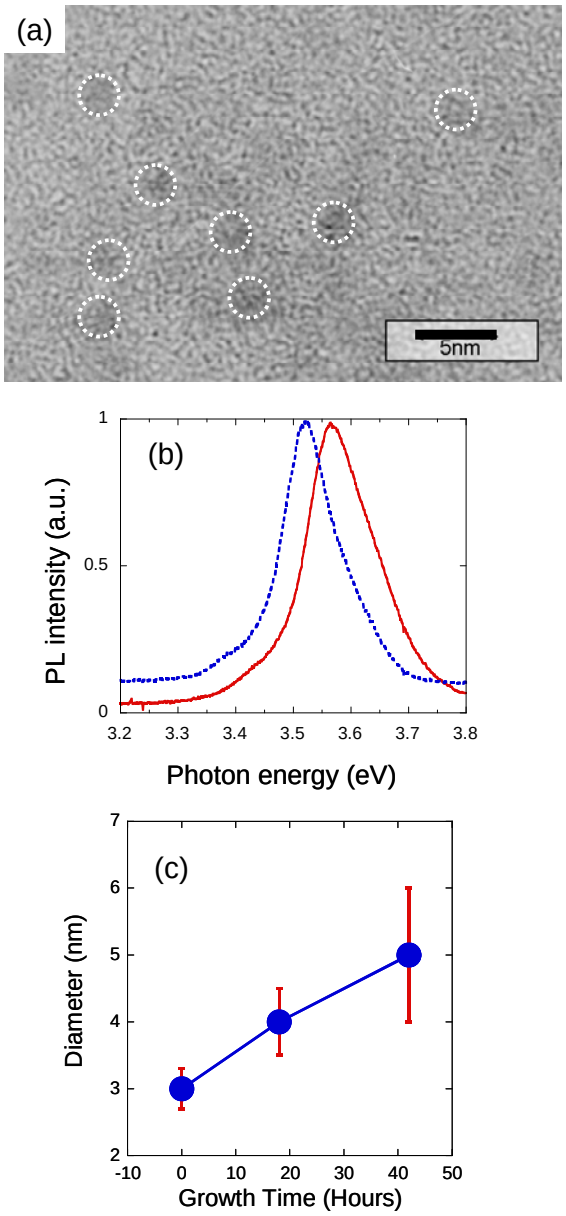

Fig. 2. (a) TEM image of the ZnO QD. The dark areas inside the white dashed circles correspond to the ZnO QD. (b) The PL spectra observed at 5 K. The solid and dashed curves indicate growth time T_g = 0 and 42 h, respectively. (c) The growth time dependence of the mean ZnO QD diameter.

respectively). A red-shifted PL spectrum was obtained, indicating an increase in the QD diameter. Figure 2(c) shows the growth time dependence of the QD diameter. This was determined from the effective mass model, with peak energy in the PL spectra, E_g^{bulk}= 3.35 eV, m_e = 0.28, m_h = 1.8, and ε = 3.7 [14]. This result indicated that the diameter growth rate at room temperature was 1.1 nm/day.

II. Results and Discussion

Assuming that the diameters, D, of the QDS and the QDL were 3.0 and 4.5 nm, respectively, E_{S1} in the QDS and E_{L2} in the QDL resonated (Fig. 3(a)) [1]. An ethanol solution of QDS and QDL was dropped onto a sapphire substrate. The mean surface-to-surface separation of the QD was approximately 3 nm.

The spectra S and L in Fig. 3(b) correspond to the QDS and the QDL, with spectral peaks of 3.60 and 3.44 eV, respectively. The curve A in Fig. 3(b) shows the spectrum from the QDS and QDL mixture with R =1, where R is the ratio (number of QDS)/(number of QDL). The spectral peak of 3.60 eV, which corresponded to the PL from the QDS, was absent from this curve. This peak was thought to have disappeared due to energy transfer from the QDS to the QDL, because the first excited state of the QDL resonated with the ground state of the QDS. Our hypothesis was supported by the observation that when R was increase by eightfold, the spectral peak from the QDS reappeared (see spectrum C in Fig. 3(b)).

To confirm this energy transfer from the QDS to the QDL at 5 K, we evaluated dynamic effects using time-resolved spectroscopy with the time-correlated single photon counting method. The light source used was the third harmonic of a mode-locked Ti:sapphire laser (photon energy 4.05 eV, frequency 80 MHz, and pulse duration 2 ps). We compared the signals from mixed samples with ratios R = 2, 1, and 0.5. The curves T_A (R=2), T_B (R=1), and T_C (R=0.5) in Fig. 4 show the

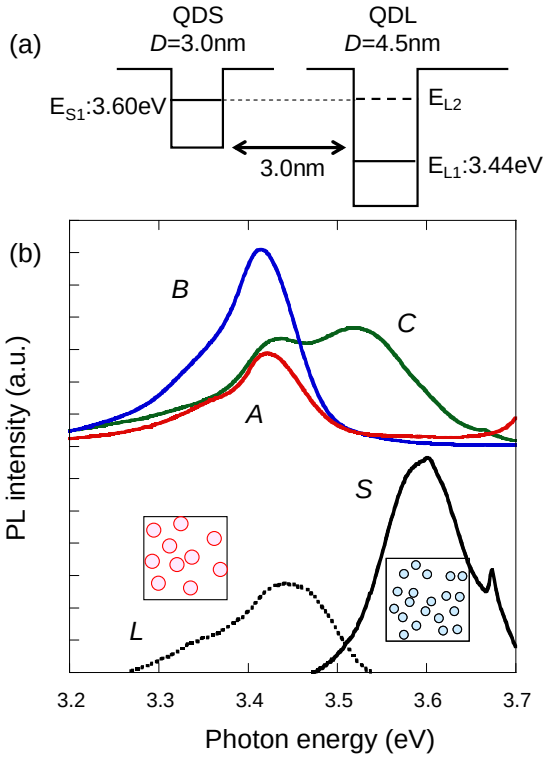

Fig. 3. (a) Schematic of the energy diagram between a QDS and QDL. (b) The PL spectra observed at 5 K. The levels S and L indicate QDS and QDL, respectively. The labels A, B, and C indicate mixes with R- ratios of 1, 4, and 8, respectively.

respective time-resolved PL intensities from the ground state of the QDS (E_{S1}) at 3.60 eV. We investigated the exciton dynamics quantitatively by fitting multiple exponential decay curve functions [15,16]:

$$TRPL = A_1 \exp(-t/\tau_1) + A_2 \exp(-t/\tau_2) \quad (1)$$

We obtained average τ_1- and τ_2-values of 144 ps and 443 ps, respectively (see Table 1). Given the disappearance of the spectral peak at 3.60 eV in the PL spectra, it is likely that these values corresponded to the energy transfer time from the QDS to the QDL and the radiative decay time from the QDS, respectively. This hypothesis was supported by the observation that the average value of τ_1 (144 ps) was comparable with the observed energy transfer time in CuCl quantum cubes (130 ps) [1], ZnO quantum well structures (130 ps) [4], and CdSe QD (135 ps) [3].

We also investigated the value of coefficient ratio A_1/A_2 (see Table 1); this ratio was inversely proportional to R, hence proportional to the number of QDL. This result indicated that an excess QDL caused energy transfer from QDS to QDL, instead of direct emission from the QDS.

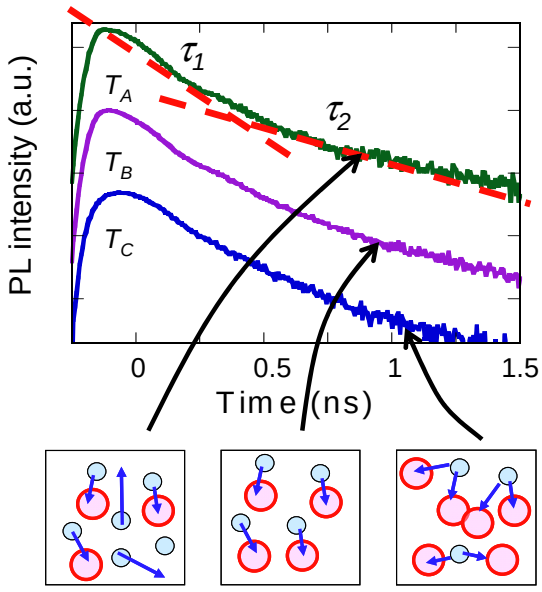

Fig. 4. Time-resolved PL spectra observed at 5 K. The values of R were 2, 1, and 0.5 for curves T_A, T_B, and T_C, respectively.

Table 1. Dependence of the time constants (τ_1 and τ_2) on R as derived from the two exponential fits of the time-resolved PL signals and the coefficient ratio A_1/A_2.

R=QDS/QDL	τ_1 [ps]	τ_2 [ps]	A_1/A_2
2	133	490	12.4
1	140	430	13.7
0.5	160	410	14.4
Average	144	443	

V. Conclusion

We observed the dynamic properties of exciton energy transfer and dissipation between ZnO QD *via* an optical near-field interaction, using time-resolved photoluminescence spectroscopy. Furthermore, we successfully increased the energy transfer ratio between the resonant energy state, instead of the radiative decay from the QD. Chemically synthesized nanocrystals, both semiconductor QD and metallic nanocrystals [17], are promising nanophotonic device candidates, because they have uniform sizes, controlled shapes, defined chemical compositions, and tunable surface chemical functionalities.

Acknowledgement

The author wishes to acknowledge the assistance and support of the COE Steering Committee.

References

[1] T. Kawazoe, K. Kobayashi, S. Sangu, M. Ohtsu, *Appl. Phys. Lett.* 82, 2957 (2003).
[2] T. Kawazoe, K. Kobayashi, M. Ohtsu, *Appl. Phys. Lett.* vol. 86, 103102 (2005).
[3] W. Nomura, T. Yatsui, T. Kawazoe, M. Ohtsu, *J. Nanophot.* Vol. 1, 011591 (2007).
[4] T. Yatsui, H. Jeong, and M. Ohtsu, *Appl. Phys. B: Lasers and Optics*, Vol. 93, 199 (2008).
[5] T. Yatsui, S. Sangu, T. Kawazoe, M. Ohtsu, S. J. An, J. Yoo, G.-C. Yi, *Appl. Phys. Lett.* vol. 90, 223110 (2007).
[6] T. Yatsui, S. Sangu, K. Kobayashi, T. Kawazoe, M. Ohtsu, J. Yoo, and G.-C. Yi, *Appl. Phys. Lett.*, Vol. 94, 083113 (2009).
[7] A. Ohtomo, K. Tamura, M. Kawasaki, T. Makino, Y. Segawa, Z. K. Tang, K. L. Wong, Y. Matsumoto, H. Koinuma, *Appl. Phys. Lett.* vol. 77, 2204 (2000).
[8] M.H. Huang, S. Mao, H. Feick, H. Yan, Y. Wu, H. Kind, E. Weber, R. Russo, P. Yang, *Science* vol. 292, 1897 (2001).

[9] H.D. Sun, T. Makino, Y. Segawa, M. Kawasaki, A. Ohtomo, K. Tamura, H. Koinuma, *J. Appl. Phys.* vol. 91, 1993 (2002).
[10] W.I. Park, G.-C. Yi, M.Y. Kim, S.J. Pennycook, *Adv. Mater.* Vol. 15, 526 (2003).
[11] W.I. Park, S.J. An, J. Long, G.-C. Yi, S. Hong, T. Joo, M.Y. Kim, *J. Phys. Chem. B* vol. 108, 15457 (2004).
[12] E.A. Meulenkamp, *J. Phys. Chem. B* vol. 102, 5566 (1998).
[13] L. Spanhel, M.A. Anderseon, *J. Am. Chem. Soc.* Vol. 113, 2826 (1991).
[14] L.E. Brus, *J. Chem. Phys.* vol. 80, 4403 (1984).
[15] S.A. Crooker, T. Barrick, J.A. Hollingsworth, and V.I. Klimov, *Appl. Phys. Lett.* vol. 82, 2793 (2003).
[16] M.G. Bawendi, P.J. Carroll, L.W. William, and L.E. Brus, *J. Chem. Phys.* vol. 96, 946 (1992).
[17] M. Brust, C.J. Kiely, *Colloids Surf. A* vol. 202, 175 (2002).

Nanophotonic fabrication in sub-nm scale

Takashi Yatsui* and Motoichi Ohtsu
School of Engineering and The Nanophotonics Research Center, The University of Tokyo, 2-11-16 Yayoi, Bunkyo-ku, Tokyo 113-8656, Japan

ABSTRACT

Nanophotonics, a novel optical technology, utilizes the local interaction between nanometric particles via optical near fields. The optical near fields are the elementary surface excitations on nanometric particles. Of the variety of qualitative innovations in optical technology realized by nanophotonics, this talk focuses on fabrication. A realization of an ultra-flat silica surface with angstrom-scale average roughness using noadiabatic optical near-field etching and repairing are demonstrated and its origin is discussed.

Keywords: Optical near-field, Dressed photon, Nonadiabatic photochemical reaction, Self assembly, Near-field desorption, Ultra-flat surface, Repairing

1. INTRODUCTION

An ultra-flat surface substrate of sub-nm scale roughness is required for various applications including the manufacture of high quality, extreme UV optical components, high-power lasers, ultra-short pulse lasers, plus future photonic devices at the sub-100 nm scale; it is estimated that the required surface roughness, R_a, will be less than 1 Å [1]. This R_a value is an arithmetic average of the absolute values of the surface height deviations measured from the best-fitting plane, and is given by

$$R_a = \frac{1}{l}\int_0^l |f(x)|dx \cong \frac{1}{n}\sum_{i=1}^{n}|f(x_i)| \quad (1)$$

where the $|f(x_i)|$ are absolute values measured from the best-fitting plane and l is the evaluation length. Physically, dx corresponds to the spatial resolution in the measurement of $f(x)$ and n is the number of pixels in the measurement; $n=l/dx$. Conventionally, chemical-mechanical polishing (CMP) has been used to flatten the surface [2]. However, CMP has difficulties reducing R_a to less than 2 Å because the polishing pad roughness is as large as 10 μm and the diameters of the polishing particles in the slurry are as large as 100 nm. In addition, polishing causes scratches or digs due to the contact between the polishing particles and/or impurities in the slurry and the substrate.

Our interest in applying an optical near field to nanostructure fabrication was generated because of its high resolution capability, beyond the diffraction limit, and its novel photochemical reaction, which is classified as nonadiabatic due to its energy transfer via a virtual exciton-phonon-polariton [3,4]. In this chemical vapor deposition, photo-dissociation of the molecules is driven by the light source at a lower photon energy than the molecular absorption band edge energy by a multiple step excitation via vibrational energy levels [5,6]. Following this process, we proposed a novel method of polishing using nonadiabatic optical near-field etching [7].

Furthermore, because localized optical near-fields are generated preferably on a surface with nanoscale curvature, they can be induced on fine scratches, contributing to repair them. In addition, the repairing process stops automatically after the scratches disappear. Such selective self-assembling optical near-field interactions previously have been used for depositing nanoparticles [8], photo-chemical vapor deposition [9], sputtering [10], and photochemical etching [7]. Here, we employ this novel technique to repair the scratches on polycrystalline Al_2O_3 ceramics [11].

Synthesis and Photonics of Nanoscale Materials VII, edited by Jan J. Dubowski, David B. Geohegan, Frank Träger, Proc. of SPIE Vol. 7586, 75860D · © 2010 SPIE · CCC code: 0277-786X/10/$18 · doi: 10.1117/12.846328

2. REALIZATION OF AN ULTRA-FLAT SILICA SURFACE USING NONADIABATIC OPTICAL NEAR-FIELD ETCHING

2.1 Nonadiabatic optical near-field etching

A continuum wave laser (λ= 532 nm) was used to dissociate the Cl_2 gas through a nonadiabatic photochemical reaction.This photon energy is lower than the absorption band edge energy of Cl_2 (λ = 400 nm) [12], so that the conventional Cl_2 adiabatic photochemical reaction is avoided. However, because the substrate has nanometer scale surface roughness, the generation of a strong optical near-field on the surface is expected from the simple illumination with no focusing being required (Fig. 1(a)). Since a virtual exciton-phonon-polariton can be excited on this roughness, a higher molecular vibrational state can be excited than on the flat part of the surface, where there are no virtual exciton-phonon-polariton. Cl_2 is therefore selectively photo-dissociated wherever the optical near-field is generated (Fig. 1(b)). These dissociated Cl_2 molecules then etch away the surface roughness; the etching process automatically stops when the surface becomes flat (Fig. 1(c)).

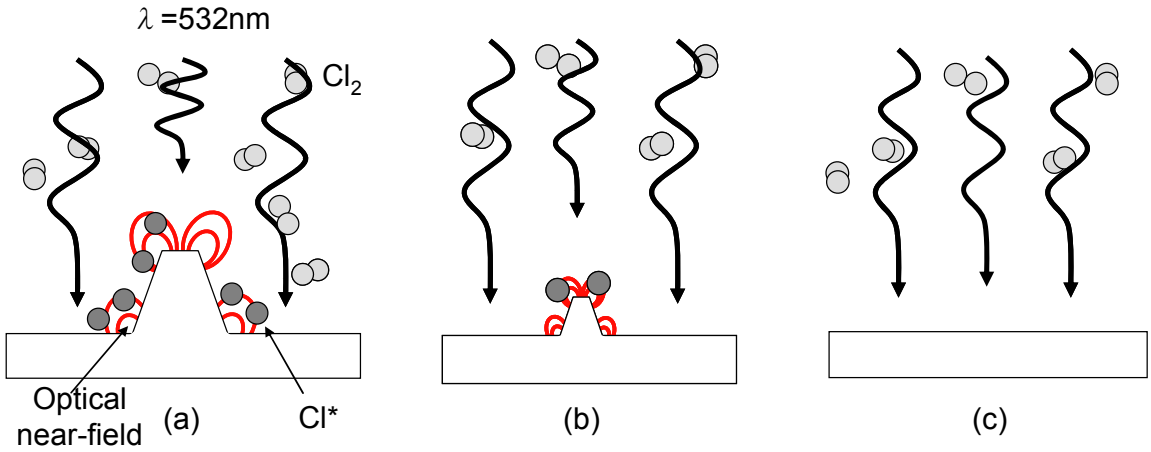

Figure 1. Schematic of the near-field etching. Cl*: Activated Cl.

2.2 Experiment

We used 30-mm-diameter planar synthetic silica substrates built by vapor-phase axial deposition with an OH group concentration of less than 1 ppm [13]. The substrates were preliminarily polished by CMP prior to the nonadiabatic optical near-field etching. We performed the nonadiabatic optical near-field etching at a Cl_2 pressure of 100 Pa at a room temperature with a continuum wave laser (λ= 532 nm) having a uniform power density of 0.28W/cm^2 over the substrate (see Fig. 2(a)). Surface roughness was evaluated using an atomic force microscope (AFM). Since the scanning area of the AFM was much smaller than the substrate, we measured the surface roughness R_a in nine representative areas, each 10 μ m×10 μ m, separated by 100 μ m (see Fig. 2(b)). The scanned area was 256×256 pixels with a spatial resolution of 40 nm. The average value $\overline{R_a}$ of the nine R_a's, obtained before the nonadiabatic optical near-field etching, and evaluated through the AFM images, was 2.36 ± 0.02 Å. We cleaned the substrate ultrasonically using deionized water and methanol before and after the nonadiabatic optical near-field etching.

2.3 Results and Discussion

Figures 3(a) and 3(b) show typical AFM images of the scanned 10 μ m×10 μ m silica substrate area before and after nonadiabatic optical near-field etching, respectively. Note that the surface roughness was drastically decreased, as supported by the cross-sectional profiles in Figs. 3(a) and 3(b) (see Fig. 3(c)). We found a dramatic decrease in the value of the peak-to-valley from 1.2 nm (curve B) to 0.5 nm (curve A). Furthermore, note that the scratch seen in AFM image before nonadiabatic optical near-field etching disappeared. This indicates that rougher areas of the substrate had a higher etching rate, possibly because of greater intensity of the optical near-field, leading to a uniformly flat surface over a wide area.

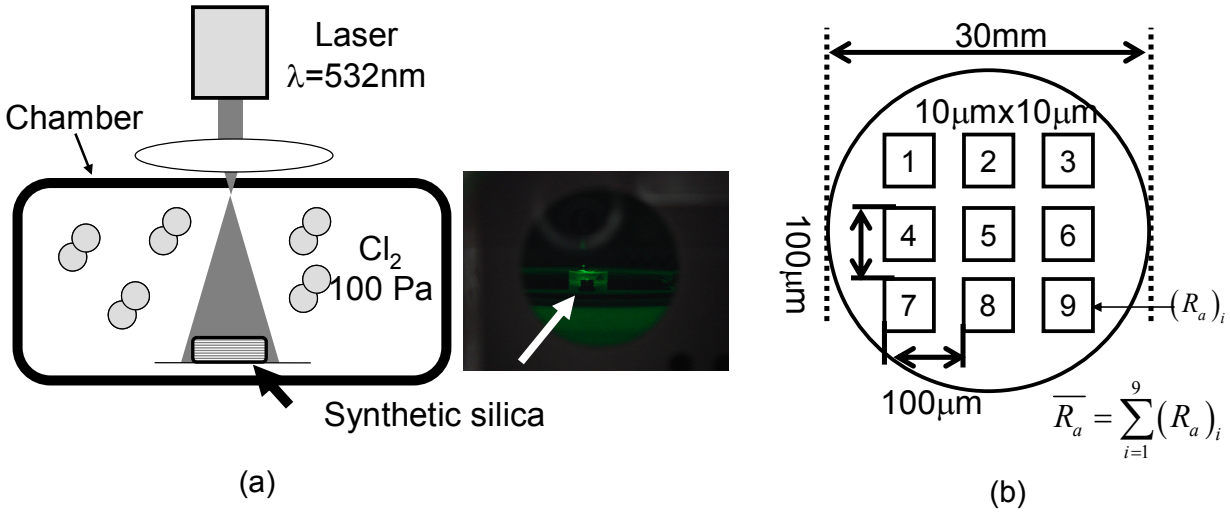

Figure 2. Schematic of (a) the experimental set-up and (b) the AFM measurement.

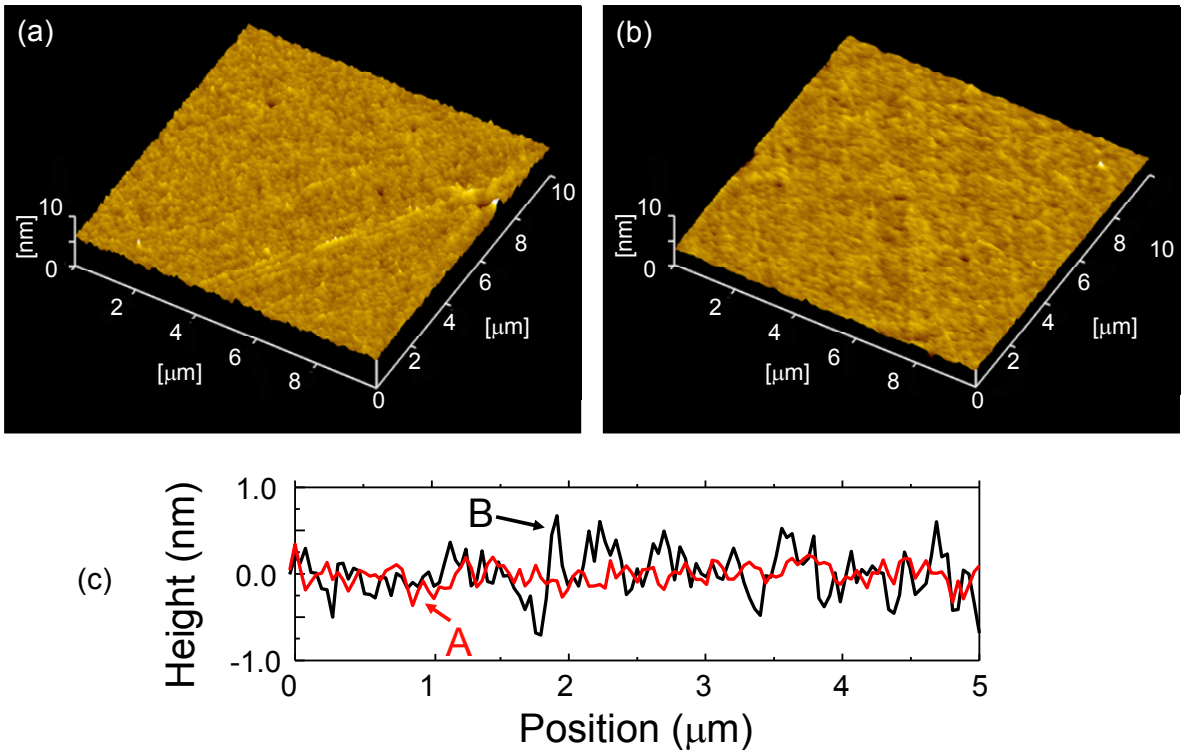

Figure 3 Typical AFM images of the silica substrate (a) before and (b) after nonadiabatic optical near-field etching. (c) Cross-sectional profiles in (a) and (b). Curve A and B correspond to the profile after and before etching, respectively.

Figure 4(a) shows the etching time dependence of $\overline{R_a}$. We found that $\overline{R_a}$ decreases as the etching time increases. The minimum in $\overline{R_a}$ was 1.37 Å at an etching time of 120 minutes, while the minimum R_a among the nine areas was 1.17 Å. Because the process is performed in a sealed chamber, the saturation in the decrease of $\overline{R_a}$ might originate from the decrease in Cl_2 partial pressure during etching, A further decrease in $\overline{R_a}$ would be expected under constant Cl_2 pressure.

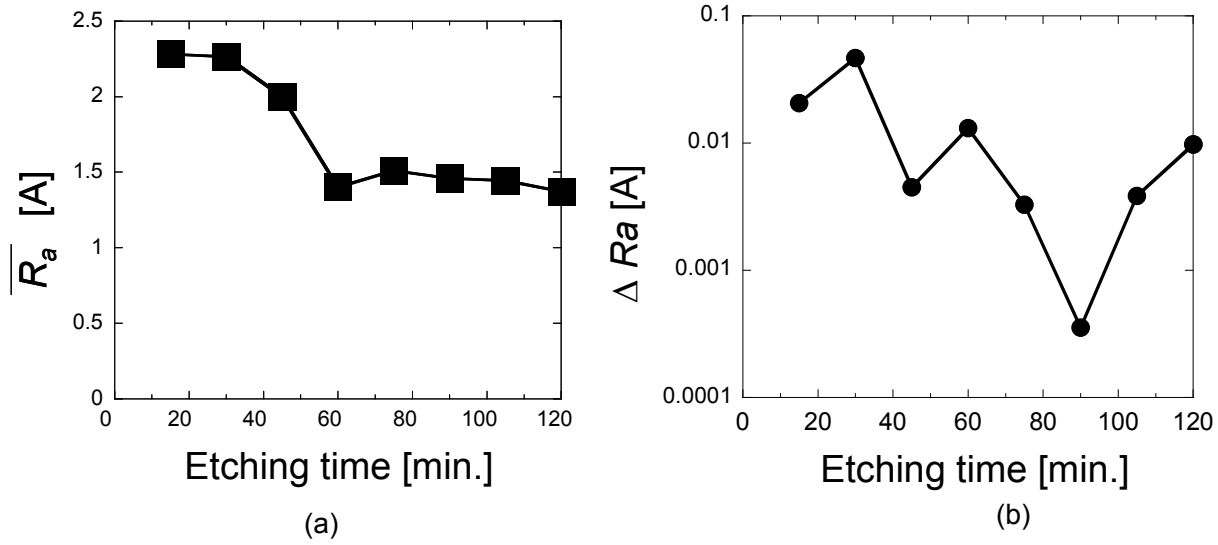

Figure 4 The etching time dependence of (a) the average R_a ($\overline{R_a}$) and (b) the standard deviation of R_a (ΔR_a).

Figure 4(b) shows the time dependence of the standard deviation of R_a (ΔR_a) among the nine areas, which was obtained in one scanning area. Although we found a dramatic decrease in ΔR_a after 60 minutes, the increase in ΔR_a in the early stages of nonadiabatic optical near-field etching might be caused by impurities, such as OH, in the substrate surface.

3. REPAIRING NANOSCALE SCRATCHED GROOVES USING OPTICAL NEAR-FIELD ASSISTED SPUTTERING

3.1 Nonadiavatic optical near-field repairing

Figure 5 shows a schematic of our method. As a result of preliminary polish of the Al_2O_3 ceramic, its surface contains nanoscale scratched grooves. Because the edges of the grooves have larger surfaces areas than the flat surface, the sputtered Al_2O_3 particles have a higher deposition rate at the edge after migration on the surface [14, 15]. As shown in Figure 1(a), it therefore is expected that Al_2O_3 will be deposited preferentially at the edges of scratched grooves, which will not help to repair the scratches. To avoid extra deposition on the edge of the grooves and to repair the scratches, we used the near-field desorption [10]. Because the optical near-field (i.e., the dressed photon) can excite coherent phonons in the nanoscale structure, a virtual exciton–phonon–polariton (EPP) is generated on the substrate. A multistep transition via the EPP can accelerate the photochemical reaction although the photon energy is lower than the absorption band edge energy of the material [3]. When the ceramic is irradiated, a highly localized optical near-field is generated at the edges of scratches, causing the photodesorption of depositing Al_2O_3 nanoparticles. As shown in Fig. 5(b), if the light has a lower energy than the absorption band edge of the nanoparticles, effective deposition will decrease at the edge, and Al_2O_3 will accumulate on the bottom of the groove [10]. This process automatically stops after the scratches disappear, so that the optical near-field can no longer be generated.

We performed optical near-field assisted sputtering to repair the scratches on the surface of the translucent Al_2O_3 ceramic SAPPHAL® [16]. Planar surfaces of SAPPHAL® substrate were prepared by polishing using diamond abrasive grains with a diameter of 0.5 μm. The Al_2O_3 was deposited using radio-frequency (RF) magnetron sputtering (RF power: 300 W; frequency: 13 MHz). The total gas pressure was 7×10^{-1} Pa, with a gas flow of 16 sccm Ar and 1.2 sccm O_2 [17]. We also used SAPPHAL® as the target material for sputtering. The CW second harmonic of a Nd:YAG laser with wavelength of $\lambda = 473$ nm was used as the light source for optical near-field generation. During the sputtering process, the surface was irradiated with light with an optical power density of 2.7 W/cm^2. As stated previously, the photon energy of this laser was lower than the absorption band edge energy of Al_2O_3 ($\lambda = 250$ nm) [18]. The light was introduced to the ceramic surface through a multimode optical fiber.

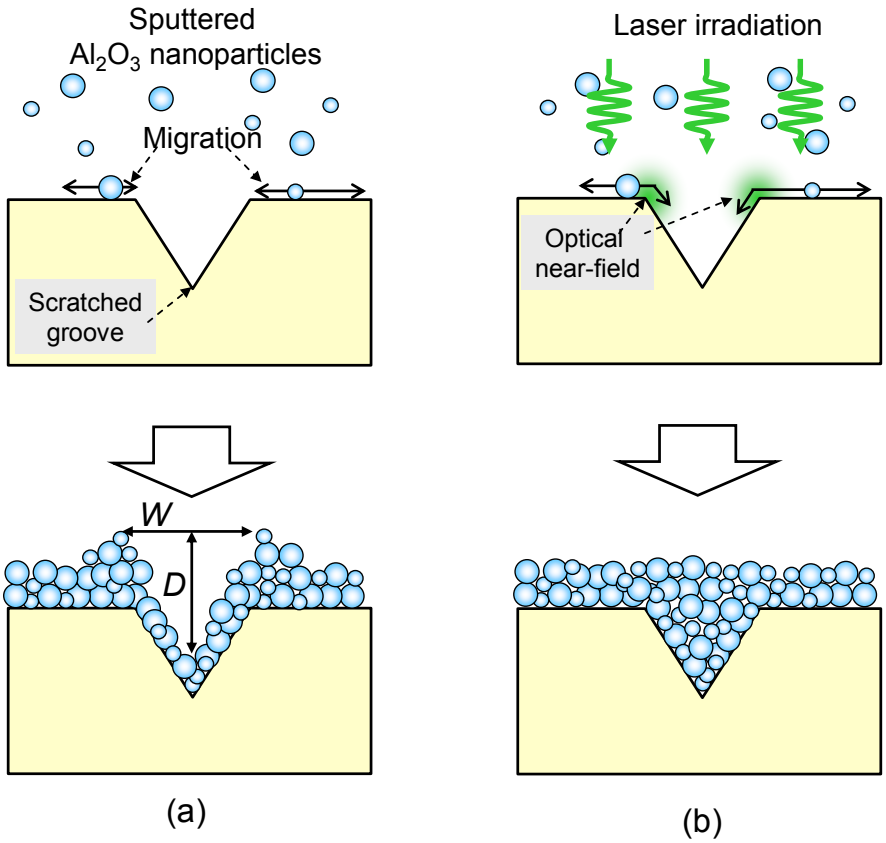

Figure 5 Schematics of deposition on the scratched substrate surface (a) without and (b) with irradiation during the sputtering. *D* is the depth and *W* is the width of the scratched groove.

After 30 min of sputtering, the thickness of the deposited Al_2O_3 layer was about 100 nm. We observed the surface of the substrates using AFM.

3.2 Result and discussion

Figures 6(a)-6(c) show typical AFM images of SAPPHAL® surfaces before sputtering, after sputtering without irradiation, and after sputtering with irradiation, respectively. Figures 6(d)-6(f) show the cross-sectional profiles of typical scratches along the white dashed lines in Figs. 6(a)-6(c), respectively. The depth of the scratched grooves in Fig. 6(e) is 4.4 nm, which is deeper than that in Fig. 6(d) (4.0 nm). This was caused by the extra deposition at the edges of the scratch due to the low surface potential, as described in Fig. 5(a). In contrast, Fig. 6(f) shows that the depth decreased to 1.8 nm without extra deposition at the edges of scratches after sputtering with irradiation. For more quantitative evaluation, we calculated the surface roughness *Ra*. The R_a values over the AFM images of Figs. 6(a)-(c) were Ra_A = 1.3 nm, Ra_B = 1.1 nm, and Ra_C = 0.49 nm, respectively. These results indicated that the repair of scratched grooves by optical near-field desorption at the edge of the scratches resulted in a drastic decrease in the surface roughness.

To selectively evaluate the profiles of the scratched grooves, we used the Hough transform [19]. After the AFM image of Fig. 7(a) was leveled by a least square method and binarized, the linear features of scratches were automatically extracted using a Hough transform; see Fig. 7(b). Through this method we obtained the depth *D* and width *W* of the detected scratches. Figures 7(c) and 7(d) show statistical analyses of *D* and *W* obtained from the images in Figs. 6(a)-6(c), respectively. As shown in Fig. 7(c), the average values of *D* were $\overline{D_A}$ = 3.2 nm, $\overline{D_B}$ = 3.8 nm, and $\overline{D_C}$ = 0.79 nm, respectively, which confirmed that the depth of the scratches were drastically decreased using the near-field assisted sputtering. Figure 7(d) shows that the width of the scratches after the sputtering without irradiation (W_B) was increased

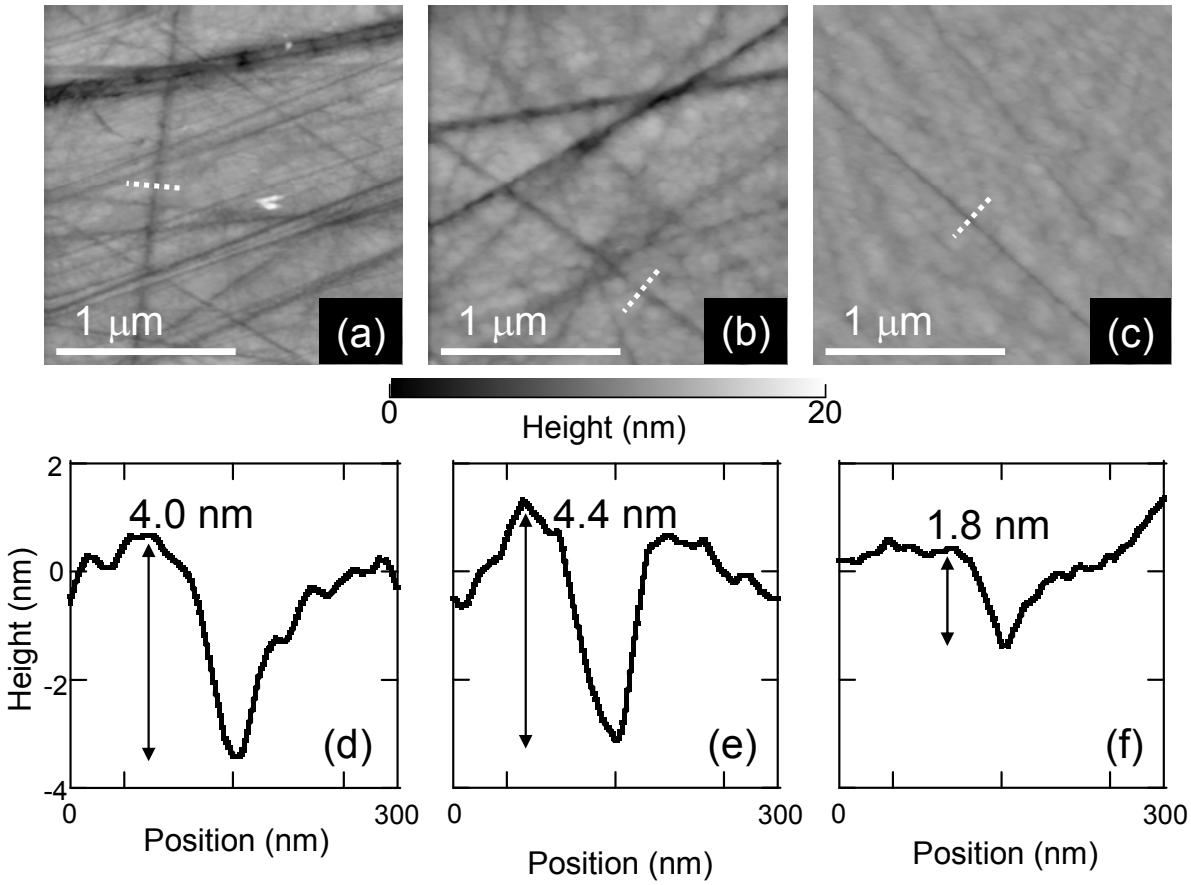

Figure 6 AFM images of substrates (a) before sputtering (substrate A), (b) after sputtering without irradiation (substrate B), and (c) after sputtering with irradiation (substrate C). (d), (e), and (f) Cross-sectional profiles along the white dashed lines in (a), (b), and (c), respectively.

beyond the original value W_A, which also supports our deposition model; see Fig. 5(a). In addition, the width W_C also increased in comparison to W_A, supporting the model of Fig. 5(b). Further decreases in the width could be achieved by optimizing laser and sputtering conditions.

4. CONCLUSIONS

We propose a new polishing method that uses near-field etching based on a non-adiabatic process, with which we obtained ultra-flat silica surface that had a minimum roughness of 1.37 Å. We believe our technique is applicable to a variety of substrates, including amorphous and crystal substrate. Since this technique is a non-contact method without a polishing pad, it can be applied not only to flat substrates but also to three-dimensional substrates that have convex or concave surfaces, such as micro-lenses and the inner wall surface of cylinders.

Furthermore, we proposed an optical near-field assisted sputtering method for repairing the scratched grooves on a translucent polycrystalline Al_2O_3 ceramic surface. We confirmed that the depth of the grooves was decreased by RF sputtering of Al_2O_3 with laser irradiation at a wavelength of λ = 473 nm. We found a drastic decrease in surface roughness and obtained an average depth of 0.79 nm. Furthermore, we analyzed the surface profile using a Hough transform. This approach clearly revealed the effects of the optical near-field assisted sputtering, which selectively repaired the scratched grooves.

We believe our techniques are applicable to a variety of substrates, including amorphous, ceramic, and crystal substrate. Furthermore, these methods are compatible with mass production.

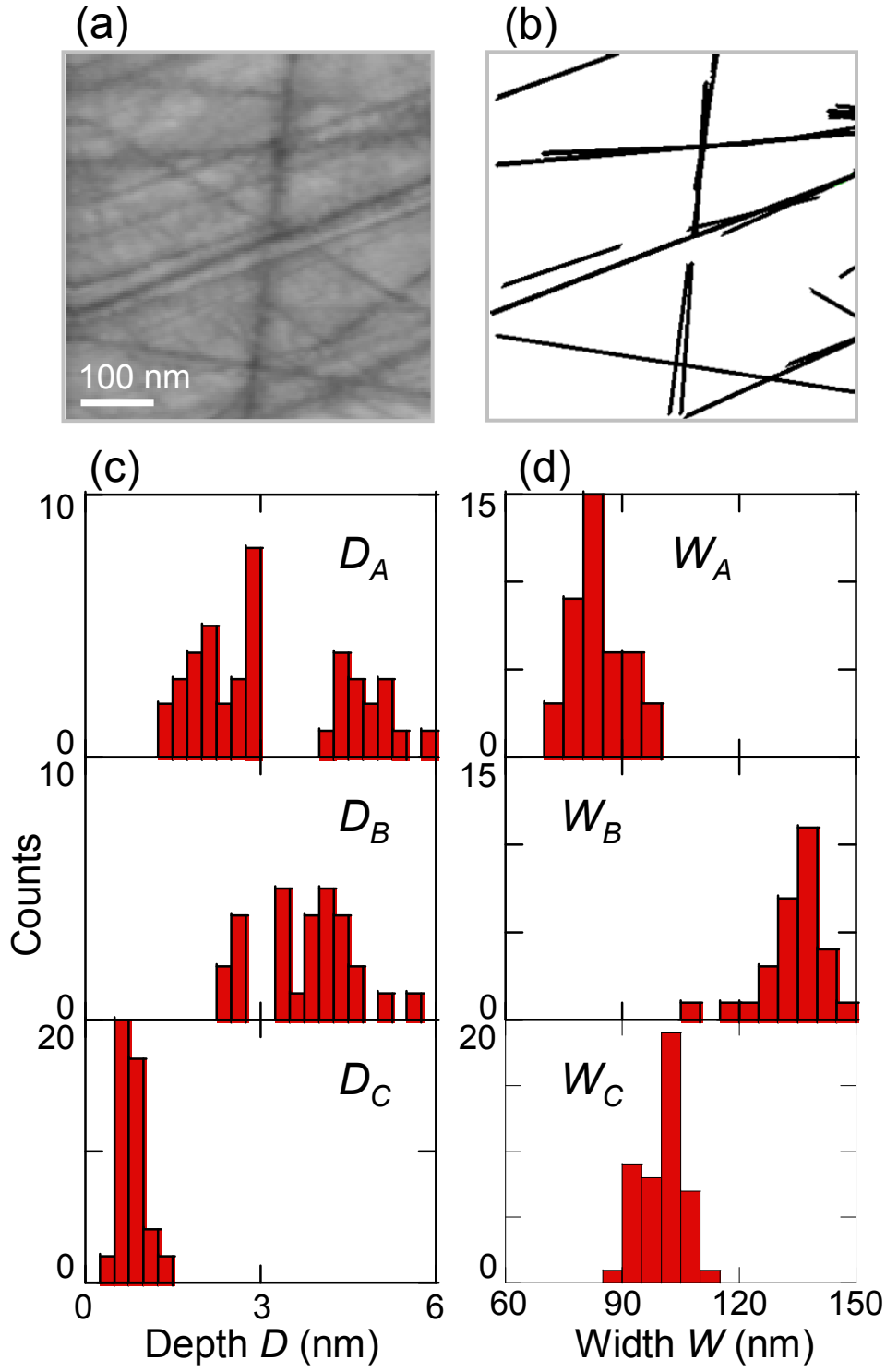

Figure 7 (a) An AFM image is leveled by a least square method. (b) Schematic of the Hough transform. Straight lines of the scratches are detected using the Hough transform of (a). (c) Histograms of depths, D_n. (d) widths (W_n) of scratches on alumina ceramics substrates; A (before sputtering), B (after sputtering without irradiation), and C (after sputtering with irradiation).

5. ACKNOWLEDGEMENT

We thank Drs. W. Nomura and T. Kawazoe (University of Tokyo), M. Naruse (NICT), Mrs. K. Hirata and Y. Tabata (SIGMA KOKI Co., Ltd.), Dr. Y. Yanase, Mrs. K. Suzuki, M. Fujita, A. Kamata (Covalent Materials Corporation) for valuable discussions. This work was supported by the New Energy and Industrial Technology Development Organization (NEDO) Special Courses: A comprehensive activity for personnel training and industry-academia collaboration based on NEDO projects, the Research and Development Program of Innovative Energy Efficiency Technology, and the program of Strategic Development on Rationalization Technology using Energy.

REFERENCES

[1] Wua, B. and Kumar, A., "Extreme ultraviolet lithography: A review," J. Vac. Sci. Technol. B 25(6), 1743-1761 (2007).
[2] Cook, L.M., "Chemical processes in glass polishing," J. Non-Crystalline Solids 120(1-3), 152-171 (1990).
[3] Kawazoe, T., Kobayashi, K., Takubo, S., and Ohtsu, M., "Nonadiabatic photodissociation process using an optical near field," J. Chem. Phys. 122(2), 024715 (2005).
[4] Kobayashi, K., Kawazoe, T., and Ohtsu, M., "Importance of Multiple-Phonon Interactions in Molecular Dissociation and Nanofabrication Using Optical Near Fields," IEEE Transactions on Nanotechnology 4(5), 517-522 (2005).
[5] Kawazoe, T., Yamamoto, Y., and Ohtsu, M., "Fabrication of nanometric Zn dots by nonresonant near-field optical chemical-vapor deposition," Appl. Phys. Lett. 79(8), 1184-1186 (2001).
[6] Yatsui T. and Ohtsu, M., "Production of size-controlled Si nanocrystals using self-organized optical near-field chemical etching," Appl. Phys. Lett., 95(4), 043104 (2009).
[7] Yatsui, T., Hirata, K., Nomura, W., Tabata, Y., and Ohtsu, M., "Realization of an ultra-flat silica surface with angstrom-scale average roughness using nonadiabatic optical near-field etching," Appl. Phys. B: Lasers and Optics, 93(1), 55-57 (2008).
[8] Yatsui, T., Nomura, W., and Ohtsu, M., "Size-, position-, and separation-controlled one-dimensional alignment of nanoparticles using an optical near field," IEICE Trans. Electron. E88-C(9), 1798-1802 (2005).
[9] Yatsui, T., Takubo, S., Lim, J., Nomura, W., Kourogi, M. and Ohtsu, M., "Regulating the size and position of deposited Zn nanoparticles by optical near-field desorption using size-dependent resonance," Appl. Phys. Lett. 83(9), 1716-1718 (2003).
[10] Yatsui, T., Nomura, W., Ohtsu, M., "Self-assembly of size- and position-controlled ultra-long nanodot chains using near-field optical desorption," Nano Lett. 5(12), 2548-2551 (2005).
[11] Nomura, W., Yatsui, T., Yanase, Y., Suzuki, K., Fujita, M., Kamata, A., Naruse, M., and Ohtsu, M., "Repairing nanoscale scratched grooves on polycrystalline ceramics using optical near-field assisted sputtering," Appl. Phys. B- Lasers and Optics (2009), DOI:10.1007/s00340-009-3797-0.
[12] Kullmer R. and Büerle, D., "Laser-induced chemical etching of silicon in chlorine atmosphere III. Combined cw and pulsed irradiation," Appl. Phys. A: Materials Science & Processing, 47(4), 377-386 (1988).
[13] Izawa T. and Inagaki, N., " Materials and processes for fiber preform fabrication—Vapor-phase axial deposition," Proc. IEEE, 68(10), 1184-1187 (1980).
[14] Himpsel, F. J., Ortega, J. E., Mankey, G. J., and Willis, R. F., "Magnetic nanostructures," Adv. Phys. 47(4), 511-597 (1998).
[15] Menke, E. J., Li, Q., Penner, R. M., "Bismuth Telluride (Bi_2Te_3) nanowires synthesized by cyclic electrodeposition/stripping coupled with step edge decoration," Nano Lett. 4(10), 2009-2014 (2004).
[16] A product of the Covalent Materials Corporation: http://www.covalent.co.jp/
[17] Wachtman, J. B., Haber, A. R., [Ceramic Films and Coatings], William Andrew Publishing, New York, (1993).
[18] Benabid, F., Notcutt, M., Loriette, V., Ju, L., Blair, D. G., "X-ray induced absorption of high-purity sapphire and investigation of the origin of the residual absorption at 1064 nm," J. Phys. D 33(6), 589-594 (2000).
[19] Duda, R. O. and Hart, P. E., "Use of the hough transformation to detect lines and curves in pictures," Commun. ACM 15(1), 11-15 (1972).

Nanophotonics: Application to nonadiabatic fabrication

M. Ohtsu
Department of Electrical Engineering and Information Systems,
Nanophotonics Research Center,
the Univ. of Tokyo
2-11-16 Yayoi, Bunkyo-ku, Tokyo 113-8656, Japan
*E-mail: ohtsu@ee.t.u-tokyo.ac.jp

The author reviews the recent progress of his studies on *nanophotonics*, which utilizes the optical near-field[1,2]. The key to utilizing optical near-fields is to realize novel nanometric device operation, fabrication, and energy conversion, etc., by the control of an intrinsic interaction between nanometer-sized materials via optical near-fields. The nature of optical near-fields was studied by regarding the optical near-field as an electromagnetic field that mediates the interaction between nanometric materials. As a result, the physically intuitive concept of a *dressed photon* was established to describe optical near-fields, *i.e.*, the interaction between nanometric materials is mediated by exchanging dressed photons[3,4].

Since nanophotonic devices have been demonstrated in the previous AP-NFO6[5], this presentation focuses on nanophotonic fabrications based on nonadiabatic processes triggered by optical-near-field interactions. These processes represent *qualitative* innovation in photochemical vapor deposition and photolithography, suggesting that large, expensive ultraviolet light sources are no longer required, although they are indispensable for conventional adiabatic photochemical vapor deposition, photolithography, and photochemical etching. It also suggests that nonadiabatic photochemical vapor deposition can even dissociate optically inactive molecules (i.e., inactive to the propagating light), which is advantageous for environment protection because most optically inactive molecules are chemically stable and harmless. For example, optically inactive $Zn(acac)_2$ molecules have been dissociated to deposit nanometric Zn particles[6]. In addition, in the case of nonadiabatic photolithography, an optically inactive resist film for electron-beam lithography has been used to fabricate fine patterns [7]. A prototype of the commercial lithography system has been produced in collaboration with industry[8], and has been used for fabricating a diffraction grating[9] and a Fresnel's zone plate[10] for the soft X-ray. Furthermore, in nonadiabatic photochemical etching has realized an ultra-flat glass surface with the roughness as low as 1.3 Angstrom without using any photomasks[11].

References

[1]M. Ohtsu, et al., *IEEE J. Selected Topics in Quantum Electronics*, **8**, 839 (2002).
[2]M. Ohtsu, et al., *IEEE J. Selected Topics in Quantum Electronics*, **14**, 1404 (2008).
[3]M. Ohtsu and K. Kobayashi, *Optical Near Fields*, Springer-Verlag, Berlin, 109 (2003).
[4]M. Ohtsu, et al., *Principles of Nanophotonics*, London, England: Tailor & Francis, (2008).
[5]M. Ohtsu, Abstract of the 6th Asia-Pacific Conf. on Near-Field Opt., 1 (2007).
[6]T. Kawazoe, et al., *Appl. Phys. B*, **84**, 247 (2006).
[7]T. Kawazoe, et al., *Progress in Nano-Electro-Optics V*, (ed)M. Ohtsu, Springer-Verlag, Berlin, 109 (2006).
[8]Y. Inao, et al., *Microelectronic Eng.*, **84**, 705 (2007).
[9]M. Koike, et al., *Nanophotonics and Nanofabrication*, (ed)M. Ohtsu, Wiley-VCH, Weinhelm, 179 (2009).
[10]T. Kawazoe, et al., *Appl. Phys. B*, **96** (2009), in press.
[11]T. Yatsui, et al., *Appl. Phys. B*, **93**, 55 (2008).

Information Theoretic Analysis of Hierarchical Nano-Optical Systems

M. Naruse[1,2], H. Hori[3], K. Kobayashi[3], N. Tate[2], and M. Ohtsu[2]*
[1]National Institute of Information and Communications Technology,
4-2-1 Nukui-kita, Koganei, Tokyo 184-8795, Japan
[2]Department of Electrical Engineering and Information Systems and Nanophotonics Research Center,
School of Engineering, The University of Tokyo, 2-11-16 Yayoi, Bunkyo-ku, Tokyo 113-8656, Japan
[3]Interdisciplinary Graduate School of Medicine and Engineering, University of Yamanashi,
Kofu, Yamanashi 400-8511, Japan
**E-mail: naruse@nict.go.jp*

Optical near-field interactions exhibit a hierarchical response, which is one of the most unique attributes of light–matter interactions occurring locally on the nanometer scale [1,2]. It allows hierarchical nano-optical systems that break through the integration restrictions posed by the diffraction limit of conventional propagating light and offers multiple hierarchical functionalities at different physical scales in the sub-wavelength regime. Besides physical insights and technological methodologies [2], it is important, in developing practical systems, to grasp the fundamental properties from the viewpoint of information and communication [3]. Here we demonstrate an information theoretic approach to nano-optical systems so that the information capacity of the system is quantitatively analyzed which leads to the design of optimal nano-optical systems.

In the analysis, assuming a hierarchical system that exhibit a two-layer response (the *first layer* and the *second layer*) based on an array of four oscillating electrical dipoles as shown in Fig. 1(a), we first assess the electromagnetic and logical aspects of the hierarchy in optical near-fields via angular-spectrum analysis [1]. We then formulate the mutual information at each level of the hierarchy that quantitatively reveals the capability as an information system. Here, we assume two types of environmental disturbances; one is what we call the *near-field disturbance* that locally disturbs the polarizations of each of the dipoles. The other is the *far-field disturbance* that selectively couples to the system taking account for the optical selection rules.

Figure 1(b) summarizes the layer- and disturbance-dependent mutual information as a function of the error probability affecting the system. The mutual information for the first layer (dashed curves A and C) is constant regardless of the error probability. In particular, the first layer mutual information exhibits always 1 with the far-field disturbance, meaning that the first layer is *completely robust* to the errors. The second layer mutual information (curves B and D) increases as the error probability decreases. With the near-field disturbance, the second layer is superior to the first layer in terms of its mutual information. Based on those analyses, we can derive the optimal design of hierarchical systems and the optimal coding strategy that maximizes the information capacity of the hierarchical systems.

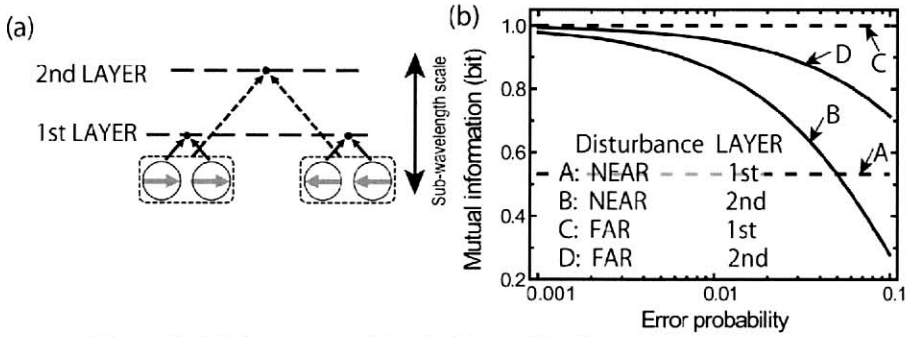

Figure 1: (a) System model of a hierarchical nano-optical system
(b) Analysis of the layer- and disturbance-dependent mutual information

References

[1] M. Naruse, T. Inoue, and H. Hori, *Jpn. J. Appl. Phys.* **46**, 6095 (2007).
[2] M. Ohtsu et al., *Principles of Nanophotonics* (Taylor and Francis, 2008).
[3] T. M. Cover and J. A. Thomas, *Elements of Information Theory* (Wiley, Hoboken, 1991).

Nonadiabatic wavelength-selective sensitization of the P3HT/ZnO photodetector using optical near field.

S. Yukutake[1], T. Kawazoe[1,2], T. Yatsui[1,2], and M. Ohtsu[1,2]
[1]Department of Electrical Engineering and Information Systems, Graduate School of Engineering, The University of Tokyo, 2-11-16 Yayoi, Bunkyo-ku Tokyo, 113-8656, Japan
[2]Nanophotonic Research Center, Graduate School of Engineering, The University of Tokyo, 2-11-16 Yayoi, Bunkyo-ku, Tokyo 113-8656, Japan
E-mail: yukutake@nanophotonics.t.u-tokyo.ac.jp

Nonadiabatic processes based on a dressed-photon description of an optical near field have realized unique nanometer-scale fabrication methods, e.g., CVD[1], photolithography [2], surface flattening[3], and frequency up-converting device[4] which is able to broaden the sensitive bandwidth of photodetector. So far, the structure for generating the optical near field was fabricated by using expensive and low-through put methods, e.g., EB-lithography[2] or by using recrystallization technique[3] to realize above dressed photon technology. In this presentation, we report a unique photodetector fabricated by nonadiabatic method with self-assembled manner.

Figure 1 shows the schematic structure of the fabricated photodetector. After ITO and ZnO layers with respective thickness of 200 nm and 100 nm were deposited by the sputtering method on the sapphire substrate, P3HT(poly(3-hexylthiophene)) layer of 50 nm in thickness was spin coated. After thin Ag layer of a few nm was deposited to apply the bias voltage, additional Ag was deposited under the conditions of the reverse bias voltage of 1.5 V and an irradiation of a laser light with power of 70 mW and wavelength of 660 nm. Total thickness of Ag layer was 1 μm. These deposition conditions promote the structural formation of Ag-P3HT interface which is optimized to generate the optical near field for the wavelength of irradiated laser light.

The conventional P3HT/ZnO photodetector fabricated without bias voltage and irradiation of light has a photosensitivity for the wavelength shorter than 570 nm as shown in the inset in Fig.2. However, the present photodetector had a significant photosensitivity for the red light in wavelength region longer than 600 nm as shown in Fig.2. This is because the incident light passing through the P3HT/ZnO hetero-structure generated the optical near field at the interface between P3HT and Ag layers and the successively-induced nonadiabatic transition[4] in P3HT. The difference between the peak of the sensitivity of 620 nm and the applied laser light of 660 nm at the sputtering is attributed to the energy shift due to the bias voltage at the fabrication.

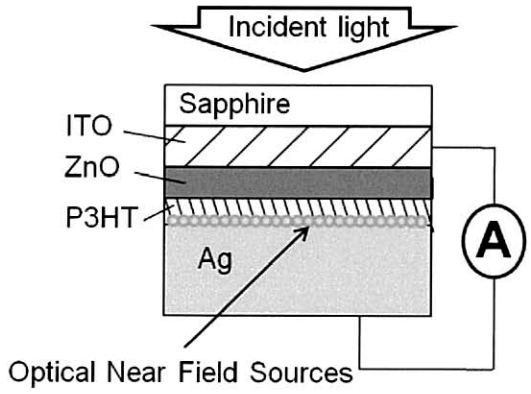

Fig.1. Schematic structure of the fabricated photodetector.

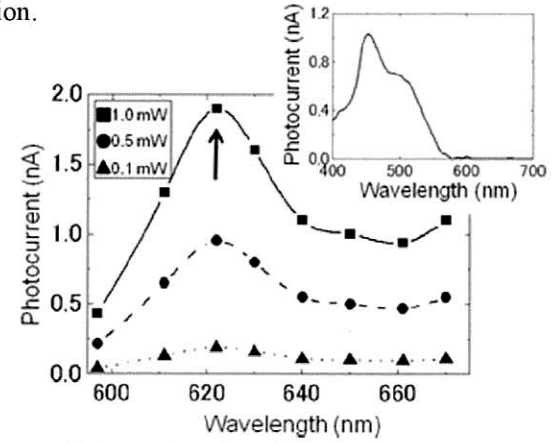

Fig.2. Wavelength dependence of photo current.

References

[1] T. Kawazoe, K. Kobayashi, S. Takubo, and M. Ohtsu, J. Chem. Phys., 122, 024715, (2005).
[2] T. Kawazoe, M. Ohtsu, Y. Inao, and R. Kuroda, J. Nanophoton. 1, 011595, (2007).
[3] T. Yatsui, K. Hirata, W. Nomura, M. Ohtsu, and Y. Tabata, Appl. Phys. B: Laser and Optics, 93, 55, (2008).
[4] T. Kawazoe, H. Fujiwara, K. Kobayashi, and M. Ohtsu, J. Sel. Top. Quant. Electron, in press (2009).

Numerical simulation for nonadiabatic optical near-field etching

Y. Fujiyoshi[1], M. Haraguchi[1], M. Fukui[1], T. Okamoto[1], T. Yatsui[2], M. Ohtsu[2]*
1Department of Optical System and Technology, The University of Tokushima
Minami jousanjima 2-1 , Tokushima 770-8506 ,Japan
2Department of Electrical Engineering and Information Systems, School of Engineering, The University of Tokyo
2-11-16 Yayoi, Bunkyo-ku, Tokyo 113-8656, Japan
fujiyosi@opt.tokushima-u.ac.jp

Recently, nonadiabatic optical near-field etching [1] has been proposed as a new method providing an ultra-flat-surface substrate with sub-nm scale roughness. Compared with other etching methods, there are many unclear problems, e.g., variation of surface structure in terms of time, the optimal experiment condition for various materials. In order to understand the process of the etching and solve such problems, the development of numerical simulation method for the etching is important. In this study, our purpose is to propose a numerical model of nonadiabatic optical near-field etching with FDTD method.

We divide the etching process to two stages. The first one is the gas decomposition stage where a molecule in an etching gas is dissociated to generate radicals by the nonadiabatic optical process. The second one is the surface etching stage by radicals where radicals attack surface atoms to remove them by chemical reactions. For the former, the chance of the nonadiabatic optical process is proportional to the time integral value of the production between the light intensity and its space derivation [2]. The proportional constant is α. We have developed a program based on the two-dimensional finite-difference time-domain method.

Figure 1 is an example of the initial surface structure employed: the height is 100 nm, and the width is 50 nm. The refractive index of the substrate was set to 1.5. We have evaluated the surface roughness by RMS value in the width of 500 nm. In Fig.2, We show typical result of the time dependence of RMS for various α. We can find that the RMS is strongly depends on α and is unstable to time in the range of α employed here.

This work was partially supported by NEDO under the program of Strategic Development on Rationalization Technology using Energy.

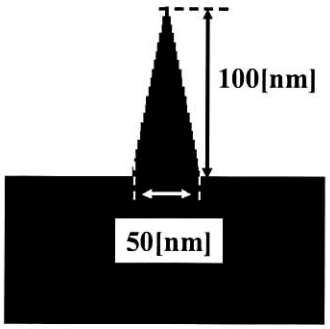

Fig.1 Initial structure

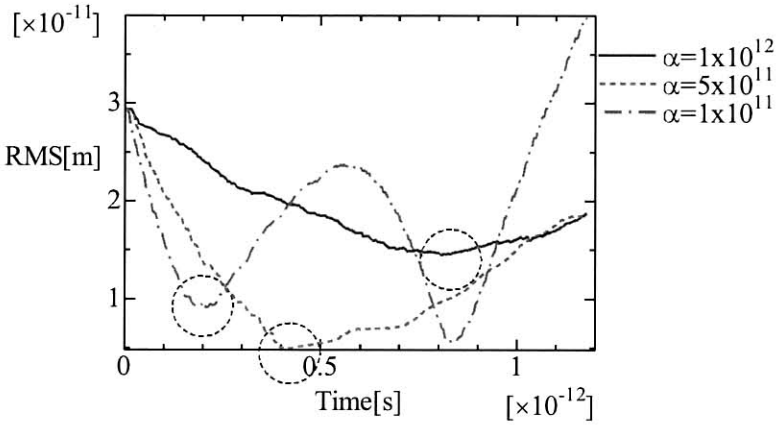

Fig.2 The change of RMS in terms of time

References

[1] T. Yatsui, K. Hirata, W. Nomura, Y. Tabata, and M. Ohtsu, *Appl. Phys. B* **93**, 55 (2008).
[2] T. Kawazoe,Y. Yamamoto and M. Ohtsu, *Appl Phys. Lett.*, **79**, 1184 (2001).

Visible light emission from DCM dye grains via infrared excitation due to the nonadiabatic transition induced by the optical near field

Tadashi Kawazoe1,2, Hiroyasu Fujiwara3, and Motoichi Ohtsu1,2

1. Department of Electrical Engineering and Information Systems, Graduate School of Engineering, The University of Tokyo, 2-11-16 Yayoi, Bunkyo-ku, Tokyo 113-8656, Japan
2. Nanophotonics Research Center, Graduate School of Engineering, The University of Tokyo, 2-11-16 Yayoi, Bunkyo-ku, Tokyo 113-8656, Japan
3. Central Research Laboratories, Hamamatsu Photonics K.K., Hirakuchi 5000, Hamakita-ku, Hamamatsu, 434-8601, Japan
**E-mail: kawazoe@ee.t.u-tokyo.ac.jp*

Frequency up-conversion of light is advantageous for infrared photodetectors or imaging sensors. Conventional methods for frequency up-conversion, *e.g.*, second harmonic generation (SHG) and phosphorescence, have some problems, *e.g.*, requiring a high-power and coherent incident light for high efficiency and saturation of the emitted light intensity, respectively. The nonadiabatic response and transition due to the optical near-field (ONF) excitation can avoid these problems. This phenomenon has been observed as photochemical reactions[1], which have been theoretically described by the dressed photon model. In this model, the ONF efficiently excites the optically forbidden molecular vibrational state. Thus, even though the photon energy of the ONF is lower than the energy of the optically allowed level, the electronic states of the molecule can be excited via a multistep transition. It has been applied to nanometric fabrication, *e.g.*, CVD [1,2], lithography [3], and chemical polishing [4]. In this presentation, we report the application of this phenomenon to the highly efficient frequency up-conversion of infrared light.

The grains of 4-dicyanomethylene-2-methyl-6-p-dimethylaminostyryl-4H-pyran (DCM) dye molecules were used for the visible light emission by the infrared ONF excitation. Figure 1 shows the emission spectra by the excitation using infrared light (λex = 805 nm). The emitted light intensity increased with the infrared excitation intensity, in agreement with the theoretical results of the dressed photon model, as shown in Fig.2. This dependence supports that the visible light emission originated from the nonadiabatic transition process due to optical near-field features. The frequency up-conversion efficiency was experimentally estimated to be higher than that of the SHG from a potassium dihydrogen phosphate (KDP) crystal.

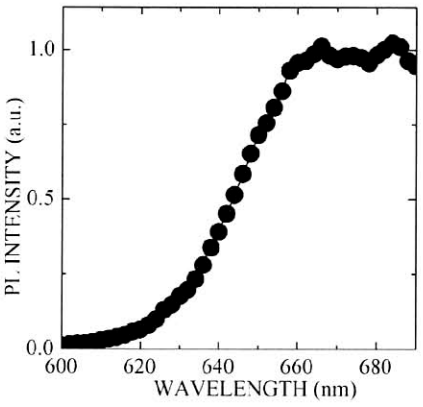

Fig.1.

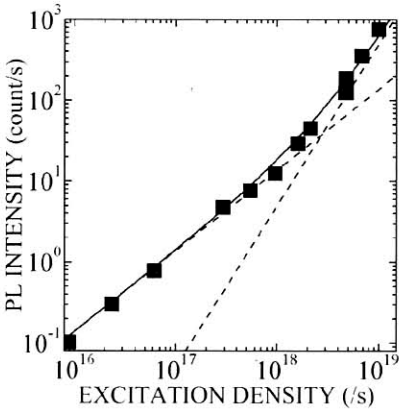

Fig.2.

References

[1] T. Kawazoe, K. Kobayashi, S. Takubo, and M. Ohtsu, J. Chem. Phys., Vol.122, No.2, pp.024715 (2005).
[2] T. Kawazoe, Y. Yamamoto, and M. Ohtsu, Appl. Phys. Lett., Vol.79, No.8, pp.1184 (2001).
[3] T. Kawazoe, M. Ohtsu, Y. Inao, and R. Kuroda, J. Nanophoton. Vol. 1, pp.011595 (2007).
[4] T. Yatsui, K. Hirata, W. Nomura, M. Ohtsu, and Y. Tabata, Appl. Phys. B: Lasers and Optics, Vol. 93, pp.55 (2008).

Self-organized nanophotonic signal transmission device

T. Yatsui [a,b*], Y. Ryu[a], T. Morishima[a], W. Nomura[a], T. Yonezawa[c], M. Washizu[a], H. Fujita[d], and M. Ohtsu[a,b]
[a] *School of Engineering, the University of Tokyo, Japan*
[b] *Nanophotonic Research Center, Graduate School of Engineering, The University of Tokyo*
[c] *Graduate School of Engineering, Hokkaido University, Japan*
[d] *Institute of Industrial Science, the University of Tokyo, Japan*
* Corresponding author: yatsui@ee.t.u-tokyo.ac.jp

Innovations in optical technology are required for the development of future information processing systems, which includes increasing the integration of photonic devices by reducing their size and levels of heat generation. To meet this requirement, we proposed nanophotonic signal transmission (NST) devices that consist of semiconductor quantum dots (QDs) [1]. These NST devices operate using excitons in QDs as the signal carrier, due to optical near-field interactions between closely spaced QDs. The exciton energy transfers to another QD when the exciton energy levels are resonant and, therefore, the optical beam spot may be decreased to be as small as the QD size. To produce the NST device, a new technique is required for positioning and alignment of QDs with precise separation.

Figure 1(a) illustrates our approach for the development of a self-assembling NST device with angstrom-scale controllability in spacing among QDs using silane-based molecular spacers and DNA [2]. First, ZnO QDs 5 nm diameter in diameter were synthesized using the Sol-Gel method [3]. Then, the surfaces of QDs were coated with a silane coupling agent 0.6 nm in length. The function of the agent is to maintain the spacing between QDs, and to be adhesive to anionic DNA, due to its cationic nature. We used λ DNA (stretched length = 16 μm) as a template, and when the QDs are mixed, the QDs are self-assembled onto the DNA by electrostatic interactions. Dense packing of the ZnO QDs along the DNA was obtained, as shown by transmission electron micrography (TEM) (Fig. 1(b)). The separation between QDs (S) was determined by TEM and shown to be 1.2 nm, which was in good agreement with twice the length of silane coupling agents. Such a high density of packing, despite the electrostatic repulsion between ZnO QDs, was due to the quaternary ammonium group of the silane coupling agent [3].

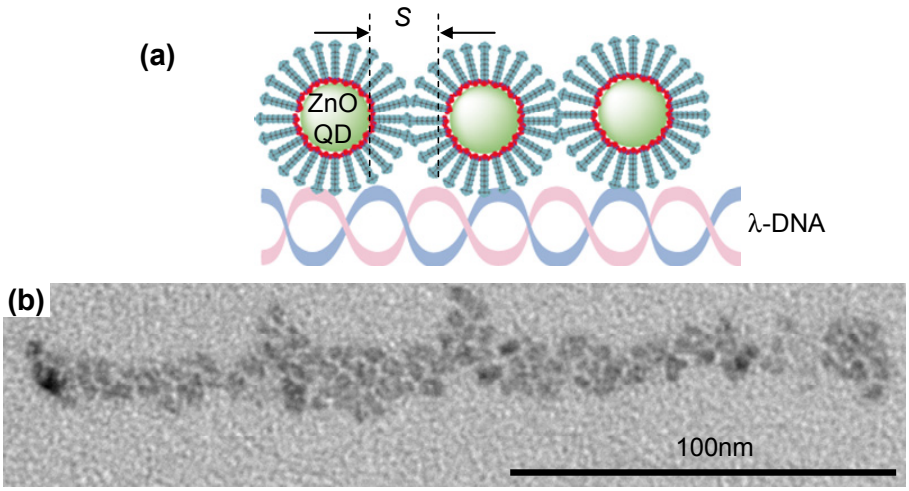

Fig. 1. Fabrication and evaluation of nanophotonic signal transmission device. (a) Schematic of ZnO QD alignment along the λ DNA. S: separation between QDs (b) TEM picture of the aligned ZnO QDs.

References

[1] M. Ohtsu, T. Kawazoe, T. Yatsui, M. Naruse, IEEE J. Select. Top. Quant. Electron. **14**, 1404 (2008).
[2] T. Yonezawa, S. Onoue, N. Kimizuka, Chem. Lett. **31**, 1172 (2002).
[3] E.A. Meulenkamp, J. Phys. Chem. B **102**, 5566 (1998).

Nanophotonics: Dressed photon science and technology

M. Ohtsu
Department of Electrical Engineering and Information Systems,
Nanophotonics Research Center,
the Univ. of Tokyo
2-11-16 Yayoi, Bunkyo-ku, Tokyo 113-8656, Japan
ohtsu@ee.t.u-tokyo.ac.jp, http://uuu.t.u-tokyo.ac.jp

This presentation reviews the principles and practices of the novel optical technology of *nanophotonics*, which utilizes the optical near-field, *i.e.*, the nanometer-sized light that is localized on the surface of a nanometric material[1,2]. The key to utilizing optical near-fields is to realize novel nanometric device operation, fabrication, and energy conversion, etc., by the control of an intrinsic interaction between nanometer-sized materials via optical near-fields. This has not been realized using conventional optical science and technology. The nature of optical near-fields was studied by regarding the optical near-field as an electromagnetic field that mediates the interaction between nanometric materials. As a result, the physically intuitive concept of a *dressed photon* was established to describe optical near-fields, *i.e.*, the interaction between nanometric materials is mediated by exchanging dressed photons[3,4].

Nanophotonics has produced some interesting new devices such as nanophotonic AND- and NOT-gates, and an optical nanofountain. AND-gate operation has been demonstrated by CuCl quantum dots (QDs)[5] and by ZnO nanorod with double quantum wells[6]. For room-temperature operation of NOT-gate devices, we have used InAlAs, a promising candidate material. We fabricated two layers of $In_{0.5}Al_{0.5}As$ QDs using molecular beam epitaxy[7]. They were grown just above the QDs in the lower layer, so that the lower and upper QDs were aligned vertically owing to the residual lattice strain induced as a result of growing the lower QD. The temporal evolution of the output signal was evaluated. The outstanding advantages of these nanophotonic devices are their low power consumption and small size. We estimated that the power consumption was about five orders of magnitude lower than that of a conventional electronic gate[8]. The optical nanofountain can be used as a far-field to near-field optical signal conversion device to connect a conventional diffraction-limited photonic device to a nanophotonic device[9].

Nonadiabatic processes triggered by optical-near-field interactions have been used as representative examples of nanophotonic fabrication. These processes represent *qualitative* innovation in photochemical vapor deposition and photolithography, suggesting that large, expensive ultraviolet light sources are no longer required, although they are indispensable for conventional adiabatic photochemical vapor deposition, photolithography, and photochemical etching. It also suggests that nonadiabatic photochemical vapor deposition can even dissociate optically inactive molecules (i.e., inactive to the propagating light), which is advantageous for environment protection because most optically inactive molecules are chemically stable and harmless. For example, optically inactive $Zn(acac)_2$ molecules have been dissociated to deposit nanometric Zn particles[10]. In addition, in the case of nonadiabatic photolithography, an optically inactive resist film for

978-0-9798064-2-1/μTAS2009/$20

electron-beam lithography has been used to fabricate fine patterns [11]. Furthermore, in nonadiabatic photochemical etching has realized an ultra-flat glass surface with the roughness as low as 1.3 Angstrom without using any photomasks[12].

In conventional optical science and technology, light and matter are discussed separately, and the flow of optical energy in a photonic system is considered unidirectional, from a light source to a photodetector. By contrast, in nanophotonics, light and matter have to be regarded as being coupled to each other and the energy flow between nanometric particles is bidirectional. This means that nanophotonics should be regarded as a *technology fusing optical fields and matter*. The term nanophotonics is occasionally used for photonic crystals, plasmonics, metamaterials, silicon photonics, and quantum dot lasers using conventional propagating light, although they are not based on optical near-field interactions. The development of nanophotonics requires far-reaching physical insights into the local electromagnetic interaction in the nanometric subsystem composed of electrons and photons.

References

[1]M. Ohtsu, et al., *IEEE J. Selected Topics in Quantum Electronics*, vol.8, p.839, 2002.

[2] M. Ohtsu, et al., *IEEE J. Selected Topics in Quantum Electronics*, vol.vol.14, p.1404, 2008.

[3]M. Ohtsu and K. Kobayashi, *Optical Near Fields*. Berlin, Germany: Springer-Verlag, 2003, p.109.

[4]M. Ohtsu, et al., *Principles of Nanophotonics*, London,England: Tailor & Francis, 2008.

[5]T. Kawazoe, et al., *Appl. Phys. Lett.,* vol.82, p.2957, 2003.

[6]T. Yatsui, et al., *Appl. Phys. Lett*., vol.90, p.223110, 2007.

[7]L. Goldstein, et al., *Appl. Phys. Lett*., vol.47, p.1099, 1985.

[8]T. Kawazoe, et al., *Appl. Phys. Lett*., vol.82, p. 2957, 2003.

[9]T. Kawazoe, et al., *Appl. Phys. Lett*., vol.86, p.103102, 2005.

[10]T. Kawazoe, et al., *Appl. Phys. B,* vol.84, p.247, 2006.

[11]T. Kawazoe, et al., *Progress in Nano-Electro-Optics V*, M. Ohtsu, Ed. Berlin, Germany: Springer-Verlag, 2006, p.109.

[12] T. Yatsui, et al., *Appl. Phys. B*, vol.93, p.55, 2008.

Progress in developing nanophotonic fabrication

Takashi Yatsui and Motoichi Ohtsu
School of Engineering, The University of Tokyo
2-11-16 Yayoi, Bunkyo-ku, Tokyo, Japan 113-8656
Email: yatsui@ee.t.u-tokyo.ac.jp

For future optical transmission systems with high data transmission rates and capacity, we have proposed nanometer-scale photonic devices (i.e., nanophotonics devices) [1]. These devices consist of nanometer-scale dots, and an optical near-field is used as the signal carrier.

Since the nanophotonics devices is composed of sub-100-nm scale dots and wires, and their size and position must be controlled on a nanometer-scale to fabricate the device. To realize this level of controllability, this talk reviews bottom-up method using optical near-field. First, we demonstrate that optical near-field desorption can dramatically regulate the growth of metallic nanoparticles during optical chemical vapor deposition. The trade-off between the deposition and desorption due to the optical near-field light allowed the fabrication of a single 15-nm Zn dot [2], while regulating its size and position. For realization of mass-production of nanometer-scale structures, the possibilities of applying such a near-field desorption to other deposition technique such as sputtering, which does not use any fiber probes or photomasks, will be discussed [3]. Finally, we performed a new polishing method that uses near-field etching based on a non-adiabatic process [4], which does not use any polishing pad, with which we obtained ultra-flat silica surface with angstrom-scale average roughness (see Fig. 1) [5].

References

1. M. Ohtsu, T. Kawazoe, T. Yatsui, and M. Naruse, IEEE J. of Sel. Top. Quantum Electron. **14**, 1404 (2008). [Invited Paper]
2. T. Yatsui, S. Takubo, J. Lim, W. Nomura, M. Kourogi, and M. Ohtsu, Appl. Phys. Lett., **83**, 1716 (2003).
3. T. Yatsui, W. Nomura, and M. Ohtsu, Nano Lett., **5**, 2548 (2005).
4. T. Kawazoe, K. Kobayashi, S. Takubo, and M. Ohtsu, J. Chem. Phys., **122**, 024715 (2005).
5. T. Yatsui, K. Hirata, W. Nomura, M. Ohtsu, and Y. Tabata, Appl. Phys. B, **93**, 55 (2008).

978-1-4244-3681-1/09/$25.00 ©2009 IEEE

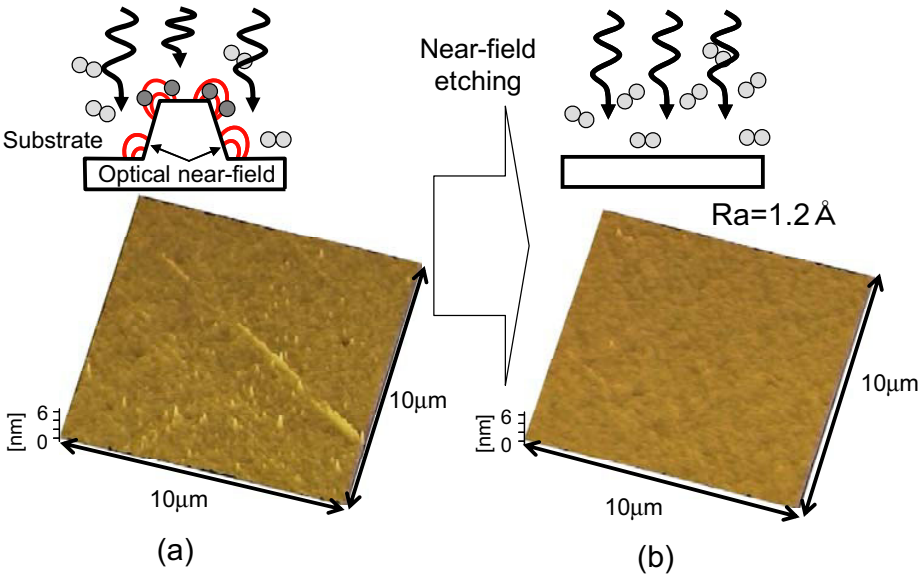

Fig. 1. Schematic of near-field etching. Atomic force microscopic images of (a) before and (b) after the optical near-field etching.

Parallel Retrieval of Nanometer-Scale Light-Matter Interactions for Nanophotonic Systems

Naoya Tate[1,2], Wataru Nomura[1,2], Takashi Yatsui[1,2], Tadashi Kawazoe[1,2], Makoto Naruse[1,2,3], and Motoichi Ohtsu[1,2]

[1] Department of Electrical Engineering and Information Systems, School of Engineering, The University of Tokyo, 2-11-16 Yayoi, Bunkyo-ku, Tokyo, 113-8656, Japan
[2] Nanophotonics Research Center, School of Engineering, The University of Tokyo, 2-11-16 Yayoi, Bunkyo-ku, Tokyo, 113-8656, Japan
[3] National Institute of Information and Communications Technology, 4-2-1 Nukuikita, Koganei, Tokyo, 184-8795, Japan

Abstract. Exploiting the unique attributes of nanometer-scale optical near-field interactions in a completely parallel manner is important for innovative nanometric optical processing systems. In this paper, we propose the basic concepts necessary for parallel retrieval of light–matter interactions on the nanometer-scale instead of the conventional one-dimensional scanning method. One is the *macro-scale observation* of optical near-fields, and the other is the *transcription* of optical near-fields. The former converts effects occurring locally on the nanometer scale involving optical near-field interactions to propagating light radiation, and the latter magnifies the distributions of optical near-fields from the nanometer scale to the sub-micrometer one. Those techniques allow us to observe optical far-field signals that originate from the effects occurring at the nanometer scale. We numerically verified the concepts and principles using electromagnetic simulations.

1 Introduction

Nanophotonics is a novel technology that utilizes the optical near-field, which is the electromagnetic field that mediates the interactions between closely spaced nanometric matter [1,2]. By exploiting optical near-field interactions, nanophotonics has broken the integration density restrictions imposed on conventional optical devices by the diffraction limit of light. This higher integration density has enabled realization of *quantitative* innovations in photonic devices and optical fabrication technologies [3,4]. Moreover, *qualitative* innovations have been accomplished by utilizing novel functions and phenomena made possible by optical near-field interactions, which are otherwise unachievable with conventional propagating light [5,6].

One of the most important technological vehicles that has contributed to the study of nanophotonics so far is high-quality optical near-field probing tips, such

F. Peper et al. (Eds.): IWNC 2009, PICT 2, pp. 298–307, 2010.

as those based on optical fiber probes [7]. They have achieved high spatial resolution and high energy efficiency, up to 10% optical near-field generation efficiency in some cases. For instance, near-field optical microscopes (NOMs) have been widely applied for obtaining ultrahigh-resolution images [8]. However, methods of characterizing optical near-fields using probing tips require one-dimensional (1D) scanning processes, which severely limit the throughput in obtaining two-dimensional (2D) information on the nanometer scale. Additionally, precision technologies are indispensable in fabricating probe tips and also in controlling their position during measurement; such technologies are large obstacles to developing more practical and easy characterization or utilization of optical near-fields. Therefore, eliminating one-dimensional scanning processes, or in other words, *probe-free nanophotonics*, is an important step toward further exploiting the possibilities of light–matter interactions on the nanometer scale.

In fact, we have successfully utilized optical near-field interactions without any scanning processes in nano-optical fabrication: For instance, optical near-field lithography, utilizing the near-field interactions between photomasks and photoresists, has already been developed [9]. Furthermore, non-adiabatic processes, meaning that optical near-field interactions activate conventionally light-insensitive materials, are additional novelties that are available in fabricating nano-structures by nanophotonics [10]. Optical near-field etching is another example of probe-free nanophotonics, where photochemical reactions are selectively excited in regions where optical near-fields are generated; this approach has been successfully demonstrated in flattening the rough surfaces of optical elements [11].

We consider that eliminating optical near-field probe tips is also important for characterization of optical near-fields and information processing applications. In this paper, we discuss the concept of parallel processing in nanophotonics, and we propose two techniques that allow parallel retrieval of optical near-fields: *macro-scale observation* of optical near-field interactions, which involves quadrupole–dipole transformation of charge distributions in engineered nanostructures, and *magnified transcription* of optical near-fields based on the photoinduced structural changes in metal complexes that exhibit photoinduced phase transitions.

In related applications, we have proposed shape-engineering of metal nanostructures so that optical near-field interactions between two nanostructures control the resultant far-field radiation [12]. Here we can also find probe-free utilization of optical near-field interactions. Although they are well matched with some applications, such as optical security [12], they are not applicable to nanostructures in general. They still require well-controlled shape-engineering processes, as well as precise alignment between planar nanostructures. In fact, another motivation of this study is to overcome such stringent alignment issues that are unavoidable in typical situations involving nanostructures. The concept of transcription of optical near-fields proposed in this paper would solve such problems by inducing unique processes enabled by the materials themselves—metal complexes in the particular demonstrations described below.

2 Nanometric Optical Processing Based on Nanophotonics

Nanometric optical processing systems, whose features include high integration density, low-energy operation, and innovative functions, are practical embodiments of such qualitative innovations offered by nanophotonics. Several fundamental proposals have been developed for their implementation, such as nanophotonic devices [13,14,15] and interconnect technologies [16]. However, regarding the interfaces between those nanometric systems and their associated surrounding systems, existing concepts that apply to conventional optical systems are not applicable since the physical basis is completely different between conventional propagating light and optical near-fields. Appropriate interfacing concepts and techniques that are well matched with the features of nanophotonics are strongly demanded. Eliminating the conventional scanning processes is also important to significantly improve the throughput in obtaining information on the nanometer scale.

Figures 1(a) and (b) show schematic diagrams that conceptually illustrate two kinds of representative nanometric processing systems. The system shown in Fig. 1(a) is operated by the host processing system located in the center. All of the processing nodes around the center are precisely controlled by the host system. In the case of nanometric processing, however, such a centralized architecture is difficult to apply since it is technically difficult to precisely align the nanometric components and to precisely and flexibly interconnect each component. On the other hand, we propose the system schematically shown in Fig. 1(b) for the implementation of nanometric optical processing systems. The processing components are connected in an autonomous manner, and the global control signals do not specify the detailed operations of each component. The local interactions between components in the system, involving optical near-field interactions, bring about certain behavior in the system as a whole.

In order to realize the parallel processing system shown in Fig. 1(b), it is necessary to retrieve the information located at the nanometer scale and expose it at the sub-micrometer scale so that the outputs of the system are obtainable in the optical far-field. For this purpose, here we propose two fundamental techniques: one is the *macro-scale observation* of optical near-field interactions, and the other is the *transcription* of optical near-field interactions, as schematically shown in Fig. 1(c). These techniques eliminate one-dimensional scanning processes; in other words, *probe-free nanophotonics* is accomplished.

3 Nanophotonic Matching Utilizing Macro-scale Observation of Optical Near-Field Interactions

For the macro-scale observation of optical near-fields, here we demonstrate that two nanostructures can be designed to exhibit far-field radiation only under the condition that the shapes of the two structures are appropriately combined and

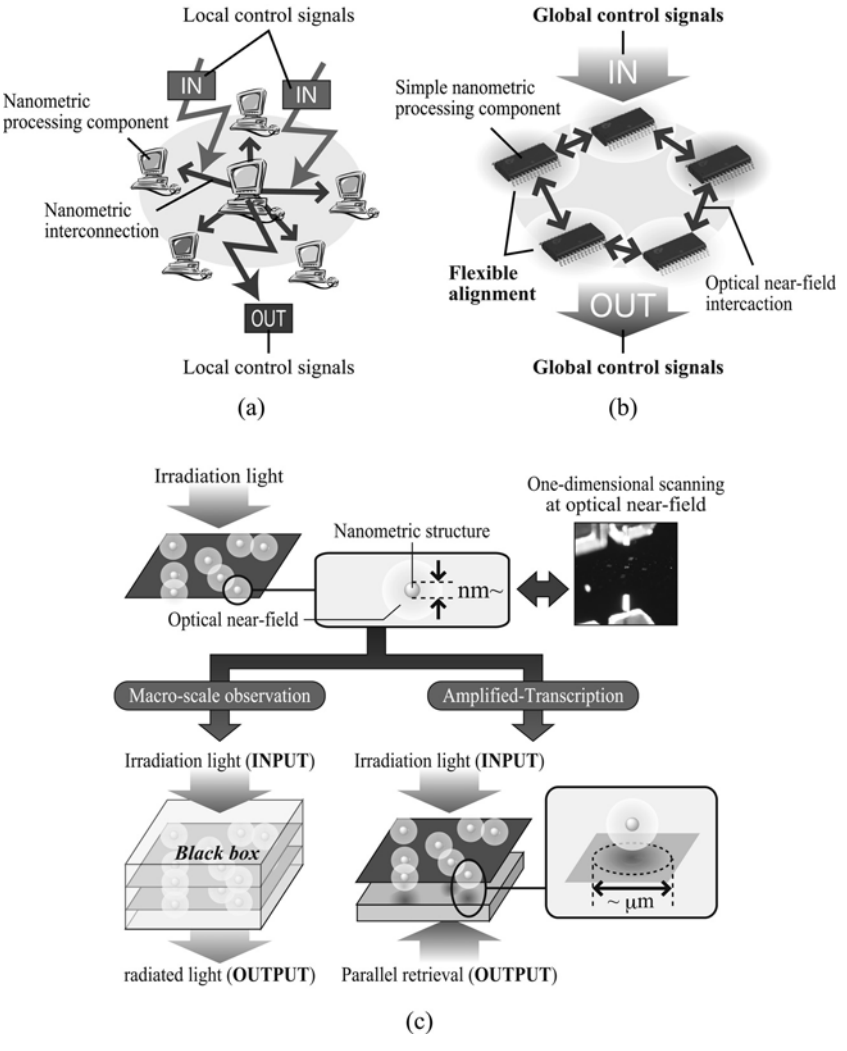

Fig. 1. Basic concept of nanometric processing systems (a) based on existing processing protocol and (b) utilizing nanophotonics. (c) Proposed fundamental processes of spatially parallel data retrieval for the nanometric optical processing system.

closely stacked. This function of the two nanostructures can be regarded effectively as a lock and a key, because only an appropriate combination of a lock and a key yields an output signal, namely, far-field radiation [12]. Figure 2 shows a schematic diagram of the nanophotonic matching system based on this function.

We design two nanostructural patterns, called *Shape A* and *Shape B* hereafter, to effectively induce a quadrupole–dipole transform via optical near-field interactions. Shape A and Shape B are designed as rectangular units on the xy-plane with constant intervals horizontally (along the x-axis) and vertically

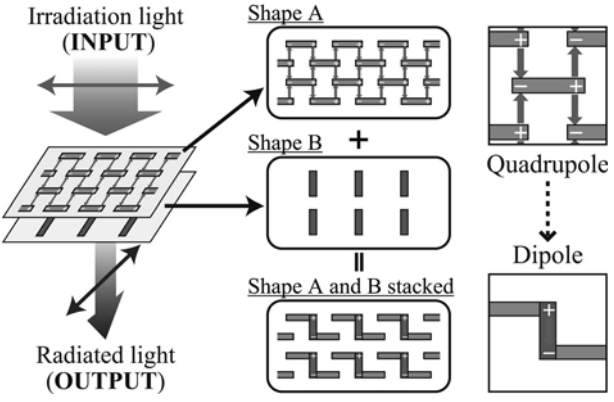

Fig. 2. Schematic diagram of nanophotonic matching system. The function is based on a quadrupole–dipole transform via optical near-field interactions, and it is achieved through shape-engineered nanostructures and their associated optical near-field interactions.

(along the y-axis), respectively. When we irradiate Shape A with x-polarized light, surface charges are concentrated at the horizontal edges of each of the rectangular units. The relative phase difference of the oscillating charges between the horizontal edges is π, which is schematically represented by + and − marks in Fig. 2. Now, note the y-component of the far-field radiation from Shape A, which is associated with the charge distributions induced in the rectangle. We draw arrows from the + mark to the − mark along the y-axis. We can find that adjacent arrows are always directed oppositely, indicating that the y-component of the far-field radiation is externally small. In other words, Shape A behaves as a quadrupole with regard to the y-component of the far-field radiation. It should also be noted that near-field components exist in the vicinity of the units in Shape A. With this fact in mind, we put the other metal nanostructure, Shape B, on top of Shape A. Through the optical near-fields in the vicinity of Shape A, surface charges are induced on Shape B. What should be noted here is that the arrows connecting the + and − marks along the y-axis are now aligned in the same direction, and so the y-component of the far-field radiation appears; that is, the stacked structure of Shape A and Shape B behaves as a dipole. Also, Shape A and Shape B need to be closely located to invoke this effect since the optical near-field interactions between Shape A and Shape B are critical. In other words, a quadrupole–dipole transform is achieved through shape-engineered nanostructures and their associated optical near-field interactions.

In order to verify this mechanism of the quadrupole–dipole transform by shape-engineered nanostructures, we numerically calculated the surface charge distributions induced in the nanostructures and their associated far-field radiation based on a finite-difference time-domain (FDTD) electromagnetic simulator (*Poynting for Optics*, a product of Fujitsu, Japan). Figure 3(a) schematically

represents the design of (i) Shape A only, (ii) Shape B only, and (iii) a stacked structure of Shape A and Shape B, which consist of arrays of gold rectangular units. The length of each of the rectangular units is 500 nm, and the width and height are 100 nm. As the material, we assumed a Drude model of gold with a refractive index of 0.16 and an extinction ratio of 3.8 at a wavelength of 688 nm [17].

When irradiating these three structures with continuous-wave x-polarized input light at a wavelength of 688 nm, Figs. 3(b), (c) and (d) respectively show the induced surface charge density distributions (simply called surface charge hereafter) by calculating the divergence of the electric fields. For the Shape A only structure (Fig. 3(b)), we can find a local maximum and local minimum of the surface charges, denoted by + and − marks. When we draw arrows from the + marks to the − marks between adjacent rectangular units, as shown in

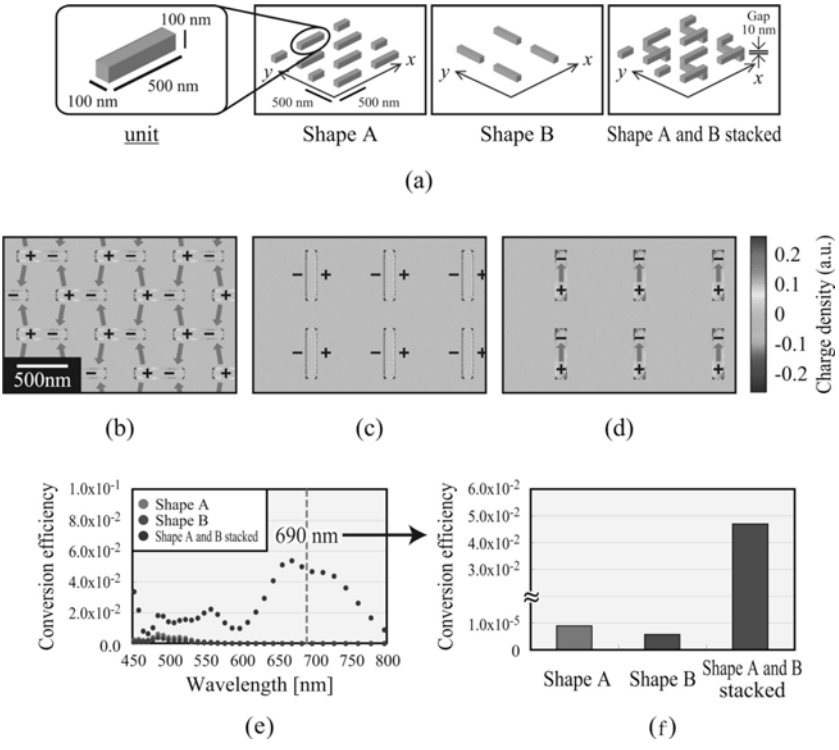

Fig. 3. (a) Specifications of the three types of nanostructures used in numerical evaluation of the conversion efficiency based on the FDTD method: Shape A only, Shape B only, and a stacked structure of Shapes A and B. (b,c) Surface charge density distributions induced in (b) Shape A only and (c) Shape B only. (d) Surface charge density distribution induced in Shape B only when it is stacked on top of Shape A. (e) Calculated performance figures of the quadrupole–dipole transform, namely, polarization conversion efficiency, with the three types of nanostructures. (f) Selective comparison at a wavelength of 690 nm.

Fig. 2, we can see that the arrows are always directed oppositely between the adjacent ones, meaning that the Shape A only structure behaves as a quadrupole for the y-components of the far-field radiation. For the Shape B only structure (Fig. 3(c)), the charges are concentrated at the horizontal edges of each of the rectangular units, and there are no y-components that could contribute to the far-field radiation. Figure 3(d) shows the surface charge distributions induced in Shape B when it is stacked on top of Shape A. We can clearly see that the charges are induced at the vertical edges of each of the rectangular units, and they are aligned in the same direction. In other words, a dipole arrangement is accomplished with respect to the y-component, leading to a drastic increase in the far-field radiation.

Now, one of the performance figures of the quadrupole-dipole transform is $I_{\mathrm{conv}} = I_{y-\mathrm{OUT}}/I_{x-\mathrm{IN}}$, where $I_{x-\mathrm{IN}}$ and $I_{y-\mathrm{OUT}}$ represent the intensities of the x-component of the incident light and the y-component of the radiated light, respectively. We radiate a short optical pulse with a differential Gaussian form whose width is 0.9 fs, corresponding to a bandwidth of around 200 to 1300 THz. Figure 3(e) shows I_{conv} as a function of the input light wavelength, and Fig. 3(f) compares I_{conv} specifically at 690 nm. I_{conv} appears strongly with the stacked structure of Shapes A and B, whereas it exhibits a small value with Shape A only and Shape B only. We can clearly observe the quadrupole–dipole transform in the optical near-fields as the change of I_{conv} in the optical far-fields.

4 Transcription Based on Photoinduced Phase Transition

The second fundamental technique to realize our proposal is spatial magnification of optical near-fields with a certain magnification factor so that the effects of optical near-fields can be observed in optical far-fields. We call this transcription of optical near-fields. It is schematically shown in Fig. 4.

In our proposal, it is necessary to spatially magnify the optical near-field from the nanometer scale to the sub-micrometer scale in the resultant transcribed pattern so that it becomes observable in the optical far-field. It turns out that the magnification factor should be about 10–100. It has been reported that some metal complexes exhibit photoinduced phase transitions with quantum efficiencies (QEs) of more than ten, as schematically shown in the upper half of Fig. 4. This suggests the possibility of transcription of optical near-fields with a certain magnification factor using such materials. Once the spatial pattern is detectable in the far-field, various concepts and technologies common in parallel optical processing will be applicable.

A photoinduced phase transition has been observed in several cyano-bridged metal complexes [18]. They exhibit bistable electronic states at room temperature. The energy barrier between these bistable states maintains a photoinduced state even after irradiation is terminated. Also, the state can easily be reset via either optical irradiation or temperature control. Moreover, typical phase transitions are excited in a cascaded manner, meaning that they exhibit high quantum efficiencies. This transition between the high-temperature (HT) phase and the

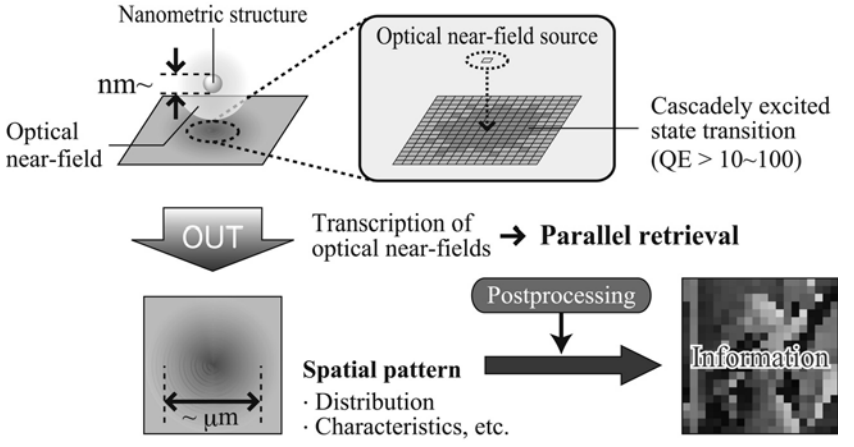

Fig. 4. Fundamental process of optical parallel data retrieval based on the transcription of optical near-fields. In our proposal, it is necessary to spatially magnify the optical near-field from the nanometer scale to the sub-micrometer scale in the resultant transcribed pattern so that it is observable in the optical far-field.

low-temperature (LT) phase is accompanied by a structural change from a cubic to a tetragonal structure due to Jahn–Teller distortion, and their physical properties are strongly changed by the transition. Rubidium manganese hexacyanoferrate [19] is a suitable material for the transcription medium.

To validate the transcription effect numerically, we simulated the difference of the optical response between the LT- and HT-phase materials using FDTD simulation. A nanometric fiber probe with a radius of 20 nm and an illumination light source with an operating wavelength of 635 nm were included in the calculation model, as shown in Fig. 5(a). Figure 5(b) compares the electric field intensities at the surfaces of the LT- and HT-phase materials.

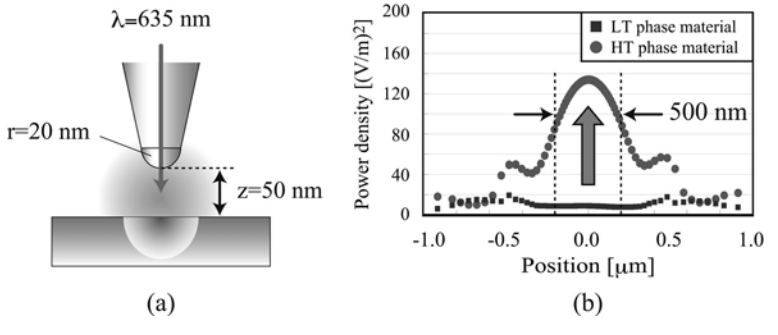

Fig. 5. (a) Schematic diagrams of calculation model for numerical validation of the transcription. (b) Numerical results. The signal intensity in the near-field is obviously increased by the irradiation.

The power density at the surface of the HT-phase material was much stronger than that of the LT-phase material, and the scale of the distribution was magnified from 20 nm, comparable to the size of the fiber probe, to 500 nm, comparable to the size of the transcribed area. From these results, we can confirm the fundamental principle of the magnified transcription of optical near-fields using a cyano-bridged metal complex as a transcription medium.

5 Conclusions

In summary, we have proposed the concepts of macro-scale observation and transcription of optical near-fields as fundamental techniques for nanometric optical processing. We numerically demonstrated the principles with practical calculation models based on FDTD methods. These are key, fundamental techniques for parallel retrieval in nanometric optical processing. We will further investigate the principles and show experimental demonstrations for exploiting the unique physical processes originating at the nanometer scale and making them available as valuable system-level functions for implementation of nanometric processing systems.

The authors thank Prof. Ohkoshi, Dr. Tokoro, and Dr. Takeda of the Department of Chemistry, School of Science, the University of Tokyo, for their valuable contributions to our collaborative research.

This work was supported in part by a comprehensive program for personnel training and industry–academia collaboration based on NEDO projects funded by the New Energy and Industrial Technology Organization (NEDO), Japan, as well as the Global Center of Excellence (G-COE) “Secure-Life Electronics” and Special Coordination Funds for Promoting Science and Technology sponsored by the Ministry of Education, Culture, Sports, Science and Technology (MEXT), Japan.

References

1. Ohtsu, M., Kobayashi, K., Kawazoe, T., Sangu, S., Yatsui, T.: Nanophotonics: Design, Fabrication, and Operation of Nanometric Devices Using Optical Near Fields. IEEE J. Sel. Top. Quantum Electron. 8(4), 839–862 (2002)
2. Naruse, M., Miyazaki, T., Kawazoe, T., Kobayashi, K., Sangu, S., Kubota, F., Ohtsu, M.: Nanophotonic Computing Based on Optical Near-Field Interactions between Quantum Dots. IEICE Trans. Electron E88-C(9), 1817–1823 (2005)
3. Nishida, T., Matsumoto, T., Akagi, F., Hieda, H., Kikitsu, A., Naito, K.: Hybrid recording on bit-patterned media using a near-field optical head. J. Nanophotonics B, 011597 (2007)
4. Ozbay, E.: Plasmonics: Merging Photonics and Electronics at Nanoscale Dimensions. Science 311, 189–193 (2006)
5. Ohtsu, M.: Nanophotonics in Japan. J. Nanophotonics 1, 0115901–7 (2007)
6. Naruse, M., Kawazoe, T., Yatsui, T., Sangu, S., Kobayashi, K., Ohtsu, M.: Progress in Nano-Electro-Optics V. Ohtsu, M. (ed.). Springer, Berlin (2006)

7. Mononobe, S.: Near-Field Nano/Atom Optics and Technology, pp. 31–69. Springer, Berlin (1998)
8. Maheswari Rajagopalan, U., Mononobe, S., Yoshida, K., Yoshimoto, M., Ohtsu, M.: Nanometer level resolving near field optical microscope under optical feedback in the observation of a single-string deoxyribo nucleic acid. Jpn. J. Appl. Phys. 38(12A), 6713–6720 (1999)
9. Inao, Y., Nakasato, S., Kuroda, R., Ohtsu, M.: Near-field lithography as prototype nano-fabrication tool. Science Direct Microelectronic Engineering 84, 705–710 (2007)
10. Kawazoe, T., Ohtsu, M., Inao, Y., Kuroda, R.: Exposure dependence of the developed depth in nonadiabatic photolithography using visible optical near fields. J. Nanophotonics 1, 0115951–9 (2007)
11. Yatsui, T., Hirata, K., Nomura, W., Tabata, Y., Ohtsu, M.: Realization of an ultra-flat silica surface with angstrom-scale. Appl. Phys. B 93, 55–57 (2008)
12. Naruse, M., Yatsui, T., Kawazoe, T., Tate, N., Sugiyama, H., Ohtsu, M.: Nanophotonic Matching by Optical Near-Fields between Shape-Engineered Nanostructures. Appl. Phys. Exp. 1, 112101 1-3 (2008)
13. Kobayashi, K., Sangu, S., Kawazoe, T., Shojiguchi, A., Kitahara, K., Ohtsu, M.: Excitation dynamics in a three-quantum dot system driven by optical near field interaction: towards a nanometric photonic device. J. Microscopy 210, 247–251 (2003)
14. Kawazoe, T., Kobayashi, K., Akahane, K., Naruse, M., Yamamoto, N., Ohtsu, M.: Demonstration of a nanophotonic NOT gate using near-field optically coupled quantum dots. Appl. Phys. B 84, 243–246 (2006)
15. Yatsui, T., Sangu, S., Kawazoe, T., Ohtsu, M., An, S.-J., Yoo, J.: Nanophotonic switch using ZnO nanorod double-quantum-well structures. Appl. Phys. Lett. 90(22), 223110-1-3 (2007)
16. Nomura, W., Yatsui, T., Kawazoe, T., Ohtsu, M.: Observation of dissipated optical energy transfer between CdSe quantum dots. J. Nanophotonics 1, 011591-1-7 (2007)
17. Lynch, D.W., Hunter, W.R.: Comments on the Optical Constants of Metals and an Introduction to the Data for Several Metals. In: Palik, E.D. (ed.) Handbook of Optical Constants of Solids, pp. 275–367. Academic Press, Orlando (1985)
18. Sato, O., Hayami, S., Einaga, Y., Gu, Z.Z.: Control of the Magnetic and Optical Properties in Molecular Compounds by Electrochemical, Photochemical and Chemical Methods. Bull. Chem. Soc. Jpn. 76(3), 443–470 (2003)
19. Tokoro, H., Matsuda, T., Hashimoto, K., Ohkoshi, S.: Optical switching between bistable phases in rubidium manganese hexacyanoferrate at room temperature. J. Appl. Phys. 97, 10M508 (2005)

Tuesday, September 22 · 09:30 - 10:45

Room: Hall F2

3.6: Nanophotonics

Chair: Christian Lerminiaux, Université de Technologie de Troyes, France

9:15 3.6.1

Tutorial: Nanophotonics: Dressed Photon Technology for Innovative Optical Devices, Fabrications and Systems

Motoichi Ohtsu, The University of Tokyo, Japan

♦ This tutorial reviews recent progress in nanophotonics, a novel optical technology proposed in 1993 by the author. Nanophotonics utilizes the local interaction between nanometric particles via optical near fields. The optical near fields are the elementary surface excitations on nanometric particles, that is, dressed photons that carry the material excitation. The principles of device operation are reviewed considering the excitation energy transfer via the optical near-field interaction and subsequent relaxation. The operations of logic gates, an optical nano-fountain, a nano-coupler, a pulse generator, a nonadiabatic light emitter, etc. are described as well as their single photon emission and extremely low power consumption capability. Experimental results using quantum dos at the room temperature are described. Using a systems-perspective approach, the principles of content-addressable memory for optical router, a multilayer memory retrieval system, etc. are demonstrated. Application to nonadiabatic lithography, etching, etc. are also reviewed.

System Architectures for Nanophotonics for Information and Communications Applications

Makoto Naruse[1,2], Naoya Tate[2], Motoichi Ohtsu[2],

[1] *Photonic Network Group, New Generation Network Research Center, National Institute of Information and Communications Technology, 4-2-1 Nukui-kita, Koganei, Tokyo 184-8795, Japan*

[2] *Department of Electrical Engineering and Information Systems and Nanophotonics Research Center, School of Engineering, The University of Tokyo, 2-11-16 Yayoi, Bunkyo-ku, Tokyo 113-8656, Japan*

E-mail: naruse@nict.go.jp

Abstract: We demonstrate system architectures for nanophotonics that enable optical near-field interactions in the nanometer-scale expolited for ultra-high density system integrations beyond the diffraction limit of light and achieving novel functionalities in information and communications applications.

Keywords: Nanophotonics, System architecture, Optical near-field

Recent advances in nanophotonics and sub-wavelength-precision fabrication technology allow the design of optical devices and systems at densities beyond those conventionally limited by the diffraction of light. Such higher integration density, however, is only one of the benefits of nanophotonics over conventional optics and electronics. From a system architectural perspective, nanophotonics drastically changes the fundamental design rules of functional optical systems, and suitable architectures may be built to exploit this. As a result, it also gives qualitatively strong impacts on various systems including information and communications applications [1]. In this talk, two kinds of system architectures will be demonstrated that exploit unique physical processes in light-matter interactions in the nanometer-scale. One is based on optical excitation transfer via optical near-field interactions [2], and the other is based on their hierarchical properties [3].

Firstly, optical excitation transfer are briefly reviewed from a signal transfer perspective and its enabling architectures will be discussed, such as memory-based architecture in which any functionality or computations are associated with table lookup operations [2]. The fundamental processes, such as summation and broadcast of signals, are demonstrated based on geometry-controlled quantum dots and inter-dot interactions via optical near-fields [4,5]. Also, we show that such systems exhibit higher tamper resistance, or high security, compared with conventional devices by analyzing the physical scale associated with the required energy dissipation [6].

Secondly, we focus on the hierarchical properties in optical near-field interactions. Optical near-fields behave differently depending on the physical scales involved [1,3]. They have been applied to various applications such as information and communications devices and systems [1,7] and nano-fabrications [8]. Technological vehicles for such architectures include shape-engineered nanostructures [7], quantum nanostructures [9], and many others. Those hierarchical architecture will be useful for solving interconnection bottlenecks between nano-scale devices and macro-scale systems [2], retrieving information from high-capacity, high-density data storage [10], and security-related applications such as traceability [7], authentication [11], anticounterfeit [12].

Through those architectural and physical insights, nanophotonic information and communications systems will be demonstrated that overcome the integration-density limit imposed by the diffraction of light as well as providing unique functionalities which are only achievable using optical near-field interactions.

REFERENCES

[1] M. Naruse, "Fundamentals of Nanophotonic Systems," in Principles of Nanophotonics, M. Ohtsu, K. Kobayashi, T. Kawazoe, T. Yatsui, and M. Naruse Eds. Boca Raton: Taylor and Francis, 2008, pp. 165-197.

[2] M. Naruse, T. Kawazoe, T. Yatsui, S. Sangu, K. Kobayashi, M. Ohtsu, "Architectural Approach to Nanophotonics for Information and Communication Systems," in Progress in Nano-Electro-Optics V, M. Ohtsu Ed. Berlin: Springer, 2006, pp. 163-182.

[3] M. Naruse, T. Inoue, and H. Hori, "Analysis and Synthesis of Hierarchy in Optical Near-Field Interactions at the Nanoscale Based on Angular Spectrum," Jpn. J. Appl. Phys., vol. 46, pp. 6095-6103, Sep. 2007.

[4] M. Naruse, T. Miyazaki, F. Kubota, T. Kawazoe, K. Kobayashi, S. Sangu, M. Ohtsu, "Nanometric summation architecture using optical near-field interaction between quantum dots," Opt. Lett., vol. 30, pp. 201-203, Jan. 2005.

[5] M. Naruse, T. Kawazoe, S. Sangu, K. Kobayashi, and M. Ohtsu, "Optical interconnects based on optical far- and near-field interactions for high-density data broadcasting," Opt. Express, vol. 14, pp. 306-313, Jan. 2006.

[6] M. Naruse, H. Hori, K. Kobayashi, and M. Ohtsu, "Tamper resistance in optical excitation transfer based on optical near-field interactions," Opt. Lett., vol. 32, pp. 1761-1763, June 2007.

978-1-4244-3830-3/09/$25.00 © 2009 IEEE

[7] M. Naruse, T. Yatsui, T. Kawazoe, Y. Akao, M. Ohtsu, “Design and simulation of a nanophotonic traceable memory using localized energy dissipation and hierarchy of optical near-field interactions,” IEEE Trans. Nanotechnol., vol. 7, pp. 14-19, Jan. 2008.

[8] M. Naruse, T. Yatsui, H. Hori, K. Kitamura, and M. Ohtsu, “Generating small-scale structures from large-scale ones via optical near-field interactions,” Opt. Express, vol. 15, pp. 11790-11797, Aug. 2007.

[9] M. Naruse, K. Nishibayashi, T. Kawazoe, K. Akahane, N. Yamamoto, and M. Ohtsu, “Scale-dependent Optical Near-fields in InAs Quantum Dots and their Application to Non-pixelated Memory Retrieval,” Appl. Phys. Express, vol. 1, pp. 072101 1-3, June 2008.

[10] M. Naruse, T. Yatsui, W. Nomura, N. Hirose, and M. Ohtsu, “Hierarchy in optical near-fields and its application to memory retrieval,” Opt. Express, vol. 13, pp. 9265-9271, Nov. 2005.

[11] M. Naruse, T. Yatsui, T. Kawazoe, N. Tate, H. Sugiyama, and M. Ohtsu, “Nanophotonic Matching by Optical Near-Fields between Shape-Engineered Nanostructures,” Appl. Phys. Express, vol. 1, pp. 112101 1-3, October 2008.

[12] N. Tate, W. Nomura, T. Yatsui, M. Naruse, and M. Ohtsu, “Hierarchical hologram based on optical near- and far-field responses,” Opt. Express, vol. 16, pp. 607-612, Jan. 2008.

[III] REVIEW PAPERS

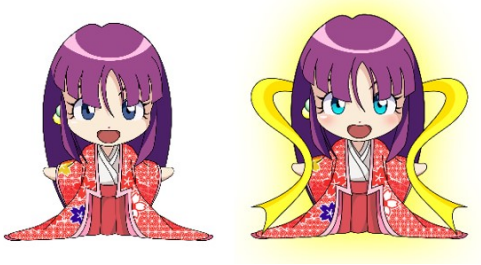

NEDO 特別講座
――光技術の最先端分野を推進する技術者・研究者育成――

大津元一

NEDO Special Course: On-the-Research-Training of Engineers and Scientists for Promoting Advanced Optical Technology

Motoichi OHTSU

This paper reviews the activities of NEDO special course on nanophotonics, which has been founded for meeting the requirements of the Ministry of Economy, Trade and Industry, and NEDO organization. The mission of this course is the On-the-Research-Training of the active engineers and scientists for promoting nanophotonics, which is an advanced optical technology.

Key words: nanophotonics, training, research, dressed photon

経済産業省，（独）新エネルギー・産業技術総合開発機構（NEDO）では長期にわたり産学連携による多数の大型プロジェクトを実施しているが，これはモノ作り・製品開発にかかわる事業で，人材育成事業ではない．したがって開発された試作品をプロジェクト終了後にさらに改良し新市場を確保することは難しく，市場に出ないまま終わる例がみられた．この問題を解決するために，経済産業省，NEDO では大型プロジェクト推進の大学側代表者が企業技術者に対して関連技術の基礎を教育啓蒙し，新技術を使いこなし発展させることのできる人材を育成する事業を企画した．NEDO はその第2期中期計画においてこの事業を重点課題のひとつとして位置づけている（NEDO のホームページ http://www.nedo.go.jp/jyouhoukoukai/tsusoku/cyuukikeikaku2.pdf を参照のこと）．

一方，工学系の学問は，産業界と連携することにより初めて社会に貢献できる．光科学技術の歴史は 18 世紀の I. Newton による光の粒子説以来長く，1960 年のレーザーの発明後，1980 年代に長足の進歩を遂げた．しかしその原理・概念は欧米で生まれ，日本はおもに改良・モノ作りで貢献してきた．この状況下で，日本のアカデミアはおもに原理を輸入・翻訳し産業界に紹介することにより社会貢献を果たしてきた．しかし近年，日本からも新しい原理・概念・技術が生まれるようになった．その代表例が，近接場光とそれを dressed photon（ドレスト光子：物質励起の衣をまとった光子）ととらえて応用し，新規デバイス，加工，システム構築を実現する「ナノフォトニクス」という質的変革技術である[1]．この技術を社会貢献に供するには，日本のアカデミアが引き続き先駆的な基礎研究を推進して国内外をリードし，同時に産業界の技術者を啓蒙し，さらに研究現場に受け入れて on-the-research-training（ORT）を行い，新技術開発の共同研究への道を切り開くことが重要である．

本稿で紹介するプロジェクトは，上記のような経済産業省，NEDO からの人材育成のニーズと，社会貢献に関するアカデミアの使命感とが結びついて発展し，NEDO 特別講座「ナノフォトニクスを核とした人材育成，産学連携等の総合的展開」と命名され，日本初の試みとして平成 18 年より 5 年間，東京大学に委託された（図 1）．

1. 構成と実施内容

NEDO 特別講座発足の核となった産学連携プロジェクトは，筆者が代表を務める NEDO「大容量光ストレージ技

東京大学大学院工学系研究科電気系工学専攻（〒113-8656 東京都文京区弥生 2-11-16）　E-mail: ohtsu@ee.t.u-tokyo.ac.jp

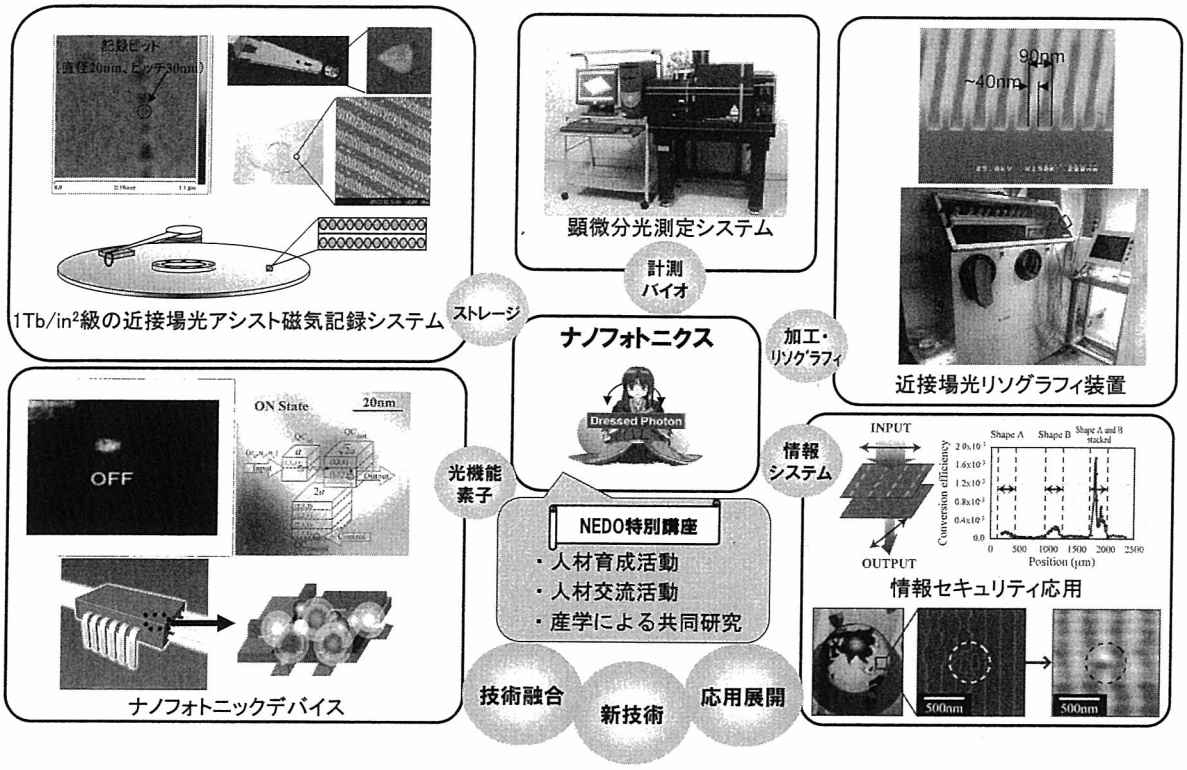

図1　NEDO 特別講座の目的と，カバーする光技術分野．

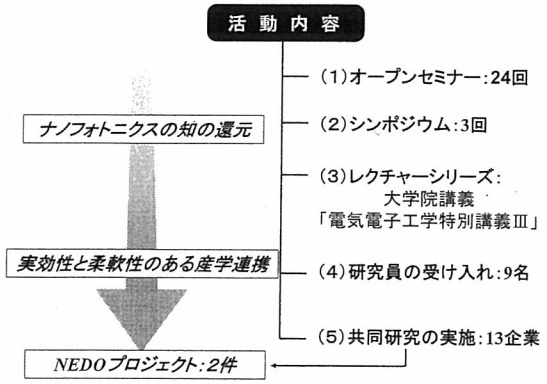

図2　NEDO 特別講座の活動内容．

術の開発」プロジェクト（平成 14〜18 年度）[2,3]，および NEDO「低損失オプティカル新機能部材技術開発」プロジェクト（平成 18 年度より 5 年間）である（NEDO のホームページ http://www.nedo.go.jp/activities/portal/p06020.html を参照のこと）．両者ともナノフォトニクスにかかわる日本発の概念に基づき実施され，前者は情報記録密度 1 Tb/in² の近接場光アシスト磁気記録システムを世界で初めて実現して成功裏に終了した．その後は産業界が継続して自己資金により実用化開発を展開しており，このたび新会社発足の運びとなった．さらに，記録密度 10 Tb/in² を経由して，2025 年の 1 Pb/in² の目標にむけた開発の技術ロードマップが策定されている[4]．一方，後者は昨年末の中間評価できわめて高い評価を得た後，ナノフォトニックデバイスが室温動作し，モジュール化が進み，システム応用へと至っている（NEDO のホームページ http://www.nedo.go.jp/iinkai/kenkyuu/hyouka/20h/21/4-2-1.pdf を参照のこと）．

本講座は筆者の研究室に設置され，准教授 1 名（委嘱），特任助教3名，産学連携マネージャー1名，事務職員 2 名を雇用して業務を行っている．そのおもな内容は次のとおりである（図 2）．

(1) オープンセミナー： 有識者 2 名を講師に招きほぼ毎月開催される自由聴講の産業界向け講演会である．活発な質疑応答の時間を十分確保するため，聴講者はおおむね30名以下に限っている．平成 21 年 12 月の時点ですでに 24 回実施している．

(2) シンポジウム： 本講座の成果報告のために年 1 回開催されるシンポジウムである．産業界に向けた情報発信が目的であるため，開催案内は産業界のみに発送している．これまでに 3 回開催したが，毎回全国から 300 名近い技術者が参加し，会場は満員となり立ち見も出る盛況で，本技術に対する関心の高さがうかがえる（図3）．シンポジウムの最後には別会場に移動して本講座の研究者・技術者と参加者との間の個人面談の

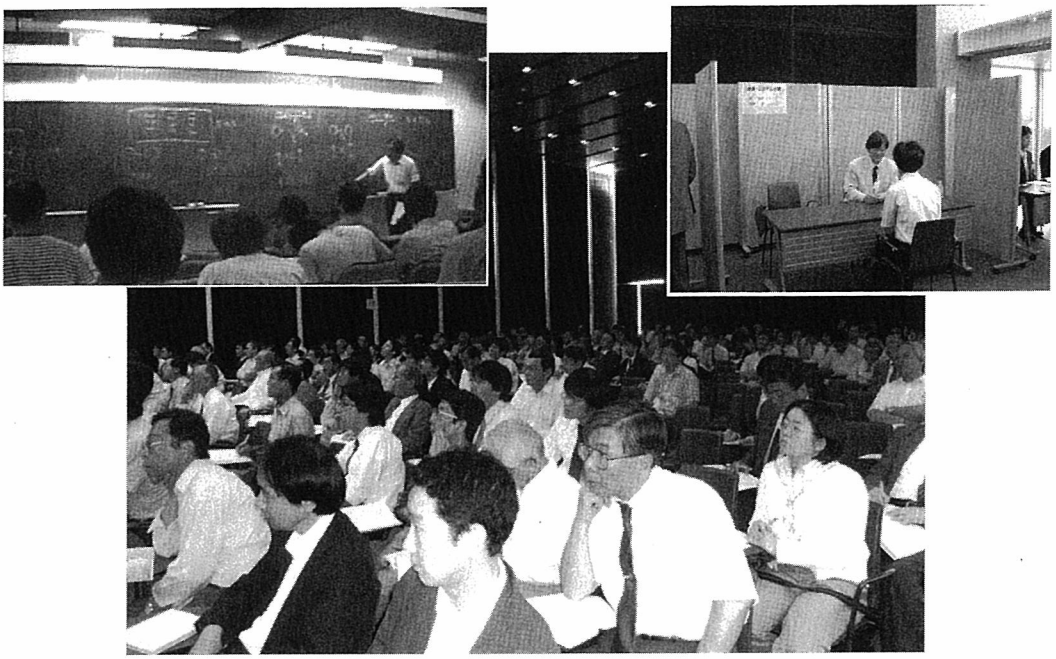

図3　第3回シンポジウム（平成20年7月2日開催）の会場の様子．右上の写真は個人面談の様子．左上はレクチャーシリーズの様子．

時間を設け，ナノフォトニクスを産業界に導入する具体的な方策，開発対象について意見交換している．

(3) レクチャーシリーズ： ナノフォトニクスの原理・基礎に関する大学院講義として「電気電子工学特別講義Ⅲ」を各年度後期に開設しており，下記 (4) の技術者が聴講している．受講生の大半は正規の大学院学生であるが，技術者が活発に質問するので大学院学生にもよい刺激となっている．

(4) 研究員の受け入れ： 下記 (5) の共同研究を推進する若手技術者を産業界から受け入れ，ORT を実施している．これまでの受け入れ人数は延べ9名である．

(5) 共同研究の実施： 上記 (2) の面談などをきっかけに具体的なアイデアを出し合い，これに基づいて産業界と共同研究を実施している．これまで延べ13社と実施している．

2. 成果と波及効果

前章 (1)〜(5) の各業務を通じ，(4) の若手技術者もすでに学術誌での原著論文発表[5]，学会講演会で成果発表を行っており，本講座発足時の予想以上に人材育成の実績が上がっている．同時に本講座の教職員は多数の原著論文，国内外の講演会での研究発表，技術書の執筆，特許申請を行い，活発に活動している．また，(5) の共同研究は小規模予算で開始されるが，そのうちのいくつかは共同研究の初期成果がもとになり，外部資金を獲得する大型開発研究プロジェクトへと発展している．たとえばNEDO「エネルギー使用合理化技術戦略的開発」事業において，近接場光エッチング法および近接場光堆積法を用いた光学素子用基板表面のサブナノ平坦化技術開発が始まった（各々平成20年度，平成21年度より3年間）（NEDO のホームページ https://app3.infoc.nedo.go.jp/informations/koubo/koubo/FK/rd/2008/P03033/nedokoubo.2008-06-17.2881926733/, および https://app3.infoc.nedo.go.jp/informations/koubo/koubo/FK/rd/2009/P03033/nedokoubo.2009-05-07.9881219591/ を参照のこと）．これは特に複雑な加工装置を必要とせず，ガラス，セラミックス，半導体など，多様な基板表面の制御に応用可能な革新技術であり，多方面から大きな関心が寄せられている．このような発展には (4) の ORT が有効に機能し，新技術を使いこなしさらに発展させる能力を備えた産業界の若手技術者が育ったことが決め手となっている．

一方，本プロジェクトを組織的に支援するため，次の2つの事業が発足した．

(1) ナノフォトニクス研究センター（図4）： 本講座を支援するために，本学大学院工学系の中に昨年4月より発足した．筆者がセンター長を務め，工学系の教員がメンバーとなっている．メンバー間の情報交換・共同研究によりナノフォトニクスの研究を深め広げて，次の社会貢献の新たな核を形成することを目標としている．また，前章 (2) の個人面談などでは筆者の研

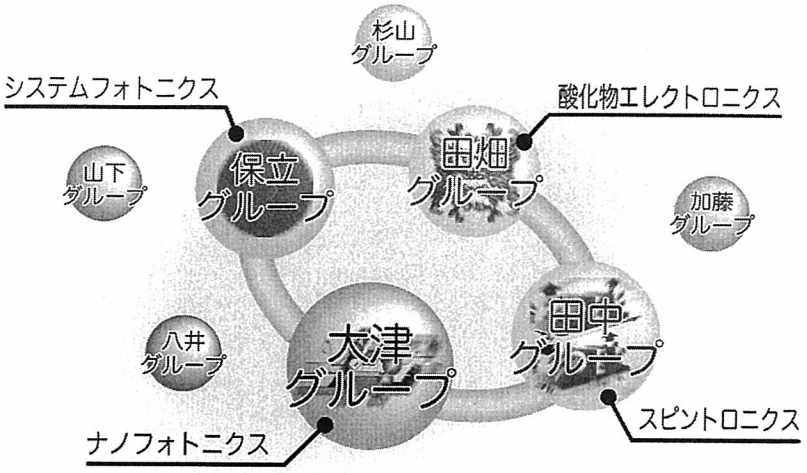

図4　ナノフォトニクス研究センターの構成.

究グループのみで対応しきれない境界領域分野に関する提案がしばしばみられるが，これを本研究センターのメンバーと共有し，産学連携の幅を広げている.

(2) 特定非営利活動法人（NPO）「ナノフォトニクス工学推進機構」: 前記のNEDO「大容量光ストレージ技術の開発」プロジェクト後の実用化開発を推進すること等を目的とし，平成17年に発足した．筆者が理事長を務めている．最近では事業の幅を広げ，本年度からは前章 (3) のレクチャーシリーズよりも初歩的なナノフォトニクスの知識を学ぶセミナー「ナノフォトニクス塾」(初級編，中級編とも2日間にわたる集中講義)，技術の将来動向を深く探索するためのフォーラムなどの教育啓蒙事業を実施した（NPOのホームページ http://www.nanophotonics.info/seminar.html を参照のこと）．また，発光ダイオード1個のみを光源とする超低消費電力のデスクトップ型の近接場光リソグラフィー装置の販売も開始した.

以上のように，本講座と連携した教育啓蒙活動が急速に進み，それが国外からも注目されるようになった．欧米では日本がナノフォトニクスの基礎・応用をリードしていることを認識し，近年は日本との情報交換・研究交流の希望が多く寄せられるようになった．これを受けて筆者らは日本と相手国との二国間交流を企画し，これまでに米国，豪州，ドイツを相手とし，ワークショップを複数回実施している[6]．この会合には二国から10名程度の少数のトップランナー研究者の参加のみに限っているが，これに本講座に関連する産業界の技術者の参加を呼びかけ，技術成果の発信の機会を供与している．技術者の世界舞台へのデビューという観点でも，この活動は人材育成の効果を挙げている．さらに，これがもとになり，新たな共同研究が始まっている.

1993年に筆者がナノフォトニクスを提案した後，しばらくは他機関・他国からの関連する研究発表件数はきわめて少なかったが，近年はそれが激増している．これは，欧米でナノフォトニクスに対する関心が急増したことを反映している．米国でのナノフォトニクスに関連する研究開発の状況は，参画企業61社，関連する研究機関数21，関連プロジェクト予算327億円（平成21年度）であり，EUではそれぞれ74社，16，100億円（平成19年度）にのぼっている．これは日本の数値と比べると膨大である．特にEUではナノフォトニクスを次世代の光通信システム技術の中核に置いており，技術開発がきわめて強力に推進されている[7]．ただし欧米ではナノフォトニクスの定義が曖昧かつ広義になっており[8]，その中には波動（回折）光学技術も含まれるので，技術の質的変革を生むことは難しい．新しい技術の確立のためには，ナノ寸法の局所領域での光子の実体をはじめとする基礎原理を探索し，これを応用に結びつける努力が必要である．これにかかわる実績では日本がリードを保っており，筆者の研究グループではナノフォトニクスにかかわる各種技術開発に関し，本講座発足の前後にわたり積算すると延べ29社との共同研究が進んでいる.

本講座が実施する人材育成は短期間で達成できるものではない．本講座を継続発展するために，長期的な展望にたった施策が必須である．一方，このような産学連携の活動にはマネージャーの活躍が不可欠である．知財の取り扱いなどの調整に慣れ，また両組織間の主張を調整できる能力のある調整役がいなければ実質的な活動はできない．今

後はこのようなマネージャーを育成する事業も重要になると思われる.

文　献

1) 大津元一："ナノフォトニクスによる光技術の質的変革"，応用物理，**77** (2008) 1341-1352.
2) 大津元一編著：大容量光ストレージ（オーム社，2008).
3) 大津元一："ナノフォトニクス技術とその将来—大容量光ストレージの開発事業を例として—"，光アライアンス，**19** (2008) 41-43.
4) (財)光産業技術振興協会編：情報記録テクノロジーロードマップ((財)光産業技術振興協会，2006).
5) H. Fujiwara, T. Kawazoe and M. Ohtsu: "Nonadiabatic multi-step excitation for the blue-green light emission from dye grains induced by the near-infrared optical near-field," Appl. Phys. B, **98** (2010) 283-289.
6) 大津元一："「なぜ？」に答えるには二国間セミナーで"，応用物理，**78** (2009) 473-474.
7) MONA consortium: "A European roadmap for photonics and nanotechnologies," MONA (Merging Optics and Nanotechnologies Association) consortium, 2008 (http://www.ist-mona.org/partners.asp)
8) National Research Council of the National Academies: Nanophotonics Accessibililty and Applicability (National Academy Press, 2008).

(2010年1月13日受理)

特集 ナノフォトニクス

ナノフォトニックデバイス

東京大学 大学院工学系研究科 電気系工学専攻
八井 崇，大津 元一

1. はじめに

情報通信の高速化・大容量化により，演算素子の微細化が急務となっている。現在の演算素子を支えるシリコン電子デバイスにおいても，配線などにおける熱の発生が大きな問題となり，微細化の限界が見え始めている。このような状況において，MIT Microphotonics Center により取りまとめられた2005年版「Communications Technology Roadmap」に予想されるように，回路の微小化だけでなく既存の電子デバイスから光デバイスの移行が，PC内部のチップ間配線などにおいても必要となってきている。このような光デバイスに求められる寸法は，10年以内には100nm以下になると予測されており，現状の光デバイスを単純に微細化するだけでは，光の回折限界の壁を乗り越えられない。つまり，単に小寸法化という「量的変革」ではなく，伝搬光を用いたのでは実現できないデバイス機能の開発という「質的変革」が求められている[1),2)]。

この問題を解決する有効な手段として，近年，量子ドットにより構成され，近接場光によって動作するナノフォトニックデバイスが提案されている[3)]。その一例が，ナノフォトニックスイッチ（波長変換素子）であり，その基本原理を**図1**を用いて説明する。基本動作は，寸法の制御された大小2つの量子構造によって達成される。ここでは，小さい量子箱（QD_A）の励起子基底準位（E_{A1}）と大きい量子箱（QD_B）の励起子第一励起準位（E_{B2}）のエネルギーが一致するような寸法比（立方体の場合1：$\sqrt{2}$）となっている。この場合，E_{B2}の波動関数は奇関数となり，伝搬光では励起することができない電気双極子禁制な準位となる。この系に対して，図1(a)バリアー層を励起した場合において，QD_AとQD_Bの間隔が十分大きい場合には，それぞれの基底準位からの発光が観測されるが，この間隔がQD_Aの寸法と同程度になると，エネルギー的に共鳴するE_{B2}を通してE_{B1}への緩和が発生し，その結果，E_{B1}からの発光しか観測されないことになる（E_{A1}での発光を観測していると非発光であるために“オフ”状態となる）。次に，図1(b)バリアー層を励起しつつE_{B1}に共鳴する光を入射すると，E_{B1}が占有されることで，E_{B2}からE_{B1}へのサブレベル緩和が抑制されるため，E_{A1}からの発光が観測される（“オン”状態）。ここで，従来光学禁制であるE_{B2}は，隣の量子箱における局所的な電場勾配（こうばい）により初めて励起されるものである。つまり，このデバイスは数nmの量子箱によって構成されているため，非常に寸法が小さいという利点

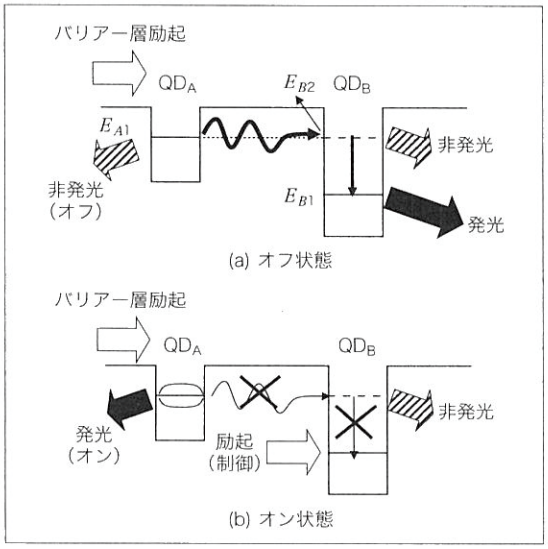

図1 ナノフォトニックスイッチの概念図

やつい たかし，おおつ もといち

だけでなく，近接場光によってのみ動作するという特長を有する。さらには，このデバイスによって消費されるエネルギーは，サブレベル間のエネルギー差（$E_{B2}-E_{B1}$）のみであるために，超低消費電力であるという利点がある。以上の基本原理は，3端子に拡張され，CuCl量子箱によりスイッチング動作が実験的に確認されている[4]。

本稿では，ナノフォトニックデバイスを室温で安定に動作させるため，近年筆者らが研究を進めているZnOを用いた取り組みについて紹介する。

2. ZnOナノロッド量子井戸構造

電子デバイスとしても良質な特性を示すZnO[5]の光デバイスとしての特長は，①励起子結合エネルギーが大きい（60meV，量子構造にした場合には110meVまで大きくなることが報告されている）[6]，②振動子強度が大きい[7]ことから，室温において強い励起子発光強度が得られることである。

本稿で紹介するZnOの量子構造は，Metal–Organic Vapor Phase Epitaxy（MOVPE）法により作製されたZnOナノロッド先端に作製されている[8]。この手法により，ナノロッド先端の単一量子井戸構造とした場合でも，井戸幅に依存して強い励起子発光が観測されている[9]。本手法では，量子井戸の幅および間隔を原子層レベルで自在に制御することができるため，任意のナノフォトニックデバイス作製が可能となる。

図1で説明したスイッチング動作を実現させるため，2つの量子井戸構造からなる2重量子井戸構造（DQWs）の作製を行った。井戸の幅を調整し，広い井戸幅を有する量子井戸（QW_B）の励起子第一励起準位（E_{B2}）と狭い井戸幅を有する量子井戸（QW_A）の励起子基底準位（E_{A1}）が共鳴する寸法でDQWsを作製した[**図2**(a), (b)]。それぞれの井戸幅L_wは3.2nm（QW_A）および3.8nm（QW_B）であり，E_{A1}（E_{B2}）およびE_{B1}に相当する波長は361nm，362nmである［図2(c)］。これにより，QW_Aにポピュレーションを生成させた場合でも，共鳴するエネルギー準位を介してポピュレーションが移動し，この際に失うサブバンド間エネルギーにより，励起が逆流することなくQW_Bの基底準位（E_{B1}）からの発光のみが観測されることが期待される。これは，この際にQW_Bの第一励起準位は光学禁制であるため，基底準位

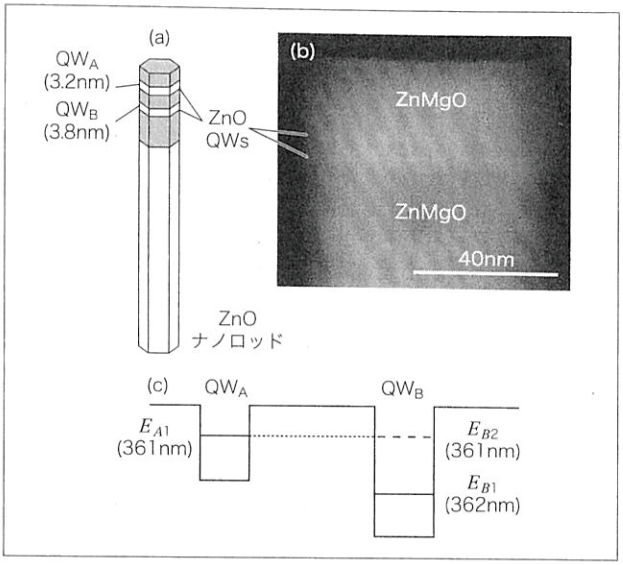

図2 ZnOナノロッドDQWsの(a)概念図，(b)透過型電子顕微鏡像，(c)DQWsのエネルギー準位図

からの発光しか観測されないからだと考えられる。

3. 近接場エネルギー移動の制御

近接場エネルギー移動の一方向性を確認する実験として，まずQW_AとQW_Bの井戸を励起するために，入力光としてHe–Cdレーザー（λ=325nm）による励起を行った結果について説明する。この状態で得られた近接場光スペクトル［**図3**(a)の$NF_{オフ}$］から，362nm付近に発光のピークを有するスペクトル（E_{B1}）が観測された。QW_AとQW_Bの井戸が孤立して存在した場合には，それぞれの基底準位に対応する波長361nmおよび362nmでの発光ピークが観測されるが，この場合には，QW_Bの基底準位に相当するピークからの発光しか観測することができなかった。これは，先に予測したように，共鳴する励起子準位間でのエネルギー移動を示す結果であるといえる［図1(a)の“オフ”状態に対応］。次に，このエネルギーの流れを止めるために，制御光（Ti:Sapphireレーザーの2次高調波：波長362nm，パルス幅2ps）としてE_{B1}を共鳴励起［図3(a)の$NF_{コントロール}$］させた状況下において，He–Cdレーザー光を照射したスペクトルを図3(a)の$NF_{オン}$に示す。この結果，He–Cdレーザー単独励起では観測されなかったE_{A1}（λ=361nm）に相当する発光ピーク（出力光）が観測された［図1(b)の“オン”状態に対応］。以上の結果は，前述した近接場エネルギー移動制御によるナノフォトニックスイッチの基

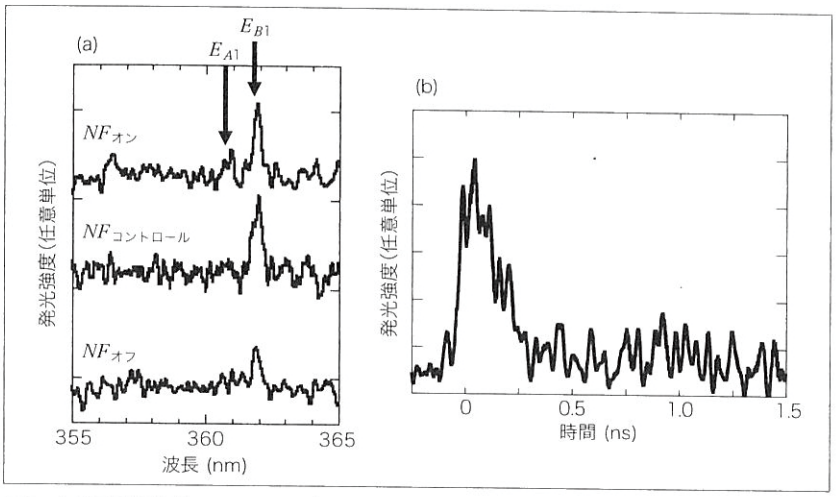

図3 (a)近接場分光スペクトル（$NF_{オフ}$：入力光のみ入射，$NF_{コントロール}$：制御光のみ入射，$NF_{オン}$：入力光および制御光入射），(b)オン状態における時間分解発光強度信号（波長361nm）

本的動作原理を実証するものである[10]。

さらに，ナノフォトニックスイッチの動的特性評価を行った。バリアー層励起用光源，および制御光同時照射下における波長361nmでの時間分解発光強度信号を図3(b)に示す。信号の立ち上がり時間から，スイッチの動作時間が約100psであることが示された。

4. エネルギーアップコンバージョン

前節では，量子構造内でのサブレベル緩和を利用したデバイスについて紹介した。ここで，サブレベル緩和において生じるエネルギー損失は，周りの物質に格子振動としてエネルギーを与えている。

一方，ナノ寸法物質に光を照射した時に発生した分極は，周囲に大きな機械的ひずみを誘起し，その結果，コヒーレントフォノンを局所的に生成する場合がある［**図4**(a)］[11),12)]。これは熱源とはならず，励起子ポラリトンとフォノンとの混合状態である励起子フォノンポラリトン，言い換えると，ナノ寸法物質間の近接場光相互作用を媒介する仮想励起子フォノンポラリトン（ドレストフォトン）を形成する。すなわち，ナノ寸法物質の励起子ポラリトンのエネルギーとフォノンのエネルギーが，近接するナノ寸法物質に移動可能となる。

このエネルギー移動を使うと，入射光の光子エネルギーが量子構造中の励起準位を励起させるほど高くなくても，フォノンのエネルギー移動により近接物質中の格子振動が誘起され，この格子振動エネルギー準位を介した多段階励起により励起準位の電子が励起される［図4(b)］[13)]。

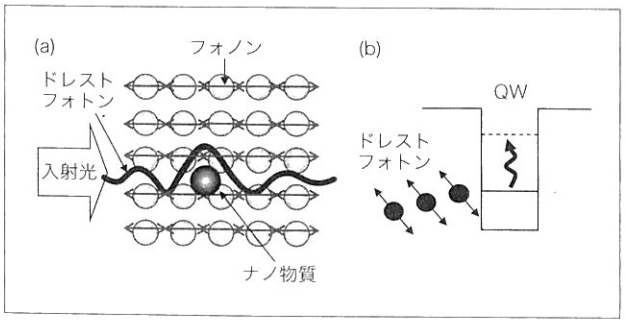

図4 (a)ナノ物質におけるドレストフォトン生成の概念図，(b)ドレストフォトンによる非断熱励起過程

この予測を確認する実験として，ナノフォトニックスイッチの実験に用いた2重量子井戸を用い，入力光としてTi:Sapphireレーザーの2次高調波（波長362nm，パルス幅2ps）による励起を行った結果について説明する［**図5**(a)］。この状態で得られた近接場光スペクトルを図5(b)に示す。この結果に示されるように，励起光よりも短波長側である361nm付近に発光のピークを有するスペクトルが観測された。361nm付近で観測される発光のうち，QW_Bの励起準位E_{B2}は光学禁制準位であるため，この発光はエネルギーアップコンバージョンによってE_{B2}が励起されたことに加えてQW_Aの基底準位であるE_{A1}が励起され，この光学許容準位から発光が観測されたことを意味している。以上の結果は，前述した非断熱励起過程によるエネルギーアップコンバージョンの基本的動作原理を実証するものである。

5. あとがき

本稿では，ZnO量子構造を用いたナノフォトニックデバイスへの応用について解説した。本稿で述べたデバイスの特長は，半導体量子構造による「量的」に変革された微小なデバイスということだけではなく，伝搬光を用いたのでは駆動することのできない機能を持つ「質的」に変革されたデバイスということである[1),2)]。今回は，2端子による単純な構造でのエネルギー移動の観測およ

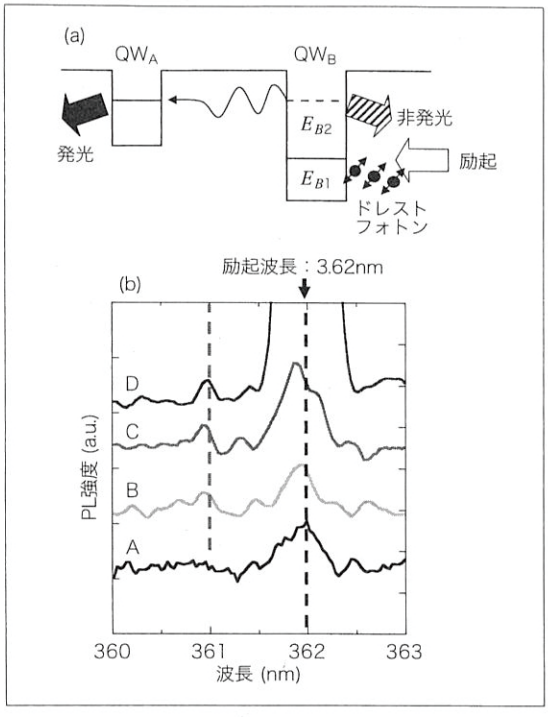

図5 (a)ZnOナノロッドDQWsを用いたエネルギーアップコンバージョン検証実験，(b)近接場光強度スペクトルの励起光強度依存性［A (1mW)，B (2mW)，C (10mW)，D (60mW)］

び制御を行ったが，本構造は結晶性・寸法の制御性にも非常に優れており，ナノフォトニックスイッチに限らず，さらに複雑で高機能なナノフォトニック機能デバイス（集光器[14]やパルス発生器[15]など）の実現にも理想的な系であると考えられる。

謝辞

本稿をまとめるにあたり，有益な議論をいただいた三宮俊氏（㈱リコー），川添忠氏（東京大学），小林潔教授（山梨大学），試料を提供いただいた李奎哲准教授（韓国浦項工科大学校）に感謝します。

参考文献

1) M. Ohtsu, K. Kobayashi, T. Kawazoe, S. Sangu, and T. Yatsui: "Nanophotonics: design, fabrication, and operation of nanometric devices using optical near fields," IEEE J. Sel. Top. Quant. Electr., Vol. 8, No. 4, pp. 839～862 (2002)
2) M. Ohtsu, K. Kobayashi, T. Kawazoe, S. Sangu, and T. Yatsui: "Nanophotonics: Application of dressed photons to novel photonic devices, and systems," IEEE J. Sel. Top. Quant. Electr., Vol. 14, No. 6, pp. 1404～1417 (2008)
3) T. Kawazoe, K. Kobayashi, J. Lim, Y. Narita, and M. Ohtsu: "Direct observation of optically forbidden energy transfer between CuCl quantum cubes via near-field optical spectroscopy," Phys. Rev. Lett., Vol. 88, No. 6, 067404 (2002)
4) T. Kawazoe, K. Kobayashi, S. Sangu, and M. Ohtsu: "Demonstration of a nanophotonic switching operation by optical near-field energy transfer," Appl. Phys. Lett., Vol. 82, No. 18, pp. 2957～2959 (2003)
5) W. I. Park, J. S. Kim, G.-C. Yi, and H.-J. Lee: "ZnO nanorod logic circuits," Adv. Mater., Vol. 17, No. 11, pp. 1393～1397 (2005)
6) H. D. Sun, T. Makino, Y. Segawa, M. Kawasaki, A. Ohtomo, K. Tamura, and H. Koinuma: "Enhancement of exciton binding energies in ZnO/ZnMgO multiquantum wells," J. Appl. Phys., Vol. 91, No. 13, pp. 1993～1997 (2002)
7) D. C. Reynolds, D. C. Look, B. Jogai, C. W. Litton, G. Cantwell, and W. C. Harsch: "Valence-band ordering in ZnO," Phys. Rev. B, Vol. 60, No. 4, pp. 2340～2344 (1999)
8) W. I. Park, G.-C. Yi, M. Y. Kim, and S. J. Pennycook: "Quantum confinement observed in ZnO/ZnMgO nanorod heterostructures," Adv. Mater., Vol. 15, No. 6, pp. 526～529 (2003)
9) W. I. Park, S. J. An, J. Long, G.-C. Yi, S. Hong, T. Joo, and M. Y. Kim: "Photoluminescent properties of ZnO/$Zn_{0.8}Mg_{0.2}O$ nanorod single-quantum-well structures," J. Phys. Chem. B, Vol. 108, No. 40, pp. 15457～15460 (2004)
10) T. Yatsui, S. Sangu, T. Kawazoe, M. Ohtsu, S. J. An, J. Yoo, and G.-C. Yi: "A nanophotonic switch using ZnO nanorod double-quantum-well structures," Appl. Phys. Lett., Vol. 90, No. 22, 223110 (2007)
11) T. Kawazoe, K. Kobayashi, S. Takubo, and M. Ohtsu: "Nonadiabatic photodissociation process using an optical near field," J. Chem. Phys., Vol. 122, No. 2, 024715 (2005)
12) Y. Tanaka and K. Kobayashi: "Optical near field dressed by localized and coherent phonons," J. Microsc., Vol. 229, No. 2, pp. 228～232 (2008)
13) T. Yatsui, S. Sangu, K. Kobayashi, T. Kawazoe, M. Ohtsu, J. Yoo, and G.-C. Yi: "Nanophotonic energy up-conversion using ZnO nanorod double-quantum-well structures," Appl. Phys. Lett., Vol. 94, No. 9, 083113 (2009)
14) T. Kawazoe, K. Kobayashi, and M. Ohtsu: "Optical nanofountain: A biomimetic device that concentrates optical energy in a nanometric region," Appl. Phys. Lett., Vol. 86, No. 10, 103102 (2005)
15) A. Shojiguchi, K. Kobayashi, S. Sangu, K. Kitahara, and M. Ohtsu: "Superradiance and dipole ordering of an N two-level system interacting with optical near fields," J. Phys. Soc. Jpn., Vol. 72, No. 11, pp. 2984～3001 (2003)

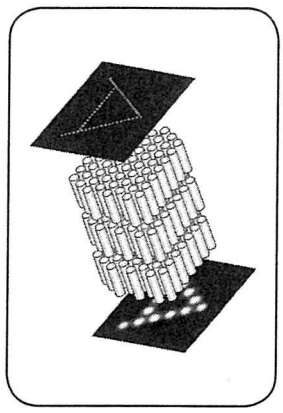

最近のナノフォトニック加工技術

八井　崇，大津　元一

1. まえがき

近接場光を加工に用いることで，光の回折限界を超えた微細加工が可能となっている。応用例として，超高速・超高密度光記録[1]，近接場光リソグラフィー[2]などがある。上記の手法では，光の局在性を利用しており超高分解能を達成している。しかしながら，これらの技術開発は寸法を微細化したいわば「量的変革」である。これに対して，近年伝搬光とは異なる近接場光特有な性質を活かした「質的に変革」された加工技術が達成されている。一例として，寸法依存共鳴現象の発見により[3]，従来はいわゆる一筆書き加工であった微細加工の分野において一括大面積加工の可能性をもたらした[4]。本稿では，このような一括加工技術のうち，非断熱光化学反応の特長を積極的に活かした一括加工技術について紹介する。

2. 原理：非断熱光化学反応

本節ではナノフォト二クス特有な反応である非断熱光化学反応について概説する。まず，ナノ寸法物質に光を照射したときに発生した分極が，周囲に大きな機械的ひずみを誘起し，その結果，コヒーレントフォノンを局所的に生成する場合がある（**図1**(a))[5~6]。これは熱源とはならず，励起子ポラリトンとフォノンとの混合状態である励起子フォノンポラリトン，言い換えるとナノ寸法物質間の近接場光相互作用を媒介する仮想励起子フォノンポラリトン（ドレスト光子）を形成する。すなわち，ナノ寸法物質の励起子ポラリトンのエネルギーとフォノンのエネルギーが，近接するナノ寸法物質に移動可能となる。

このエネルギー移動を使うと，入射光の光子エネルギーが近接するナノ寸法物質中の電子を励起準位に励起させるほど高くなくとも（すなわち断熱過程による光化学反応が起こらなくとも），フォノンのエネルギー移動により近接物質中の分子振動が誘起され，分子振動エネルギー準位を介した多段階励起により電子が励起される（非断熱励起過程，図1(b)）。従って，従来の加工で使われる紫外光などの短波長光源が不要となる。さらには，ドレスト光子が励起されるナノ物質の周りのみで反応が励起されるため，従来の伝播光加工において必要であった近接場光発生用のためファイバプローブやマスクが不必要となり，高効率に一括加工を実現することが可能となる。

この非断熱励起過程の現象は，近接場光化学気相堆積（Chemical Vapor Deposition: CVD）において最初に実証された[7]。近接場光CVD法の一例として，亜鉛（Zn）ナノ微粒子の堆積が行われた。亜鉛の原料としてジエチル亜鉛（Diethyl Zinc: DEZn）分子を用い，DEZn雰

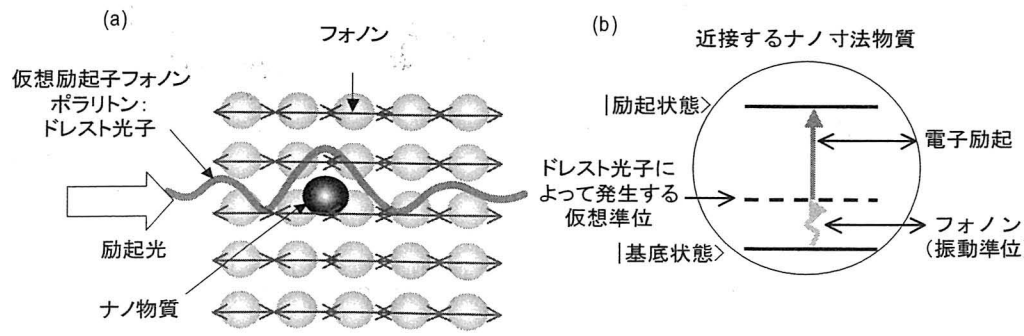

図1　(a)ナノ物質におけるドレスト光子生成の概念図。(b)隣接するナノ物質における非断熱励起過程

東京大学大学院 工学系研究科

囲気中のチャンバーに近接場光発生するための先鋭化ファイバを導入する（**図2**(a)）。ここでDEZnの吸収端波長は波長300nmであるが，これよりも長い波長である325nmの光を導入した場合でも，亜鉛ナノ微粒子の堆積が確認された（図2(b)）[8]。これは，先鋭化ファイバ先端にドレスト光子が発生し，その結果DEZnが分解されZnナノ微粒子が堆積した。また，堆積結果の表面形状像から，Znナノ微粒子近傍での堆積は発生しておらず，堆積前のサファイヤ基板の原子ステップが観測されていることからも，近接場光はナノ物質近傍のみ発生していることがわかる。

以上述べた非断熱光化学反応の原理を利用した一括加工の例について以下に紹介する。

3. 非断熱光化学反応によるオングストローム平坦化[9]

近年の光産業は目覚しい発展を遂げており，この発展を支えるレーザ機器において，高出力化，短波長化，短パルス化への要望が強まっている。このような産業界の要請に答える為には，レーザ機器を構成するレンズやミラー等の光学素子の高性能化を達成する必要がある。光学素子の高性能化にとって現在一番の問題となるのが表面粗さ（以下R_a値）の低減である。これは，表面粗さが大きいと，

①光学素子表面での散乱損失が大きくなる

②レーザ損傷閾値が上げられない

などの問題が生じるためである。ここで，R_a値は平均線（面）からの絶対値偏差の平均値として下記の式(1)で表される（**図3**）。

$$Ra = \frac{1}{l}\int_0^l |f(x)|dx \cong \frac{1}{n}\sum_{i=1}^{n}|f(x_i)| \quad (1)$$

（l：測定長さ，dx：AFM測定時の面内分解能に対応，$|f(x)|$：平均線からの表面高さの絶対値，n：評価時の測定点数。）

しかしながら，市販されている光学素子のR_a値は2～5Å程度であり，近年，下げ止まりを余儀なくされている。その原因のひとつは，光学素子の製造方法にある。現在，光学素子は機械化学方式と呼ばれる方法により製作されており，その手法は，研磨パットの間に，被研磨材料であるガラスを挟み，研磨剤（酸化セリウム等）を流しながら擦る。この方法では，研磨パットの平坦性や研磨剤の粒径などの制限から，R_a値は2A程度が限界になっている。さらに，細かい領域での凹凸だけでなく，大面積に渡る溝（スクラッチ）や数十nmの穴（ディグ）が発生する。以上の現状より，光学素子の高性能化（R_a値低減）の為には，全く新しい手法による研磨方法が必要となっている。上記の問題を解決するために，従来の機械化学的手法ではなく，近接場光エッチングを使うことにより，次世代レーザ用光学素子向けの平坦化基板を実現する技術について説明する。

紫外領域を中心に，ミラー基板として最も需要の大

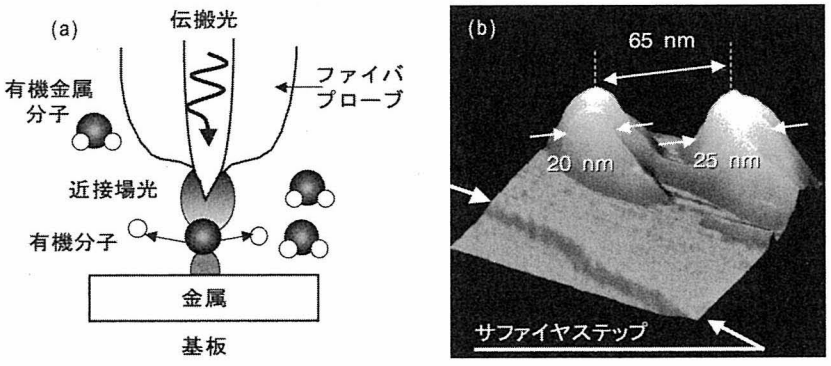

図2 (a)近接場光CVDの概念図。(b)波長325nmの光によって堆積されたZn原子の表面形状像

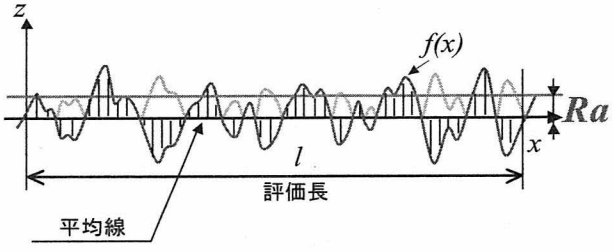

図3 表面粗さR_aの定義

きい合成石英を用いて，近接場光エッチングの詳細を紹介しよう。合成石英をエッチングする気体としては塩素ラジカル（Cl*：塩素分子が分解されたもの）がある。合成石英とは反応しない不活性な塩素分子（光吸収端波長400nm[10]）雰囲気中に基板を導入し，レーザ光（波長532nm）を照射する（**図4**(a)）。この光の波長は光吸収端波長より長いので，塩素分子に吸収されず基板とは反応しない。一方，この光により，基板表面の局所的な凹凸部に近接場光が発生すると非断熱光化学過程[9, 11, 12]により塩素分子は分解し，塩素ラジカルが発生する（図4(a)）。その結果，この塩素ラジカルが合成石英表面と反応し，凹凸構造のみがエッチングされ基板が平坦化される（図4(b)）。そして，最終的に基板に凹凸部がなくなると近接場光は発生しなくなるため，反応が自動的に停止し余計なエッチングを防ぐことが可能となる（図4(c)）。

R_a値の評価方法には，原子間力顕微鏡（AFM）を用いる。従来，R_a値の観測には，白色干渉計が用いられているが，横分解能が波長程度と大きく，またR_a値の測定限界能が5Å程度であるため，横分解能が10nm程度で，凹凸の分解能が0.1A程度であるAFMを使用する。AFMでは走査範囲が10μmと狭いため，測定領域による誤差が大きくなる。そこで，平行平面基板の中心付近9点を100μmピッチでAFMにより測定を行い（**図5**(a)），各エリアで算出される表面粗さ$(R_a)_i$の値を得る。その値を平均した

$$\overline{R_a} = \sum_{i=1}^{9} (R_a)_i \tag{2}$$

によってその基板の表面粗さR_a値を決定する。基板エッチングのためのガスには塩素を選択し，塩素導入後のチャンバーの圧力を100Paとする。照射光源についてはレーザ（波長532nm）を使用する（図5(b)）。

図6は近接場光エッチング前後のAFM像の比較を示している。この比較像より表面の凹凸が低減することが明らかである。さらに，図6(a)に示されるように，近接場光エッチング前には多く見られたスクラッチ（白楕円の内側）がなくなっていることが分かる。このAFM図の変化をより詳細に比較するために，それぞれの像における白破線を通る断面図を図6(c)に示す。この図からピーク－バレー値が近接場光エッチングによって1.2nmから0.5nmに減少していることが分かる。

最後にR_a値の平均値のエッチング時間依存性を**図7**(a)に示す。この結果より，基板への光照射時間に応じて単調に表面粗さR_a値が減少する結果となっている。光照射時間120分では，R_a値は1.4Åまで減少する。この値は9点での平均であり，その中で得られたR_a値として最小1.1Åである。また，各照射時間におけるR_a値の分散（図7(b)）も光を照射することで減少することが分かる[9]。

本手法は光化学反応を利用したものであるため，平坦基板のみならずレンズやミラーなどの曲率を有する基板

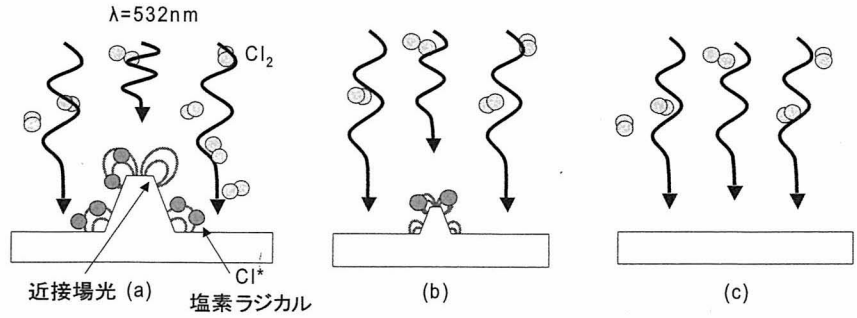

図4　近接場光エッチングの概念図

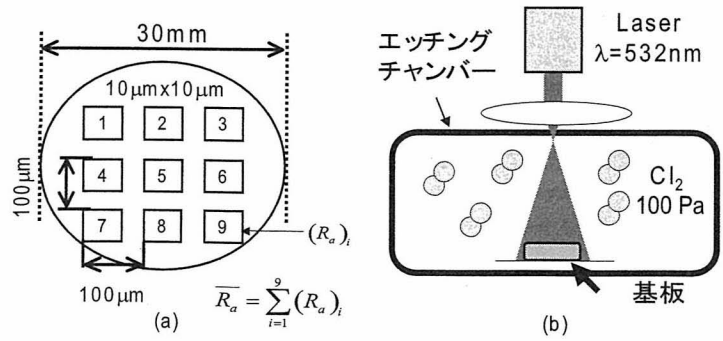

図5　(a)表面形状測定の概念図。$(R_a)_i$：領域iにおけるR_a。(b)近接場光化学エッチング実験の概念図

びトリメチルガリウム（TMG）の流量を，2000sccm・0.5sccmとした。堆積はいずれも60分であった。

図10にIn原料となるトリエチルインジウム（TEI）の流量（r_{TEI}）を変化させて堆積した結果を示す。この結果，光照射スポット内部への堆積が確認された（図10(a)）。また，In流量を変化させた場合の表面形状の電子顕微鏡像（SEM）から（図10(b)-(b)），何れの場合にも縞状形状が確認された。

次に，堆積物の組成比を見積もるために，発光スペクトルを測定した。励起にはCWのHe-Cdレーザ（波長325nm）を用い，基板温度5Kで測定を行った。その結果を**図11**(a)に示す。この結果から，TEIの流量（r_{TEI}）の増大に伴い，発光スペクトルのピークエネルギーが低エネルギー側にシフトする結果が得られた。このピーク値からIn組成比を推定し[14]，このIn組成比と，原料ガスのTEI・TMGの供給流量比との関係を図11(b)に示す。その結果，両者には比例関係が見られ，光CVDにおいても，原料ガスの流量比によってIn組成比が制御可能であるという結果が得られた。ガス流量によるInの組成制御は熱を用いた有機金属CVD（Metal-organic chemical vapor deposition; MOCVD）においては報告があったが，光CVDにおいては世界初の成果である。

以上の実験続いて，光CVDに脱離用光源を導入した場合の堆積結果について述べる。光CVDによる堆積用光源にはNd: YAGレーザの5倍波を用い，基板をサファイア（0001）とし室温で堆積（60分）を行った。原料ガスは，NH_3，TMGの流量を，2000sccm・0.5sccmとした。

以上の堆積用光源に加えて，脱離用光源として，2.71eV（波長457nm：青色）を照射した結果を曲線X'（**図12**(a),

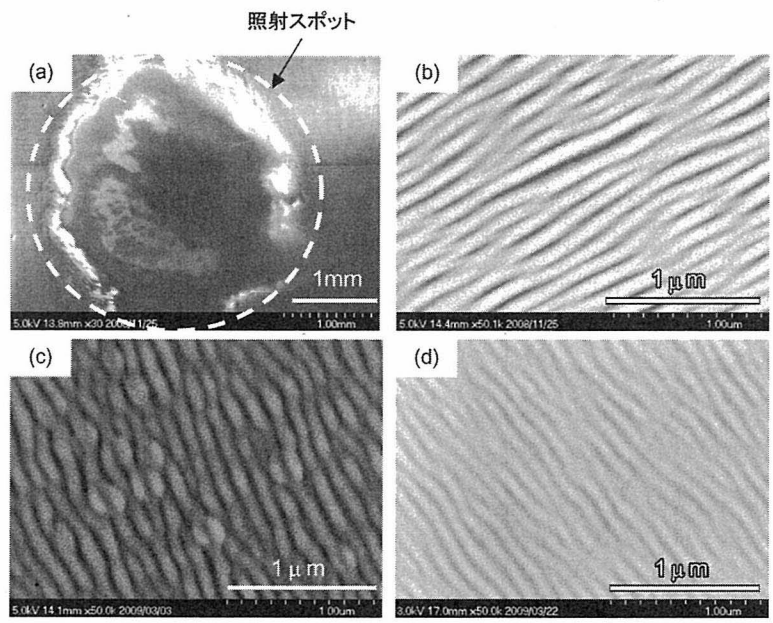

図10 堆積結果のSEM像。(a)全体像。TEI流量r_{TEI}依存性：(b)r_{TEI}=0 sccm，(c)r_{TEI}=2.5×10^{-3}sccm，(f)r_{TEI}=5.0×10^{-3}sccm

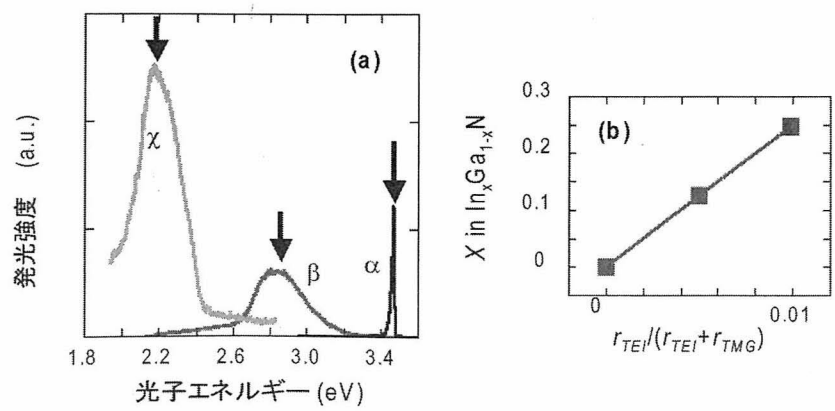

図11 (a)PLスペクトル。r_{TEI}=0sccm（曲線α），r_{TEI}=2.5×10^{-3}sccm（曲線β），r_{TEI}=5.0×10^{-3}sccm（曲線γ）。測定温度5K。(b)原料ガス供給流量比（$r_{TEI}/(r_{TEI}+r_{TMG})$）とIn組成比

$r_{TEI}=2.5\times10^{-3}$sccm)に示す。脱離用光源を照射しなかった場合の結果（図12(a)の曲線X）との差分強度曲線I_{diff}から（図12(b)），脱離用光源の光子エネルギー以下において発光強度の低減が見られた。この結果，スペクトルの半値幅として50meV程度の減少を確認した。すなわち，図8で説明した通り，脱離用光源によって，In組成比の高い（つまりは発光のフォトンエネルギーが低い）成分が脱離され，In組成比の均一化が達成されたことを示す結果が得られた。同様な結果は，脱離用光源のフォトンエネルギーを変化させた場合でも観測された。**図13**に，脱離用光源として2.33eV（波長532nm：緑色）を用いた場合の結果を示す（曲線Y'[図13(a)]：$r_{TEI}=2.5\times10^{-3}$sccm，および曲線Z'[図13(a)]：$r_{TEI}=5.0\times10^{-3}$sccm)。それぞれの場合についての脱離用光源を照射しなかった場合の結果（図13(a)の曲線YおよびZ）との差分強度曲線I_{diff}から（図13(b)），脱離用光源の光子エネルギーに応じて，発光強度が低減される波長領域の変化が観測された。

本実験で示された結果は光脱離反応に起因するため，MOCVD法[15]や，分子線エピタキシー法[16]，パルスレーザ堆積法[17]など他のあらゆる堆積法にも適用可能であると期待される。また，同時にInGaAs[18]などの他の化合物半導体の堆積についても同様な効果が期待される。

5. むすび

本稿では，ナノフォトニック加工の例として「表面平坦化」と「組成制御」について紹介した。これらは，全く異なる応用例であるが，「非断熱光化学反応」に基づくものであり，従来の伝搬光の概念では達成し得ない，「質的に変革」された革新技術である。このように，ナノフォトニック加工は，多様な光システム実現のための基盤技術として発展しており，今後は多様な分野に波及すると考えられる。当面は，これらの応用分野を精選して技術レベルをさらに高めることが重要であろう。

謝　辞

本研究を遂行するにあたり，多大なる協力を頂いた川添忠（東京大学），野村航（東京大学）の各氏に深く感謝致します。本稿で紹介させていただいたオングストローム平坦化の研究についてデータをご提供下さった多幡能徳，平田和也（シグマ光機株式会社）の各氏，および組成制御の研究についてデータをご提供下さった伊藤圭一，川村博（日東光器株式会社），水村通伸（株式会社ブイ・テクノロジー）の各氏に深く感謝致します。

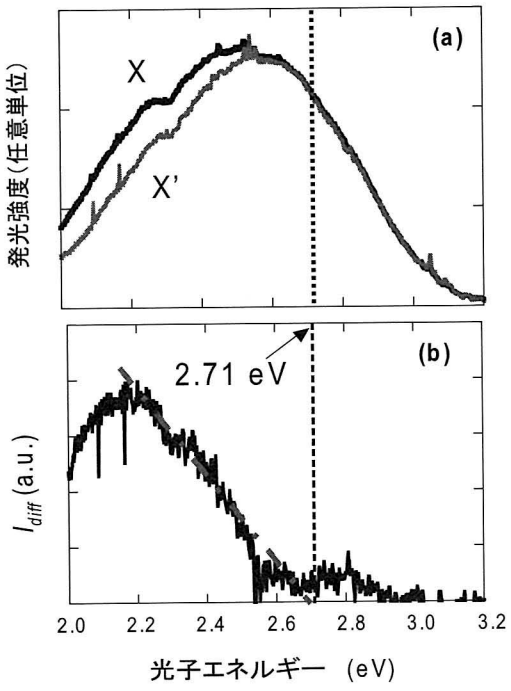

図12 脱離用光源を同時照射して堆積したInGaNからのPLスペクトル。(a)曲線A：堆積用光源のみ，曲線A'：堆積用光源＋脱離用光源（2.71eV），TEI：2.5×10^{-3}sccm。(b)曲線B：堆積用光源のみ，曲線B'：堆積用光源＋脱離用光源（2.33eV），TEI：2.5×10^{-3}sccm。(c)曲線C：堆積用光源のみ，曲線C'：堆積用光源＋脱離用光源（2.33eV），TEI：5.0×10^{-3}sccm

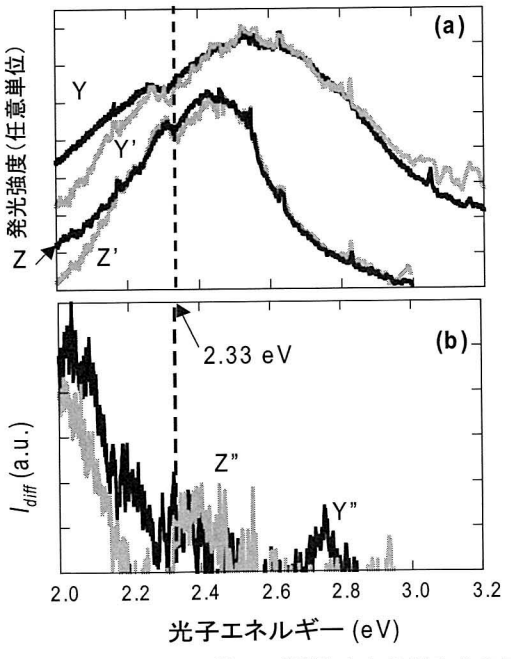

図13 脱離用光源を同時照射して堆積したInGaNからのPLスペクトル。(a)曲線A：堆積用光源のみ，曲線A'：堆積用光源＋脱離用光源（2.71eV），TEI：2.5×10^{-3}sccm。(b)曲線B：堆積用光源のみ，曲線B'：堆積用光源＋脱離用光源（2.33eV），TEI：2.5×10^{-3}sccm。(c)曲線C：堆積用光源のみ，曲線C'：堆積用光源＋脱離用光源（2.33eV），TEI：5.0×10^{-3}sccm

参考文献

1) T. Yatsui, M. Kourogi, K. Tsutsui, J. Takahashi, and M. Ohtsu, "High density/speed optical near field recording/reading with a pyramidal silicon probe on a contact slider," Opt. Lett., **25**, pp. 1279–1281 (2000).

2) Y. Inao, S. Nakasato, R. Kuroda, and M. Ohtsu, "Near-field lithography as prototype nano-fabrication tool," Science Direct Microelectronic Engineering, **84**, pp. 705–710 (2007).

3) T. Yatsui, S. Takubo, J. Lim, W. Nomura, M. Kourogi, and M. Ohtsu, "Regulating the size and position of deposited Zn nanoparticles by optical near-field desorption using size-dependent resonance," Appl. Phys. Lett., **83**, pp. 1716–1718 (2003).

4) T. Yatsui, W. Nomura, and M. Ohtsu, "Self-assembly of size- and position-controlled ultra-long nanodot chains using near-field optical desorption," Nano Lett., **5**, pp. 2548–2551 (2005).

5) T. Kawazoe, K. Kobayashi, S. Takubo, and M. Ohtsu, "Nonadiabatic photodissociation process using an optical near field," J. Chem. Phys., **122**, 024715 (2005).

6) Y. Tanaka and K. Kobayashi, "Optical near field dressed by localized and coherent phonons," J. Microsc., **229**, pp. 228–232 (2008).

7) T. Kawazoe, Y. Yamamoto, and M. Ohtsu, "Fabrication of nanometric Zn dots by nonresonant near-field optical chemical-vapor deposition," Appl. Phys. Lett., **79**, pp. 1184–1186 (2001).

8) T. Yatsui, T. Kawazoe, M. Ueda, Y. Yamamoto, M. Kourogi, and M. Ohtsu, "Fabrication of nanometric single zinc and zinc oxide dots by the selective photodissociation of adsorption-phase diethylzinc using a nonresonant optical field," Appl. Phys. Lett., Vol. 81, pp. 3651–3653 (2002).

9) T. Yatsui, K. Hirata, W. Nomura, Y. Tabata, and M. Ohtsu, "Realization of an ultra-flat silica surface with angstrom-scale average roughness using nonadiabatic optical near-field etching," Appl. Phys. B: Lasers and Optics, **93**, pp. 55–57 (2008).

10) R. Kullmer and D. Buerle, "Laser-induced chemical etching of silicon in chlorine atmosphere," Appl. Phys. A, **43**, pp. 227–232 (1987).

11) T. Kawazoe, M. Ohtsu, Y. Inao, and R. Kuroda, "Exposure dependence of the developed depth in nonadiabatic photolithography using visible optical near fields," J. Nanophotonics, **1**, 011595 (2007).

12) H. Yonemitsu, T. Kawazoe, K. Kobayashi, and M. Ohtsu, "Nonadiabatic photochemical reaction and application to photolithography," J. Luminescence, **122-123**, pp. 230–233 (2007).

13) T. Yatsui, S. Yamazaki, K. Ito, H. Kawamura, M. Mizumura, T. Kawazoe, and M. Ohtsu, "Increased spatial homogeneity in a light-emitting InGaN thin film using optical near-field desorption," Appl. Phys. B: Lasers and Optics, **97**, pp. 375–378 (2009).

14) M. D. McCluskey, C. G. Van de Walle, C. P. Master, L. T. Romano, and N. M. Johnson, "Large band gap bowing of InxGa1-xN alloys," Appl. Phys. Lett. **72**, pp. 2725–2727 (1998).

15) S. Nakamura, "The roles of structural imperfections in InGaN-based blue light-emitting diodes and laser diodes," Science **281**, pp. 956–961 (1998).

16) R. Singh, D. Doppalapudi, T. D. Moustakas, and L. T. Romano, "Phase separation in InGaN thick films and formation of InGaN/GaN double heterostructures in the entire alloy composition," Appl. Phys. Lett. **70**, pp. 1089–1091 (1997).

17) A. Kobayashi, J. Ohta, and H. Fujioka, "Low temperature epitaxial growth of In0. 25Ga0. 75N on lattice-matched ZnO by pulsed laser deposition," J. Appl. Phys. **99**, 123513 (2006).

18) K. Akahane, N. Ohtani, Y. Okada, and M. Kawabe, "Fabrication of ultra-high density InAs-stacked quantum dots by strain-controlled growth on InP (311) B substrate," J. Cryst. Growth **245**, pp. 31–36 (2002).

八井　崇 YATSUI, Takashi
東京大学大学院 工学系研究科 電気系工学専攻
准教授
〒113-8656 東京都文京区弥生 2－11－16
工学部 9 号館 213 号室

大津　元一 OHTSU, Motoichi
東京大学大学院 工学系研究科 電気系工学専攻
教授
〒113-8656 東京都文京区弥生 2－11－16
工学部 9 号館 213 号室

表面科学 Vol. 30, No. 11, p. 599, 2009

巻　頭　言

光・物質融合科学技術が進む

大　津　元　一

レーザーが発明されて半世紀を迎える昨今，光技術の独創的研究開発は停滞期に入っている。シリコンを使って光デバイスと電子デバイスを組み合わせる技術など，外国発の試みがあるが，これは従来の光技術を踏襲したものに過ぎないにもかかわらずその実用化は2025年まで待たなければならい。ブレークスルーをもたらすには従来の光技術の延長とは異なる新概念が必要である。このような中で現れた新概念の一つが本号で取り扱うドレスト光子であり，その応用技術がナノフォトニクスである。この技術ではナノ寸法領域において光と物質が互いに融合した状態になっていると考えることにより，光技術の質的変革をもたらしている。すでに大容量情報記録，計測，微細加工などの実用化が進んでおり，エネルギー，環境，情報セキュリティ等の分野への応用も2017年の実用化の目途がたち始めている。いよいよナノ寸法領域での光・物質融合科学技術が大きく進み始めた。

従来の光技術では光と物質を互いに独立に扱い，波長，屈折率といった巨視的物理量を用いて記述していたが（実はこのように扱ってきたために上記の停滞期を迎えたのであるが），ナノフォトニクスではナノ寸法領域での光と物質との相互作用に関する理解，ナノ寸法領域での光子の描像に関する考察が必要なので，今後は研究人口を増やすための啓蒙が一層重要となる。そのような中，最近欧米ではナノフォトニクスとその周辺技術に対する興味が高まり，応用に特化して技術開発が進んでいる。このように割り切った技術開発の柔軟性では欧米は日本と比して一日の長がある。翻って日本では欧米からの輸入技術を尊重する一方，自国発の概念に基づく新技術には拒否反応を示す傾向がある。さらに，新概念をもとに大きな市場を育てるという大局的戦略を忘れ，「いつ実用化されるのか？」という近視眼的な質問がすぐ寄せられる。

ナノフォトニクスの名を冠した研究機関，学会，学術誌などの数は欧米で急増している。日本発の技術であるにもかかわらず，日本の研究開発はいずれ世界の流れの中に埋没してしまうかもしれない。ただし，似たようなテーマで多くの研究者技術者が盛り上がりを見せているという状況，すなわち流行しているテーマに従事することは，先導性・独創性とはかけ離れている。研究者の数を比較すると日本は米国，EU，中国などに太刀打ちできないのだから，量よりも質を尊重し光・物質融合科学技術において先導性・独創性を追求し続けたいものだ。

（東京大学）

Progress in Light-matter Fusion Science and Technology

Motoichi Ohtsu (The University of Tokyo)

研究紹介

表面科学 Vol. 30, No. 11, pp. 600-606, 2009
特集「近接場光を用いた光工学技術の革新的発展」

近接場光による光技術の質的変革

大津元一

東京大学大学院工学系研究科電気系工学専攻およびナノフォトニクス研究センター
〒113-8656 東京都文京区弥生 2-11-16

(2009年7月23日受理)

Qualitative Innovation of Optical Technology by Optical Near Fields

Motoichi OHTSU

Department of Electrical Engineering and Information Systems,
also with Nanophotonics Research Center, The University of Tokyo
2-11-16 Yayoi, Bunkyo-ku, Tokyo 113-8656

(Received July 23, 2009)

This article reviews the novel technology named nanophotonics, which is an innovative technology utilizing the local energy transfer between nanometric materials induced by optical near fields. As an introduction to other review articles in this issue, history of this technology, theoretical picture of optical near fields, and examples of technical developments are surveyed. Among a variety of applications, progresses in developing devices, fabrications, system applications, and energy conversions are introduced. Recent status of research and development in US and EU, cooperation between industry and academia, and future outlook are also described.

KEYWORDS : nanophotonics, optical near field, dressed photon, forbidden level, nonadiabatic process

1. まえがき

光がナノ寸法物質に入射すると散乱し遠方へ伝搬していくが，同時に近接場光と呼ばれる膜状の光がその物質表面に発生する。この近接場光によって引き起こされるナノ寸法物質間でのエネルギー移動を活用し，光デバイス機能を発現したり，微細な加工を行う技術はナノフォトニクスと呼ばれている[1]。したがってこれは「ナノ寸法物質を用いた波動光学技術」や「伝搬光によりナノ寸法物質を作製・加工する技術」とは全く異質である。ナノフォトニクスは光技術の方法論として提案され，新しい基盤技術として研究開発が進み，最近では多岐にわたり応用されるようになった。この技術は光の回折に起因するデバイスや加工の微小化限界を打破し，光技術の量的変革をもたらした。

近接場光に関する詳細な研究により，これは物質中の励起と光子とが結合した場であり，「物質励起の衣をまとった光子」(dressed photon：以下では「ドレスト光子」と記す) と呼ぶべき状態であることがわかってきた[2]。即ちナノフォトニクスはナノ寸法領域での光・物質融合技術である。ナノフォトニクスを支える近接場光の学問は「dressed photon science」と呼ばれる新しい科学であり，従来の光技術では実現不可能だった新しい機能，現象が見出されている。これは「無から有を生む」変革であり，質的変革と呼ばれている。ナノフォトニクスの本質はこの質的変革を具現することである。

この技術の事例の詳細は本特集号の他記事に譲り，本稿では総説の立場で全体を概観し将来を展望する[3]。

2. 近接場光技術の歴史的背景

近接場光を工学的応用に使うにはその発生の再現性・効率を十分高くする必要がある。それにはガラスファイバを先鋭化したファイバプローブを作って使うのが有利であり，1990年代初頭には性能の高いファイバプローブが実現した[4,5]。これらに関する筆者らの研究とは独立に，欧米でも1980年代からD.W. Pohl（当時IBM研

E-mail : ohtsu@ee.t.u-tokyo.ac.jp

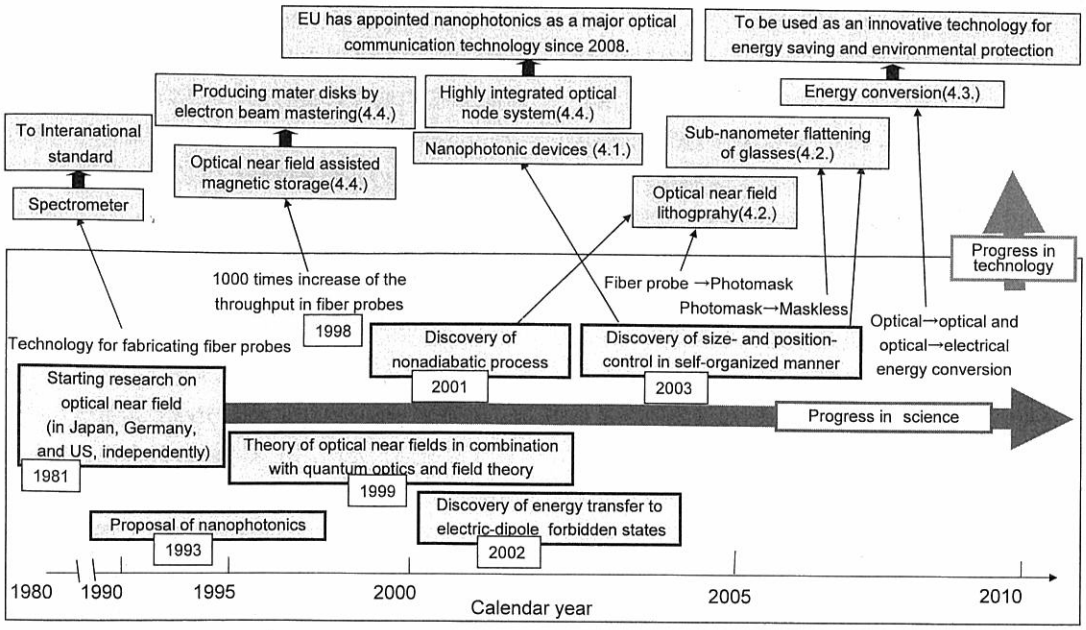

Fig. 1. (color online). Progress in science and technology realized by nanophotonics. Calendar year in the lower part of this figure represents the year of paper publication. Number in parenthesis in the upper part represents the section of this paper.

究所）らを中心に走査プローブ顕微鏡の一形態としての近接場光学顕微鏡の研究が進み始めた[6]。1990年代前半にAT＆Tベル研究所（米国）では磁気光学メモリへの応用の研究も短期間行われるという事例が見られたが[7]，その後の欧米の研究は顕微法，分光，波動光学にもとづく数値シミュレーションなどに留まり，最近ではプラズモニクス[8]，メタマテリアル[9]といった波動光学技術に移行している。これに対し日本では1993年9月にナノフォトニクスが提案され[10]，欧米とは異なる方向に進んでいる[注1]。

これまでに筆者らは**Fig. 1**に示すナノフォトニクスの基礎研究・応用展開を推進し，デバイス・加工・システムに関する質的変革を実現した。なお，ナノフォトニクスによるデバイス・加工・システムでは加工や情報記録などの処理速度を高めるためにファイバプローブを駆逐した方法を取っている。

3. 原理とその定式化

ナノフォトニクスが提案される以前の1980年代には近接場光を物質の表面波として捉え，屈折率と境界条件にもとづく波動光学の枠組みで考察されていた。その後，光の散乱問題として積分方程式（Lippman-Schwinger方程式）による自己無撞着法が[11]，さらには有限差分時間領域（Finite-Difference Time Domain : FDTD）法などの数値計算法が使われるようになった[12]。これらの計算による数値解の精度を保証するためには誤差の大きさの指標となる逆作用素のノルムを評価しなくてはならない[13]。しかし自己無撞着法では簡易化したグリーン関数が必要となり対象とする問題ごとにこれが異なる。一方FDTD法ではノルムの評価法が確立していないので，数値解の近傍に真の値が存在することを保証しないという致命的な問題がある。

以上の問題を回避するために，ナノ寸法領域における光と物質との局所的相互作用の観点から新しい理論が展開された[14]。すなわちナノ寸法物質とその表面の近接場光とが切り離せない状態になっているが，これを物質表面に存在する場としての光の立場から見ると，光は物質の衣をまとった状態と捉えることができる。したがって第1節で記したように近接場光をドレスト光子という概念で取り扱う。すなわちナノ寸法領域では物質と光は互いに強く相互作用しているが，光科学技術の進展のためにはこれを光が物質励起の衣をまとった状態にあると捉えて，光の立場から記述する。言い換えると物質外部から見て近接場光とは何か？を考える。

ここで上記のナノ寸法物質が数nm～数十nm離れて二つ置かれている場合を考える。これだけ離れていると電子のトンネリングはなく物質エネルギーは移動しない

注1 大津によるナノフォトニクスの提案（1993年9月）を受けて，（財）光産業技術振興協会では1995～2003年にわたり「ナノフォトニクス懇談会」が運営され，ナノフォトニクスに関連する技術の基礎，応用，実用化に関する産官学連携の活動が行われた。

が，近接場光によりエネルギーが移動しうる。このように光によりエネルギーが移動する事を記述するには，物質と光（電子系と光子系）が融合した状態を光の立場から考えた方が見通しがよい。この考え方の帰結がドレスト光子の描像である。すなわち二つのナノ物質間でのドレスト光子の交換により両物質間でエネルギーが移動する。

ナノフォトニクスではこのエネルギー移動を利用するので，二つのナノ寸法物質と近接場光からなるナノ系の振る舞いを理論的にうまく取り扱いたい。ただし実際にはこのナノ系は入射光・散乱光・基板からなる巨視系に囲まれて複雑な電磁相互作用をしている（**Fig. 2**）。そこで巨視系内部およびナノ系との相互作用のエネルギーをナノ系のエネルギーに繰り込むための射影演算子法にもとづき，ナノ系があたかも巨視系から孤立していると見なし，ナノ寸法物質間の相互作用の大きさが見積もられた[14]。これにより多数のエネルギー準位からなるナノ系を簡単な二準位系とみなすことができるようになった。この相互作用は有効相互作用と呼ばれるが，ここでは近接場光に関係しているので近接場光相互作用と呼ばれている。すなわちナノ系と巨視系との間の相互作用を繰り込み，繰り込まれた近接場光相互作用があたかも孤立した二つのナノ寸法物質の間に働くとみなす。

この局在した光子はナノ寸法物質中の励起と融合したドレスト光子であり，有効質量をもつ。近接場光相互作用はドレスト光子がナノ寸法物質間で交換されることにより生ずる。この相互作用は湯川関数で表され，その及ぶ範囲はナノ寸法物質の寸法程度であり，これは近接場光の染み出し長が入射光波長によらず物質の寸法程度であることに相当する。

ナノフォトニクスの多様な実験結果はドレスト光子の考え方を用いることにより定量的に説明されるようになった。これまでに得られた主な知見は新たな光学自由度としての電気双極子禁制準位への光励起，新たな局所反応場としての非断熱的光化学反応の誘起などである。これらは各々デバイス，加工の設計によく使われており，その事例を次節で順次説明する。

4. 技術開発の事例

4.1 デバイス

ナノフォトニクスによるデバイス開発の動機は光の回折限界を超えたデバイス寸法の微小化という量的変革であった。たとえば光によってコンピュータ内部の集積回路チップ間，チップ内部のデバイス間の信号伝送を行うためには光デバイス寸法を 100 nm 以下にする必要があると試算されているが[15]，上記の量的変革はこれに答えるものである。これまでに各種のデバイスが考案されている。

いずれも信号伝送の一方向性，出力信号の位置・寸法・値をナノ寸法領域で確定する必要がある。そのために近接場光相互作用によるエネルギー移動が利用されている。たとえば一辺の長さの比が $1:\sqrt{2}$ の立方体の二つの半導体量子ドット（各々 QD1，QD2 と記す）を，その寸法程度まで近づけて設置する。この寸法比の場合 QD1 の三次元形状に対応して三つの量子数（1，1，1）で表される励起子の量子化エネルギー準位は QD2 中のエネルギー準位（2，1，1）と共鳴する。

これらの準位に共鳴する周波数の光を入力信号として入射すると電気双極子許容準位である QD1 のエネルギー準位（1，1，1）には励起子が生成されるが，電気双

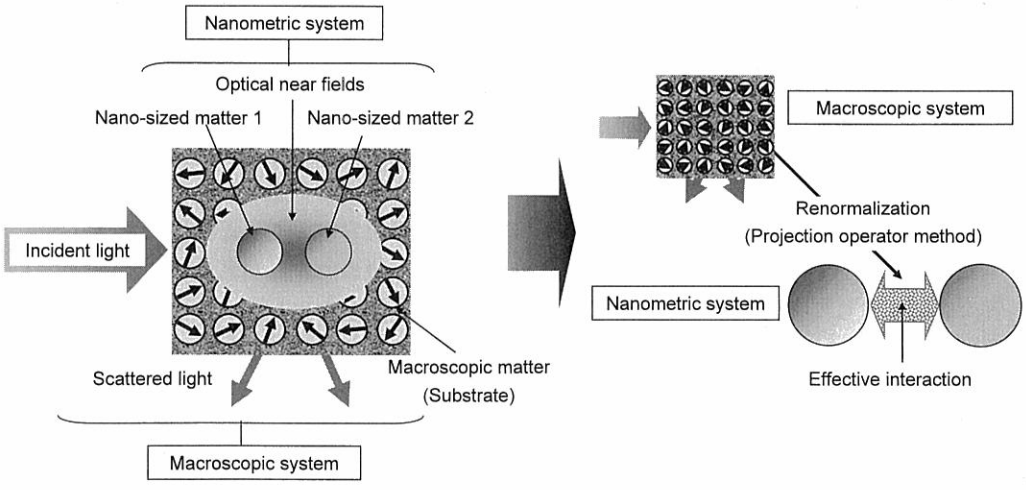

Fig. 2. (color online). Interaction in the nanometric system buried in the macroscopic system, and its theoretical treatment by using the projection operator method.

極子禁制準位であるQD2のエネルギー準位（2，1，1）には生成されない。以上によりQD1がデバイス入力端子として働く。すなわちQD1にドレスト光子が生成される。

ここで二つの量子ドット間距離が十分近いので，QD1の（1，1，1）準位に生成された励起子が光子を発生して消滅する前に近接場光相互作用によりQD2のエネルギー準位（2，1，1）に移動する。この移動は伝搬光を介さないので（2，1，1）が電気双極子禁制であっても可能である。こうしてエネルギー準位（2，1，1）にドレスト光子が生成されるが，その後短時間のうちにQD内の下方のエネルギー準位（1，1，1）へと緩和する。したがってエネルギーはQD1へ逆流せず，信号の移動の一方向性が確定し，QD2が出力端子となる。

こうしてナノ寸法領域でのQD1からQD2への信号伝送が可能となる。従来技術では電気双極子禁制準位へのエネルギー移動は不可能であるが，ここでは近接場光相互作用によって実現し，これがデバイス機能の質的変革を意味する。また，デバイス寸法が回折限界以下なので量的変革も実現する。

なおこのデバイス動作におけるエネルギー散逸量はQD2中のエネルギー準位（2，1，1）から下方のエネルギー準位（1，1，1）への緩和に起因するのみなので微小であり，発熱量が非常に低い。また，このデバイスは単一光子によって動作することが99.3%以上の確度で確認されている[16]。これらの低発熱量・単一光子動作はこのデバイスが高度集積化・低消費エネルギー動作可能という利点をもつことを表している。

従来の電子回路では出力信号値を確定するためにデバイス外部の配線・電源・負荷などの外部回路が必要なので，伝送される信号はアース地点でのもれ信号を検出することにより傍受することができ，したがって盗聴に対する耐性が低い。しかしナノフォトニクスによるデバイスでは近接したQD1，QD2の間での信号が伝送され，出力信号の値はQD2内部で決まるので，デバイス寸法とシステム寸法が同一である。さらにQD2でのエネルギー散逸のみで信号伝送が確定するので，伝送信号の傍受は極めて困難となる[17]。この特性も質的変革の例である。

以上の原理に基づき，これまでにANDゲート[18]，NOTゲート[19]などの機能デバイス動作が確認されている。これらを組み合わせるとOR，NAND，NORゲートなどが可能となり，論理ゲートの完備系が形成される。またANDゲートのデバイス体積・スイッチング時間・制御信号エネルギー・出力信号のオン/オフ強度比などの組み合わせで定義される性能指数は従来の関連する光デバイスなどにくらべ10-100倍高いことなども指摘されている[20]。さらに，二つの量子ドットの間でエネルギーを閉じ込める光バッファ機能[21]，伝搬光を近接場光に変換しエネルギーを蓄積する光ナノファウンテン[22]，上記のデバイス間をつないで信号を伝送するための配線デバイス[23]，協同現象を利用した短パルス信号発生デバイス[24,25]などが考案され，その動作が検証されている。以上のデバイス機能の検証のためにCuClなどの量子ドットを低温で用いる実験が行われていたが，近年は室温で動作するデバイスの実現を目指した開発が進んでいる。InAs[19]，ZnO[26]は励起子の閉じ込めポテンシャルが深く，離散化されたエネルギー準位が広い等の特徴をもつので，室温動作用の材料として採用されている。

4.2 加工

ここで紹介する加工の形態はFig. 2中の第一，第二のナノ寸法物質を各々加工機，加工対象とするものである。すなわち第一のナノ寸法物質に近接場光を発生させ，近接場光相互作用により第二のナノ寸法物質に化学反応を誘起し，その形状，構造を変える。実用的な加工技術の実現のためにはまず質的変革の観点から

①従来の光技術では不可能であった加工技術であること，

さらに量的変革の観点から

②加工位置，寸法をナノメートル精度で制御できること，

③加工速度が十分大きいこと，

などの条件を満たす必要がある。以下ではこれらを満たすための最近の技術開発について記す。

まず①について考える。第一のナノ寸法物質に光を入射したときに発生したドレスト光子が周囲に大きな機械的歪みを誘起し，その結果コヒーレントフォノンを局所的に生成する場合がある。このフォトンは熱源とはならず，ドレスト光子と結合する。すなわちドレスト光子がフォノンのエネルギーの衣もまとうことになる[27~29]。この結果，第一のナノ寸法物質のドレスト光子のエネルギーとフォノンのエネルギーとが第二のナノ寸法物質に移動し得る。

このエネルギー移動を利用すれば，たとえ入射光の光子エネルギーが第二のナノ寸法物質中の電子を励起準位に励起させる程高くなくとも（すなわち断熱過程による光化学反応が起こらなくとも），フォノンのエネルギー移動により分子振動が誘起され，分子振動エネルギー準位を介した多段階励起により電子が励起される。これは非断熱過程により光化学反応が起こること，したがって従来の加工で使われる紫外光よりも光子エネルギーの低い可視光を使うことができること，さらには光により電

子遷移できない光学不活性物質さえも加工対象となり得ることを意味しており，上記①の質的変革に相当する。

非断熱過程による加工は光化学気相堆積において実証されている[27,30]。さらには光リソグラフィにも応用され[31~33]，特に上記②，③を実現するために産学連携により実用機の雛形が開発された[34,35]。これにはフォトマスクのステップ・リピート移動機構，装置内のクリーンルーム化，装置の耐振化，基板搬送用の計算機制御ロボットシステムなどが配備されている。この装置は2006年度より全国公開利用に供され，波長1 nmの軟X線用の回折格子（刻線数7600本/mm）[36]，4.1で記した室温動作NOTゲートのデバイスのためのInAs量子ドットの二次元配列[37]などが作製されている。

以上の光リソグラフィではフォトマスクを使っているが，加工速度の向上・装置の簡易化のためにはフォトマスクを使わない（マスクレスの）方法が望ましい。ナノ寸法物質の表面には常に励起子やフォノンといった物質励起の衣をまとったドレスト光子が発生しうるという普遍的現象に注意すればマスクレスの方法が可能となる。その例として光化学エッチングによるガラス表面の平坦化が行われ，合成石英ガラス基板表面の凹凸が約0.13 nmまで減少することが確認されている[38]。同様の方法で蒸着金属微粒子の寸法と間隔を制御する自己組織的なマスクレスの方法も実施されている[39]。これは加工速度の向上・装置の簡易化とともに，形成されるパターンの位置と寸法を高い精度で制御できる利点を有する。なぜならこれらの精度はファイバプローブやフォトマスクの位置と寸法ではなく，照射する光の光子エネルギーの値によって決まるからである。

4.3 エネルギー変換

4.1のデバイスの原理であるエネルギー移動と緩和は入出力信号の光周波数を比較すると光周波数下方変換と，また4.2の加工における非断熱過程は光周波数の上方変換と各々捉えることができる。これらは従来の非線形光学における電子遷移の非線形光学応答とは異なり，特に後者の非断熱過程では分子振動準位を介した多段階励起である。この特性を使い近赤外光（波長803 nm）をDCMやローダミン6Gなどの有機色素の微粒子（吸収端波長は各々560 nm，580 nm）に照射し，可視光を発生させることに成功している[40]。これは従来からある蛍光の発生機構（吸収端波長よりも短波長の光を入射し，それより長波長の蛍光を発生させる）とは異なる。

この例は発光と受光に対して近接場光相互作用における非断熱過程を利用することにより，従来使われていなかった長波長の光による光エネルギー変換が可能であることも意味している。

4.4 システム

上記のデバイス・加工などの技術を組み合わせると新規のシステム開発が可能となる。まず情報伝送システムへの展開について略記する。現在の光通信システムや計算機システムでは通信容量や計算能力のさらなる向上と消費電力の低減が問題となっており，これを解決するための将来技術の一つとして量子情報通信や量子計算が開発されているが[41]，これらの未来技術が実現する以前に使用する次世代技術として，欧州ではナノフォトニクスを採用することが検討されている。わが国ではそれに先んじてナノフォトニクスによる三チャンネルの光スイッチとデジタル・アナログ変換デバイスを用いた光ルータ用検索機能の動作が実証された[42]。

次に情報記録システムでは近接場光の空間分布の特徴の一つである階層性（近接場光相互作用によるナノ寸法物質間でのエネルギー移動において，近接場光エネルギーの空間的分布の大きさと物質間距離が1対1に対応しているという性質）を使う多重記録[43]，また盗聴に対する耐性が高いこと（これはナノフォトニクスによるデバイスでのエネルギー散逸はエネルギー準位間での励起子の緩和のみに依存し，デバイス外部に散逸エネルギーが漏れ出さないことに起因する）を使う情報セキュリティ機能付き記録[44]などが提案され，実証されている。これらは情報記録における質的変革の事例である。一方，情報記録密度に関する限界を超えて高密度化するという量的変革も実現している。すなわちこれは熱アシスト磁気記録システムであり，近接場光により磁気記録媒体表面を局所的に加熱して媒体の保持力を下げ，その直後に磁気記録する方法である。これにより磁気記録媒体の熱揺らぎによって制限される記録密度の上限を超えることができる。著者らは産学連携により，近接場光発生用デバイス，その安定走行機構，磁気記録用のナノパターン媒体，磁気ディスク原盤製造用のナノマスタリング装置などを開発し，1Tb/inch^{2}級記録技術を世界に先駆けて実現した[45]。この技術を微細改良すれば記録密度10Tb/inch^{2}程度まで実現可能と試算されている。さらに最近では2025～2030年に記録密度1Pb/inch^{2}を実現することをめざした技術ロードマップが策定された[46]。

5. 最近の国際的状況

筆者らはこれまでに**Fig. 3**に示すようにナノフォトニクスに関わる各種技術の実用化の産学連携を実施してきた（図中の括弧内の数字は筆者と産学連携を実施した企業数を表す。一部は現在も推進中である。）。この図に見られるようにナノフォトニクスは従来の光技術の多くの分野に取って代わることのできる可能性を示している。

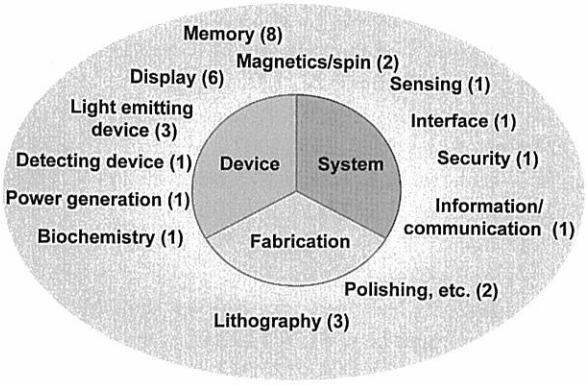

Fig. 3. (color online). Examples of industry-academia collaborations. Number in parenthesis represents the number of company participated in these collaborations.

1993年に筆者がナノフォトニクスを提案した後しばらくは関連研究発表件数は極めて少なかったが，近年はそれが激増している。これは欧米でもナノフォトニクスに対する関心が急増していることの証左であり，ここ一，二年の間に欧米では多数の機関が大型研究開発事業を立ち上げている。特にEUではナノフォトニクスを次世代の光通信システム技術の中核に置いており，技術開発が極めて協力に推進されている[47]。ただし欧米ではナノフォトニクスの定義が曖昧かつ広義になっており[48,49]，そのうちの多くは波動（回折）光学技術なので，「質的変革」を生むことは難しいと思われる。新しい技術の確立のためには，ナノ寸法の局所領域での光子の実体をはじめとする基礎原理を探索し，これを応用に結びつける努力が必要であろう。

近年はナノフォトニクスに関する情報交換・研究交流の希望が欧米から日本に多く寄せられるようになった。これを受けて筆者らは日本と相手国との2国間交流を企画し，これまでに米国，豪州，ドイツ，スウェーデン，フィンランドとワークショップを複数回実施している[50]。

なお，1980年代から継続する応用の例として，回折限界を超えた空間分解能を有する顕微鏡や分光分析装置が開発されている。特に後者はわが国の産業界により世界に先駆けて製品化され高い性能を示している[51]。これはファイバプローブの性能の高さに負うところが大きいが，本稿ではこれらの計測技術への応用の記述は割愛した。なぜならば2節で記したようにナノフォトニクスは脱プローブ技術により実現したからである。さらにまた，試料の形状や構造の計測にはファイバプローブと試料との間のエネルギー移動が利用されるが，試料への非接触性・非破壊性を保つためにはエネルギー移動量を0に外挿して測定結果を解釈する必要があり，これはエネルギー移動を積極的に利用するナノフォトニクスの方法論とは整合しないからである。ただしこれらの計測技術も成熟しつつあり，AFM技術と共に国際標準化の動きが始まっている[51]。

6. むすび

従来の光科学技術は長い歴史をもつが，そこでは光を「古典論 vs 量子論」と対比して捉えていた。これに対し本稿で紹介した光技術の質的変革の事例は「大きい vs 小さい」という対比，すなわち従来の光科学技術の研究とは異なった切り口から捉えることにより生まれた。小さい光とは近接場光であるが，我々はこれをドレスト光子と捉えた。これにより電気双極子禁制準位への励起，非断熱的光化学反応などが理論的に記述可能となり，この描像は質的変革を実現した光デバイス，光加工，光システムの設計にも使われるようになった。

ナノフォトニクスによるデバイスと加工は多様な光システム実現のための基盤技術として発展しており，その市場規模に関する技術ロードマップも策定されている[52]。当面はこれらの応用分野を精選して技術レベルをさらに高め，並行して光科学，場の量子論，固体物理学をまたがってドレスト光子の概念の記述を精密化し，局所領域での光子の実体，ナノ空間での励起輸送と緩和，非断熱的光化学反応の素過程，フォノン以外のいろいろな素過程とドレスト光子との結合可能性などについて詳しく考え，ドレスト光子による光・物質融合技術を一層進展させる事が我々に科せられた急務である。

謝　辞

本稿で紹介させていただいた研究の萌芽的な時期から長きにわたり情報を交換して下さった堀裕和，小林潔（ともに山梨大），物理学，情報科学の観点からご教示頂いた北原和夫（国際基督教大），塚田捷（東北大），大石進一（早稲田大）の各氏に深く感謝致します。また，産学連携でのデバイス，加工，システム開発に参画頂いた産業界の関係各位に深く感謝します。

文　献

1) M. Ohtsu, K. Kobayashi, T. Kawazoe, S. Sangu and T. Yatsui : IEEE J. Selected Topics in Quantum Eletcton. **8**, 839 (2002).
2) M. Ohtsu, T. Kawazoe, T. Yatsui and M. Naruse : IEEE J. Selected Top. Quantum Electron. **14**, 1404 (2008).
3) 大津元一：応用物理 **77**, 1341 (2008).
4) S. Jiang, N. Tomita, H. Ohsawa and M. Ohtsu : Jpn. J. Appl. Phys. **30**, 2107 (1991).

5) T. Pangaribuan, K. Yamada, S. Jiang, H. Ohsawa and M. Ohtsu : Jpn. J. Appl. Phys. **31**, L1302 (1992).
6) D.W. Pohl and D. Courjon : "Near Field Optics" (Kluwer Academic Publishers, Dordrecht, 1992) pp. 1-410.
7) E. Betzig, J.K. Trautman, R. Wolfe, E.M. Gyorgy and P.I. Finn : Appl. Phys. Lett. **61**, 142 (1992).
8) V.A. Podolskiy, A.K. Sarychev and V.M. Shalaev : Opt. Exp. **11**, 735 (2003).
9) J.B. Pendry : Phys. Rev. Lett. **85**, 3966 (2000).
10) X. Zhu and M. Ohtsu (ed.) : "Near-Field Optics : Principles and Applications" (World Scientific, Singapore, 2000) pp. v-vi.
11) C. Girard and D. Courjon : Phys. Rev. B**42**, 9340 (1990).
12) A. Taflove : "Computational Electrodynamics" (Artech House, Boston, 1995).
13) 大石進一 : "精度保証付き数値計算" (コロナ社, 2001) p. 13.
14) K. Kobayashi, S. Sangu and M. Ohtsu : "Progress in Nano-Electro-Optics I" ed. by M. Ohtsu (Springer-Verlag, Berlin, 2003) p. 119.
15) The Microphotonics Center at MIT (ed.) : "2005 Communications Technology Roadmap" (The Microphotonics Center at MIT, Boston, 2005). ホームページは http://mph-roadmap.mit.edu/about_ctr/report2005/
16) T. Kawazoe, S. Tanaka and M. Ohtsu : J. Nanophotonics **2**, 029502 (2008). Technical Digest of Quantum Electronics Science Conference, San Jose, 2008, QTuE4 (Optical Society of America, Washington, D.C., 2008).
17) M. Naruse, H. Hori, K. Kobayashi and M. Ohtsu : Opt. Lett. **32**, 1761 (2007).
18) T. Kawazoe, K. Kobayashi, S. Sangu and M. Ohtsu : Appl. Phys. Lett. **82**, 2957 (2003).
19) T. Kawazoe, K. Kobayashi, K. Akahane, M. Naruse, N. Yamamoto and M. Ohtsu : Appl. Phys. B **84**, 243 (2006).
20) T. Kawazoe, K. Kobayashi, S. Sangu and M. Ohtsu : "Progress in Nano-Electro-Optics V" ed. by M. Ohtsu (Springer-Verlag, Berlin, 2006) p. 109.
21) T. Kawazoe, M. Naruse and M. Ohtsu : "Technical Digest of Conference on Lasers and Electro-Optics" Long Beach, 2006, CFE3 (Optical Society of America, Washington, D.C., 2006).
22) T. Kawazoe, K. Kobayashi and M. Ohtsu : Appl. Phys. Lett. **86**, 103102 (2005).
23) W. Nomura, T. Yatsui, T. Kawazoe and M. Ohtsu : J. Nanophotonics **1**, 011591 (2007).
24) A. Shojiguchi, K. Kobayashi, S. Sangu, K. Kitahara and M. Ohtsu : J. Phys. Soc. Jpn. **72**, 2984 (2003).
25) 八井 崇, G.C. Yi, 大津元一 : 第55回応用物理学関係連合講演会講演予稿集 (2008) p. 79.
26) T. Yatsui, S. Sangu, T. Kawazoe, M. Ohtsu, S.J. An, J.K. Yoo and G.C. Yi : Appl. Phys. Lett. **90**, 223110 (2007).
27) T. Kawazoe, K. Kobayashi, S. Takubo and M. Ohtsu : J. Chem. Phys. **122**, 024715 (2005).
28) Y. Tanaka and K. Kobayashi : J. Microsc. **229**, 228 (2007).
29) 川添 忠 : 応用物理 **77**, 662 (2008).
30) T. Kawazoe, K. Kobayashi and M. Ohtsu : J. Photopolymer Sci. and Technol. **20**, 129 (2007).
31) T. Kawazoe, M. Ohtsu, Y. Inao and R. Kuroda : J. Nanophotonics **1**, 011595 (2007).
32) H. Yonemitsu, T. Kawazoe, K. Kobayashi and M. Ohtsu : J. Luminescence **122/123**, 230 (2007).
33) 大津元一 : "ナノフォトニックデバイス・加工" (オーム社, 2008) p. 181.
34) Y. Inao, S. Nakasato, R. Kuroda and M. Ohtsu : Microelectronic Eng. **84**, 705 (2007).
35) 黒田 亮 : オプトロニクス **314**, 108 (2007).
36) M. Koike, S. Miyauchi, K. Sano and T. Imazono : "Nanophotonics and Nanofabrication" ed. by M. Ohtsu (Wiley-VCH, Weinheim, 2009) p. 179.
37) T. Kawazoe, H. Yonemitsu and M. Ohtsu : Proceedings on The 5th Asia-Pacific Conference on Near-Field Optics, Niigata, 2005 (Opt. Soc. Jpn, Tokyo, 2005) p. 72.
38) T. Yatsui, K. Hirata, W. Nomura, Y. Tabata and M. Ohtsu : Appl. Phys. B : Lasers and Optics **93**, 55 (2008).
39) T. Yatsui, W. Nomura and M. Ohtsu : Nano Lett. **5**, 2548 (2005).
40) T. Kawazoe, H. Fujiwara, K. Kobayashi and M. Ohtsu : IEEE J. Selected Topics in Quantum Electron. **15**, 1380 (2009).
41) D.P. DiVincenzo : Science **270**, 255 (1995).
42) M. Naruse, T. Miyazaki, T. Kawazoe, S. Sangu, K. Kobayashi, F. Kubota and M. Ohtsu : IEICE Trans. Electron. **E88-C**, 1817 (2005).
43) N. Tate, W. Nomura, T. Yatsui, M. Naruse and M. Ohtsu : Opt. Express **16**, 607 (2008).
44) M. Naruse, T. Yatsui, T. Kawazoe, Y. Akao and M. Ohtsu : IEEE Trans. Nanotechnol. **7**, 14 (2008).
45) 大津元一(編著) : "大容量光ストレージ" (オーム社, 2008).
46) (財)光産業技術振興協会編 : "情報記録テクノロジーロードマップ報告書" ((財)光産業技術振興協会, 東京, 2006) p. 31.
47) MONA consortium 編 : A European roadmap for photonics and nanotechnologies, MONA (Merging Optics and Nanotechnologies Association) consortium, 2008 (http://www.ist-mona.org/partners.asp).
48) National Research Council of the National Academies 編 : "Nanophotonics Accessibility and Applicability" (National Academy Press, Washington, D.C., 2008).
49) A. Neogi 教授(North Texas Univ., USA) からの私信. 広義にすることにより必ずしもナノフォトニクスには直結しない技術分野へも政府から資金を導入することがその意図とのこと.
50) 大津元一 : 応用物理 **78**, 473 (2009).
51) 成田貴人 : オプトロニクス **314**, 114 (2007).
52) (財)光産業技術振興協会編 : "極限インフォニクス技術に関する調査研究報告書" (近接場光技術等の現状と将来) ((財)光産業技術振興協会, 2000) p. 217.

OA0812-17　0917-026X/09/￥500/論文/JCLS

東京大学大学院工学系研究科大津・八井研究室

＝ドレスト光子の科学とナノフォトニクス技術の開拓＝

東京大学　大津　元一

1．はじめに

当研究室ではナノ寸法の光である近接場光をドレスト光子（dressed photon：物質エネルギーの衣をまとった光子）と捉える光科学と、それを光技術に展開して従来技術の質的変革をもたらすナノフォトニクスとを提唱し、引き続きその研究開発を行っている[1]。2008年より本学工学系研究科にナノフォトニクス研究センターが新設され、大津はセンター長を兼務している。また、同年に八井崇准教授が着任以降、現在は両名で研究室を共同運営している。外部資金による研究プロジェクトを複数運営しており研究室の人員数は32名（特任准教授、特任助教、特別研究員、研究補助員、産学連携担当マネージャー、企業派遣研究員、事務補佐員、大学院・学部学生）である（写真1）。

2．研究活動のようす

ドレスト光子の基礎研究はKASTにおいて、その後JSTのERATOとその継続のSORSTプロジェクトにおいて推進してきた。その成果はデバイス、加工、システム、エネルギーなど公汎に応用可能なのでNEDOの産学連携大型プロジェクトへと展開している。また、わが国で生まれたナノフォトニクスの基礎概念を産業界に啓蒙する為に本学大学院工学系研究科にNEDO特別講座が設置された。この人材育成型啓蒙活動を通じ、省エネルギー技術の産学共同NEDOプロジェクトも始まった（図1）。

写真1　大津・八井研究室のメンバー（2008年12月撮影）

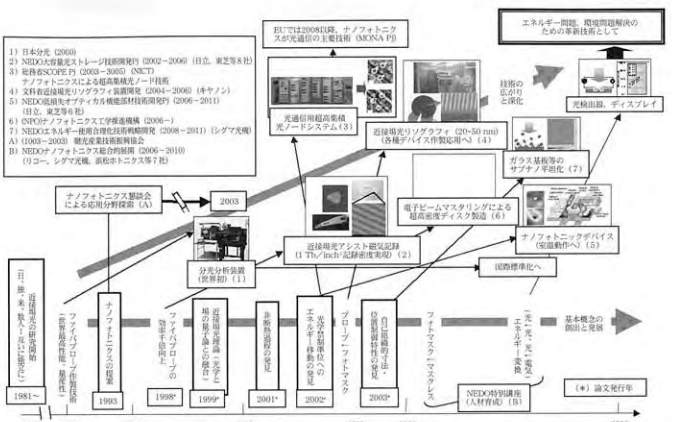

図1　ドレスト光子の科学、ナノフォトニクスの技術の創始から現在までの進展の様子

ナノフォトニクスの研究開発は外国でも興味が急増しており、それを創始した我々の研究グループを含む日本との共同研究、情報交換の希望が多く寄せられるようになった。それを受け、大津が代表となりここ数年間で日米、日独、日豪の二国間セミナーを実施した。これは両国の公的機関の支援を受け、20名程度の先進研究者が参加し活発な議論をかわす会議である。これが契機となり日独では昨年より共同研究が始まった。今年はスウェーデン、フィンランドとの交流が実施される。

3．おわりに

ドレスト光子の科学は従来の光科学に欠落していた「ナノ領域での光子の実体、エネルギー輸送、緩和」を研究するものであり、その応用としてのナノフォトニクスの適用範囲は広い。これは光技術の多くを置換える可能性を含むので、光の新しい基盤技術と位置づけられている。今後の発展にむけて一層努力したい。なお、研究活動の詳細情報は我々のHPを参照されたい（http://uuu.t.u-tokyo.ac.jp）。

<参考文献>

(1) 大津元一：応用物理，第77巻，p.1341（2008）

【筆者紹介】

大津元一
東京大学　大学院　工学系研究科
電子工学専攻　教授
〒113-8656　東京都文京区弥生2-11-16
TEL：03-5841-1189
FAX：03-5841-1140

OA0904-08

NEDO特別講座「ナノフォトニクス総合的展開」

東京大学　大津　元一

1．はじめに

工学系の学問は産業界と連携することにより初めて社会に貢献することができる。光科学技術の歴史は18世紀のI. Newtonによる光の粒子説以来長く、1960年のレーザの発明後、1980年代に長足の進歩を遂げた。しかしその原理・概念は欧米で生まれ、日本は主に改良・もの作りで貢献してきた。この状況下で日本のアカデミアは原理を輸入・翻訳し産業界に紹介することにより社会貢献を果たしてきた。しかし近年、日本発の新しい原理・概念・技術が生まれるようになった。その代表例が近接場光とそれをdressed photon（ドレスト光子：物質励起の衣をまとった光子）と捉えて応用し新規デバイス、加工、システム構築を実現する「ナノフォトニクス」という革新技術である[1]。この技術を社会貢献に供するには、日本のアカデミアが引き続き先駆的な基礎研究を推進して国内外をリードし、同時に産業界の技術者を啓蒙し、さらに研究現場に受け入れてOn the research training（ORT）を行い、新技術開発の共同研究への道を切り開くことが重要である。

一方、経済産業省、NEDOではかねてより産学連携に関わる多数の大型プロジェクトを実施しているが、これはもの作り・製品開発に関わる事業で、人材育成事業ではない。従って開発された試作品をプロジェクト終了後にさらに開発し新市場を確保することは難しく、市場に出ないまま終わる例が見られた。経済産業省ではこの問題を解決するために大型プロジェクト推進の大学側代表者が企業技術者に対して関連技術の基礎を啓蒙し、技術を使いこなし開発できる人材を育成する事業を企画した。

0917-026X/09/¥500/論文/JCLS

以上のように本プロジェクトは経済産業省、NEDOからの人材育成のニーズと、社会貢献に関するアカデミアの使命感とが結びついて発足した。この点において本プロジェクトは極めてユニークで新しい性格を有する。

2．本講座の構成と実施内容

本プロジェクトは前述の経緯により経済産業省、NEDOが企画した新しい啓蒙教育事業であり、日本初の試みとして平成18年度より５年間、東京大学に委託された。本プロジェクトは通称NEDO特別講座「ナノフォトニクス総合的展開」と呼ばれ、ナノフォトニクスを核とした人材育成、産官学連携等の総合的展開を目指している（図１）。この講座発足の核となった大型プロジェクトは筆者が代表を務めるNEDO「大容量光ストレージ技術の開発」プロジェクト（平成1418年度)[2][3]、およびNEDO「低損失オプテフィカル新機能部材技術開発」プロジェクト（平成18年度より５年間)[4]である。両者ともナノフォトニクスに関わる日本発の概念にもとづき実施され、前者は情報記録密度１Tb/inch^{2}の近接場光アシスト磁気記録システムを世界で初めて実現して成功裏に終了した。その後は産業界が継続して自己資金により実用化開発を展開しており、記録密度10Tb/inch^{2}を経由して、2025年の１Pb/inch^{2}の目標にむけた開発の技術ロードマップが策定されている[5]。一方、後者は昨年末の中間評価で極めて高い評価を得た後[6]、開発の後半にむけて技術の進展が著しい。

本プロジェクトは本学大学院工学系研究科の大津研究室に設置され、特任准教授１名(客員)、特任助

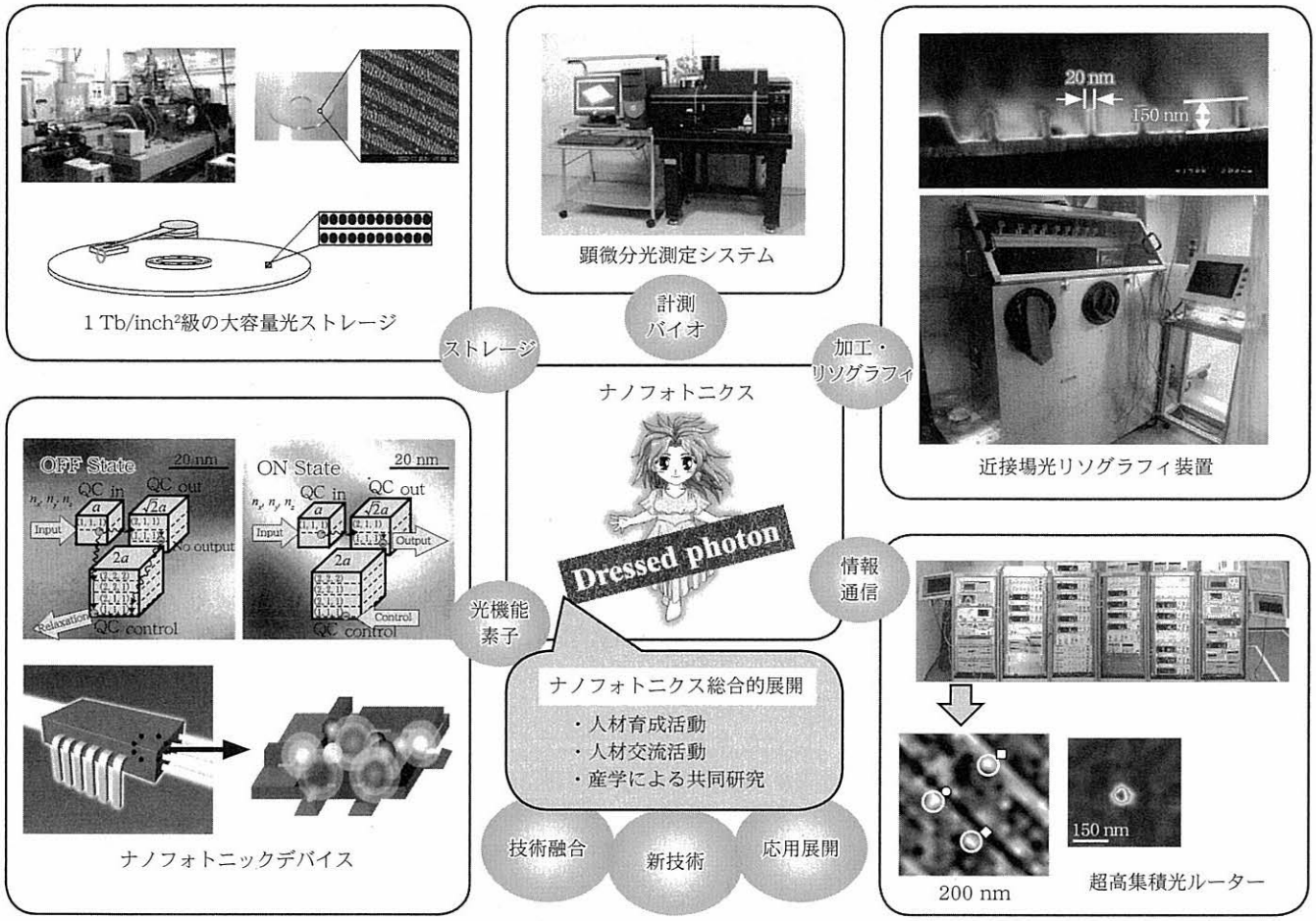

図1　本プロジェクトとその核になるナノフォトニクスの技術の広がり

教３名、産学連携マネージャー１名、事務職員１名を雇用して業務を行っている。その主な内容は次のとおりである（図２）。

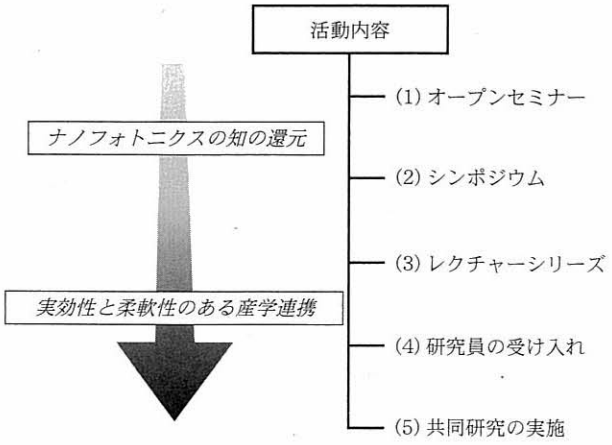

図2　本プロジェクトの業務内容

(1) オープンセミナー

有識者２名の講師を招き、ほぼ毎月開催される自由聴講の産業界向け講演会である。活発な質疑応答の時間を十分確保するため、聴講者はおおむね30名以下に限っている。本年４月の時点ですでに18回実施している。

(2) シンポジウム

本プロジェクトの成果報告のために年１回開催されるシンポジウムである。産業界に向けた情報発信を目的としているため開催案内は産業界のみに発送している。これまでに３回開催したが、毎回全国から300名近い技術者が参加し、会場は満員となり立ち見も出る盛況で、本技術に対する関心の高さが伺える（写真１）。シンポジウムの末尾には別会場に移動して本講座の研究者・技術者と参加者との間の個人面談の時間を設け、ナノフォトニクスを産業界に導入する具体的な方策、開発対象について意見交換している（写真２）。

(3) レクチャーシリーズ

ナノフォトニクスの原理・基礎に関する大学院講義と

して「電子工学特別講義Ⅲ」を各年度後期に開設しており、下記(4)の技術者が聴講している。受講生の大半は正規の大学院学生であるが、技術者が活発に質問するので大学院学生にもよい刺激となっている（写真３）。

写真１　シンポジウムの様子

写真２　本講座の研究者・技術者とシンポジウム参加者との間の個人面談の様子

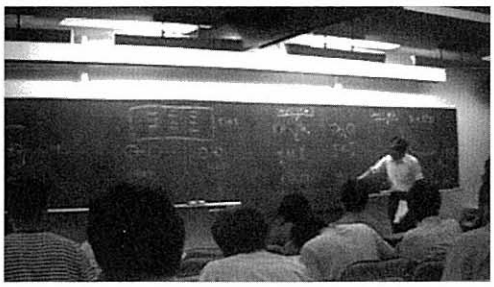

写真３　レクチャーシリーズの様子

(4)　研究員の受け入れ

下記(5)の共同研究を推進する若手技術者を産業界から受け入れ、ORTを実施している。これまでの受け入れ人数は延べ８名である。

(5)　共同研究の実施

上記(2)の面談などをきっかけに具体的なアイデアを出し合い、これに基づいて産業界と共同研究を実施している。これまで延べ13社と実施している。

３．成果と波及効果

２章(1)～(5)の各業務を通じ、(4)の若手技術者もすでに学会講演会で成果発表を行っており、プロジェクト発足時の予想以上に人材育成の実績が上がっている。同時に本講座の職員は多数の原著論文、国内外の講演会での研究発表、技術書の執筆、特許申請を行い、活発に活動している。また(5)の共同研究は小規模予算で開始されるが、そのうちのいくつかは共同研究の初期成果がもとになり、外部資金を獲得する大型開発研究プロジェクトへと発展している。たとえば「NEDOエネルギー使用合理化技術戦略的開発」事業において、近接場光エッチング法を用いた光学素子用基板表面のサブナノ平坦化技術の開発が始まった（平成20年度より３年間）[7]。これは特に複雑な加工装置を必要とせず、ガラス、セラミックス、半導体など、多様な基板表面の制御に応用可能な革新技術であり、多方面から大きな関心が寄せられている。このような発展には(4)のORTが有効に機能し、新技術を使いこなし更に発展させる能力を備えた産業界の若手技術者が育った事が決め手となっている。

一方、本プロジェクトを組織的に支援するため、次の２つの事業が発足した。

(1)　ナノフォトニクス研究センター（図３）

本プロジェクトの支援組織を確保する為に本学大学院工学系の中に昨年４月より発足した。筆者をセンター長とし、工学系の教員がメンバーとなっている。メンバー間の情報交換・共同研究によりナノフォトニクスの研究を深め広げて次の社会貢献の新たな核を形成する事を目標としている。また、２章(2)の個人面談などでは筆者の研究室のみでは対応しきれない境界領域分野に関する提案がしばしば見られるが、これを本研究センターのメンバーと共有し、産学連携の幅を広げている。

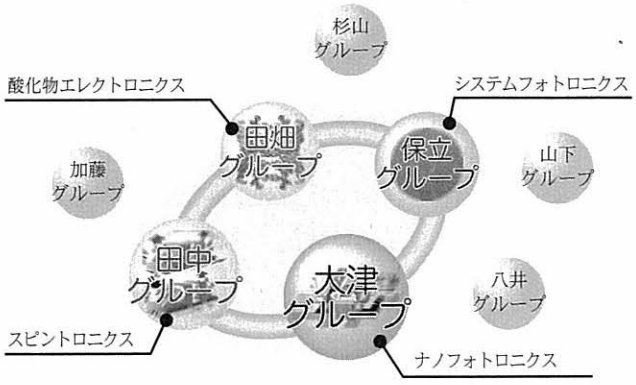

図３　ナノフォトニクス研究センターの構成

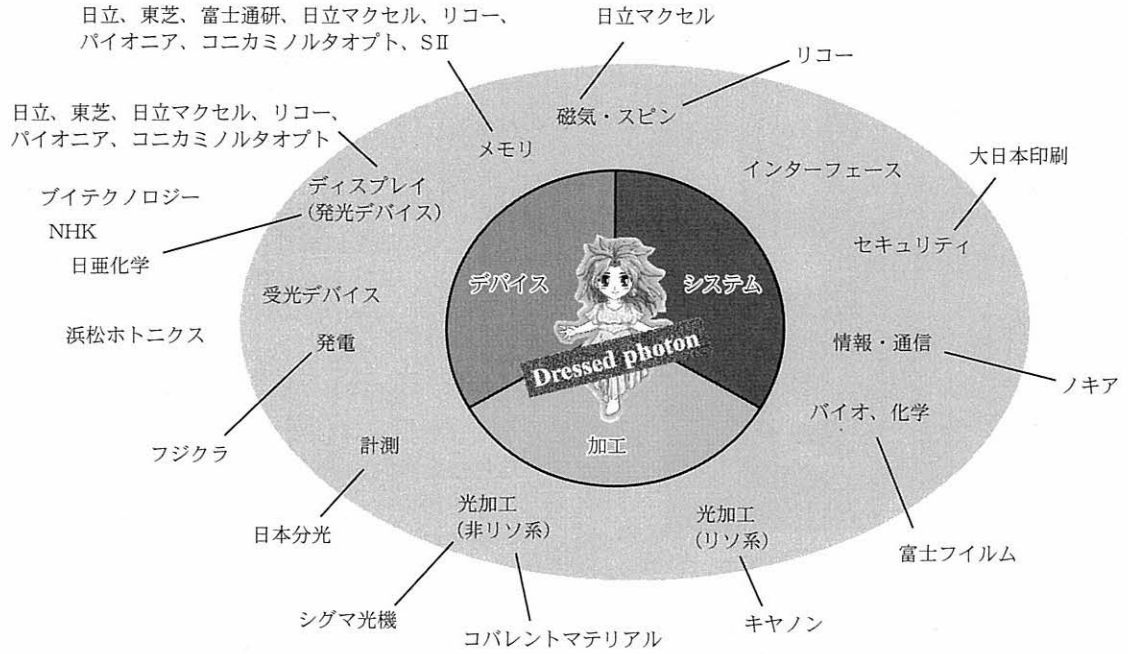

図4　ナノフォトニクスの多様な応用に関する産学連携の様子

(2) 特定非営利活動法人（NPO）「ナノフォトニクス工学推進機構」

1章のNEDO「大容量光ストレージ技術の開発」プロジェクト後の実用化開発を推進する事等を目的とし、平成17年に発足した。筆者が理事長を務めている。最近では事業の幅を広げ、本年度からは2章(3)のレクチャーシリーズよりも初歩的なナノフォトニクスの知識を学ぶセミナー「ナノフォトニクス塾」（初級編、中級編とも2日間にわたる集中講義）、技術の将来動向を深く探索する為のフォーラムなどの教育啓蒙事業も行う。

以上のように本プロジェクトと連携した教育啓蒙活動が急速に進み、それが国外からも注目されるようになった。欧米では、日本のナノフォトニクスの基礎・応用をリードしている事を認識し、近年は日本との情報交換・研究交流の希望が多く寄せられるようになった。これを受けて筆者らは日本と相手国との2国間交流を企画し、これまでに米国、豪州、ドイツを相手とし、ワークショップを複数回実施している[8]。この会合には2国から10名程度の少数のトップランナー研究者の参加のみに限っているが、これに本プロジェクトに関連する産業界の技術者の参加を呼びかけ技術成果の発信の機会を供与している。技術者の世界舞台へのデビューという観点でもこの活動は人材育成の効果を挙げている。

4．おわりに：展望とまとめ

1993年に筆者がナノフォトニクスを提案した後しばらくは他機関・他国からの関連する研究発表件数は極めて少なかったが、近年はそれが激増している。これは欧米でナノフォトニクスに対する関心が急増したことを反映している。米国でのナノフォトニクスに関連する研究開発の状況は参画企業61社、関連する研究機関数21、関連プロジェクト予算327億円（本年度）であり、EUでは各々74社、16、39億円（本年度）に上っている。これは日本の数値と比べると膨大である。特にEUではナノフォトニクスを次世代の光通信システム技術の中核に置いており、技術開発が極めて協力に推進されている[9]。ただし欧米ではナノフォトニクスの定義が曖昧かつ広義になっており[10][11]、プラズモニクス、メタマテリアル、シリコンフォトニクス、フォトニック結晶などの技術も含まれている。しかしこれらは波動（回折）光学技術なので、技術の「質的変革」を生む事は難しい。新しい技術の確立の為には、ナノ寸法の局所領域での光子の実体をはじめとする基礎原理を探索し、これを応用に結びつける努力が必要である。これに関わる実績では日本がリードを保っており、筆者の研究グループではナノフォトニクスに関わる各種技術開発に関し、本プロジェクト発足の前後にわたり積算すると延べ29社との共同研究が進んでいる（図4）。しかし欧米の急追

をにらんだ対策を怠ると、日本発の本技術が将来は欧米の後塵を拝する危険性もはらんでいる。

これを避ける為には本プロジェクトが実施する人材育成は重要である。ただし人材は短期間で育成できるものではない。本プロジェクトの期間は５年であり、当初の予想以上の成果を挙げているものの、この期間に挙げられる実績はわずかである。プロジェクトを継続発展するために長期的な展望にたった施策が必須である。

一方、このような産学連携の活動にはマネージャーの活躍が不可欠である。知財の取り扱いなどの調整に慣れ、また両組織間の主張を調整できる能力のある調整役がいなければ実質的な活動はできない。今後はこのようなマネージャーを育てる人材育成活動も重要になると思われる。なお、本プロジェクトに関連する情報の詳細は筆者のHP（http://uuu.t.u-tokyo.ac.jp）を参照されたい。

〈参考文献〉

(1) 大津元一：応用物理、第77巻、第11号、pp.1341-1352 (2008)
(2) 大津元一編著：「大容量光ストレージ」、オーム社（2008年2月）
(3) 大津元一：光アライアンス、第19巻、第４号、pp.41-43 (2008)
(4) NEDOのHP、http://www.nedo.go.jp/activities/portal/p06020.html
(5) ㈱光産業技術振興協会編：情報記録テクノロジーロードマップ、㈱光産業技術振興協会（2006年3月）
(6) NEDOのHP、http://www.nedo.go.jp/iinkai/kenkyuu/hyouka/20h/21/4-2-1.pdf
(7) NEDOのHP、https://app3.infoc.nedo.go.jp/informations/koubo/koubo/FK/rd/2008/P03033/nedokoubo.2008-06-17.2881926733/
(8) 大津元一：応用物理、第78巻、第５号、pp.473-474（2009）
(9) MONA consortium編：A European roadmap for photonics and nanotechnologies, MONA (Merging Optics and Nanotechnologies Association) consortium (http://www.ist-mona.org/partners.asp) (2008)
(10) National Research Councilof the National Academies編：Nanophotonics Accessibililty and Applicability, National Academy Press (2008)
(11) A. Neogi 教授（North Texas Univ., USA）からの私信。広義にすることにより必ずしもナノフォトニクスには直結しない技術分野へも政府から資金を導入する事がその意図とのこと。

【筆者紹介】

大津元一
東京大学　大学院　工学系研究科
電気系工学専攻　教授
〒113-8656　東京都文京区弥生2-11-16
TEL：03-5841-1189　FAX：03-5841-1140

[V] PUBLISHED BOOKS